Modelling the diffusion of aluminium and manganese solutes and oxygen for low-density dual phase steel oxidation in short annealing conditions

Jack L. Isaacs

BSc. Hons in Applied Physics, University of Portsmouth

A thesis submitted to the University of Warwick for the degree of Doctor of Philosophy in Engineering

Steels Processing Group,

Warwick Manufacturing Group,

University of Warwick

June 2020

Table of Contents

List of Figures

List of Tables

Acknowledgments

It is with immense gratitude that I acknowledge Dr. Michael Auinger for all the support given on this project and thesis, without whom this project would have been very difficult.

I would also like to thank Professor Barbara Shollock and Professor Claire Davis for their guidance in helping me improve as a researcher.

Thank you to Tata Steel for the financial and material contribution to this project, and the industrial contacts Shangping Chen and Marga Zuijderwijk for their involvement.

A big thank you to my colleagues: Carl Slater for all the help with the modelling software, helping me solve many issues; Yuyi Zhu, for all the assistance with the IR furnace; Arunava SenGupta for steel modelling knowledge; Darbaz Krasraw for help with the mass spectrometer; Geoff West for the vacuum storage box and the support with the electron microscopes over the years; Stephen Spooner for the books and aiding in my transition from a physicist into a partial-chemist; Mohsen Aghadavoudi Jolfaei for help with the CCT diagrams; and all the laboratory staff at the university who helped me.

Finally, thank you to all my friends and colleagues at WMG mentioned here and elsewise, my friends outside of the university, and my family for the on-going support.

Declaration

I hereby declare that this thesis, submitted to the University of Warwick for the degree of Doctor of Philosophy in Engineering, is of my own work and has not been submitted for a degree at another university.

Abstract

The incentivisation of low density steel research is rooted in the reduction of greenhouse gases by lowering vehicle weight and increasing fuel efficiency whilst retaining the properties of conventional automotive high strength steels. Fe-Al-Mn-C steels are a promising class of monolithic low density steels that offer a combination of outstanding mechanical properties, weight reduction, high strength, and good oxidation resistance at elevated temperatures, amongst others. The incorporation of aluminium into these steels means that oxidation is prevalent at elevated temperatures both internally and externally. The dual phase steels in the Fe-Al-Mn-C category are of concern for the lack of knowledge surrounding the internal oxidation behaviour. This project focusses on the ferrite-austenite dual phase steels, which exhibit different diffusion speeds along with the different aluminium and manganese concentrations. This project was aimed at the investigation of the effects that adjacent ferrite and austenite grains have on the internal oxidation behaviour in short annealing conditions. The research involved the annealing of four low density steels of varying ferritic and austenitic crystal phases with grain sizes up to 20µm, at 850°C in different Ar + H_2O atmospheres to assess the effects of the dual phase nature of the steel on the oxidation at different surface oxygen concentrations. A computational model was built using COMSOL Multiphysics to compare and interrogate the results further. The results of the experiments did not present a significant difference in oxidation behaviour due to the dual phase nature; however, the simulation results show a slight difference in the oxidation of adjacent ferrite-austenite grains. The effect is obscured in the experimental results by the dominance of the aluminium grain-boundary flux component on the oxidation behaviour which transports the vast majority of the oxidising solute from deeper within the sample to the internal oxidation zone. Suggested further research is on the characterisation of when the dual phase nature of the steel has a large enough effect on the oxidation behaviour to become significant in terms of grain sizes. The knowledge generated by this project is this understanding of the internal oxidation

behaviour of low density dual phase Fe-Al-Mn-C steels during short industrial annealing conditions with grain sizes up to 20µm. Specifically the affirmation of the roles of the effective diffusivity, oxygen and metal solute flux, and the roles the grain boundary and grains play in the internal oxidation behaviour of low density Fe-Al-Mn-C with high aluminium and manganese under short industrial annealing conditions.

List of Abbreviations

CCT – Continuous Cooling Transformation

DP – Dew Point

IOZ – Internal Oxidation Zone

GB – Grain Boundary

LDS – Low Density Steel

RF – Reaction Front

TC – ThermoCalc Calculation

WCS – Worst Case Scenario

1. Introduction

Steel is an alloy of mostly iron with carbon contents up to 2.06 wt.% [1] and other additions such as chromium, manganese, silicon etc., used in most facets of modern industrial production and specifically heavily involved in the automotive industry. Steels are produced in a wide variety with specific compositions, microstructures, and mechanical properties for their customer's needs. The general production of steel will include: casting, heating/melting iron, recycled steel, and/or other material; shaping, generally using mechanical force to shape the steel e.g. into wires, slabs, tubes etc.; heat treatment, heating the steel to a specific temperature in specific atmospheric conditions (such as a reducing atmosphere of excess hydrogen to prevent oxidation) depending on customer's desired requirements - to alter the steel microstructure, relieve internal stresses, and/or prepare the slab for additional treatments [2]. The steels used in this project followed the processing format of: casting, reheating, rough rolling, reheating, hot rolling, coiling simulation, and cold rolling – the next step would be annealing, which is incorporated in the experimental phase of this project.

High strength steels including aluminium and manganese (Fe-Al-Mn-C) were developed around the 1950s [3, 4] as a candidate to replace the conventional Fe-Cr-Ni steels, but these Fe-Al-Mn-C steels were not widely implemented, and research was focussed on their mechanical properties. Within the last couple of decades serious attention has being given to the research of Low-Density Steels (LDS) with significant quantities of aluminium (3-12 wt.%). The main driving factor behind the research of low-density steel is its implementation into automotive industry products, which has been incentivised from the financial pressure placed upon steel companies by national governments in an effort to combat climate change, which the steel industry itself is a large contributor to, via reductions in CO_2 emissions by vehicles from a reduction in the vehicle weight with increased efficiency of fuel usage [3, 4]. Conventional steels used in the automotive industry are attractive due to their mechanical properties, high formability, recyclability, and relatively low cost. The Fe-

Al-Mn-C system is a promising class of monolithic low density steels that offers a combination of outstanding mechanical properties and specific weight reduction; in addition, these steels have been reported to possess many attractive properties such as high strength and toughness at room and low temperatures, good fatigue properties, as well as good oxidation resistance at elevated temperatures [3, 4]. One method to separate the properties of the steels in question is by the effects the alloying elements have on the mechanical properties:

Aluminium additions in steel, provide ferrite stabilisation, a reduction in weight, and has one of the highest oxidation potentials of any element and as such provides the majority of the corrosion protection, but can produce oxides that are difficult to remove. Aluminium is also widely used for solid solution strengthening in ferrite, and refining grains by inhibiting grain growth, creating a finer grain structure thereby increasing the strength and ductility simultaneously [3-10], although this effect on ductility sharply reduces with aluminium additions above 7wt.% [3]. It is also broadly used to stabilise nitrogen via aluminium nitride formation to improve impact toughness and reduce the cold brittle tendency; however, AlN formation removes the nitrogen from the solution thereby reducing its interstitial solid solution strengthening effect [3, 4, 9, 10].

Manganese is a broadly applied alloying element in steel which acts as an austenitic stabiliser, whilst often acting in conjunction with carbon for improved mechanical properties [3, 4, 6-8]. Although reducing a steel's ductility, manganese is commonly known to enhance hardness, strength, abrasion resistance, and hardenability, manganese generally provides better hardenability than most other alloying elements [3, 7-9, 11-13]. Manganese also is used to combine with oxygen and sulphur, aiding the steel in reducing the cracking and tearing during rolling, whilst enhancing the machinability by integrating with sulphur to form a soft manganese sulphide inclusion in the steel enabling consistent edge when cutting [11, 12].

The low-density Fe-Al-Mn-C steels may replace some conventional steels for automotive applications because of their high strength and low weight; a 1.3% reduction in density but with a 2% reduction in Young's modulus are obtained per 1 wt.% addition of aluminium [3]. The exciting possibilities of dual phase low density steels has propagated a large amount of scientific interest with primary focus on their mechanical properties [14-25], with consideration for the issues surrounding manufacturing, implementation, and product quality such as: microstructure evolution [3, 4, 26-34], materials processing [35-41], carbide precipitation [42-46], oxidation resistance [47-52], and many other research topics of a finer scope.

To the knowledge of the author there have not been any research papers or theses on the characterisation of internal oxidation behaviour of low density Fe-Al-Mn-C dual phase steels and the effect that the dual phase microstructure has on the intergranular oxidation. The vast majority of low density steel oxidation research has been conducted with focus on the external oxidation, and only mentioning internal oxidation in the explanation of the results of that. Internal oxidation research is sparse in comparison partially because there is a focus on producing external oxides, as they have been easier to treat, remove, and control the creation of, historically.

Oxygen is present during the high temperature steel manufacturing processes like casting and annealing, subjecting the metal to oxidation if the partial pressure of oxygen is higher than the oxide dissociation pressure (also called oxide formation pressure) at a given temperature, a value defined by the thermodynamic equilibrium of the metal and its corresponding oxide leading to the dissociation of the oxide when below the equilibrium partial pressure and the formation of the oxide when above [5]. The oxide formation concentration is the same concept, subject to the solubility of oxygen in the matrix, except a value with units [mol/m^3]; but whereas the formation pressure is atmospheric based, the formation concentration is solution based. Before the introduction of high aluminium concentrations to industrial steels, keeping the oxygen partial pressure below the oxide dissociation pressure, using high hydrogen and low oxygen atmospheres, was one method steel-making companies

used to prevent oxidation. This method of oxide prevention is now in need of modification as alumina formation occurs at extremely low oxygen partial pressures.

The addition of aluminium in steels sees the accompanying oxides forming externally (Oxide Scale) and internally (Internal Oxidation Zone (IOZ)). The alumina-involving scale is detrimental to the galvanisability of the steel which is the ability to coat the steel with a protective coating, commonly by submersion in a liquid Zinc bath. A poor coating adhesion reduces the surface quality of the final product and allows for further corrosion during the life of the product. Before the zinc coating is applied, the steel undergoes a very important step in the steel-making process: the annealing stage, which involves heating the steel above its recrystallization temperature and holding that temperature for a certain time to reduce the number of crystal lattice dislocations by allowing the diffusion of atoms. Although the method of heating and cooling can drastically change the final microstructure, the general aim of annealing is to reduce the hardness and increase the ductility of the steel, allowing greater ease in manipulating and forming the steel product. Standard commercial annealing procedures, from heating to cooling, can last hours; however, the industrial focus for this project was short annealing times, no greater than 10 minutes. This is also a suitable timeframe to observe the initial stages of internal and external oxidation, which is a relatively fast process at the high temperature of annealing.

Research into the formation of surface oxides and their effect on coating is on-going but before a complete picture of the external oxidation behaviour is complete, the sub-surface situation should be understood first as the migration of atoms through the steel substrate affects the surface oxidation mechanisms in many ways, including:

- The diffusion of solutes to the surface of the steel will change the reactants composition and affect the oxide stoichiometry, structure, and oxide surface adhesion.
- If the steel contains a critical concentration of a dense-oxide-forming solute (Cr, Al, or Si) the steel will see the production of a slowly growing external

layer of a stable oxide (Cr_2O_3, Al_2O_3, or SiO_2) which is dense and most often protects the underlying material from further oxidation [6]; but there are many interactions between the oxide phases produced which can alter this, such as manganese oxide disrupting a protective alumina scale.

- Microstructure variations affect the diffusivity of a species by the ratio of high-diffusivity pathways like Grain Boundaries (GB) to lower-diffusivity Grain/Bulk regions, affecting the species' diffusive flux, as well as the difference in diffusivities between steel phases themselves (e.g. α-iron (with BCC crystal structure, called Ferrite) vs γ-iron (with FCC crystal structure, called Austenite))
- The phases of steel Ferrite and Austenite contain different amounts of solutes, (phase stabilising qualities used in LDS - Austenite is richer in Mn, and Ferrite is richer in Al [5, 7, 8]) leading to varying surface and GB oxidative reactant concentrations as the different local grain phases contribute an unequal amount of solute flux. This can lead to an inhomogeneous dispersion and stoichiometry of internal oxides affecting the local area uniquely.

Fe-Al-Mn-C steels can have matrix phases consisting of Ferrite (α/δ), Austenite (γ), or a mixture of the two in what is called Ferrite-based Duplex steel, and Austenite-based Duplex steel- subject to the solute composition and production refinement methods (such as annealing) [3]. There are four steels investigated in this project, two dual phase (a and b), one austenitic (c), and one ferritic (d) steel:

Table 1.1 Project steel grades compositions, in wt.% and at.%

		Fe	Al	Mn	Si	C
wt.%	a) Fe-3Al-5Mn	91.61	2.87	4.85	0.51	0.16
	b) Fe-5Al-5Mn	89.73	4.75	4.85	0.51	0.16
	c) Fe-6Al-16Mn	78.19	6.00	15.00	0.01	0.80
	d) Fe-10Al	90.12	9.70	0.13	0.01	0.04
at.%	a) Fe-3Al-5Mn	87.88	5.70	4.73	0.97	0.71
	b) Fe-5Al-5Mn	84.45	9.26	4.64	0.95	0.70
	c) Fe-6Al-16Mn	71.34	11.34	13.91	0.02	3.39
	d) Fe-10Al	81.52	18.17	0.12	0.02	0.17

The steel grades in Table 1.1 were chosen for several reasons:

1. Industrial Relevance – These steels encompass a sizeable range of dual phase low-density steels with high Al and Mn, used at the forefront of Tata Steel's research.
2. Microstructure – The steel grades include two dual phase (ferrite-austenite), one pure ferrite, and one pure austenite microstructures. By comparing the kinetics of the pure ferritic and pure austenitic steels, the intergranular ferrite-austenite diffusion mechanics can be better elucidated. Albeit, whilst including compositional effects on kinetics, which are unavoidable in this type of research.
3. Composition – These dual phase steel grades were chosen as the window of ferrite-austenite Fe-Al-Mn-C dual phase microstructure relative to aluminium and manganese content is small, but this difference in Al content was expected to produce significant oxidation variances. The window of dual phase microstructure can be seen in Figure 2.4 and Table 2.1, which show that with a 2 wt.% Al difference, the phase fraction varies from Fe-3Al-5Mn (ferrite ~47.5%; austenite ~52.5%) to Fe-5Al-5Mn (ferrite ~69.3%; austenite ~30.7%).

The comparison of the internal oxidation phenomena in dual phase steel with the pure phase ferritic and austenitic steels allows the characterisation of the differences in the specific oxidation behaviour. The model will be created using the concept of Worst-Case-Scenario (WCS) where it is viable to do so, such as a surface oxygen flux minimum limit at 10% the initial. The experimental phase of this project involves the oxidation of these steels at an isothermal temperature of 850°C, in the presence of water vapour contents up to 2.5%, in noble N5 Argon (purity 99.999%) from a gas flow through liquid water (water in the flask is at temperatures 0°C, 10°C, and 20°C) in a round bottom flask; there will also be a variation of oxidation time to help identify the extent of oxidation through oxidation rate. The dew point is a temperature representative of the equilibrium between gaseous and liquid water where the atmosphere can contain gaseous water up to a maximum value called the

saturation vapour pressure. For example, if an atmosphere is saturated with water vapour at 50°C and the atmospheric temperature is reduced, there will be condensation. A variation in these dew points allows the management of the available surface oxygen concentration to be dissolved into the steel (subject to the hydrogen/water vapour equilibrium), comparing the oxidation behaviour by manipulating the oxygen penetration, and limiting the formation of certain oxide phases due to not meeting the respective dissociation concentrations.

The modelling work in this project was presented at the COMSOL UK 2019 conference in poster format.

1.1 Project Objective

There is a lack of specific understanding of the oxidation behaviour in local areas of differing adjacent steel phases (ferrite-austenite) in low density dual phase steels with aluminium and manganese additions in annealing atmospheres with grain sizes up to 20µm, and this project aims to alleviate that through the gained knowledge of:

- The understanding of the diffusing species of the oxidant (oxygen) and solutes (aluminium and manganese) with their effects on the fundamental internal oxidation behaviour of low-density dual phase steels with aluminium and manganese, with experimental verification in annealing atmospheres

This research, and its industrially relevant objectives, aims to fill a suitable void in literature and provide the industrial partner of this project with knowledge to better understand how industrial annealing conditions can affect low density steel oxidation; thereby, allowing greater informed discussions and decisions to be made in regards to low density steel production and utilisation.

To elucidate low density dual phase steel internal oxidation, this project will see annealing experiments carried out in industrially relevant conditions, coupled with an isothermal mathematical model using the software COMSOL Multiphysics.

Minimising variables to efficiently characterise active effects is a key part of experimental procedure and this project's most important variable to isolate is the total dissolved oxygen concentration, as this will affect where and when oxide formation occurs the greatest, in isothermal conditions. As a species' flux is a time-dependant variable consisting of diffusion speed and concentrations, altering the annealing duration is an effective way of controlling the total dissolved oxygen content.

1.2 Research Questions

The main research questions nucleating this project include:

- What is the internal oxidation profile of high Al and high Mn ferrite/austenite dual phase low-density steels?
- How does a low density steel's dual phase microstructure affect the internal oxidation?
- Does the dual phase nature of the steel affect the intergranular oxidation between two heterogeneous crystal phases?

1.3 Hypothesis

The main hypothesis of this project is that there will be a visible significant difference in oxidation behaviour due to the dual phase nature of the steel. This is because a diffusing species' speed through austenite and ferrite are different, as well as the compositional differences between the two phases contributing unequal solute fluxes to the oxide formation.

2. Literature Theory Review

2.1 Thermodynamic Fundamentals

The energy of a system is subject to change from temperature, pressure, and constituents. The free energy of a substance depends on its quantity, chemical nature, state (solid, liquid, or gas), temperature, and pressure [5, 7, 53]. The chemical potential μ of a system (called partial molar free heat content) is defined as:

$$\mu = \left(\frac{\partial G}{\partial n_i}\right)_{T,p,n_j}$$

Equation 2.1

Where *G* is the Gibbs energy.

Relating the change in enthalpy of a system when 1 mol of component *i* is added to the system while other variables (*T, p,* n_j) are constant.

Energy differentials are the driving forces for thermodynamic interactions, with the possibility of a reaction occurring being represented by the Gibbs free energy (*G'*) of that system (Second Law of Thermodynamics) [5, 6]:

$$G = H - TS$$

Equation 2.2

Where *H'* is enthalpy, *S'* is entropy of the system, and *T* is temperature.

The free-energy change of a process will affect the outcome of the interaction, depending on the value [6]:

$\Delta G' < 0$ - a spontaneous reaction is expected

$\Delta G' = 0$ - the system is in equilibrium, no macroscopic reaction

$\Delta G' > 0$ - the process is thermodynamically impossible, or going in the other direction

The Gibbs free energy of an oxidative system enables the researcher to calculate the possibility of a reaction, the rate of reaction, and the oxygen formation pressure for the different possible oxide species. The categorisation of the reaction starting

conditions (oxygen concentration) for different oxide species is important in creating an accurate model, as a critical concept of the oxide barrier effect might be based around the local oxide density forming from the reactions. For a certain chemical reaction [7]:

$$aA + bB = cC + dD$$

Equation 2.3

Where,

$$\Delta G = \sum \mu_{products} - \sum \mu_{reactants}$$

Equation 2.4

ΔG can be also expressed in terms of the Mass Action Law, the ratio of product activities to reactant activities including stoichiometric coefficients, as [5, 54]:

$$\Delta G = \Delta G° + RT\ ln\left(\frac{a_C^c a_D^d}{a_A^a a_B^b}\right)$$

Equation 2.5

Where *ΔG°* is the free-energy change when all species are present in their standard states, *a* is the thermodynamic activity which describes the deviation from the standard state for a certain species, and *a, b, c, d* are stoichiometric coefficients from the reaction.

The standard free-energy change (*ΔG°*) can be expressed as [6, 7]:

$$\Delta G° = c\Delta G°_C + d\Delta G°_D - a\Delta G°_A - b\Delta G°_B$$

Equation 2.6

Where $\Delta G°_i$ etc. are standard molar free energies of formation for component *i*.

2.2 Activity

The activity of a gaseous species is related to the deviation of the chemical potential from its standard state and in an example of a gas:

$$a_i = \frac{p}{p^\circ}$$

Equation 2.7

Where p and p° are the partial pressure of a species and the same quantity in its standard state (1 [atm]).

The equilibrium state of a system with constant temperature and pressure is characterised by the minimum free energy [6]. For a binary system, the uniformity of the chemical potential μ is the minimum free energy, represented in terms of Gibbs energy as:

$$G = (1 - X)\mu_A + X\mu_B$$

Equation 2.8

Where μ_A and μ_B are the chemical potentials and *(1 - X)* and *X* are the mole fractions of *A* and *B* respectively.

The molar free energy of mixing incorporates the unmixed components in their standard states and Equation 2.8 to give:

$$\Delta G^M = (1 - X)(\mu_A - \mu^\circ{}_A) + X(\mu_B - \mu^\circ{}_B)$$

Equation 2.9

If ΔG^M is plotted against *X*, the tangent intercepts are $(\mu_A - \mu^\circ{}_A)$ and $(\mu_B - \mu^\circ{}_B)$, these quantities are the partial molar free energies of mixing, related to the activities by [6, 7]:

$$\mu = \mu^\circ + RT \ln a$$

Equation 2.10

2.3 Chemical Equilibrium

Chemical equilibrium is when a system does not have a propensity to change the concentrations of the reactants and products thereby effectively keeping the properties of the system the same. All systems tend towards an equilibrium point if no additions of reactants, products, or energy are made, with an equilibrium constant based on Gibbs free energy of formation used to define this point. The Equilibrium constant in terms of reaction constituents and coefficients [5, 7, 53]:

$$K_{eq} = \frac{[C]^c[D]^d}{[A]^a[B]^b}$$

Equation 2.11

2.4 Thermodynamic Stability Diagrams and Project Steel Data

The "Ellingham-Richardson Diagram", is one that expresses the standard free-energy of formation of selected oxides as a function of temperature and oxygen partial pressure (e.g. H_2O/H_2); this diagram is useful as it allows the comparison of the relative stabilities of each compound, giving the reader a lot of information at a glance; the diagram can be used to illustrate different compounds e.g. carbides, oxides, sulphides, chlorides, nitrides etc., with the lower the position of the line the more stable the compound.

The Ellingham-Richardson diagram is a useful tool for oxide stability calculations, other tools like thermodynamics software FactSage [55] and ThermoCalc [56] allow the construction of accurate stability diagrams to be produced for the relevant compositions and conditions.

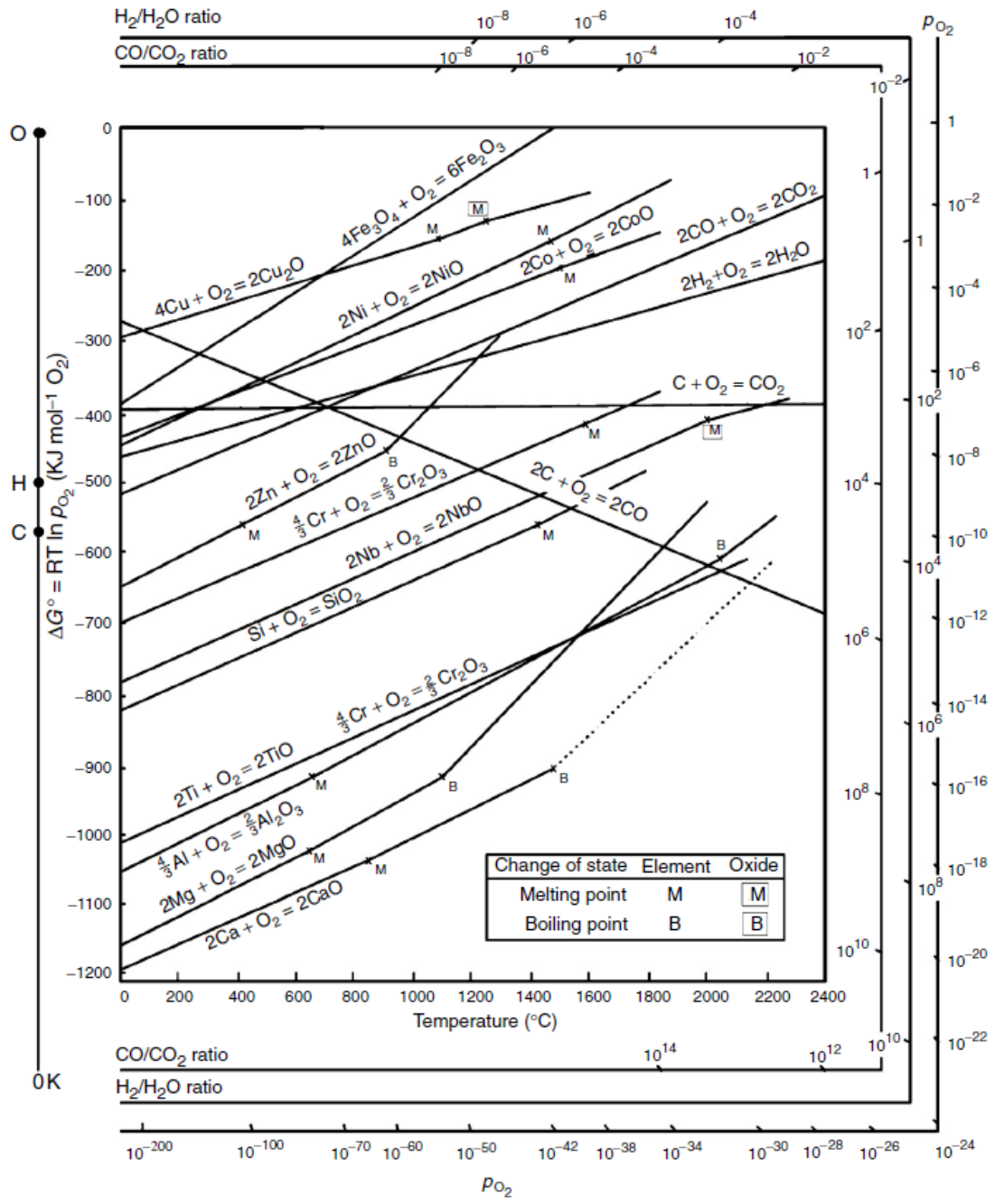

Figure 2.1 The Ellingham-Richardson Diagram [57, 58], showing the Standard Free-Energy of formation of selected oxides as a function of temperature, with partial pressure of oxygen given with additional relations to H_2/ H_2O, and CO/CO_2 ratios

2.4.1 Oxide Thermodynamic Stability Diagrams

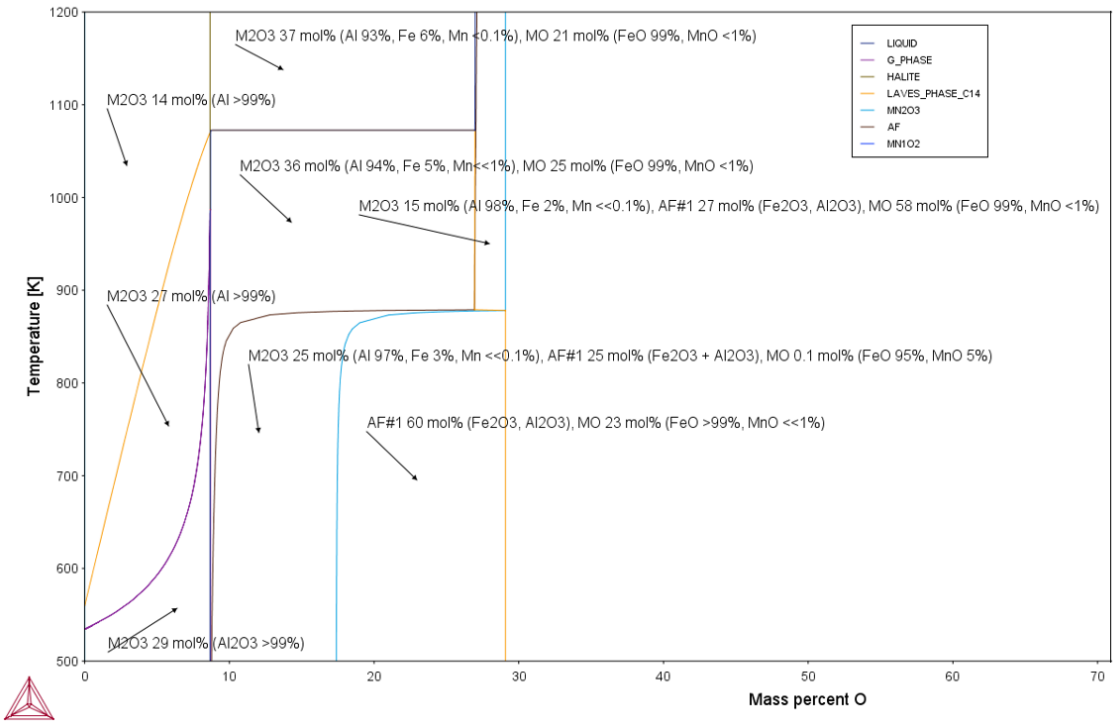

Figure 2.2 Fe-10Al Temperature - Mass percent oxygen stability diagram 1 atm, calculated using the software ThermoCalc without limiting the stable phases

Different types of diagrams are necessary to understand oxidation in its fullest (in absence of kinetics), Temperature - Mass % oxygen diagrams allow a specific system of constituents to be defined and investigated, above is the steel grade Fe-10Al.

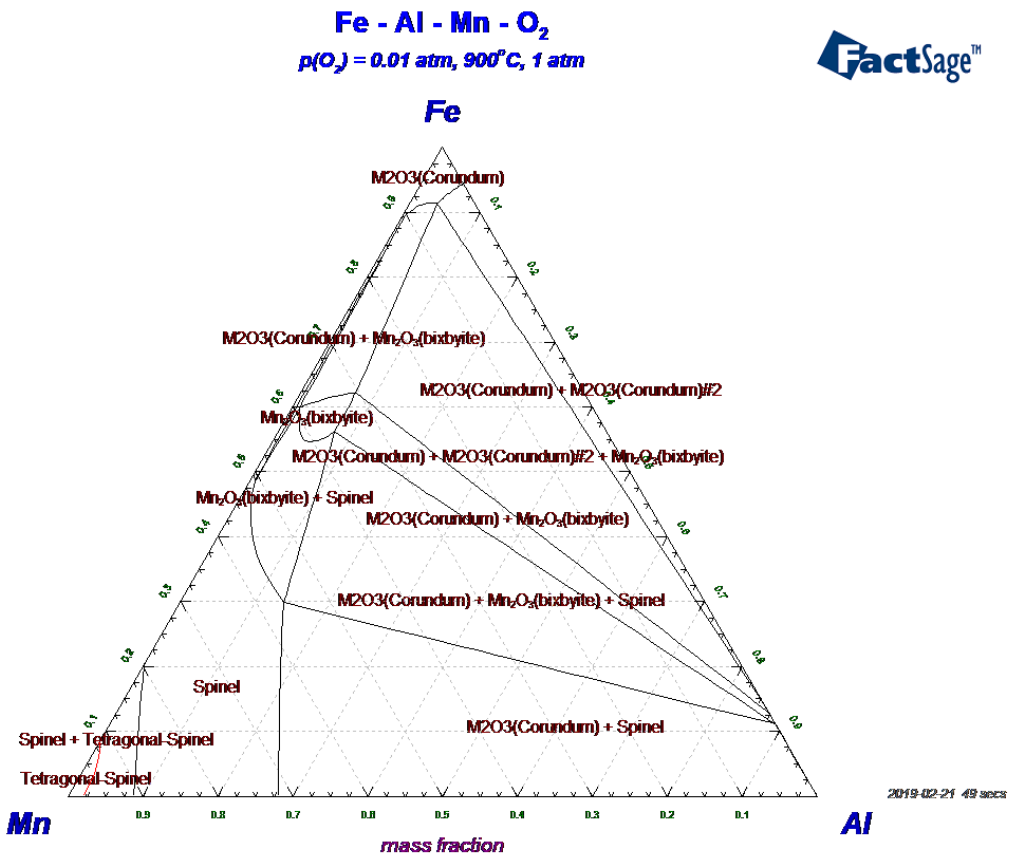

Figure 2.3 Fe-Al-Mn Ternary Phase Diagram at 0.01 atm partial pressure of oxygen at 900°C, calculated using the software FactSage

Figure 2.3 is a ternary diagram, where the corner of the respective element is considered as being composed of 100% of that element and the opposite side of the triangle being 0%, the fractions lines run from the corner towards the opposite side, with the respective scale running along the anti-clockwise edge. This diagram defines a system's temperature and oxygen content and allows the variation of constituents.

The different types of stability diagrams give an extensive view of what to expect during oxidation experiments, however, the full picture is only understood when coupled to the system kinetic information.

Supporting ThermoCalc phase diagrams have been presented below for all the steel grades investigated in this project, without silicon and other minor concentrations, except for carbon:

Fe-3Al-5Mn

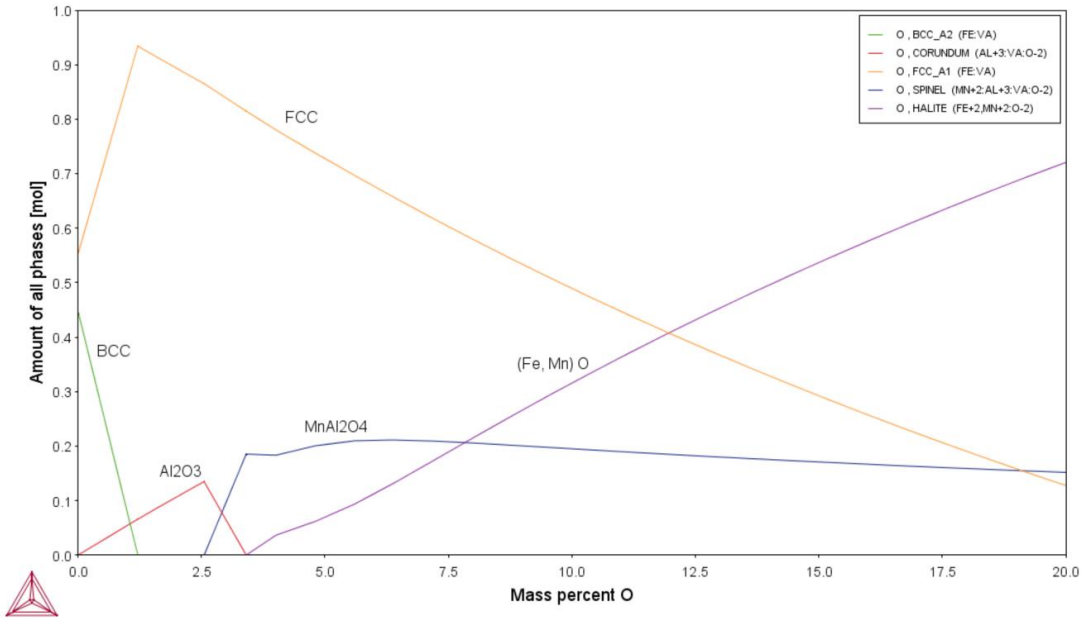

Figure 2.4 ThermoCalc phase diagram of Fe-3Al-5Mn grade steel (silicon removed); with amount of phase vs. the mass percent oxygen (up to 20%), at 1 atm, 850°C

Fe-5Al-5Mn

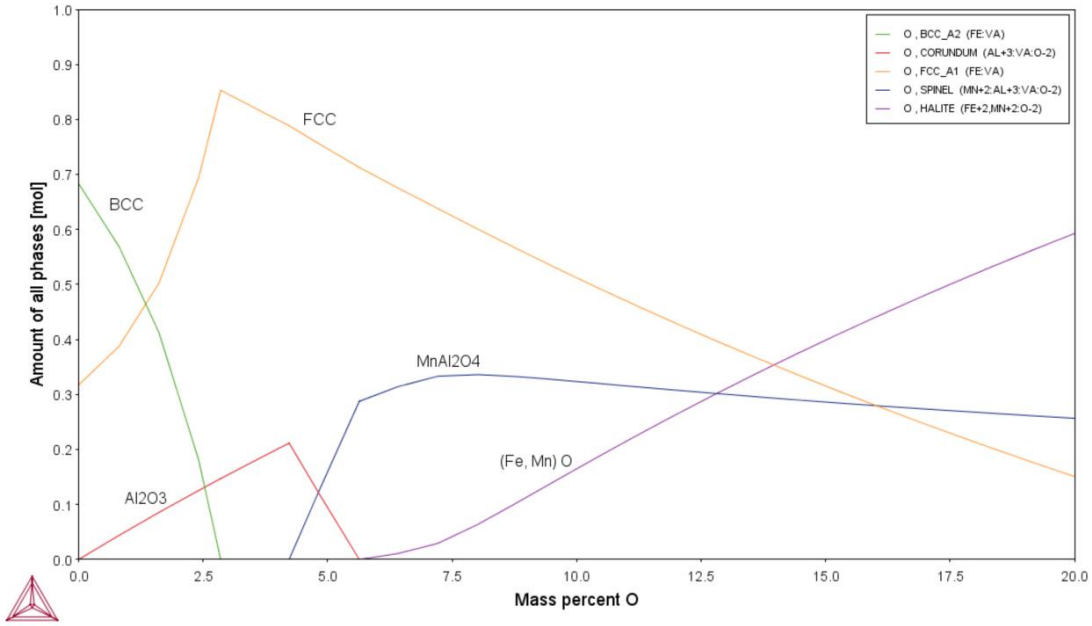

Figure 2.5 ThermoCalc phase diagram of Fe-5Al-5Mn grade steel (silicon removed); with amount of phase vs. the mass percent oxygen (up to 20%), at 1 atm, 850°C

Fe-6Al-15Mn

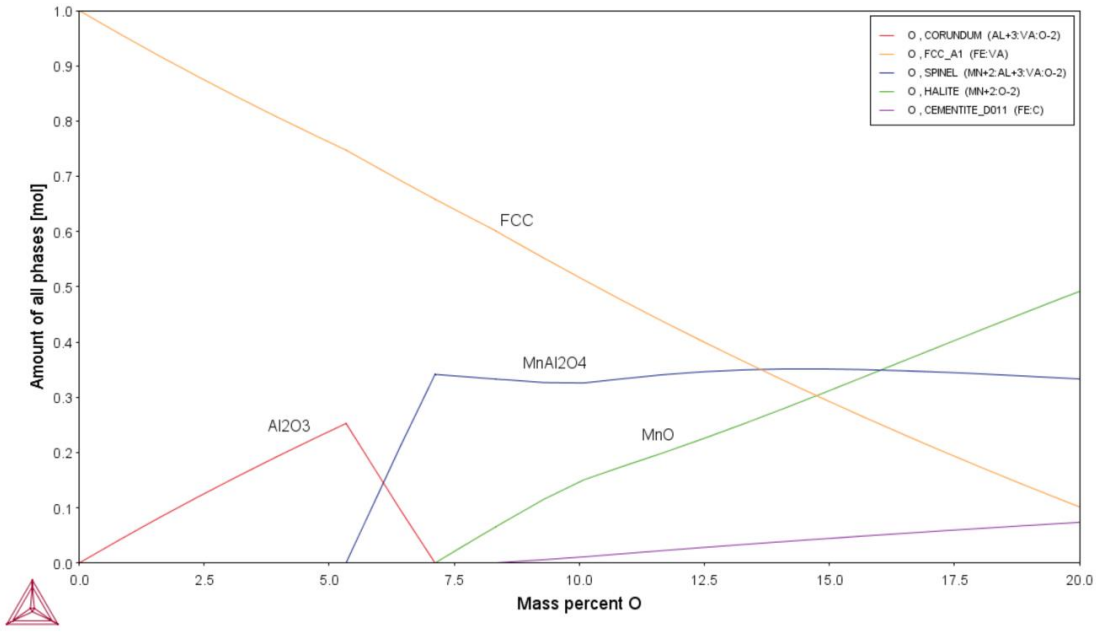

Figure 2.6 ThermoCalc phase diagram of Fe-6Al-15Mn grade steel (silicon removed); with amount of phase vs. the mass percent oxygen (up to 20%), at 1 atm, 850°C

Fe-10Al

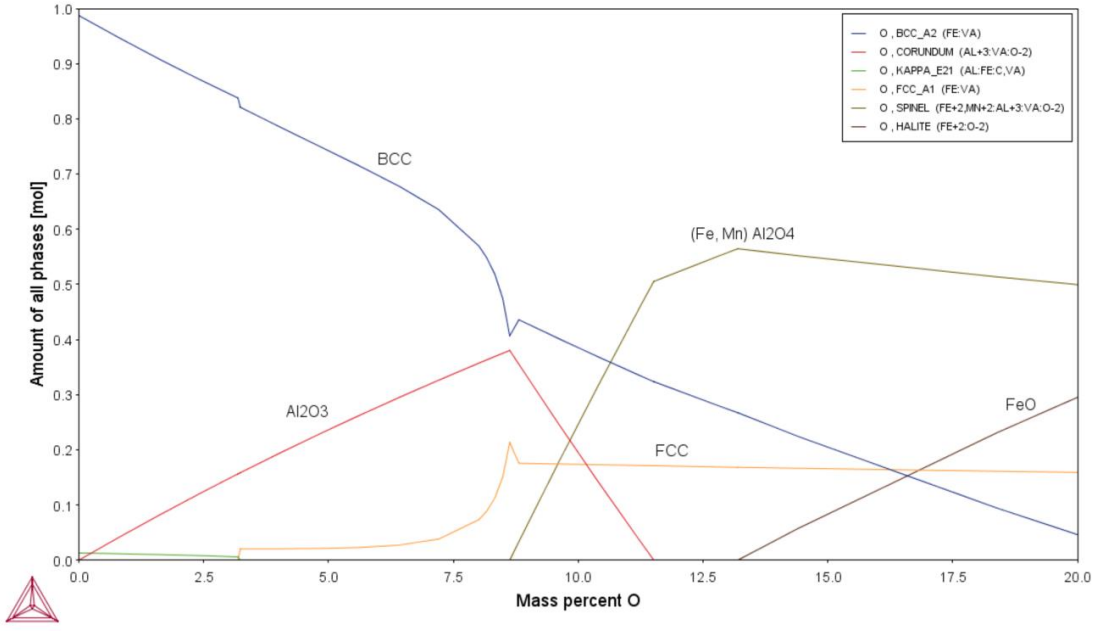

Figure 2.7 ThermoCalc phase diagram of Fe-10Al grade steel (silicon removed); with amount of phase vs. the mass percent oxygen (up to 20%), at 1 atm, 850°C

The above figures give an almost comprehensive expectation of experimental reaction products, and what sequence of reactions can be applied to the model. Aluminium is oxidised first, producing alumina (Al_2O_3), until depleted; when manganese is present, the alumina will be further oxidised to produce manganese aluminate ($MnAl_2O_4$) until the alumina is depleted; If manganese concentration persists, manganese oxide (MnO) will form until depletion of manganese; when the local oxygen concentration passes the wüstite formation concentration, a halite (Fe,Mn)O will form. This sequence of reactions is expanded upon in Section 3.5 for the model.

2.4.2 Steel Thermodynamic Stability Diagram

As a steel is heated up to the annealing isothermal temperature the microstructure will most likely change phases according to the current temperature, local composition, and a number of other factors like strain energy, initial microstructure, and the presence of precipitates. Both temperature and composition are the most relevant criteria of consideration for this project. Thermodynamics software allows researchers to track the microstructure with changes to initial steel composition and experimental temperatures as these will differ to the results seen in SEM at room temperature. This project uses two dual phase steels of similar composition, the effects on microstructure can be seen below in the ThermoCalc diagram which shows the stabilisation effects of aluminium and manganese on steel phases, ferrite and austenite respectively. Included also is a table showing the phase and elemental compositions of the dual phase steels.

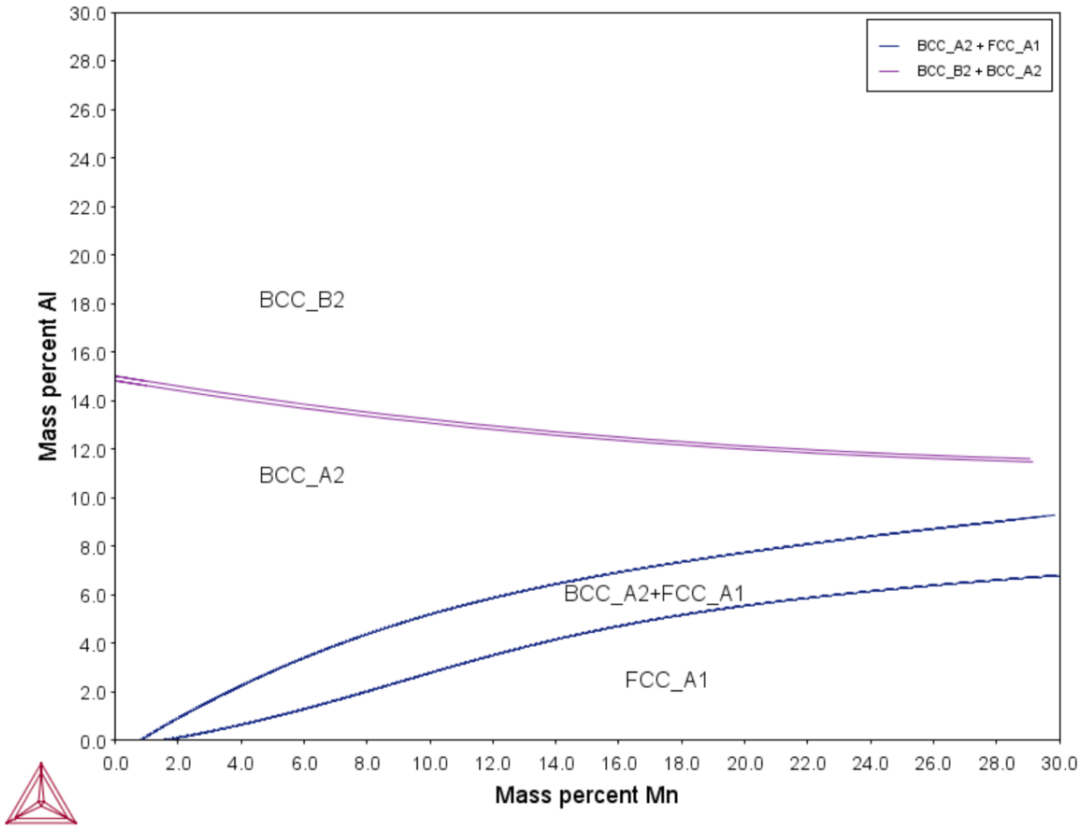

Figure 2.8 ThermoCalc diagram showing the stabilisation effects of aluminium on ferrite (BCC) and manganese on austenite (FCC) steel (zero carbon) phases at 850°C and 1 atm

Table 2.1 Project dual phase steels ferritic and austenitic elemental composition, 850°C, 1 atm. Equilibrium concentrations are calculated using the ThermoCalc software

850°C, 1atm	**Fe-3Al-5Mn**				
Phase Fraction	*Fe wt.%*	*Al wt.%*	*Mn wt.%*	*Si wt.%*	*C wt.%*
BCC (47.46%)	92.870	3.269	3.394	0.460	0.007
FCC (52.53%)	90.467	2.508	6.171	0.556	0.299
	Fe-5Al-5Mn				
BCC (69.23%)	90.564	4.991	3.940	0.496	0.009
FCC (30.76%)	87.834	4.203	6.918	0.542	0.502

Fe-3Al-5Mn

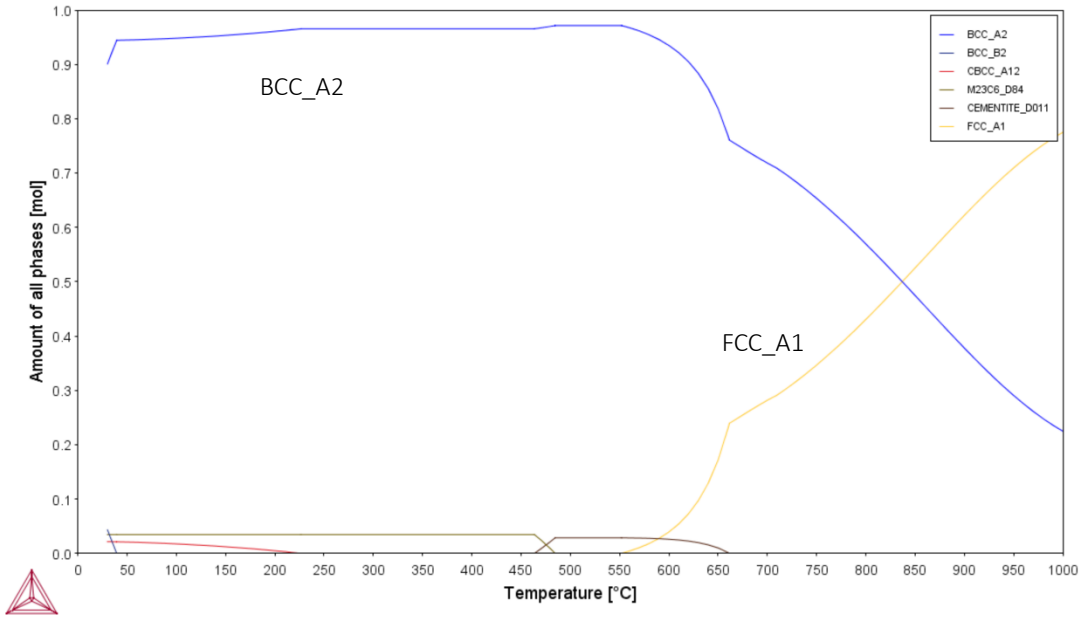

Figure 2.9 ThermoCalc phase diagram of Fe-3Al-5Mn grade steel (silicon removed); with amount of phase vs. temperature (up to 1000°C), at 1 atm, showing dual phase microstructure at 850°C

Fe-5Al-5Mn

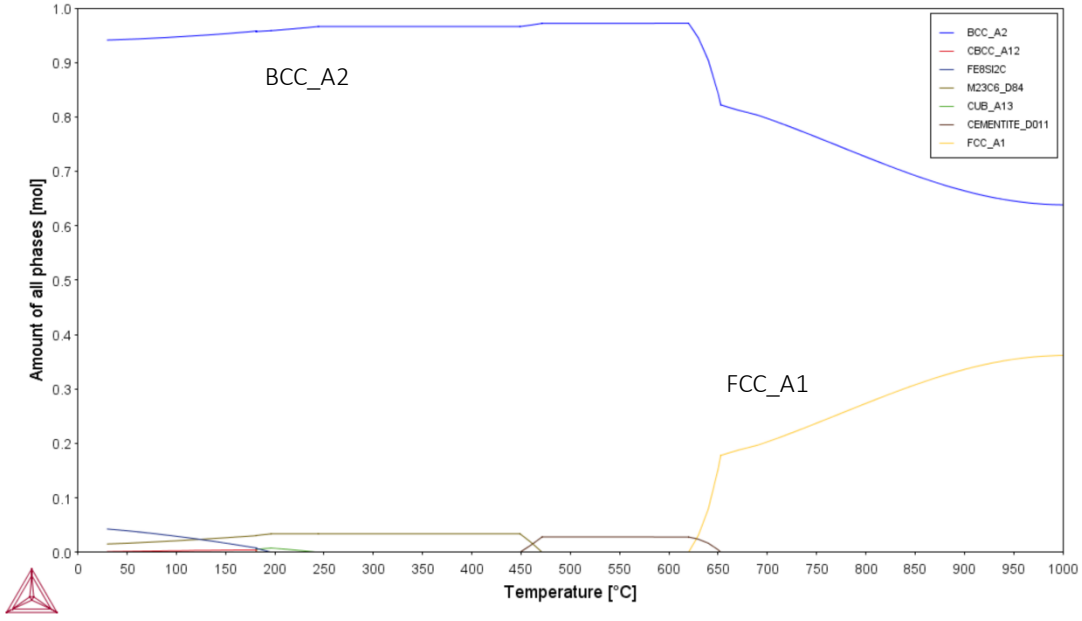

Figure 2.10 ThermoCalc phase diagram of Fe-5Al-5Mn grade steel (silicon removed); with amount of phase vs. temperature (up to 1000°C), at 1 atm, showing dual phase microstructure at 850°C

Fe-6Al-15Mn

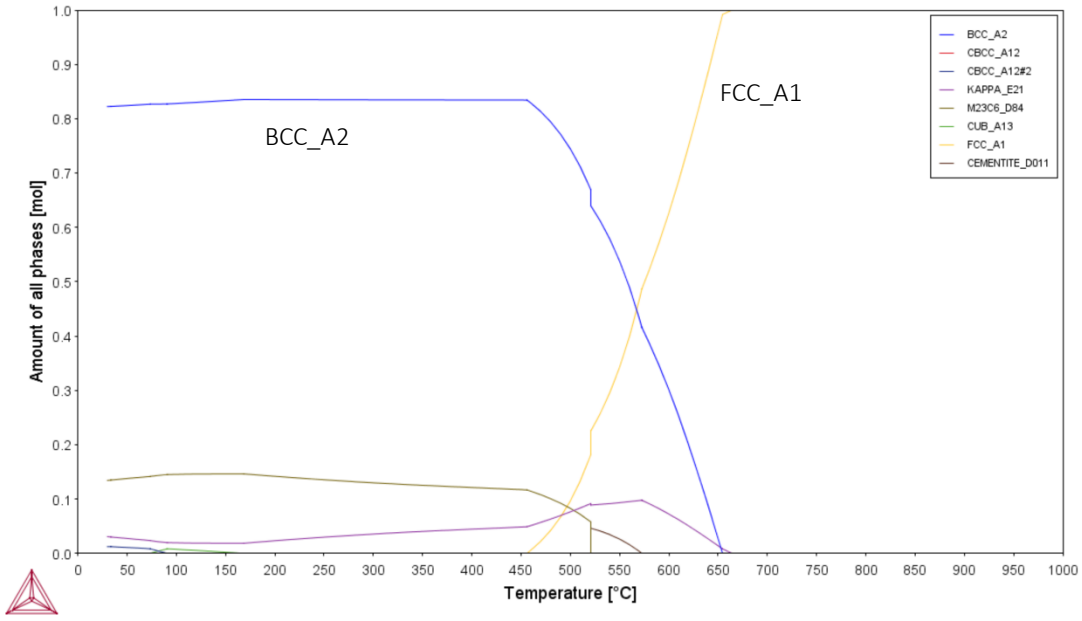

Figure 2.11 ThermoCalc phase diagram of Fe-6Al-15Mn grade steel (silicon removed); with amount of phase vs. temperature (up to 1000°C), at 1 atm, showing fully austenitic microstructure at 850°C

Fe-10Al

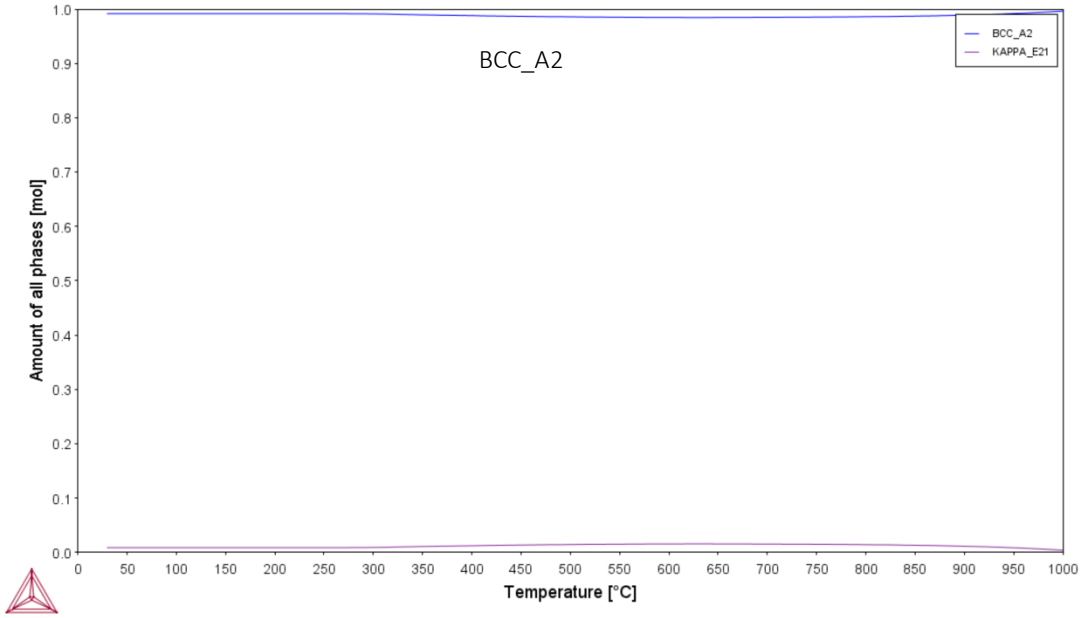

Figure 2.12 ThermoCalc phase diagram of Fe-10Al- grade steel (silicon removed); with amount of phase vs. temperature (up to 1000°C), at 1 atm, showing fully ferritic microstructure at 850°C

It is possible to retain similar or the actual microstructure at room temperature through a very fast cooling rate, known as “quenching” and phase stabilising elements such as aluminium and manganese. Quenching can lead to various microstructure constituents based on the cooling rate, in this project a software called JMatPro [59] is used to predict the microstructure using the cooling rates obtained from the temperature profiles.

2.5 Steel Structure

Oxygen occupies and diffuses in interstitial sites which are sites created from the voids between parent lattice atoms. The most common iron lattices are made up of Body Centred Cubic (BCC, in steel called Ferrite) and Face Centred Cubic (FCC, in steel called Austenite) lattice structures [3, 5, 8, 60]; these lattice structures form in the liquid to solid transformation where the nucleation of the solid phase will occur in multiple areas, and as the solid phase grows with the attachment of more atoms to the crystal it will come into contact with another solid phase area (called a grain) with a mismatch of atoms between called a grain-boundary (GB). Grain-boundaries are generally characterized by the relative orientation and distance of one planar crystal surface to a second crystal surface [53]. Once solidification is complete the material will be considered polycrystalline (made up of many crystals). Different phases of these grains will form depending on their compositions and conditions; these are shown in phase diagrams.

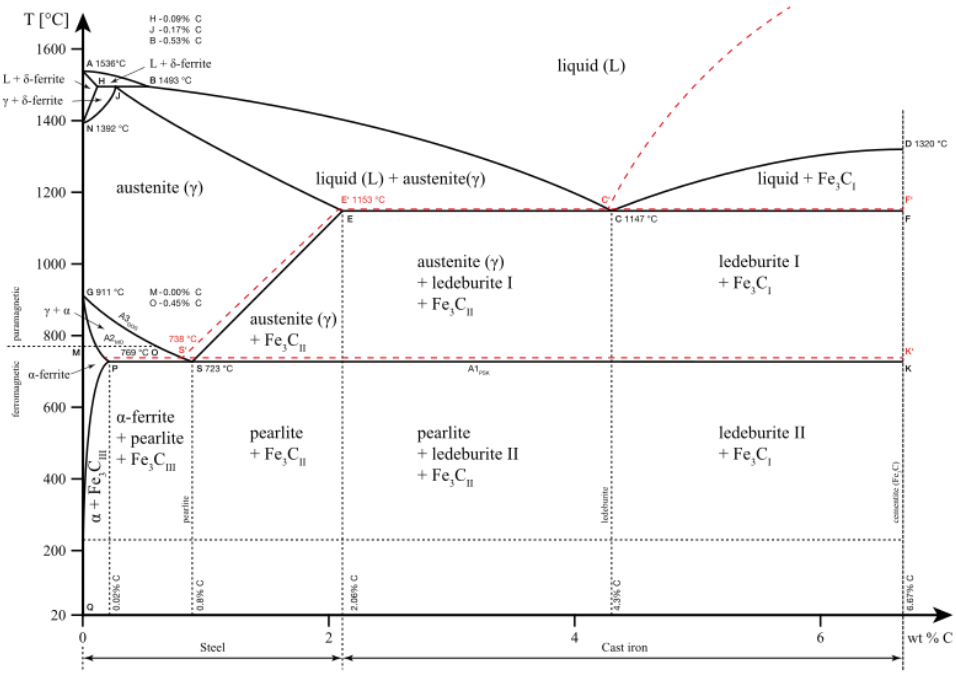

Figure 2.13 Iron - carbon phase diagram, up to 6.67 w.t% which is the composition of cementite (Fe_3C) [61]

The crystal grain is the low energy state for the conditions present and has the most efficient packing structure, which for iron is mostly BCC and FCC structures [8]. The grain boundary is a mismatch between the adjacent grains and that means a less efficient packing structure and the atoms occupy sites that are farther away on average than the crystal lattice [62].

2.6 Surface Oxidation

Oxidants in an atmosphere react at the surface of a clean steel sample with the equation:

$$\frac{2x}{y}M_{(s)} + O_{2(g)} = \frac{2}{y}M_xO_{y\,(s)}$$

Equation 2.12

Where *M* is the metal species, and *x* and *y* are the stoichiometric coefficients of the metal and oxidant [7]

The species of oxide formed is subject to the standard free energy of reaction of the species, the partial pressure of oxygen, and the composition of the steel. The relationship between standard free energy of reaction $\Delta G°$ and oxygen partial pressure pO_2 is defined by the difference in chemical potential of the products and reactants [5]:

$$\Delta G° = \mu°_{MO} - \mu°_{M} - \frac{1}{2}\mu_{O_2} = \frac{1}{2}RT \ln pO_2$$

Equation 2.13

Leading to an equation for the dissociation partial pressure of oxide:

$$pO_2 = e^{\left(\frac{2\Delta G°}{RT}\right)}$$

Equation 2.14

Which for 850°C, calculated using FactSage, is:

$pO_2(FeO) = 1.56 \times 10^{-18}$ [atm]

$pO_2(Al_2O_3) = 5.44 \times 10^{-40}$ [atm]

This initial stage of oxidation sees the establishment of a thin growing oxide scale which separates the reactants and any further reaction must rely on the transport of one or both the reactants and electrons across the scale [63]. Surface oxidation of a binary alloy by cation migration through the scale will grow at the gas-scale interface, the migration of oxygen anions across the scale will see new oxide formation at the scale-metal interface.

In a steel with multiple alloying elements, like Fe-Al-Mn-C LDS, the scale separates the reactants and the concentration of oxygen will vary with depth, surface oxygen partial pressure, and oxide stoichiometry (n-type or p-type semiconductor behaviour). This variance in the oxygen concentration across the scale leads to different phases of oxides forming with the higher oxides (least stable) forming at the

gas-scale interface [5] (such as MnO), and the lower oxides (most stable) forming at the scale-metal interface (such as Al_2O_3).

There is a special class of very stable oxides to be considered with steel production, those that form compact, protective oxides such as Al_2O_3, Cr_2O_3, and SiO. If the initial concentration of or the flux of the metal ions from the steel bulk is enough to combat the oxygen penetration, an exclusive and dense scale will form at the surface and prevent further oxidation [5]. This is because the mechanisms of diffusion of oxygen and the solute through the scale layer are hindered enough to effectively stop the migration; this is seen in alumina formation which is characterised by such a small stoichiometric window that the diffusion through lattice defects is extremely unlikely. If the solute flux to the surface is insufficient to form this protective scale, the migration of ions will continue and the external formation of higher oxides, and the internal oxidation of the substrate are possible.

There are far more aspects to external oxidation than those discussed in this project, but there is little relevancy in further consideration.

2.7 Mass Transport via Diffusion

Diffusion can be seen considered to be matter moving from one part of a system to another. In an isothermal, field-free system it can be specified that for a certain amount of matter dn_{A2} of component A moves from region 2 to region 1, and while each region is homogenous, the changes are shown as [5]:

$$dU = -T\,dS = \; -p_1\,dV_1 - p_2\,dV_2 + (\mu_{A1} - \mu_{A2})dn_{A2}$$

Equation 2.15

Where, dnA1 = - dnA2.

In a slow process, the pressure is said to not vary the equation [6], and from the second law of thermodynamics we know for a spontaneous process:

$$d(U - TS) < dw$$

Equation 2.16

Therefore, the necessary condition for isothermal mass to transfer is:

$$(\mu_{A1} - \mu_{A2})dn_{A2} < 0$$

Equation 2.17

Equation 2.17 shows that for a positive transfer of component A, the chemical potential of region 2 must be greater than that of region 1, meaning diffusion generally occurs down the chemical potential gradient. The Gibbs energy of a phase can be written as:

$$G^{\alpha} = X_A^{\alpha}\mu_A^{\alpha} + X_B^{\alpha}\mu_B^{\alpha}$$

Equation 2.18

Where X_A is the composition of A in phase α in mole fraction, representing this equation in graphical form:

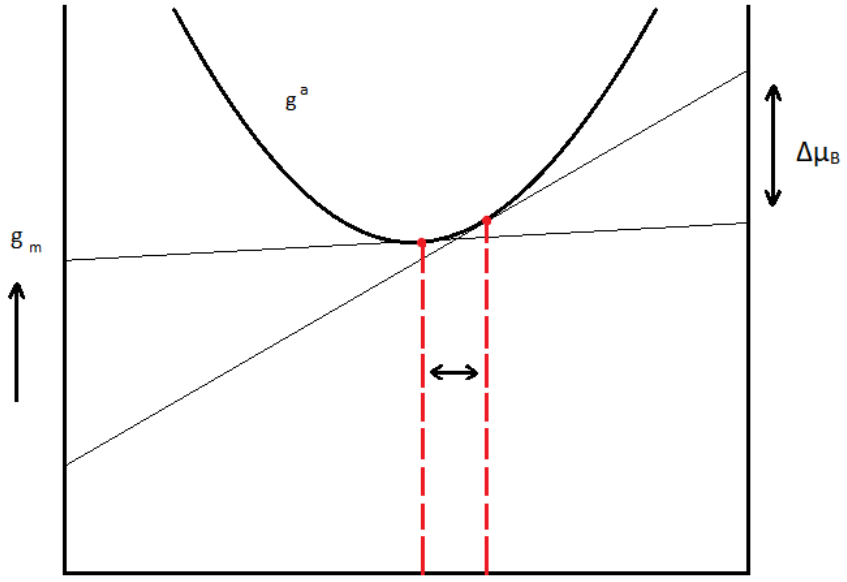

Figure 2.14 Diagram showing the Gibbs energy (g) on the y-axis, and composition (x) on the x-axis, and the chemical potential (μ) of a species is given by the intercept of the tangent on the right-hand side. Seen in the book Thermodynamics, Diffusion and the Kirkendall Effect in Solids [64]

With the chemical potential difference of A and B in α-phase equal to the slope of the tangent represented as [64]:

$$\frac{dG^{\alpha}}{dx_B} = \mu_B^{\alpha} - \mu_A^{\alpha}$$

Equation 2.19

The positive curvature provides a driving force for diffusion by the rectification of compositional differences. In an example of two regions with differing non-zero amounts of a component B coupled to each region's Gibbs energy with G_B, with the difference in G_B directly related to the decrease in Gibbs free energy from the transfer of one mole of component B. Therefore with the assumption that the rate of transfer is directly proportional to the decrease in Gibbs free energy, and that the number of B atoms per volume $\frac{x_B}{v_m}$ and inversely proportional to the transport distance Δy, leads to an expression for the flux of B [64]:

$$J_B = -\frac{M_B x_B}{v_m}\frac{\Delta G_B}{v_m} = -\frac{M_B}{v_m} X_B \frac{dG_B}{dx_B}\frac{\Delta x_B}{\Delta y}$$

Equation 2.20

Where the constant of proportionality M_B is regarded as the mobility of *B*.

By introducing the curvature of the graph, and in incorporating Fick's concepts we get:

$$D_B = M_B x_A x_B \frac{d^2 G}{dx_B^2}$$

Equation 2.21

With consideration of the phenomenological constant for *B*, which is $L_B = M_B C_B$ and remembering the relation between chemical potential and activity, the flux of component B, J_B, in terms of chemical potential μ_B can be given as [5, 64]:

$$J_B = -L_B \frac{d\mu_B}{dx}$$

Equation 2.22

And the flux can be written in terms of concentration for B, which is known as Fick's First Law [5, 64]:

$$J_B = -D_B \frac{dC_B}{dx}$$

Equation 2.23

By this it can be seen that diffusion is driven by chemical potential gradient which is also most of the time the same direction as the concentration gradient. The chemical potential for alumina formation (the most stable oxide in Fe-Al-Mn-C steel grades) is so large that the equilibrium constant is around 15 magnitudes higher than Fe, Mn oxides formation seen in FactSage data in Table 2.1. α-Al_2O_3 (corundum) is the most protective and stable oxide among all the oxides commonly encountered in high temperature oxidation [7].

Table 2.2 FactSage - oxide equilibrium constants Keq at 850°C, (FeOf represents FeO formation from ferrite etc.)

Name	***Expression***	***Value***	***Description***
KeqAl2O3	(exp((-rAl2O3)/(R*T)))	6.58E+30	Al_2O_3 reaction Keq
KeqMnO	(exp((-rMnO)/(R*T)))	1.23E+14	MnO "
KeqFeOf	exp((-rFeOf)/(R*T))	7.75E+08	FeOf "
KeqFeOa	exp((-rFeOa)/(R*T))	7.98E+08	FeOa "
KeqMnAl2O4	(exp((-rMnAl2O4)/(R*T)))	2.04E+15	$MnAl_2O_4$ "
KeqFeAl2O4f	(exp((-rFeAl2O4f)/(R*T)))	4.17E+09	$FeAl_2O_4$f "
KeqFeAl2O4a	(exp((-rFeAl2O4a)/(R*T)))	4.29E+09	$FeAl_2O_4$a "

2.7.1 Harrison Regimes of Diffusion

Harrison's regimes of diffusion are categories of diffusion profiles based on the Fisher model [65] which is the most commonly accepted representation of the grain-boundary diffusion system applying Fick's laws of diffusion to a simple homogenised geometry of structure grain-GB-grain for a polycrystalline substance. Le Claire [66] generalised the exact solution which involved a number of parameters, but the most relevant are the mathematical limits of the regimes: the Le Claire parameter (α) relating the effective GB diffusion width ($s\delta$) to the crystal grain diffusion speed (D_V); the parameter Λ relating the grain size (d) to D_V; and the dimensionless parameter (β) [53] which are represented by the equations:

$$\alpha \equiv \frac{s\delta}{2\sqrt{D_V t}}$$

Equation 2.24

$$\Lambda^* \equiv \frac{d}{\sqrt{D_V t}}$$

Equation 2.25

$$\beta = (\Delta - 1)\alpha = (\Delta - 1)\frac{s\delta}{2\sqrt{D_V t}} \approx \frac{s\delta D_{GB}}{2D_V\sqrt{D_V t}}$$

Equation 2.26

Where, Δ is the ratio of GB and grain diffusion speeds:

$$\Delta = \frac{D_{GB}}{D_V}$$

Equation 2.27

Harrison's regimes generally describe the differences temperature, elapsed time, and grain size (when $D_{DB} >> D_V$) have on GB - grain diffusion in polycrystalline materials like steels [53, 67, 68].

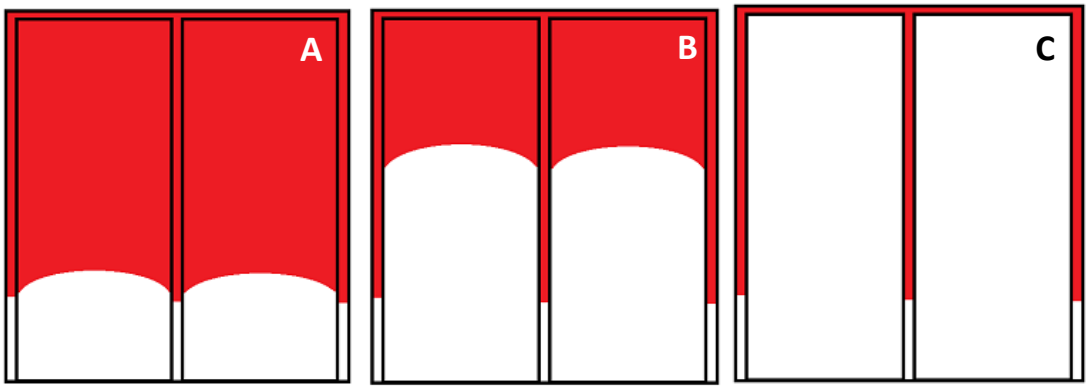

Figure 2.15 Harrison Regimes of Diffusion: Regime A, B, and C, displayed using the Fisher model [7, 53]

A) *Regime A* ($\alpha < 0.1$, $\Lambda < 0.4$): High temperatures or very long diffusion times, where grain-boundary diffusivity and grain diffusivity are similar.

B) *Regime B* ($\alpha < 0.1$, $\beta > 10$, $\Lambda > 3$): As the Temperature decreases from Regime A, the difference between the grain-boundary and grain diffusivities becomes significant.

C) *Regime C* ($\alpha > 1$): Corresponds to low temperatures, short diffusion times, and where the grain diffusivity is negligible and diffusion almost exclusively occurs in the grain-boundaries. This can also correspond to a system of very large grain sizes, as the penetration of the grain will be negligible compared to the GB.

2.8 Diffusion Mechanics

Atoms in the solid phase are not stationary, they vibrate around their mean energy position. Diffusivity of an atom relies on a jump site being vacant, and that the vibrating atom has sufficient energy to pass the activation energy barrier -Q_A and move through [62].

Oxygen, carbon, and nitrogen are small and occupy iron interstitial sites and diffuse to and from interstitial sites in BCC and FCC lattice structures; due to the low solubility of these interstitial elements, there is unlikely to be a certain interstitial site

containing an atom, therefore the diffusion is high as it does not rely on the probability of the neighbouring site being vacant.

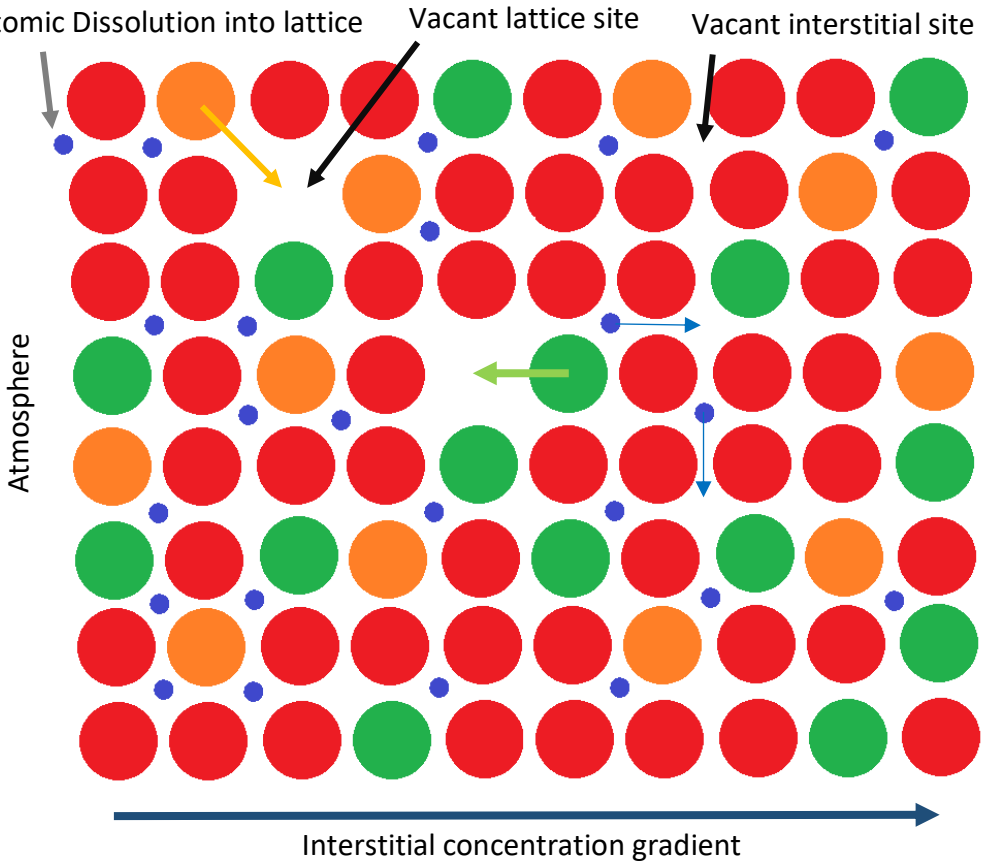

Figure 2.16 Simple 2D image of a red lattice with green and orange alloying element atoms, with blue interstitial occupiers; the vacant lattice and interstitial sites are point defects where related atoms can jump to – indicated by the black arrows; the grey arrow indicates that the surface of the lattice where an interstitial occupier has dissolved into a vacant site; blue, green, and orange arrows indicate some - but not all - possible atomic diffusive jumps

Elements like aluminium and manganese occupy lattice sites and diffuse through substitutional diffusion, which rely on a vacant lattice sites; when a substitutional atom diffuses, it swaps place with the vacancy. Substitutional diffusion relies on the probability of the neighbouring site being vacant and the probability that specific atom will have the energy necessary, so diffusion by this method is usually slower than interstitial diffusion by 4 - 8 magnitudes [62].

Diffusion and self-diffusion occurs about one hundred times more rapidly in ferrite (BCC) than in austenite (FCC) [8, 53, 62] because of the difference in packing density of the lattice [14, 16]. This is also relevant when describing the difference in diffusion

speeds between grains and grain-boundaries. As the grain boundary atoms are farther apart on average than the grain, the activation energy barrier of the diffusing atom is lower as the parent lattice atoms are less able to block the diffusional path.

Grain diffusion is also called bulk or volume diffusion, in this project diffusivities for a species X for grains and grain-boundaries are represented as D_{XV} and D_{XGB} respectively. The expression for diffusion speed D_X (also called Diffusivity) of a species *i* is presented below [5, 6, 7, 53, 64]:

$$D_i = D_{0_i}\, e^{\frac{-Q}{RT}}$$

Equation 2.28

Where *R* and *T* have their usual meanings, and D_{0i} with units [m^2/s] is the Arrhenius pre-exponent of which incorporates the terms of: the probability of finding an atom in the jump destination, the frequency at which the atom approaches the energy barrier, the density of sites, the activity coefficient, and the effective charge of the jump destination.

For 3D geometries, the grain boundary diffusivity is usually multiplied by the grain boundary width to acquire units of [m^3/s], but the model in this project is 2D so this was not done, and the units remain [m^2/s], this does not affect the results as the software calculates the diffusion profile of the grain boundary regardless.

As this project is based on Fe-Al-Mn-C steels, the consideration of the differences from conventional metals needs to be considered. Birks et al [6] have set out some ideas about alloy oxidation:

- The metals in the alloy will have different affinities for oxygen reflected by the different free energies of formation of the oxides
- Ternary and higher oxides may be formed
- A degree of solid solubility may exist between the oxides
- The various metal ions will have different mobilities in the oxide phases

- The various metals will have different diffusivities on the alloy
- Dissolution of oxygen into the alloy may result in sub-surface precipitation of oxides of one or more alloying element (internal oxidation)

The diffusion speed is affected by the size of atoms of the parent lattice as it changes the activation energy of diffusion, and as stated above, the composition of a steel is relevant to the diffusivity values. However, the diffusivity values in validated and trustworthy literature sources covering the diffusivities of oxygen, iron, aluminium, and manganese in Fe-Al-Mn-C (FCC and BCC) gains and grain-boundaries, and the relevant oxide phases is scarce to non-existent; values for most iterations of grain diffusivity in iron were found but not grain-boundaries and not all in the relevant oxides, due to this reason and considering the differences mentions in grain vs. grain-boundary activation energy and the terms incorporated into the Arrhenius pre-exponent, the values for the grain diffusivity were modified to represent the grain-boundary diffusivity, which is a common practice in high temperature modelling given the scarcity of reliable data in literature [69, 70, 71, 72]. This was done by increasing the Arrhenius pre-exponent by two orders of magnitude, and halving the activation energy; this method is somewhat common in grain boundary diffusion modelling [71, 73-75]. Two different sources provided iron grain-boundary diffusion speeds in iron, and these values are comparable - although all the grain-boundary diffusions speeds used in the model are all derived from the grain diffusion speeds to retain consistency, and are presented below with Diffusivities for 850°C:

Table 2.3 Diffusivity parameters table, including Diffusion coefficients, Arrhenius pre-exponential components, and activation energies for BCC and FCC steel phases. All values taken from "Numerical Data and Functional Relationships in Science and Technology" [76]

Diffusing species 850°C	Diffusivity (BCC) [m^2/s]	Diffusivity (FCC) [m^2/s]	D_0 (BCC) [m^2/s]	D_0 (FCC) [m^2/s]	Q_A (BCC) [kJ]	Q_A (FCC) [kJ]
Iron D_{FeV}	$1.38 * 10^{-15}$	4.99∗10−18	$1.90 * 10^{-4}$	$1.8 * 10^{-5}$	239.50	270.00
Aluminium D_{AlV}	$4.39 * 10^{-15}$	4.39∗10−15	$1.80 * 10^{-4}$	$1.80 * 10^{-4}$	228.20	228.20
Manganese D_{MnV}	$2.04 * 10^{-15}$	1.08∗10−17	$1.49 * 10^{-4}$	$1.6 * 10^{-5}$	233.60	261.70
Oxygen D_{OV}	$6.80 * 10^{-11}$	2.48∗10−12	$1.00 * 10^{-5}$	$1.3 * 10^{-4}$	111.12	166.00
Iron D_{FeGB}	$5.12 * 10^{-8}$	9.48∗10−10	$1.90 * 10^{-2}$	$1.8 * 10^{-3}$	119.75	135.00
Aluminium D_{AlGB}	$8.89 * 10^{-8}$	8.89∗10−8	$1.80 * 10^{-2}$	$1.80 * 10^{-2}$	114.10	114.10
Manganese D_{MnGB}	$5.51 * 10^{-8}$	1.32∗10−9	$1.49 * 10^{-2}$	$1.6 * 10^{-3}$	116.80	130.85
Oxygen D_{OGB}	$2.6 * 10^{-6}$	1.79∗10−6	$1.00 * 10^{-3}$	$1.3 * 10^{-2}$	55.60	83.00

These diffusivity parameters values are from well-sourced literature, values taken ascribe to the closest available appropriate variables such as temperature, host lattice composition, research group, and other parameters. Fick's First Law of diffusion, seen in Equation 2.23 for the relation between flux and concentration gradient is only concerned with the diffusion of one species, whereas Fick's Second Law works with what is known as "counter-diffusion", where in steel research is usually the diffusion of the solute to the internal oxidation zone.

Below is the expression for Fick's Second Law:

$$\frac{\partial N_B}{\partial t} = D_B \frac{\partial^2 N_B}{\partial x^2}$$

Equation 2.29

A useful tool for modelling, is the Diffusive Length expression, a value describing an estimation of the upper limit the diffusive species can travel [5, 7, 53].

$$\bar{l}_D = (Dt)^{\frac{1}{2}}$$

Equation 2.30

This value is useful in modelling internal oxidation as it helps with the determination of potential mesh elements densities, with the suggested 5-7 mesh elements per diffusive length.

2.9 Internal Oxidation

The phenomenon of internal oxidation occurs when the solubility of oxygen in the base metal is a non-zero value and the concentration of oxygen is (at least initially) below that for the oxidation of the base metal, but high enough for the solutes B and C. This leads to the penetration of oxygen into the steel substrate and subsequent diffusion driven mostly by potential and concentration gradients. Alternatively, if the concentration of oxygen is high enough to oxidise the base metal the local area's thermodynamic equilibrium will decide which metal species will oxidise.

Birks et al. [6] set out criteria for Internal Oxidation:

- The value of ΔG^o of formation (per mole O_2) for the solute metal oxide, BO_v, must be more negative than ΔG^o of formation (per mole O_2) for the base metal oxide
- The value for ΔG for the reaction B + v$\underline{O}$ = BO_v must be negative. Therefore, the base metal must have a solubility and diffusivity for oxygen which is sufficient to establish the required activity of dissolved oxygen $\underline{O}$ at the reaction front
- The solute concentration of the alloy must be lower than that required for the transition from internal to external oxidation
- No surface layer must prevent the dissolution of oxygen into the alloy at the start of the oxidation

In the initial stages of oxidation, the oxidants (H_2O, O_2 and radical species including OH^-, O^- etc.) bond to the free surface of the steel. Free conduction band electrons will enable the dissociation of the H_2O/O_2 molecules [77]. An equilibrium is established between the arriving oxidants and the metal/scale surface where the limiting step is access to a free surface site or in dilute atmospheres, the probability of the non-inert component arriving close to the surface. This equilibrium for the dissociation of water at the surface is given by the equation:

$$H_2O_{(g)} \Leftrightarrow \underline{O} + H_{2(g)}$$

Equation 2.31

Where $\underline{O}$ is the dissolved oxygen atom.

If there is a scale present, the diffusion of Hydroxyl (OH) species on oxygen oxide sites, and hydrogen on metal interstitial sites has been suggested [78] as being the most likely transport mechanism, disparaging the theory around the molecular water transport, based on their experimental data, however other suggestions for water transport through pores and cracks in the scale have been presented [79]. The dissociation of water at the metal surface or metal-scale interface [79, 80] then leads to the dissolution of the oxygen anions into the metal. This is applied to the model via a boundary concentration condition enacted through an interpolation function at the top of the surface interface, negatively related to the volume fraction of oxide. After comparing Maxwell's and Kirkaldy's approaches [81, 82] for simple modelling applications of scale kinetics, Maxwell's was found to be superior due to Kirkaldy's overapproximation of the blocking potential of the oxides. This is applied on the Concentration boundary condition restricting the surface oxygen flux via the concentraion component with a lower limit of 10% of the initial oxygen concentration, as stated before. This is the most viable method for a heuristic implementation of oxygen scale transport, whilst keeping an effective worst-case-scenario for the model.

The maximum amount of oxygen able to dissolve in the steel (without chemical reaction) is known as the solubility; presented as the equation relating change in Gibbs free energy *ΔG* to atmospheric partial pressure of oxygen [5, 7]:

$$\Delta G = \Delta\overline{H} - T\Delta\overline{S}^{X\,S} + RT\ lnN_O - \frac{1}{2}RT\ lnp_{O_2}$$

Equation 2.32

Using Equation 2.32 and the value of the dissociation/formation pressure of wüstite (FeO) at 850°C, which has a value pO_2 (FeO) = 1.57 x10^{-18} [atm] as the partial pressure of oxygen pO_2 [83], solubilities (*No*) of oxygen in Ferrite and Austenite (with no additions of alloying elements) in mole fractions are:

No_α = 1.2661 x10^{-6} and No_γ = 1.2011x10^{-6}, respectively.

Using the concentrations of the simulation translates to:

COf = 0.1632 and COa = 0.1548 mol/m^3, respectively.

Agreement in literature on the solubility values derived from high temperature oxidation is sporadic, but these values fit within the 0.1 and 30 ppm range usually presented [5, 63, 71, 83, 84]. The values of oxygen solubility in steel vary greatly in literature as the experimental results rely on relations of other interstitial occupiers like carbon and nitrogen, the composition of the steel, and other differences in initial conditions like microstructure.

Sievert's equation describes the equilibrium at the surface, relating the atom fraction N_O of the oxidant to the respective atmospheric partial pressure p_{O_2} for a diatomic gas molecule. The experimental verification of this equation lead to the understanding that diatomic molecules first dissociate at the surface of the metal [5, 6, 7, 85]:

$$N_O = K_{eq}p_{O_2}^{\frac{1}{2}}$$

Equation 2.33

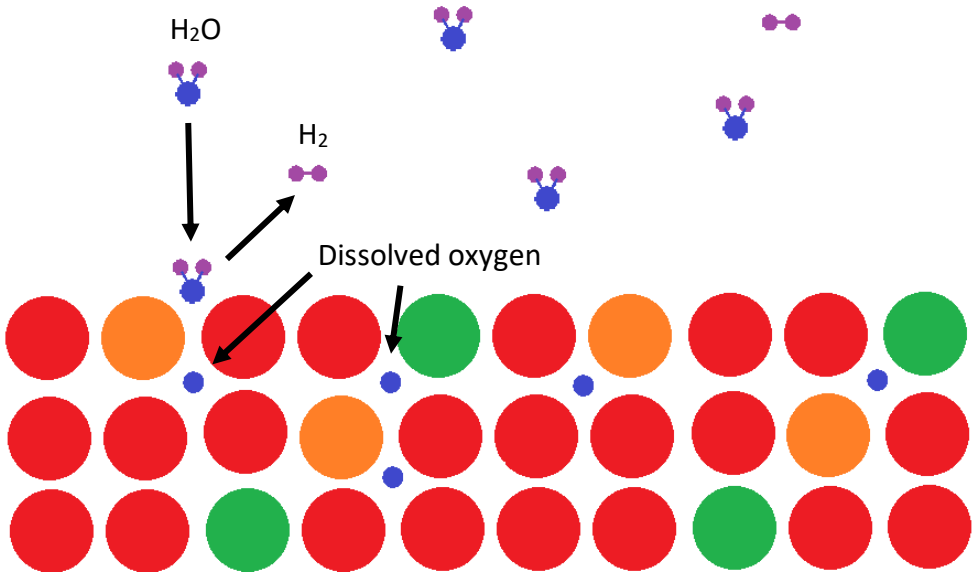

Figure 2.17 Schematic showing the dissociation of water at a clean steel lattice surface, with oxygen being absorbed into the lattice and a hydrogen molecule product being given off. The temporary occupation of the surface dissolution site provides a limit on the amount of oxygen able to dissolve at any one time, based on the rate of water vapour arriving at the site, the time taken to dissociate, time taken for oxygen to penetrate into the steel, and for the hydrogen to be removed from the site

The experimental phase of this project uses the dissociation of water vapour at the steel surface to provide the oxygen for the internal oxidation of the metal, and understanding the differences between molecular oxygen and H_2O is important for isolating the variables of the experiment. Birks et al. have provided some necessary considerations [6]:

- Water vapour can affect transport through oxides by causing the network structure to be changed
- Water vapour causes the concentration of proton defects to be increased, which can influence defect-dependent properties such as high temperature creep and diffusion
- The presence of water vapour adversely affects the selective oxidation of elements such as aluminium and chromium from iron-base and nickel-base alloys

The increased oxidation from water vapour interacting with the surface oxides is an industrially relevant issue that is not mediated, which must be understood and considered when examining the results.

There is a relation for the dissolved oxygen that can also be related to the dew point through the equations for the partial pressure of water vapour and the dissolved oxygen as a relation of the H_2O/H_2 ratio from the solubility of oxygen as atom fraction [72, 77]:

$$\log p_{H_2O} = \frac{9.8DP}{273.8 + DP} - 2.22 \qquad DP \leq O°C$$

Equation 2.34

$$\log p_{H_2O} = \frac{7.58DP}{240 + DP} - 2.22 \qquad DP > O°C$$

Equation 2.35

Where *DP* is the Dew Point in [°*C*], and p_{H_2O} is the partial pressure of water vapour in [atm].

Following, the dissolved oxygen presented in the form of atom fraction in relation to the water-hydrogen partial pressure ratio for Austenite and Ferrite solubility, respectively [72, 73]:

$$\log\left(N_{O\gamma}^{(s)}\right) = \log\left(\frac{p_{H_2O}}{p_{H_2}}\right) - \frac{5000}{T} - 0.67$$

Equation 2.36

$$\log\left(N_{O\alpha}^{(s)}\right) = \log\left(\frac{p_{H_2O}}{p_{H_2}}\right) - \frac{4050}{T} - 1.52$$

Equation 2.37

After dissolution, the oxygen anion will then occupy a free interstitial site. The solubility is determined by the phase transformation-related parameters: local concentration of reactants, temperature, internal stresses, stored lattice energy, and the local chemical/electrical potential etc. of the steel lattice [8, 86]. Solubility is usually established by the formation pressure of the most stable oxide, which would be Al_2O_3. However, as the formation pressure of alumina is extremely low it does not set a viable limit for modelling as it would introduce a large difference in the reaction

starting conditions causing great issues in convergence of the model solution along with allowing only a very small dissolved oxygen content.

The maximum dissolved oxygen content varies as the internal formation of alumina involves the depletion of solute in the local area, after complete depletion the oxygen concentration will increase until the next most stable oxide's ($MnAl_2O_4$) formation concentration is reached. When significant solute flux arrives at the local area the relation of the solubility to thermodynamics involves a kinetic consideration of the additional material arriving where the reduction of less stable oxides will occur [80]. If there is no significant solute flux to the area it is subject to the depletion of the solutes in the local area and the formation of less stable oxides will occur with the requisite oxygen concentrations.

The solubility in the local area being subject to the available components is a complicated topic, incorporating the initial available solute concentrations and the subsequent bulk solute flux, which is exacerbated in a four-component system like Fe-Al-Mn-O. The definition of oxygen solubility involves the ability of a local area to hold a discrete concentration of free oxygen before transformation to the oxide, whereby the solubility is subject to the formation of the most stable oxide, therefore if an area has the necessary dissolved oxygen concentration to react with a constituent but the thermodynamics prevent the reaction due to another reaction taking preference then both solubility limits are relevant. For example, the partial pressure of oxygen is sufficient to oxidise iron, but in a local area with high aluminium content, alumina will form and any iron-based molecules that temporarily form will be reduced, however, after the aluminium is depleted the iron will oxidise, most likely to form internal $FeAl_2O_4$. As the variability of the solubility is in the definition of the word it is not viable to consider any variation and is not considered in this project as such a complication in the model would require iterative local area equilibrium considerations and induce unnecessary instabilities from the variable start conditions in each of the model mesh elements when it can be reasonably satisfied with the solubility relating to the base metal dissociation pressure of oxide. Therefore, the solubility in this project is constant and set by the dissociation

pressure of wüstite (FeO) [5], which at 850°C has a value pO_2 (FeO) = 1.57 x10^{-18} [atm], calculated in FactSage [55].

Once the oxygen has dissolved in the steel surface, the concentration and chemical potential gradient induce a driving force on the atom causing its diffusion inwards, which occurs fastest in what is known as "high-diffusivity pathways", like grain-boundaries. The oxygen atom will occupy - for a time - an interstitial site where it is at its local low energy point, which in LDS is likely an aluminium interstitial site. Once the requisite reactants' concentration, internal lattice energy, microstructure considerations etc. are met, the transformation will occur from metal lattice and interstitial occupier, to oxide molecule. As the formation concentration of oxide for Al_2O_3 is so low the requisite conditions are simple and related mostly to the available concentrations based on equilibria values; for Al_2O_3 formation, this is implemented in the model as an irreversible reaction with a very high rate constant, with start conditions of subsequent reactions relative to the depletion of the previous most stable -oxide-forming-solute.

In a system with an oxygen permeability higher than the solutes', with the flux of a species being finite, the system establishes a concentration gradient that has a minimum of zero beyond the farthest transported oxygen atom.

The most stable oxide, Al_2O_3, is created once the formation concentration of oxide is met, as the concentration of oxygen continually increases (at a local level) the next oxide formation concentration is passed and if the transformation conditions allow, will react; this continues up to the maximum possible oxygen concentration which if allowed to occur in the presence of Fe, Al, and Mn follows the order (most stable to least stable oxide):

Al_2O_3 -> $MnAl_2O_4$ -> MnO -> $FeAl_2O_4$

Visually represented Internal Oxidation Zone (IOZ) in 1-dimension, below (not to scale):

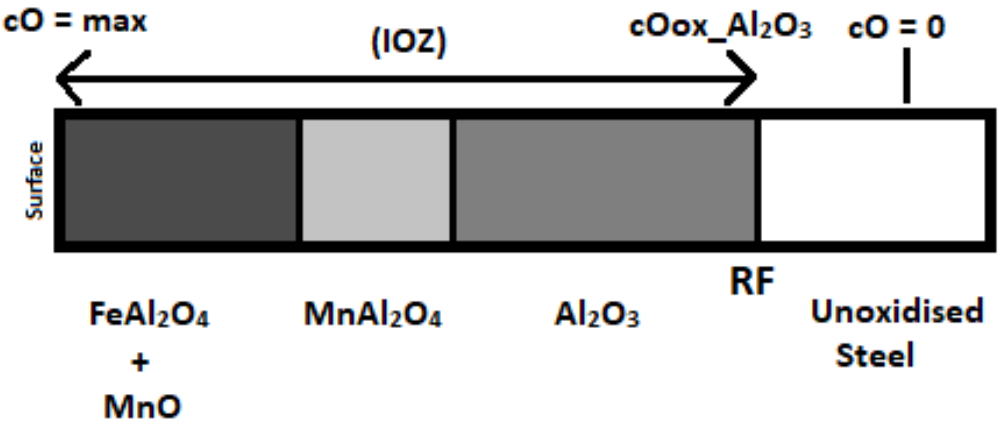

Figure 2.18 Representation of internal oxidation zone with different species of oxide's Oxidation Front if penetration continues indefinitely with increasing local oxygen concentration, in a Fe-Al-Mn-O system, where effective diffusivity on microstructure is not considered

Where *cO* is the free oxygen concentration; and *cOox_Al₂O₃* is the formation concentration of aluminium oxide which also represents the Reaction Front (RF) at the greatest depth of the IOZ, continually increasing with oxygen exposure.

Derived from Fick's laws of diffusion, Wagner's theories of internal oxidation with the consideration of diffusion-dominated kinetic processes can be presented within the scope of two scenarios [70] using the parabolic expression for Internal Oxidation Zone Depth *X* [5, 77]:

$$X = 2\gamma\sqrt{D_O t}$$

Equation 2.38

Where *X* is the Reaction Front depth, and *γ* is the common dimensionless parameter.

The first scenario is where solute B has an insignificant contribution:

$$\frac{D_B}{D_O} \ll \frac{N_O^S}{N_B^0} \ll 1$$

Equation 2.39

Leading to the equation for the dimensionless parameter *γ*:

$$\gamma = \sqrt{\frac{N_O^S}{2vN_B^0}}$$

Equation 2.40

With no consideration of the solute counter-diffusion, the oxidation zone depth *X* is represented as a function of oxidant and solute concentrations N_o^s and N_B^0, respectively:

$$X = \sqrt{\frac{2N_O^S D_O t}{vN_B^0}}$$

Equation 2.41

Where $N_B^{(o)}$ is the initial solute concentration and $N_O^{(s)}$ is the oxygen solubility in base metal A [mole fraction]; V_m [$cm^3\ mol^{-1}$] is the molar volume of the metal (for dilute solutes, of the base metal), and *v* is the atomic ratio of oxygen to metal of the oxide (e.g. Al_2O_3, v = 1.5).

The second scenario is where the diffusion of solute B is significant (applied on the condition of a single precipitate is formed that is stoichiometric and stable):

$$\frac{N_O^S}{N_B^0} \ll \frac{D_B}{D_O} \ll 1$$

Equation 2.42

Leading to the equation for the dimensionless parameter *γ*:

$$\gamma = \frac{N_O^S}{2vN_B^0}\sqrt{\frac{\pi D_O}{D_B}}$$

Equation 2.43

And the oxidation zone depth *X*:

$$X = \frac{N_O^S D_O}{\nu N_B^0} \sqrt{\frac{\pi t}{D_B}}$$

Equation 2.44

Although scenario 2 has more relevance to this project than scenario 1, it is still limited to a single oxide species. This can be used to estimate the size of the alumina oxidation zone; however, it will be an overestimation as there is no consideration for the oxygen reaction with other solutes in the IOZ to produce less stable oxides.

In relation to this project, using the steel composition of Fe-5Al-5Mn (wt.%) is calculated to be X (t=300s) = ~1.35µm, using DOfGB, and DAlfGB, and v = 3/2 for the stoichiometric ratio of oxygen to metal atoms for Al_2O_3. This within the valid zone of values for IOZ depth as the steel has been seen to form an exclusive alumina scale, and in atmospheres with higher oxygen content, small internal oxidation zones.

The chemical potential and concentration gradients create a flux competition between the oxidants and solutes; the position of the newly created oxide is subject to the Permeability which is the diffusivity multiplied by the concentration of the species. The differences in permeability can be small when comparing the fast oxidant interstitial diffusivity coupled with its low concentration, and the slow substitutional diffusivity with the high concentration of the solutes. If the initial permeability of the solute is much higher than that of the oxidant, the new oxide will form at the surface to create an external oxide layer (scale), as stated by Wagner's criterion [5 , 87] for the minimum solute concentration to form the protective compact scale:

$$N_B^{(o)} > \left[\frac{\pi g^*}{2\nu} N_O^{(S)} \frac{D_O V_m}{D_B V_{ox}}\right]^{1/2}$$

Equation 2.45

Where *g** is the critical volume fraction of oxide for the formation of the dense, compact, blocking layer; and V_m and V_{ox} are the molar volumes of the metal and

oxide, respectively. Wagner states that the transition from internal to external oxidation occurs when the volume fraction of oxide g reaches the critical value g^*, and the oxides grow laterally, preventing penetration of the oxidant further into the material, by the creation of the barrier, the volume fraction of oxide is represented by the equation:

$$g = f\left(\frac{V_{ox}}{V_m}\right)$$

Equation 2.46

If the permeability of the oxidant is much higher than the solute, then the internal oxidation will continue, without forming an effective barrier, until the solute is depleted. If the IOZ free oxygen concentration reaches sufficient levels, the next formation concentration of oxide will be reached - if not already – and could eventually reach all formation concentrations to consume all of the material creating complex Fe/Al/Mn spinel structures. As Wagner's criterion carries the assumption that the external oxide layer is compact and prevents further oxidation, the creation of new oxide from the solute diffusion through the scale to the scale-gas interface is not considered by the criterion; however, if this assumption is discarded it could lead to the continued scale growth and subsequent depletion of the solute from the subsurface region, although this is would take a much larger amount of oxidation time than is considered for this project.

The criterion also indicates the assumption around the oxide's blocking potential, but in this project the partial consideration of spinel species' porosity/density opens this assumption to scrutiny as the porosity/density could be a major factor in the internal oxidation behaviour. The disruption of the surface alumina by surface manganese oxide formation is a concern as it could allow the penetration of the oxidant due to the decrease in stoichiometry and density – and thereby also diffusivity. Also, the protective layer in context of water vapour oxidation effects is to be given consideration whereas stated before the water vapour oxidation tends to exacerbate internal oxidation through porosity increase.

2.9.1 Internal Precipitates and Effective Diffusivity

The blocking effect of internal precipitates is well-known and there have been a number of investigations into expanding scientific understanding of the blocking potential of atoms and molecules [73, 88, 89]; although there is rising interest around the formation of internal alumina rods enhancing diffusion along the oxide-steel interface, the effect has not been quantified sufficiently to be implemented accurately in the model [88] as well as preliminary experiments not showing any alumina rod formation.

The presence of obstructions in the grain boundaries can detrimentally effect the scale formation by blocking solute counter-diffusion, this is evidenced by the well-known Reactive Element effect whereby the segregation of large atoms to the grain boundaries reduces the diffusion of the solute through the high-diffusivity pathways to the surface reducing the alloy's ability to form a protective scale and therefore exacerbating internal oxidation. However, as the internal oxide molecules/particles are large compared to atomic radii and are not impenetrable objects the diffusion will be affected differently, and they will affect both oxidant and solute diffusivities.

The stoichiometry of the diffusion medium will partially determine a species' diffusivity. This means that oxides that exhibit very small stoichiometric windows [5, 7] and oxides that do not form with pores will have greatly reduced diffusion speeds relative to other oxides and the host lattice. The nature of oxygen and aluminium diffusion in α/γ/θ/δ-Al_2O_3 is complex and is still not well understood [90], but as the diffusion speed of oxidants and solutes through Al_2O_3 and $MnAl_2O_4$ is negligible compared to their diffusivity in steel [91], the diffusivity in all oxides is given a singular value in the model.

The scenario where the permeability of the oxidants is only slightly higher than that of the solutes is a major interest in this project as the variation of solute concentration and diffusivities of the different crystal phases in the subsurface region could greatly affect the oxidation behaviour and is hypothesised to produce significant differences between the two dual phase steel grades. The decrease of oxidant diffusivity due to the increase of volume fraction of oxide (f_v) will result in

the unity of the oxidant and solute fluxes with the lateral growth of the new oxides occurring at depths related to the magnitude of the initial flux difference, establishing an internal oxide barrier. As the oxide barrier inhibits the diffusion of oxygen, the composition of the oxide and the contribution of solutes from the surrounding grains is important.

The porosity/density of the oxides is the most prominent component of the transport blocking phenomenon, as consideration for the diffusivity of the oxidant through available oxide lattice and interstitial sites affecting each oxides' blocking potential is of less concern due to the minute diffusivities, but is also not considered in the model due to a lack of reliable grain-boundary diffusivity data.

Concerning the conditions for the creation of these barrier oxides and their blocking features, the focus lies on the critical volume fraction of oxide *g** from Wagner's criterion. This has been discussed by W. Zhao et al. [89], where they declare that the critical volume fraction of oxide for the transition from internal oxidation to external oxidation can be well described by the equation:

$$f_v^* = \frac{2\sqrt{\frac{V_m^{oxide}}{V_m^{alloy}}}}{\sqrt{6} + 2\sqrt{\frac{V_m^{oxide}}{V_m^{alloy}}}}$$

Equation 2.47

This is expected to be an overestimation, subject to further considerations of oxide particle geometries based on the degree of supersaturation, but suitable for the model - as is - due to the homogenised model geometry and the lack of discrete oxide particle geometries. Calculations using relevant parameters of the steel grades in this project for Equation 2.47 result in f_v^*= 0.59. W. Zhao et al. [89] have experimentally shown that the equation by Maxwell [82] is most accurate of the predictive equations compared to Kirkaldy's method [81] which overestimates the blocking effect when they tested for the effective diffusivity (D_{eff}) in the presence of non-spherical oxides in internal oxidation scenarios:

$$D_{eff} = D_O \frac{2(1 - f_v)}{2 + f_v}$$

Equation 2.48

Where D_O is the oxygen diffusivity, and f_v the volume fraction of oxide. A representation of the above equation's effect on the oxygen ferrite GB diffusivity is shown below:

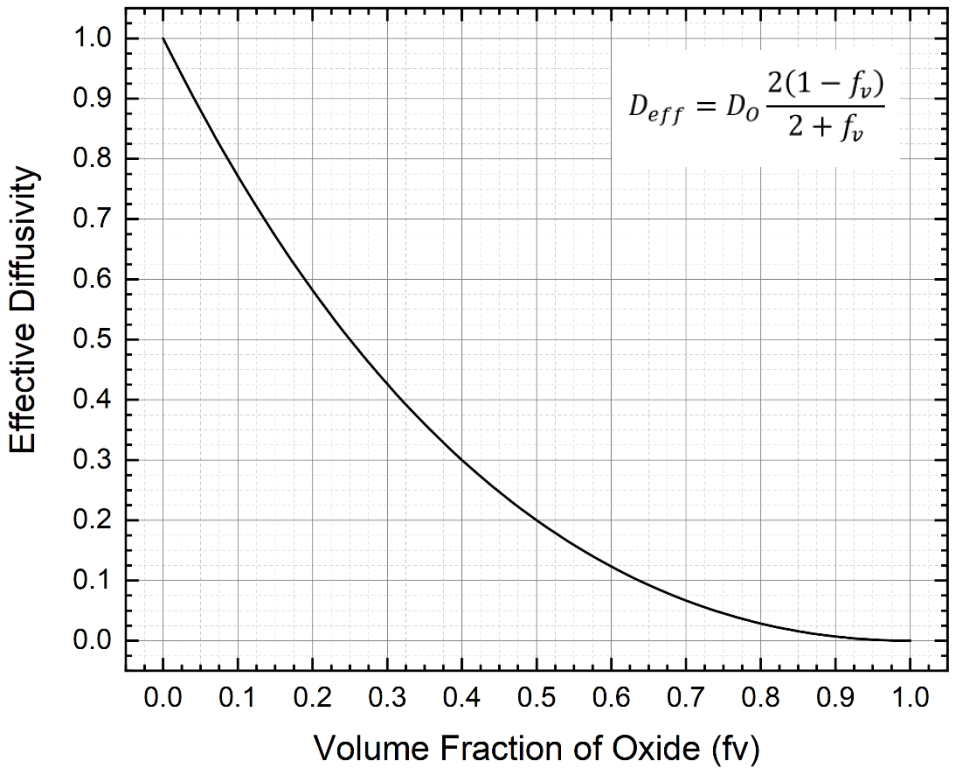

Figure 2.19 Graphical representation of the effective diffusivity to volume fraction of oxide relation

This expression for the diffusion speed decrease is related to the volume fraction of oxide, where the critical value f_v* is when the unity of oxygen and solute fluxes occurs. This has been implemented into the COMSOL Multiphysics software with a interpolation piecewise cubic function with a value for the lower limit of 0.001 instead of zero, as the software experiences issues resolving such large differences in values of diffusion coefficients, as well as difficulty handling nil values themselves.

The lower limit in the model of 0.001 is accurate up to a volume fraction of oxide (f_v) = 0.96.

When oxidation of the alloy occurs, the solutes that diffuse towards the surface leave behind a zone of depletion with can have microstructural effects such as phase transformation after enough of the phase stabiliser is gone (e.g. Austenite -> Ferrite transformation, when Mn has been depleted). As this depletion occurs, the solute is oxidised in the IOZ, where this extra material contributes to what is called solute enrichment: the increased concentration of molecular oxide/solute compared to the initial concentration.

2.9.2 Solute Enrichment

The Solute Enrichment Factor is a ratio of the accumulated solute metal in the IOZ relative to the initial conditions. The definition of solute enrichment is tied to the formation of oxides through the flux competition of oxygen and the solutes, the higher the oxygen to solute flux ratio the lower the solute enrichment of the IOZ because the oxidation front continually advances. There exists two main avenues of consideration for solute enrichment that has been seen in literature [5, 7, 73, 89]: the standard case based on the entire internal oxidation zone with a significant depth, and the other a very small and localised IOZ. The former is based on investigations with the permeability of oxygen being much higher than the solutes leading to either small solute enrichments or none at all, and the latter is based on the opposite where the transition from internal to external oxidation occurs due to the considerable solute flux to the IOZ creating dense oxides that block material transport leading to a large enrichment factor ($\alpha >> 1$).

An issue lies in the definition of the term and between the two scenarios of solute enrichment when modelling a localised geometry: the solute enrichment is a function of the initial solute concentration but has a maximum limit represented by the density of the stoichiometric oxide. If volume expansion consequences are not

considered, this can lead to the solute enrichment ratio being many magnitudes higher due to the solute constituents of the oxide crystal relative to the steel crystal. Therefore, the solute enrichment factor (related to the volume fraction of oxide per mesh element) in the model is compared to the density of the stoichiometric oxide at a standard state instead – seen in the simulation results.

There has been some investigation into the predictive solute enrichment in oxidation. Some notable studies [72, 73] include solute enrichment as modelling predictions, whilst most others offer post-oxidation analysis, both methods present values between 1.05 and 1.15, with the authors suggesting they are relatively low due to the high oxygen permeability. The solute enrichment predictive equation presented by Mao et al. [72] exists with a condition of similar oxide reaction fronts, which differs from this project's oxidation sequence of alumina formation occurring at very low oxygen concentrations with Fe/Mn oxides forming at substantially higher oxygen concentrations, establishing multiple oxidation fronts with large differences. The equation does not include kinetic terms for the Effective diffusivity too, as well as terms for the differences in oxide blocking potential. The model in this project can be seen as an avenue for another predictive method of solute enrichment of Fe-Al-Mn dual phase LDS.

2.10 Oxidation Rate

The reaction rate of internal oxidation mostly follows the parabolic expression of Equation 2.44 for significant solute counter-diffusion, however there are additional considerations in the unique dual phase environment with high solute concentrations that involve systems with initial solute contents close to Wagner's Criterion that will affect the reaction rate.

The rate of reaction is subject to certain limiting factors, these can be defined under the relevant areas of interest:

1. Alloy surface penetration of the oxidant

The penetration of the oxidant at the surface consists of multiple stages, thereby introducing multiple limiting factors:

a. Access of the oxidant to the alloy surface bonding sites involves the consideration of the atmospheric oxidant fraction, which can be split into two categories: Dilute and Concentrated.

   A concentrated atmosphere is limited by the available surface bonding sites and their occupation by the oxidant molecules. The equilibrium relation of pH_2O/pH_2 ratio is also important as the time involved in the release of molecular hydrogen from the bonding site is restricting the access for other water vapour molecules; additionally, the time taken for the dissociated oxygen atom to transfer to an interstitial alloy matrix site. An atmosphere of mostly noble composition with a dilute oxidant incurs the additional limiting step of atmospheric convection bringing the oxidant to the surface, as the immediate area above the alloy surface is depleted of oxidant.
b. The limiting steps for the remainder of the oxidant penetration factors involves the time taken for the dissociation of the oxidant and the transfer of the atom from the external bonding site to a lattice interstitial site.
c. The presence of an oxide scale induces other limiting factors to oxygen penetration of the alloy, such as the mechanisms of transport of the dissolved atom through the oxide scale (varies according to oxide stoichiometry), the transference of the dissolved atom across the alloy-scale interface, and the transport of charge carriers (vacancies, electrons, and holes) across the scale.

2. Diffusion of the oxidants and solutes to the Reaction Front

The Reaction Front (RF) is the location at which the internal reactions take place in the presence of the free solute and oxidant. As the transport of the oxidant continues, the area closest to the alloy surface is depleted of solute – leaving behind the base metal and those solutes which have not yet experienced the

concentration of oxygen required for their reaction (*cOox*). The reaction front advances with the penetration of oxygen to areas with free solute; as the diffusion coefficients of oxygen are far greater than that of the solutes ($D_O >> D_{Al}/D_{Mn}$), the limiting factor is usually the oxygen flux.

3. Internal oxide geometric blocking and stoichiometry effects on diffusivity

The reaction of oxygen and solutes to create the various Fe/Al/Mn oxides requires the consideration of their respective blocking potentials subject to porosity, density, and stoichiometry of the oxide. A small or more porous oxide will allow the transport of oxygen (and solutes) around/through its structure more easily (akin to an oxide polycrystal, with defects), but if it is dense enough (similar to an oxide monocrystal) the oxygen atoms will be subject to the oxide diffusivities, likely causing the oxygen flux to bypass the oxide via a faster route, if one exists.

In the environment of the dual phase steel grades of this project, the relatively high amount of solute content is close to Wagner's Criterion and the blocking effect may produce additional consequences. These consequences arise from the common parabolic kinetics being challenged by the formation of internal barriers, if these barriers are formed the oxidation kinetics will require further research. This is because if the chemical potential gradient of the system continues to produce a driving force of a non-zero value the arrival of aluminium to the bottom-most portion of the internal barrier will likely induce transport kinetics similar to external scale growth whereby the density and diffusion across the internal barrier will have to be considered.

Due to primarily diffusion-related limitations a model based around the above conditions with reaction rates subject to local concentrations and diffusion of extra material of any species bound to the Effective Diffusivity of the local area through oxide volume fraction rather than iterative diffusion and instantaneous equilibrium oxide formation is viable.

2.11 Published Literature Analysis

Although the research of low density Fe-Al-Mn-C steels has been increasing for a few decades, few pieces of literature exist that focus on internal oxidation during short-term annealing. The vast majority of Fe-Al-Mn-C steel literature focusses on the mechanical properties; the majority that focus on oxidation and its accompanying phenomena, such as scale oxide species layering, surface oxide nodule formation, and effects on wettability – only consider internal oxidation briefly or only as a part of the umbrella of the phenomenon and not as the focus. There are often many differences between this project and the published literature, which constitute one or more of the following variables: experimental isothermal temperature, heating and cooling rates, reaction chamber atmosphere, total isothermal annealing time, steel composition, steel microstructure, and oxidation focus. These differences are often significant and relating the results to this project can leave unsatisfactory conclusion comparisons, however this indicates that this project fills a viable void in literature that is closely linked to industrial purposes.

The review is critically conducted with individual factors for relevance being determined and considered as follows:

- Fe-Al-Mn-C steel internal oxidation
- Dual Phase Fe-Al-Mn-C Steel
- Annealing duration: Short, up to 15 minutes
- Annealing isothermal temperature: 850°C
- Fast heating rate: 4°C/s or higher
- Sample storage atmosphere pre/post-oxidation
- Reaction chamber atmosphere: contains water vapour
- Average subsurface grain size: up to 20µm

A distinction is made for a water vapour containing atmosphere as water vapour has been shown to provide different oxidation phenomena than molecular oxygen [72, 77, 92, 93] but any atmospheric oxygen content will contain relevancy, therefore the reaction chamber oxygen partial pressure is not specified.

A range of literature has been surveyed to compare the experimental methods and the ensuing conclusions drawn to this project, throughout this review it should become clear that this project adequately fills a void in literature and that the techniques employed here are done so with well-sourced scientific critical reasoning. The papers under review mostly contain dual phase steels, but due to a lack of literature some articles with single-phase steels are used - this could have a large impact on a comparison of the results.

In any regard where a phase composition was failed to be provided by the authors, ThermoCalc was used to ascertain it as where so specified as TC. Table 2.4 is provided to show the reader a comparison of most of the relevant variables considered in this study of the literature discussed below, and the two dual phase steels experimented upon in this project.

Table 2.4 Data of the experiments of the literature critically reviewed in this section, consisting of steel composition, phase composition, isothermal annealing temperature, annealing duration, and reaction atmosphere

Authors	Steel composition [wt.%]						TC Phase Composition at Temp [mol %]	Isothermal Temperature [°C]	Experiment Duration [mins]	Reaction Atmosphere
	Fe	Al	Mn	C	Other	Name				
X. Jin et al [94]	94.07	4.00	1.26	0.38	0.29	Si	56% - α; 44% - γ	815	2.5	N2-5% H2; -40C - +10 C
C-J.Wang [105]	59.43	9.70	30.10	0.77	-	-	18% - α; 78% - γ	750	1440, 8640	Air (dry)
W. Peng [107]	71.50	8.00	20.00	0.50	-	-	25% - α; 75% - γ	1000	5, 10, 30, 180	Air (dry)
H. Wang [103]	93.95	4.50	1.10	0.15	0.30	Si	85% - α; 15% - γ	800	1	N2-5% H2; -40C - +10 C
W. Peng [111]	72.38	7.77	19.80	0.34	0.01	Si	~40% - α; ~60% - γ	1000	180	Air (dry)
T. Jeong [119]	89.70	6.20	3.90	0.30	-	-	95% - α; 5% - c	800	1	N2-5% H2; -30C- -10 C
W. Peng [120]	83.90	5.25	10.60	0.25			28% - α; 72% - γ	950, 1050, 1150	180	Air (dry)
H. Liu [123]	95.81	1.50	1.61	0.41	0.55	Si	36% - α; 64% - γ	800		N2-5% H2; -30C - +10 C
Fe-3Al-5Mn	91.61	2.87	4.85	0.16	0.50	Si	47% - α; 53% - γ	850	0.5, 2.5, 5	Ar - H2O
Fe-5Al-5Mn	89.73	4.75	4.85	0.16	0.50	Si	69% - α; 31% - γ	850	0.5, 2.5, 6	Ar - H2O

X. Jin et al. (2018) [94] applied a 4°C/s heating rate to a Fe-4Al-1.3Mn-0.4C steel to reach the isothermal temperature of 815°C, which then was held for 2.5 mins, the whole process was conducted in their N_2 – 5% vol H_2 reaction atmosphere. This means that for 3.3mins on the heating ramp the sample was oxidising, 32% longer

than the isothermal experimental duration. For their purposes of studying the galvanisability of the steel it is a realistic scenario to simulate; however, in comparison to this project, it does not effectively isolate the isothermal oxidation phenomena as the aluminium will have undoubtedly begun oxidising. Along the same vein of comparison, the authors do not specify any surface resetting done to the samples nor how they were kept prior to the experiments. X. Jin et al do not mention the phase composition of the steel, using ThermoCalc it was determined as dual phase (56% Ferrite, 44% Austenite), with grain sizes taken from the images to be in a range of 6 - 10μm; there was no mention of the dual phase nature of the steel and the effect on the oxidation or galvanisability.

The internal oxidation zone is short, covering a depth of no more than 3μm, mostly consisting of aluminium oxide (Al_2O_3); the authors state that the volume expansion of the internal oxides causes the formation of surface pure iron particles. The transition of the steel through oxidation to the higher volume is a known phenomenon and been studied externally [95-98] in relation to the spallation of said surface oxides. The internal effects [99-101] of this oxide volume expansion have been known for a small while also, although the full picture is complicated as the effects are not limited to oxidation but also phase transformation, precipitate formation, and mechanical properties etc. This oxide volume expansion phenomenon could also be responsible for the depletion of metal solute elements in oxide nodules, from the subsurface oxides to the surface oxides. Apart from the differences already noted, the atmosphere is also a major factor when comparing to this project's ($Ar + H_2O$).

The authors' objective was to investigate the effect of dew point on the galvanisability of this steel related to oxidation, they conclude that the higher dew points cause the internal oxidation of aluminium to increase whilst metal iron nodules are formed at the surface which increase the wettability and form a good Fe-Al-Zn inhibition layer.

Limited comparisons can be made to this project at the most relevant higher dew points as manganese is not considered by the authors. This means that the role of manganese on the formation of the metal nodules at the surface cannot be

considered. The low concentration of manganese in the steel does not confirm nor deny the formation of these could be related to atomic size [102-104].

The experiments conducted by C - J. Wang et al. (2002) [105] on their Fe-9.7Al-30.1Mn-0.8C dual phase steel consisted of very long isothermal durations of 24hrs and 144hrs in dry air. The duration and steel compositions are the largest differences to this project, the very long oxidation times do not allow for an effective comparison of the early stages of internal oxidation phenomenon, and the composition drastically alters the flux of elements. At the surface, oxide nodules forms, and there is a significant amount of metal solute depletion in the subsurface section of the nodule. Needle-like aluminium nitride particles form below the nodule in the 144hr samples, which the authors attribute to the creation of cracks and voids in the nodule due to the transfer away of iron and manganese, alongside the formation of the less protective Fe_2O_3 and $MnAl_2O_3$ creating a viable fast diffusion pathway for the nitrogen. From work seen more recently [106], it suggests that the formation of aluminium nitride needle-like particles occurs further into the material than the aluminium oxides as the nitrogen has a faster diffusion speed [76] and is thermodynamically less stable than aluminium oxide and therefore must diffuse to a location at which the oxygen content is at a sufficiently low level for AlN formation. As the oxygen diffuses further into the sample, the aluminium will transfer from the nitrogen to form alumina and nitrogen. The depth of the AlN particles is subject to the formation of a protective Al_2O_3 scale, whereby its presence will retard or prevent both internal oxide and nitride formation. It would seem that if nitrogen is able to penetrate to below the oxide nodule, then so too should oxygen – unless oxygen is prevented from penetrating due to the participation in the oxidation reactions.

For their assertion that the oxide nodules form where voids appear below the protective alumina scale there is little explanation given for the formation of this initial void, and the long oxidation times bring the validity of this idea into question due to the lack of observation. Another point of contention is the statement that manganese and iron oxides form on the surface due to a higher mobility than

aluminium, which is contested in other more respected literature [71, 76], a statement like this requires serious proof, which is lacking here.

The Fe-8Al-20Mn-0.5C samples' 1000°C heat treatment for up to 180mins in dry air used in the literature W. Peng et al. (2017) [107] differ from this project's in a number of ways: composition, isothermal temperature and the pre-oxidation sample storage. Although the authors specify most of the standard procedures for sample preparation pre/post-oxidation such as diamond polishing, they do not state the conditions the samples are put under between the diamond polishing and annealing. During the present project, this intermediate stage has been found to be very important in altering the oxidation characteristics of high-aluminium steels, as this can produce a thin surface passivation layer of alumina which when established can greatly retard high temperature oxidation even in oxygen rich environments like air. The lack of specification on the storage of samples before the high temperature experimentation leaves a large amount of uncertainty for the reader.

The surface of the dual phase steel used in the experiments was defined as with the rolling direction, which sees the oxidation surface perpendicular to the length of the banded grain structure. This results in the surface consisting of mostly alternating ferrite (5.9 - 4.8µm) / austenite (5.2 - 3.0µm) with average grain sizes specified relating to increasing cold-rolled deformation reduction (0 – 50%). This orientation of the samples used gives a relatively uncommon perspective on Fe-Al-Mn-C oxidation, the present project's sample's surface is parallel to the rolling direction. The results show a clear contrast between the ferritic and austenitic oxidation, with the austenitic phases forming relatively thick surface oxides and some internal oxidation; whereas the ferritic grains exhibit far less internal and external oxidation. W. Peng et al. state that the higher interfacial concentration in the austenite phases seen increasing with higher deformation could be the cause of this oxidation disparity by increased cation diffusion, particularly manganese. The locations they used Raman spectroscopy to investigate focus on the external oxides with roughly 17% dedicated to the internal oxides. The authors did not discover significant proportions

of alumina despite the high concentration, with most external oxides consisting of Fe-rich and Mn-rich stoichiometries. The external oxide layer and the internal oxidation zones both increased with isothermal duration; external oxide thickness increasing from between 2 - 3µm to 12 - 20µm and the IOZ increased from between 4 - 6µm to 15 - 34µm, between 5 – 30mins oxidation times. W. Peng et al. state that a large amount of Mn and Fe preferentially diffuse out toward the surface as the fine-grained alloy increases the interfaces concentration for diffusion, leading to the formation of unstable/metastable oxides, such as FeO, MnO, Mn_2O_3 as there is insufficient oxygen to oxidise them; although oxygen is able to penetrate to the internal zone, this is smaller than it otherwise would be due to the large amount of surface cations consuming it.

There are a number of contentious points found in this individual literature and they shall be discussed below in order of magnitude of disagreement:

The authors do not reference any works by Wagner or the subsequent research of succeeding authors, meaning their conclusions do not consider well-established theories surrounding internal oxidation, namely the effect that initial steel metal solute concentration and surface oxygen partial pressure have on the internal oxidation zone depth. Simply put, a higher surface oxygen flux the farther the oxygen penetrates into the sample [5, 7, 53, 87, 108]; conversely, the higher the metal solute flux (that forms a dense oxide) the smaller the internal oxidation zone, up to the point where only external oxidation occurs. As flux is a function of concentration and diffusivity known through Fick's Laws [5, 7], both must be considered in oxidation phenomena.

W. Peng et al. considers diffusion speed the defining property of the variable oxidation behaviour, caused by an increase of grain boundaries within the austenite band. An increase of high diffusivity pathways, such as grain boundaries, would undoubtedly increase the total metal solute flux due to the higher proportion of fast to slow diffusivity zones. However, the metal solutes' high flux is due to their high concentration in spite of the relatively slow diffusion speed [5]; whereas oxygen's flux is drawn from the very high interstitial diffusivity but is coupled with a low

concentration [5]. If W. Peng et al. consider diffusion speed to be a defining factor in the oxidation variation, they did not comment on the element's diffusion speed differing in the dual crystal phases, which is disappointing for comparative reasons to this project.

It is well known that an atom's diffusion speed is related to the ability of the atom to overcome the energy barrier separating it from the destination [5, 7, 8, 53], associated partially with the distance between the intervening atoms. Hence, in the more-dense austenitic phase, diffusing atoms experience a higher energy barrier and therefore subsequently lower diffusivity than in the ferrite phase. This could partially explain the difference in oxidation behaviour between the phases. [5, 109]. Unfortunately, the authors do not present EDS elemental maps of the other shorter isothermal durations, so scrutiny of the oxide formation sequences is not possible. W. Peng et al. seem to have mistaken correlation as causation, stating: the formation of manganese oxides at the surface must mean that their diffusivity is the highest of the elements - rather than the more likely scenario that the oxidation of aluminium is occurring internally because the alumina formation concentration is sufficient to do so, whilst the manganese diffuses to the surface where the oxygen concentration is correspondingly sufficient for the formation of Mn/Fe-rich oxides, therefore aluminium does not diffuse to the surface at a comparable rate to iron and manganese. Also, the protective alumina formed at the surface of the ferritic grains is first established, as neither metal solutes nor oxygen can penetrate a sufficiently dense protective alumina scale, it can be inferred that the oxides that later develop on top of the alumina scale on the ferrite grains comes from the lateral surface diffusion of the metal solutes from areas where the metal solutes can traverse.

The diffusion of an atom is reliant upon the chemical potential creating the driving force to do so [110], the diffusion of metal atoms to the surface during oxidation is intrinsically linked to the dissolution of gaseous species which involves complex electron and hole transport in the metal and the subsequent formed oxide after the first time step. [5-8, 109]. The assertion that the creation of metastable oxides is essentially due to an overabundance of cations diffusing to the surface and awaits

oxygen does not easily fit within this framework and requires more evidence than presented by these authors.

The authors state that the high diffusion speeds of manganese and iron is why the external oxides consist mostly of those elements, however, aluminium diffusion is known to be faster than both manganese and iron [5, 76]. Aluminium is a notorious reducing agent due to its high reactability and will in most given situations involving oxygen be oxidised, thermodynamic stability is key in oxide formation and is also a major predictor of the scale composition, with less stable oxides forming farther from the original surface due to higher oxygen concentration. Following the stability calculations done by W. Peng et al. it can be seen that the scale composition mostly follows the thermodynamic stability of the oxides - although the authors only consider pure oxide phases and not spinels, which limits the accuracy of their findings. The authors also do not discuss ferrite and the increased diffusion speed [76] it's known to accommodate and the effect this has on their results.

H. Wang et al. (2018) [103] investigated the surface oxidation of a Fe-4.5Al-1.1Mn-0.15C δ-TRIP steel in a N_2 – 5% H_2 atmosphere for 1 minute at 800°C, the steel consisting primarily of ferrite with a maximum austenite phase fraction of 5% at the isothermal experimental temperature as specified by the authors. This literature has some notable similarities to this project's, specifically the short annealing time, fast heating rate, and isothermal temperature. However, the differences are significant, explicitly the mostly single-phase, low manganese content, and lack of experiment duration variability. The authors do not state the treatment and storage of the samples before the experimentation, this is important when considering steels with significant aluminium quantity as to completely reset the steel surface.

As expected of a short isothermal oxidation phase, the magnitude of oxidation was relatively small, the IOZ reaching a depth of 1.2µm, consisting mostly of aluminium-rich oxides. The authors calculate the volume expansion of the oxide using manganese and manganese oxide, aluminium and aluminium oxide unit cells. This

method while it gives a general view of the expansion ratio is somewhat flawed due to the use of the elemental unit cells which will not accurately consider their steel's lattice parameters and the proper expansion from such. Nonetheless, the authors posit that their calculations give an expansion ratio of +76.8% for aluminium (BCC) to aluminium oxide (Al_2O_3), with -7.12% and -14.62% for manganese (BCC and FCC respectively) to manganese oxide (MnO). Showing aluminium undergoes a very large volume increase, whilst the manganese oxide confers a significant reduction for the manganese. This information is gathered by the researchers to attempt to explain the formation of surface pure iron nodules, and their conclusion is volume expansion. Their conclusion is consistent with other research [102-104] and is therefore beneficial for the discussion of the results of the present study, as the expansion of the oxides provide a driving force for the diffusion of iron and this could be rationally conferred to manganese. The lack of iron oxidation at the surface and the existence of the pure iron nodules suggests that the partial pressure of oxygen was insufficient to form the iron oxides externally at the location of highest oxygen content. If the internal oxygen content is insufficient to form iron oxides but the aluminium oxidation provides a driving force in absence of a chemical potential perhaps when both driving forces are present the surface is provided with an increased metal concentration than would otherwise be present.

This suggests a phenomenon is possible when a Fe-Al-Mn-C steel is internally oxidised: the aluminium oxide formation induces lattice strain, and as manganese is a slightly smaller atom than iron, has a faster diffusion speed due to the lower activation energy and higher diffusivity pre-exponent, and higher oxygen affinity, it could be the first to experience the requisite driving force to induce diffusion compared to iron. As manganese has a relatively high oxygen affinity the position the manganese is oxidised at as it diffuses towards the surface will depend on the local oxygen concentration. If the oxygen concentration is sufficient to oxidise manganese at any point, the manganese atoms will experience a net driving force resulting from of both the chemical potential and the lattice strain. Presumably, the flux direction would be based off the net driving force, this may not necessarily be towards the

surface. The separation of the driving forces would need to be conducted in order to properly investigate the surface oxidation of Fe-Al-Mn-C steels.

The next journal article is by W. Peng et al. [111] again with a couple small adjustments to the authorship line-up, involves the internal oxidation of duplex Fe-20Mn-8Al-0.3C steels in dry air at 1000°C which offers a number of similarities to the present study. Although the isothermal experimental temperature and steel composition are the largest disparities, the grain size and the orientation of the steel are also major factors for consideration. The authors state that the steel was machined parallel to the rolling direction of the steel. The steel composition is expected to present some internal oxidation differences due to the larger pool of metal solutes which will be able to provide a higher metal solute flux over a longer duration; also the temperature difference prevents direct comparisons because chemical diffusion is temperature-dependent and 150°C is very significant. The authors do not specify the treatment of the samples prior to the experiment, nor the heating rate of the furnace/samples, as mentioned previously these both can have large impacts on the isothermal oxidation behaviour. Although, as the authors conducted several isothermal experimental durations with the steels, the magnitude of the effect of the initial heat ramp in an oxidising atmosphere diminishes with longer times as it comprises a less significant proportion of the total duration. The steels used in this literature also form relatively large grains, consisting of an average width of 25 - 50µm and a length of several hundred micrometres, due to the banding nature of the grains.

The authors suggest that the results present the same oxidation profiles between the steels but an alternating oxide morphology on the different phase grains of each steel; the researchers attribute this to the great diffusion speed of manganese at high temperatures, however this is a disputed point as aluminium has been known to be much faster than manganese at high temperatures [76]. The authors claim to present results concerning the initial internal oxidation and justify their claim of faster manganese diffusion driving the differing surface oxidation. However, the minimum

oxidation time conducted by W. Peng et al. was 5 minutes, this a significant amount of oxidation time at high temperatures and does not allow the researchers to identify initial oxidation phenomena as accurately as they suggest, especially when considering the oxidation during the time of the pre-isothermal temperature ramp. The authors suggest that the grain-boundaries are fast diffusion pathways for aluminium, which is known to be the case, but so too is the increased diffusion related to all elements due to the less efficient packing of atoms and therefore larger average distances between them thus requiring less activation energy than the grain to diffuse [7, 8, 53]. This is not mentioned the by authors, neither is how the differing surface oxides created by higher manganese diffusion relate to the crystal phase. If manganese diffusion is relatively faster at higher temperatures, then the researchers should specify how the dual phase nature of the steel is related to this. There occurs some measure of decarburisation at the steel surface along with the manganese diffusion which sees the austenite to ferrite transformation at the subsurface region. The authors state that this can be expected due to the lack of the austenite stabilisers: manganese and carbon. The researchers mention that the higher aluminium content approaching the austenite crystal boundary compared to the centre produces internal aluminium oxides in the grain boundaries. The authors of the citation provided (F. Yang et al.) [112] only briefly discuss this variation of metal solute concentration over the length of the grain, as it is used to support their discussion on the plastic deformation attributed to the different duplex steel phases. From the same publication, the authors conducted energy spectrum analysis of the duplex steel which shows a gradient of manganese and aluminium throughout the different phase grains. This gradient is apparently inversed in the austenitic and ferrite grains with manganese at a maximum in austenite and aluminium maxima in ferrite, decreasing towards the grain boundary. The diagram from the mentioned literature is presented below.

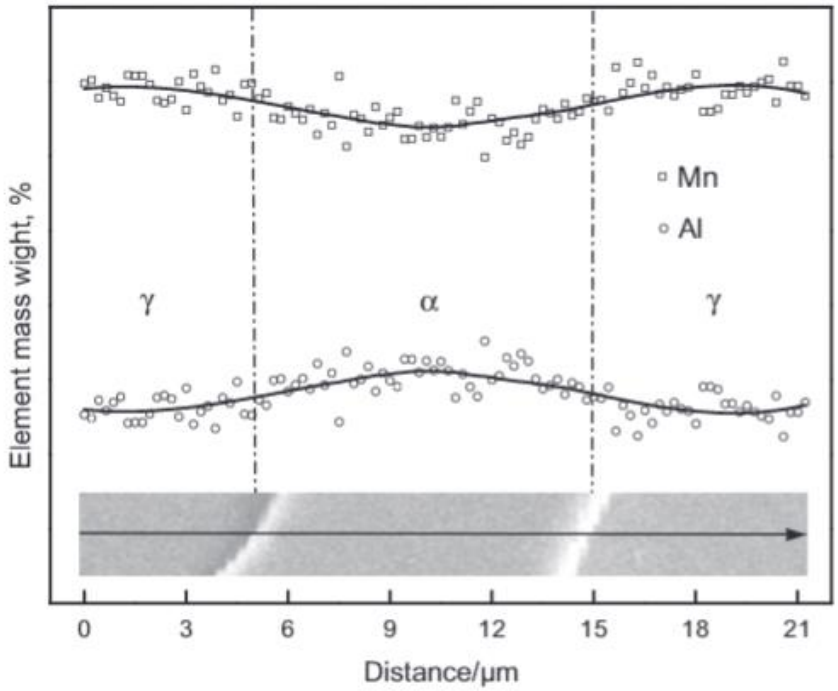

Figure 2.20 Diagram produced by F. Yang et al. [112], used by W. Peng et al. for discussion on aluminium and manganese content in adjacent ferrite and austenite phases

W. Peng et al. further discuss how the preferential diffusion and oxidation of manganese in the austenite phase contributes to higher oxidation, and the decarburisation and the outward diffusion of manganese cause the austenite phase to transform to ferrite. Aluminium begins to enrich at the austenite boundaries and at the surface of the ferritic grains due to the fast boundary diffusion of aluminium.

Unfortunately this diagram does not contain a y-axis, and neither does F. Yang et al. provide information on the composition of the ferritic phase so understanding the magnitude of this variation is not possible, although W. Peng et al. conclude that it is significant and the main reason for the abundance of alumina at the austenite grain boundary, this does not seem supported by the information presented. The austenite grain boundary in question is also the ferrite grain boundary as they are adjacent, and the higher abundance of aluminium in ferrite would likely be the true reason for the aluminium oxide's occupation of the grain boundary, if not a conglomeration of

material from nearby grain edges with the ferrite proximity increasing the total grain boundary flux significantly.

The comments of W. Peng et al. do not incorporate the established knowledge produced by researchers such as Fischer [65], Wagner [87], Rapp [108] and others [5, 7, 63], therefore they have not considered nor discussed the diffusivity differences of austenite and ferrite as would be expected, nor the fundamental oxidation theories. W. Peng et al. state that "there is preferential oxidation of manganese in austenite" which does not agree with the thermodynamic stabilities of manganese and aluminium oxides. The authors do not sufficiently discuss or determine the differences in diffusion speeds of the crystals, nor what role the higher aluminium content in ferrite might play, given its higher thermodynamic stability.

Working with the knowledge of higher ferritic than austenitic diffusion speeds, higher aluminium content in ferrite, and knowing of Fischer's model and Wagner's criterion and other fundamental and established oxidation theories, a more reasonable conclusion can be suggested:

In the initial stages of oxidation, there was a higher flux of aluminium from ferrite resulting from a faster diffusion speed and higher concentration, the individual crystal or the larger local area's contribution which was increased by the proximity to the ferrite crystals was sufficient to counteract the inward oxygen diffusion thereby forming aluminium oxides at the ferrite grain surface. The lower aluminium flux from the austenite grains was insufficient to prevent oxygen penetration into the substrate, therefore internal oxides formed. As the oxygen was able to penetrate the austenitic crystals, the chemical potential for aluminium housed in the adjacent ferritic grains was now directed towards the nearest point of high oxygen concentration, the grain boundary with the neighbouring austenite grain, as the ferrite surface now had little oxidation potential due to the effective blocking by the dense alumina layer. As the ferrite had sufficient aluminium flux to prevent oxygen penetration at the surface, where the oxygen concentration is highest, it was also able to produce sufficient aluminium flux to the grain boundary.

As seen previously [5-7, 87, 108], if a surface oxide barrier can be formed quickly, then metal solute diffusion outwards will be prevented. From W. Peng et al.'s results, there is a manganese poor region below the surface on the 5min oxidation samples in the austenite grains, whilst the adjacent ferrite grains have a higher proportion of manganese at the experiment end, this suggests that outward manganese diffusion from austenite occurred because there was not a surface oxide barrier preventing diffusion. From the same 5min sample it is possible to see some internal oxidation of the austenitic phase which corresponds to aluminium oxide. This can be explained by the higher oxygen affinity of aluminium than manganese, as the aluminium oxide formation concentration is reached in the substrate whilst manganese must diffuse towards the surface in order to reach the requisite oxygen concentration to oxidise. Oxygen diffusion through oxides is diminished compared to steel, even more so reduced when diffusion through thick and stoichiometric oxides to a point where oxygen penetration is completely prevented – aluminium is one of the best known elements to produce this effect, alongside chromium.

As seen from W. Peng et al.'s other piece of literature [107] concerning dual phase steels, when a protective surface oxide has formed on one phase grain but not the other, oxides can grow laterally over the protective oxide surface layer of the ferritic phase, in many cases the surface diffusion of elements is even faster than the same element's grain-boundary diffusion speeds. The authors suggest that the formation of the ferritic layer at the near-surface from the prior dual phase microstructure helps to prevent further internal oxidation but they do not discuss why specifically. Expanding on the above knowledge, it can be suggested that the new ferritic microstructure allows a faster diffusion of aluminium which contributes to a sufficient flux to form internal oxide barriers that prevent further oxygen penetration. The authors state that the surface manganese oxides reduce the oxygen flux into the steel is due to the drastically reduced oxygen diffusivity, this is a well-known phenomenon [113]. The new aluminium flux derived from the increase in aluminium diffusivity from the phase transformation, coupled with this reduced oxygen flux was probably at a sufficient level to produce an internal protective layer and prevent further oxygen penetration. As the researchers do not interrogate the

ferritic layer for composition variability, it is not possible to know if the self-diffusion of aluminium and manganese, driven by their concentration gradients in the ferrite grain occurred or not. Because we do not know the post-transformation composition of the ferrite layer, it is not possible to determine whether the concentration of aluminium equalising across the layer or segregating to the boundaries also had a contribution to the local concentration and driving force of the aluminium.

Steels with only high aluminium alloying contents are known to well-protect steels from oxidation. These steels were of the ferritic phase, as manganese and subsequently austenite is introduced to the system there is generally a decrease in the oxidation resistance [3, 4, 7, 53] and provides uncertainty whether the oxidation of the austenitic phase is due to the diffusion speed decrease or the lower aluminium concentration. This problem is borne from the difference in diffusion speeds in the different crystal phases of both the metal solutes and oxygen. Potentially, diffusion of all elements is faster in ferrite than austenite, therefore as the aluminium diffusion increases so does oxygen diffusion. This ratio of the diffusion of aluminium and oxygen in ferrite vs. the ratio of the diffusion of aluminium and oxygen in austenite is where the issue lies. W. Peng et al.'s work gives us a possible answer: the metal solute flux is increased to a greater degree than the oxygen flux. This answer is possible partially due to the relatively large size of the grains, 20 - 50µm, where the lower ratio of grain-boundaries to grain diffusion paths is more effective at separating each crystal phase's contribution to the total metal solute flux.

The analysis of the internal oxidation of Fe-Al-Mn-C steels will usually have multiple factors to separate at once, the relatively slow austenitic diffusivity could be the answer for the differing oxidation profiles of the dual phase steels used by W. Peng et al. However, the exact mechanism that is affected by this is uncertain as it requires knowledge of the very first few seconds of oxidation as that sets the stage for the promotion of the alumina scale. There are at least three scenarios for consideration: first, where the flux of aluminium to the surface is totally unable to produce the protective scale due to lack of diffusion speed; second, the initial alumina scale is not able to form to the required density to be protective due to the incorporation of

manganese which forms oxides and spinels which have a larger stoichiometric window [5,7, 113] and do not prevent metal solute and oxygen transport throughout to the same degree as alumina; third, the internal oxidation of the aluminium in the austenitic phase causes the volume expansion leading to cracks in the incomplete alumina scale and the formation of oxide nodules [114-118] from the expulsion and diffusion of manganese solute. The aluminium concentration in austenite should not be the issue causing this oxidation disparity as the content is far higher than what has been seen to produce a protective alumina scale [106].

The article published in Materials Science and Technology by T. K. Jeong et al. [119] focuses on the selective oxidation of Fe-(2–6wt.%)Al-4Mn-0.3C steels for galvanisability purposes, with a heating rate of 10°C/s up to 600°C and then 3°C/s and held at an isothermal temperature of 800°C for 1 minute. The experiments were conducted on three steel grades with aluminium contents of 2, 4, and 6 wt.%, named A, B, C respectively with manganese ~3.8 wt.%. The experimental atmosphere consisted of 95% Nitrogen – 5% Hydrogen with three surface oxygen partial pressures represented by dew points of -10°C, -30°C, -60°C. The authors also provide a numerical model based on Huin et al.'s model. The steel compositions involve a mole percent ratio of aluminium to manganese of 1, 2, and 3.

The samples were kept in liquid isopropanol to prevent oxidation as the authors claim, however the presence of oxygen in the isopropanol molecule as well as oxygen potentially dissolved in the solution prevents this conclusion being as certain as the researchers claim when aluminium is involved. Depending on the time taken from the surface preparation stage to the furnace, the surface oxidation could significantly affect the surface reactions and oxygen penetration. However, the existence of the isopropanol solution at the surface would reduce the surface oxygen concentration compared with the air atmosphere. The most likely scenario, given aluminium's potential for reaction with oxygen, is that a thin nanoscale film was produced at the surface, although this is not certain either due to the lack of investigation by T. K. Jeong et al. The experiments were conducted with the atmosphere in the reaction

chamber for the full heat cycle, meaning the samples were oxidising before the isothermal temperature was reached; however, the authors interrupted the thermal cycle at specific points to assess the impact of this.

The authors do not explicitly state the phase composition of the steel; ferrite and austenite are only mentioned in the oxide phase diagram and the discussion of the numerical model, where the consideration of the steel phases was taken for the input diffusion speeds. To properly interrogate T. K. Jeong's results, ThermoCalc was used to provide the phases at the given isothermal temperature. All of the steel compositions used were found to be roughly 95% ferrite with the remainder being cementite. Although the phase composition is not given by the authors, the high aluminium content provides a reasonable basis for the samples to be considered as at least mostly ferritic in this review. The single-phase nature of this steel unfortunately differs from the present project's steels and cannot be directly compared with dual phase internal oxidation in mind. However, the change in aluminium content across the steels will provide insight to the role of aluminium compared to manganese in the oxidation process.

As expected, the lower atmospheric dew points provided a lower oxygen concentration to the surface and resulted in far less surface oxidation, with the lowest (DP = -60°C) being considered as "macroscopically clean", with very thin surface alumina layers, confirmed with EDS-TEM. The researchers discuss that minimal oxidation occurred on the samples oxidised in the two highest oxygen partial pressures up to 600°C, but further oxidation up to the isothermal 800°C saw the -10°C DP sample form coarse surface oxides, whilst no major change occurred on the -30°C DP sample. The authors conducted a number of analyses on the samples post-oxidation. The glow discharge optical emission spectroscopy (GDOES) depth profiles provide aluminium and manganese compositions near the surface. It is helpful to note that as the transport of material causes the growth of the external oxidation layer, the "surface" essentially moves upwards away from the initial surface. This means that the surface defined in the GDOES origin does not correlate with the initial surface and must be considered when analysing the results.

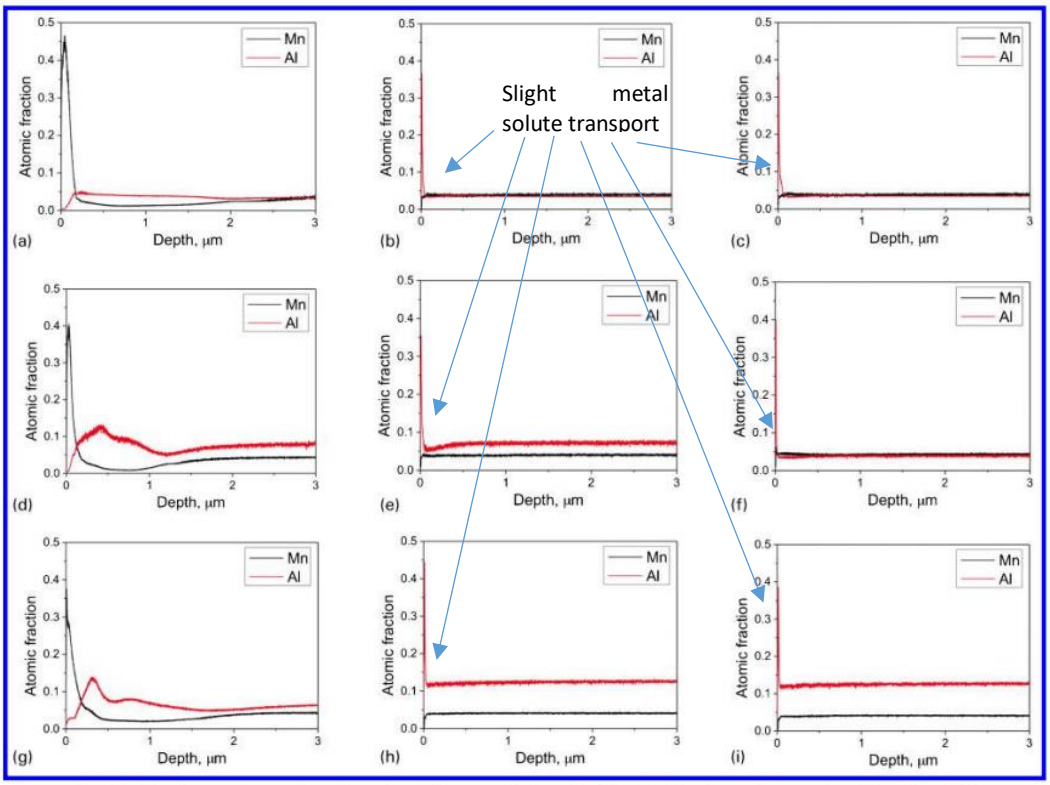

a–c alloy A with dew points −10, −30 and −60°C respectively; *d–f* alloy B with dew points −10, −30 and −60°C respectively; *g–i* alloy C with dew points −10, −30 and −60°C respectively

5 Glow discharge optical emission spectroscopy depth profiles

Figure 2.21 T. K. Jeong et al. [119] GDOES diagrams, specifying the aluminium and manganese element composition with depth, element transport indicated on b, c, e, f, h, and i for clarity as the metal solute transport for a, d, and g is quite apparent

In all sample dew points the transport of at least some material to the surface is evident, indicated by blue arrows where necessary, with aluminium transport dominating at lower oxygen contents. Surface manganese oxide formation only occurs seemingly with the -10°C DP, which decreases with increasing aluminium content. Considering the known aspects around higher aluminium concentration and decreasing internal oxidation [5, 87, 106], this is expected. Bott presented results where samples of 5 wt.% aluminium were internally oxidised whilst the samples with 8 wt.% aluminium were protected by the sufficiently dense surface alumina layer. Comparing to T. K. Jeong et al.'s results, 6 wt.% Al seems similarly insufficient to form the protective surface alumina layer. In a sample with significant aluminium and manganese concentrations, the aluminium transport to the surface is lower than manganese because the requisite oxygen concentration for alumina formation is

reached internally [5, 7]. The authors' results support this as the manganese enrichment is prevalent at the surface whilst aluminium is most abundant below the external scale, this also agrees with known scale formation thermodynamics. Significant visible manganese depletion occurs up to a depth of 2.5µm in the steel with the lowest aluminium content, decreasing to 2µm with the highest content. There seems to be two errors in the GDOES analysis in Figure 2.21 which might limit the validity of certain comparisons:

Diagram f, representing an aluminium atomic fraction of 8.2% for alloy B, shows the same aluminium content as alloy A of 4.2 at.%. Although this represents a dew point for the sample which was barely oxidised it represents a potential fault.

GDOES analyses at a depth of 3µm, whether the sample in diagram g underwent a far greater degree of aluminium depletion in the substrate is not evident because of this small range. If significant depletion of the sample does not extend beyond the range presented in the diagram it presents another error where the sample analysis appears to show an aluminium content of 8.2 at.%, when it should be 11.9 at.%. This could be a far more egregious error as it corresponds to the highest DP with the sample producing the most significant oxidation profile. If these points on the errors are valid then the potential disparity must be considered throughout.

The authors also applied a <20µm palladium-platinum layer on the surface of sample C, to confirm the oxidation behaviour compared to the initial surface. The results suggest that the surface oxides comprise manganese oxide (MnO), and the internal oxides consist of aluminium oxide (Al_2O_3), this is agrees with what was expected.

Another issue appears due to the phrasing by the authors that leads to uncertain information surrounding the state of the experiment atmosphere. The researchers do not explicitly state how the reaction atmosphere is introduced and maintained during the experiments, from the phrasing of the third conclusion paragraph by the authors it appears that the atmospheric dew point decreases over the course of the individual experiment from an initial dew point. If this is the case then it introduces a large amount of uncertainty as the size of the sample and the size of the reaction

chamber will affect the total atmospheric oxygen content and at what rate the dew point is reduced over the course of the experiment, as the writers did not specify this information. The authors only mention a constant dew point throughout in relation to the assumptions made for the numerical simulation. Due to a lack of specificity, the most reasonable conclusion must be made based on the phrasing, that an initial atmosphere of a specific dew point was introduced to the furnace reaction chamber and sealed, with no gaseous species added at any point during the experiment. This leads to a reduction of atmospheric oxygen partial pressure as the experiment proceeds as the oxygen reacts with the steel, consequently reducing the inward oxygen flux throughout the experiment duration. This method of conducting high temperature isothermal oxidation experiments and the presentation of the data by T. K. Jeong et al. could relate to the same industrial conditions they are attempting to replicate as eluded to in the introduction by the controlling of industrial atmospheres, although this is not clearly specified by the authors concerning their furnace reaction atmospheres. This technique of conducting experiments does not lend a high comparability to the present project as the reaction chamber was kept in vacuum to prevent oxidation before the isothermal stage, creating a gradient of the oxygen/water vapour partial pressure to a constant value defined by an atmospheric equilibrium over the duration of the experiment. Whereas the literature being reviewed, T. K. Jeong et al. provide results for samples that experienced an initial atmosphere with decreasing oxygen content, with oxidation occurring during the initial heating phase. The different methods of experimentation present the stark difficulties in conducting high temperature oxidation, especially when including aluminium.

The researchers state that the samples that were interrupted at 600°C in higher oxygen partial pressures formed manganese oxide at the surface with alumina forming internally. As the temperature increased to the 800°C isothermal stage, at lower oxygen partial pressures alumina surface formation appears to take over the surface manganese oxides, whereas at the higher oxygen partial pressures the surface manganese oxide formation continued. Internal oxidation does not occur at dew points -30°C and -60°C with only external alumina formation occurring; this is

expected due to the low partial pressure of oxygen reducing the inward oxygen flux. If the furnace reaction chamber atmosphere was not affected after the initialisation then it is probable that the thermodynamics of the highest dew point atmosphere (-10°C) was affected to a point where the manganese oxide formation partial pressure was negatively passed and the MnO could start to dissociate spontaneously. Introducing aluminium transport to this scenario sees the possible spontaneous reduction of manganese oxide and the transport of aluminium to the surface due to the reduced inward oxygen flux and subsequent additional reduction of manganese oxide by the free aluminium.

The thermodynamic calculations by the researchers predicted manganese aluminate ($MnAl_2O_4$) formation, however as this does not completely forecast the oxides present as the depletion and element transport will alter this behaviour. This also describes the divergence of their numerical model and experimental results. Another deviation from reality is the lack of consideration for the diffusivity of individual oxide species and the effect on the system, this is a complex issue and as the oxidation behaviour of Fe-Al-Mn-C steels is still under-investigated it is a fair exclusion in the numerical model.

Overall, this literature article presents industrial conditions for the oxidation of a ferritic Fe-Al-Mn-C steel for a short annealing simulation, with a comparison to a numerical model. The results are in agreement with well-known established principles around thermodynamic equilibrium with internal and external oxidation. There are important comparisons to this project despite the different system variables, such as the formation of external manganese oxide and internal alumina at higher oxygen partial pressures. The short annealing duration is also a major comparison as few other published literature contains this parameter, allowing a valid comparison to the initial internal oxidation stages.

Another article by W. Peng et al. (2019) [120] with small changes to the authorship credits shows how small the literature pool is for internal oxidation of dual phase Fe-Al-Mn-C steels, as well as the contribution to knowledge this thesis occupies. This team of researchers have published a good portion of the most relevant pieces of

literature to the scope of this present study. W. Peng et al. conduct annealing experiments on the steel at various temperatures to investigate the effect phase transformation this has on oxidation resistance. There are three isothermal temperatures: 950°C, 1050°C, and 1150°C, this is a large temperature range to experiment with as the phase composition and diffusivities vary wildly. The experiments were conducted in dry air.

The steel element composition used by the researchers in this article is closer than those previously reviewed here by W. Peng et al. at Fe-10.6Mn-5.25Al-0.25C with phase composition roughly 65% austenite, 35% ferrite at 950°C, which diverges to a maximum of 69% austenite and 31% ferrite at around 1050°C, and converges to the same phase composition at 1150°C as 950°C, shown below.

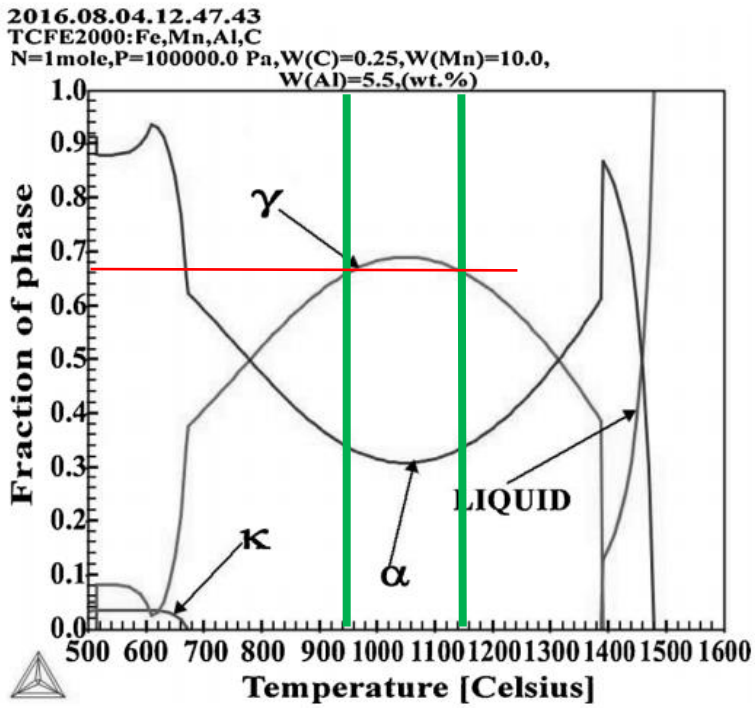

Figure 2.22 Phase diagram related to temperature for Fe-5.5Al-10Mn-0.25C, taken from published article by W. Peng [120], for analysis and comparison. Showing ferrite, austenite, and k-carbide phases from 500°C to 1600°C, with green lines showing maximum and minimum annealing temperatures, and the red related to phase fraction

The phase composition changes greatly between the maximum and minimum annealing temperatures used in this article, although the differences between the

individual phase compositions of the maximum and minimum temperatures are relatively similar, shown on Figure 2.22. However, using ThermoCalc data shows roughly 87% ferrite and 9% austenite - with other minor phases - between 25 - 500°C, with phase fraction 50 - 50% being reached at around 660°C. The oxygen exposure under these circumstances could drastically alter the oxidation behaviour.

W. Peng et al.'s experimental phase consisted of 10mins of short annealing at the specified temperature before the actual main annealing experiment phase of 180mins at the specified temperatures, hereby referred to as stage 1 and stage 2 respectively. After stage 1 the researchers allowed the sample to cool in the laboratory air without convection, there is no mention of the atmosphere in which the samples were annealed however. The samples surfaces were then mechanically polished, which presumably reset the surface, and etched for microstructure analysis. After, the samples were subjected to the specific annealing temperatures for 180mins, though it was not specified whether the surface was again reset after etching.

The authors did not specify the heating rate of the samples during the experiment so comparisons are limited, as the formation of a thin film at the surface during the heating ramp is probable and this duration is unknown to the reader. As shown by Bott [106], the heating rate can drastically affect the oxidation behaviour, so not including this information generates a large amount of uncertainty for the reader. The ~87% ferrite phase fraction from room temperature to 500°C is reduced to a minimum of around 22% at 950°C. This inflection of phase fractions could have a drastic effect on the internal oxidation behaviour not only due to the change in diffusivity as an average of the phase fraction, but also due to the large amount of crystals changing phase and what that means for the structure of high diffusivity pathways such as grain boundaries and the oxides already formed there and elsewhere. There is a phenomenon known as grain boundary pinning [121, 122] whereby the formation of internal oxides and other precipitates somewhat prevent the recrystallization of subsurface grains, there is no mention of this by the authors so therein lies an additional amount of uncertainty by way of not considering all the

possible phenomena. This grain boundary pinning could be a major factor in the oxidation behaviour as the vast majority of the steel substrate undergoes transformation, and possible multiple occurrences of transformation between austenite and ferrite at high temperature, and austenite to bainite/martensite/pearlite during cooling, although the large amount of austenite stabiliser manganese could provide major retention for the austenitic phase.

The sample annealing at 950°C shows that the dual phase nature of the steel produces inhomogeneous surface oxidation and the authors specify that the transformation of the steel phases have a significant effect on the oxidation behaviour. The other two annealing temperatures produced relatively homogeneous surface oxidation profiles. The writers present data concerning the element composition of the phases as temperature increases, showing increasing manganese and decreasing aluminium, however there is no clarification on when this data was extracted (before or after oxidation experiment) or what locations on the sample these readings were measured and whether this was consistent across the samples. The main reason this is concerning is because the manganese content appears to increase and aluminium appears to decrease in both phases, and the reasons given appear insufficient. The authors suggest that the reason for aluminium content decrease could be in the redistribution of aluminium in the enlarged bcc phase. As aluminium is a ferritic phase stabiliser, there is the possibility of ferrite to austenite transformation through depletion. It is stated "…but it [fcc] is enlarged as Mn content is enhanced in it instead. Hence, it can be concluded that the diffusion of Mn from fcc to bcc phase makes fcc phase unstable, and increases the volume of bcc phase". The phrasing of this statement suggests that the manganese diffuses to the ferritic phase from the austenite phase and this decreases the stability of austenite and contributes to the phase transformation. Or perhaps what is meant is the diffusion of elements during recrystallisation that induces this effect. The former idea does not seem sufficient to explain the transformation phenomena here, as can be seen in the phase diagram the authors provided for the stability of austenite and ferrite for Fe-5.25Al-10.60Mn-0.25C steels varies with temperature at equilibrium so the proposition that manganese diffuses between the phases causing the transformation

seems unlikely thermodynamically. As the location of the points of analysis and at which stage during the whole experiment they were taken are not specified it is difficult to interrogate the results of the phase element composition. A table is presented below consisting of experimental data (Exp) provided by W. Peng et al.'s graphs and tables compared to the equivalent data sourced from ThermoCalc (TC), by the author of this thesis.

Table 2.5 Experimental data (Exp) [provided by W. Peng et al., and ThermoCalc (TC) data presented for comparison in a table of ferrite and austenite compositions and phase fractions at 950°C, 1050°C, and 1150°C

ThermoCalc vs. Experimental Data		BCC wt.%				FCC wt.%				Phase Fraction	
		Fe	Al	Mn	C	Fe	Al	Mn	C	Austenite	Ferrite
TC	950	85.646	6.035	8.311	0.009	83.392	5.022	11.266	0.320	77.481	22.519
	1050	85.037	5.971	8.974	0.017	83.402	4.934	11.313	0.352	69.562	30.438
	1150	84.590	5.846	9.530	0.035	83.378	4.799	11.410	0.413	56.985	43.015
Exp	950	85.050	5.830	9.020	0.100	83.200	4.510	11.960	0.330	72.000	28.000
	1050	84.030	5.460	10.350	0.160	83.200	4.520	11.970	0.310	57.000	43.000
	1150	83.680	5.060	11.070	0.190	83.160	4.480	12.040	0.320	39.000	61.000

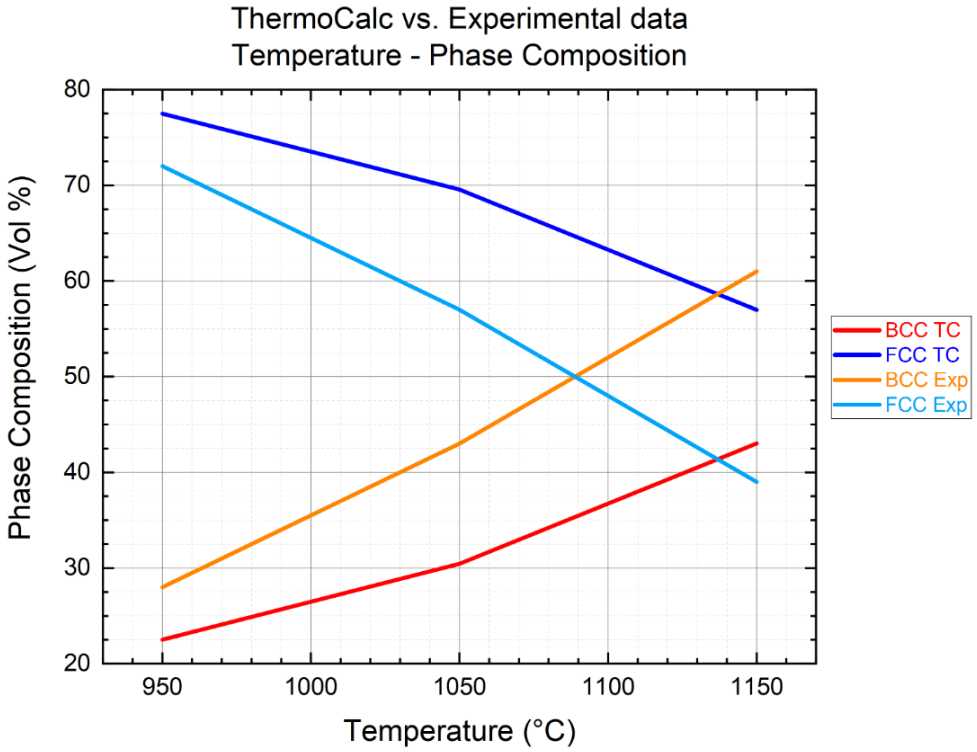

Figure 2.23 Table 2.5 phase fraction presented as a chart comparing the experimental and ThermoCalc data at temperatures 950°C, 1050°C, and 1150°C

ThermoCalc is useful tool but it is still merely a thermodynamic software and it is not prudent to compare results directly. Considering this, W. Peng et al.'s data shows a decrease in austenitic phase volume which is in agreement with the ThermoCalc data. The decrease in both theoretical and experimental austenitic composition values can be attributed to the relative stabilities at changing temperatures. The preferential oxidation of manganese is also a key factor in this W. Peng et al. state. The increase of manganese in both ferrite and austenite is suggested by the authors to be because of the austenite to ferrite phase transformation, as the density of a FCC lattice is higher than a BCC lattice and contains more manganese. However, this does not appear to be the case when comparing the values for the total mass of the system; presented in Figure 2.24 is a comparison of the values generated by ThermoCalc using the total mass of an element compared to the values given by W. Peng et al. relative to phase fraction and phase element composition. The data provided by the authors was used to calculate the total elemental mass distribution of 1 mole of their system and was tracked across the temperature range using ThermoCalc to produce the mass fractions associated with the different crystal phases. This was produced because the different densities and phase fractions of the crystal phases FCC and BCC can obfuscate the total element mass if not handled properly.

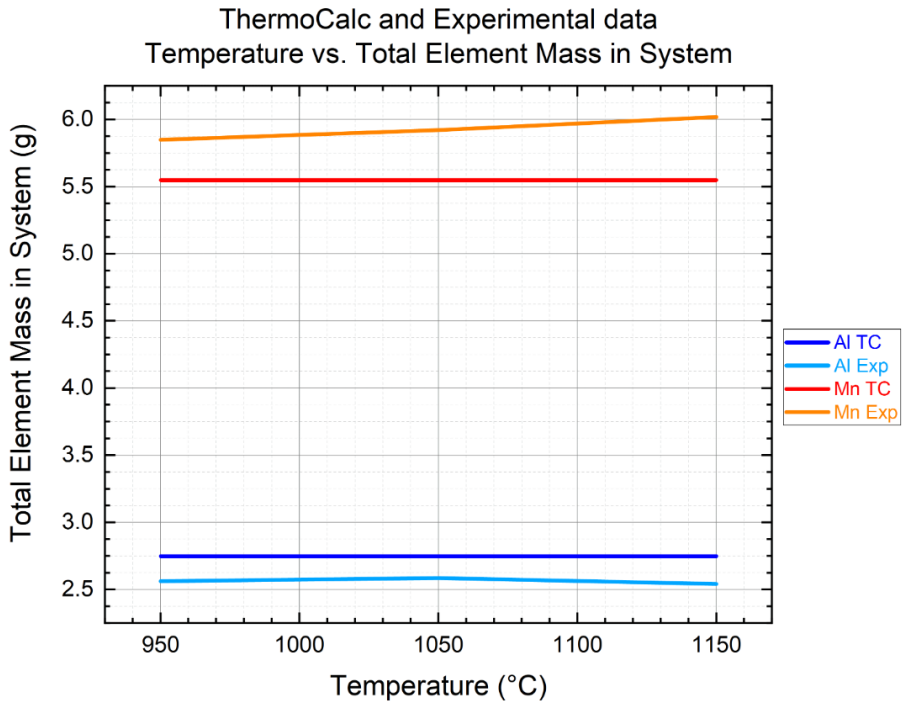

Figure 2.24 Chart comparing experimental data provided by W. Peng et al. and ThermoCalc data to understand the relative total mass of an element in the system, tracked across the phase transformation. A relative increase of manganese is present in the experimental results

The experimental data which was calculated using ThermoCalc has a very small risk of error from the calculation of the total mass of the 1 mole system as defined with the input values of the authors. The data contains maximum error uncertainty values of +0.1927% and -0.3623%, calculated from the total phase mass differences tracked across all the ThermoCalc data, this constitutes an insignificant uncertainty and is sufficient to not consider further.

Incredibly, it appears that the experimental system used by W. Peng et al. increases in the total manganese content, while the aluminium content also varies but to a lesser degree. The reason for this is unknown, however the most likely cause could be a lack of data points to provide a sufficient average and the data analysed coincidentally showed an increase in manganese content. The authors suggest that there is a decrease in the aluminium content possibly due to transformation and subsequent density difference of austenite to ferrite, Figure 2.24 suggests that this is not the case.

The authors posit that the poor oxidation resistance of austenite is due to the preferential oxidation of manganese. With significant quantities of aluminium in their steel at an average of 5.25 wt.%, this is a contentious point as thermodynamically aluminium is the primary reduction agent in the steel. The researchers do not offer an explanation for this and the data analysed by the authors appears insufficient to support their claims. Minimal post-oxidation point analysis was conducted on the internal oxidation zone and seems to be selected in areas of large particles which are absent of aluminium according to the EDS maps provided. The thermodynamic stability data of the oxides posits that the alumina will form first and the manganese and iron oxides will form afterward, the structure of the oxides after 180 mins of annealing is possibly subject to the volume expansion of the subsurface region related to all the oxides that eventually form which could distort the oxide structure. The EDAX analysis of the samples by W. Peng et al. could be a source of error when comparing visually which could be related to the attributed brightness and contrast of the micrographs potentially leading to misinterpretation, as aluminium has a similar concentration in the steel as manganese; at 1150°C, BCC: 11.36 at.% Al - 9.09 at.% Mn, FCC: 9.29 at.% Al – 10.86 at.%, but the images that represent aluminium are very dark whilst the manganese images are not.

There is evidence of aluminium enrichment below the IOZ in the lower temperature experiments, but the samples oxidised at 1150°C show the aluminium distributed throughout. The authors “ascribe this to the phase constitution transformation at different oxidation temperatures which lead to the distinct oxidation behaviour”.

The relevance of this literature under review to this present project involves the diffusion of material to the surface within a dual phase microstructure and the investigation of the proceeding effects. However, the large difference in temperature and annealing duration provides a vastly different oxidation profile for comparison as the diffusivity is temperature-dependant. This project’s isothermal annealing temperature is 850°C and the article being reviewed presents data for 950 - 1150°C, a 100 - 300°C difference. This difference in isothermal annealing temperatures can affect the diffusivity by up to three orders of magnitude in some cases [76]. The

authors do not mention the temperature dependence of diffusion and how this is affected and in relation to the other phenomena at play. The lack of consideration for diffusion speed due to the crystal phase, and the temperature-dependency throughout this publication, the seeming lack of sufficient internal analysis, and the apparent increase in total manganese content prevent unreliable comparisons to the present study. This is unfortunate given the lack of relevant literature to review that relates to this study.

H. Liu et al. [123] conducted experiments to investigate the effect dew has during the annealing of Fe-Al-Mn-Si-C steels, focusing on the selective oxidation and subsurface microstructure. The authors do not specifically state the exact phase composition of the steel in use, ThermoCalc gives 35.5% ferrite and 64.2% austenite. Using a N_2 - 5% H_2 atmosphere, the researchers annealed their sample at 800°C for 180-200s, initiated with a 4.4°C/s heating rate over a similar 180-200s period. The researchers used an electrodeposited fine nickel layer on the surface to protect the oxides during etching and analysis.

It should be noted that the authors suggest that the existence of iron oxides should be considered as contaminants, appearing due to the transfer of the samples to the analysis equipment. If iron oxides are able to form due to this fact, then so too should aluminium, manganese, and silicon oxides. Despite the low temperature, the time between the end of the experiment and the start of the analysis could significantly affect the oxidation profile in multiple regards as the samples did not appear to form a protective surface oxide layer and oxygen penetration can be assumed to occur to some degree.

As expected, the higher the dew point the greater the oxygen flux and subsequent penetration, producing internal oxides which mostly occurred at the grain boundaries and thin oxide films at the surface. The lower the dew point the less oxygen flux and penetration, producing an almost exclusive oxide scale with an IOZ depth of less than 0.5µm - the authors posit that this would be undesirable for

galvanisation. An interesting comment from the authors is the existence of Mn_2SiO_4 and $MnSiO_3$ although $MnAl_2O_4$ is thermodynamically more stable; they suggest that this could be due to the slower reaction rate of $MnAl_2O_4$ in comparison although no evidence or citations are provided. The decarburisation of the substrate and the oxidation of the austenite stabiliser manganese resulted in the transformation of austenite to ferrite of a small layer beneath the surface of up to 20µm in depth at the greatest extent. The higher the dew point the greater the effect as more oxygen was able to siphon of carbon from the steel composition.

The new ferrite region saw the formation of relatively large spherical grains from smaller and linear dimensions, with dimensions of 3 - 7µm and 10 - 25µm respectively. This is consistent with what can be expected for a steel grade with small amount of aluminium and manganese; the authors considered the differences of diffusion speeds and phase transformation and were able to give well-reasoned conclusions that are in agreement with established knowledge in that the decarburisation and transformation will occur based on surface oxygen content and surface oxide coverage/density. Although the differences in diffusion speeds are considered, the diffusivities provides by the authors are concerning: manganese has a higher diffusion in ferrite than aluminium, and the aluminium diffusion is higher in austenite than in ferrite. Both of these points are concerning, given the amount of evidence to the contrary, along with the apparent reference that is cited to depict the aluminium diffusion speeds does not actually contain any mention of diffusion. [124].

A point of contention is the handling of the samples pre/post-oxidation. The authors state that the samples were carried to the analysis equipment subjecting them to air, if the samples are treated the same at pre-oxidation then the oxidation profile will exhibit uncertainty as the sample surface was not clean before experimentation. Whether this prospect was considered due to industrial relevance was not stated.

2.11.1 Published Literature Discussion

A small array of literature can be found with some similarities to this project, but few with as many similarities as those presented above. Published literature on dual phase steels is relatively abundant, but the internal oxidation analysis is usually a by-product of the main external oxidation focus of the article [47-52, 125-135].

The differences in experimental techniques between published literature and this present project are stark. A main point of uncertainty when comparing is the lack of specificity by the published authors on the samples' treatment before experimentation as the potential for thin passivation layers to form on the surface of the steels is high due to the presence of aluminium. There are varying levels of relevancy with the reviewed literature presented above, with isothermal temperature, heating rate, reaction chamber atmosphere, grain size, steel element composition, steel phase composition, steel rolling direction orientation, and pre-experimental surface treatment being the categories that are relevant for comparison.

Although the available literature for the internal oxidation of dual phase Fe-Al-Mn-C steels in short annealing conditions is scarce, those reviewed in this section provide a good range of the closest comparisons for the experimental techniques, results, and analysis which have been discussed here. The majority of the steels contain high amounts of aluminium and manganese due to the desirable properties that both provide, the oxidation of these steels could be expected to produce the required protective surface layer but this is not always the case as various surface oxygen partial pressures have shown to produce inhomogeneous oxidation profiles and the orientation of the sample microstructure can provide avenues for attack [103, 105, 107, 111, 120]. The oxidation of Fe-Al-Mn-C steels can produce internal oxides that initially consist of aluminium, as the lowest oxygen concentrations are found at the farthest points into the steel where only the elements that have the highest oxygen affinity will react, according to the oxide's oxygen formation concentration, this is known as the reaction front (RF).

The main issue surrounding the comparison between this project's experimental results and that of other researchers is that there are so many parameters that affect oxidation with each one potentially exhibiting a large difference and that the literature with investigation conditions closest to this project's are still, in many instances, less comparable due to lack of clarification on sample storage. For example the literature by H. Wang et al. [103] has a short annealing duration with a fast heating rate, but has low manganese content altering the reactions, the annealing temperature is 50°C off which can have a significant effect on the diffusion speeds, has a vast majority ferritic microstructure, and the sample storage conditions are not specified so the existence of an initial passivation layer is uncertain. This piece of literature is considered one of closest to this project's experimental conditions. Steel composition greatly affects the oxidation behaviour of a system by altering the reactants and products as well as when a solute is depleted which can have major effects. The thermodynamic stability of solutes will be adjusted if other common alloying elements are present such as chromium and silicon altering the location, duration until, and sequence of reactions leading to their formation.

As surface oxidation is a key component in disrupting galvanisation [3, 4, 136-138] most oxidation-based research focusses on that with minimal attention given to internal oxidation. The focus of internal oxidation for this project is based on the refinement of LDS dual phase steels for industrial focus, whereby the differences in compositions and mechanical properties of these steels are becoming delicate, this can be seen later in the thesis where an addition of 2 wt.% aluminium corresponds to a significant change of phase composition that will lead to drastically different internal oxidation profile during high temperature annealing.

2.12 Mathematical Modelling and Simulations Discussion

Mathematical modelling assists a researcher in translating their problem into tractable mathematical formulations whose theoretical and numerical analysis provides insight, answers, and guidance useful for the originating application [139]. Modern computational mathematical modelling techniques are indispensable in current materials science research - enabling thorough understanding of the investigated system through enhancing precision control for the various chemical reaction dynamics, kinetic interactions, microstructures, and mechanical properties.

Various commercial entities provide optimised computing software for research purposes, the one used in this project is COMSOL Multiphysics, a cross-platform finite element analysis, solver, and multiphysics simulation software [140]. This software was chosen because of the need for high control and fidelity of the local grain-boundary geometric system and appropriate diffusion-based oxidation chemistry and physics capabilities, while providing a range of mathematical solvers and modes of simulation results formats, with a streamlined user interface with customisation options. This array of modelling options provides the user with a range of paths to navigate the limitations of the software and aids the analysis of the results.

Internal oxidation modelling is a well-established method for probing the extreme environments present in most high temperature steel treatments, providing a unique window to the internal oxidation phenomena that is currently not possible to view experimentally, through customisable systems whilst isolating the contributing factors such as surface oxygen concentration, isothermal temperature, microstructure, and solute concentrations.

Developing a model to probe the intergranular oxidation of adjacent heterogeneous phase grains of LDS coupled with experimental work fills a void in knowledge both in published experimental literature and in the numerical modelling literature.

As the industrial aim for galvanization that is present in a large portion of dual phase steel oxidation research related to oxidation, numerical modelling provides a unique window to a less appreciated portion of steel production – internal oxidation. The

modelling work in this project is unique amongst peers partially due to the simultaneous chemical and kinetic calculations, and the absence of an integrated thermodynamics software, as well as the system phases and elemental compositions being investigated.

The majority of numerical models found in literature are based on chromium-containing alloys and involve the formation of the oxide phases under thermodynamic equilibrium using standard transport mechanics with various thermodynamic software couplings calculated with alternating transport and reaction iterations [69-73, 139, 141, 142]. Most are based around 1D finite difference methodology, with some based on a 2D homogenised geometry; this project's model is a 2D geometry with maximised reaction rates coupled to the relative chemical availability, oxide stability and reaction sequence, refined for simulation stability. The benefit of this model structure is that it does not assume the establishment of a thermodynamic equilibrium due to the transport of metal solutes to the reaction zone, along with the inclusion of the geometric oxide blocking which will alter the local reactant and product concentrations; also, the reaction and transport occur simultaneously increasing the simulation efficiency comparatively to the iterative numerical models currently found in published literature.

These factors contribute to the state-of-the-art model produced in this study for the internal oxidation of dual-phase LDS of Fe-Al-Mn-C composition, where the heterogeneous make-up of the steel contributes differing diffusion zone speeds and amounts of solute to the formation of the internal oxides. The short annealing times (up to 10 minutes) involved in this project also occupy a niche in LDS modelling oxidation [69-73, 139, 141, 142] where others are usually much longer.

3. Mathematical Modelling

This project is the investigation of the internal oxidation of low density Fe-Al-Mn-C steels, with dual phase microstructure in short industrial annealing conditions and it fills a specific void in literature. The dual phase nature of the steel provides a heterogeneous contribution for the aluminium and manganese fluxes, and differing diffusivities in the Ferritic (BCC) and Austenitic (FCC) crystals. With steels that constitute solute concentrations that fall on both sides of Wagner's Criterion, the internal oxidation behaviour of this complex oxidation scenario is being examined on steels with varying solute concentrations and microstructures in the interest of verifying where the oxidative contributions lie and representing these phenomena in the modelling software COMSOL Multiphysics. The model consists of simultaneous ion transport and reactions in a simulation run over a 5-minute time frame.

COMSOL Multiphysics was chosen as the software to use in this project as it was based on Finite-Element meshing calculations, which could give an accurate representation of local compositions and an effective method for the resolution of grain boundary oxidation effects, such as effective diffusivity decrease by increasing oxide/alloy fraction. A minimisation approach was taken in regard to adapting the physics, meshing, and geometry of the model and software to reduce the solution time whilst retaining the highest possible accuracy, defined by the statement:

It is important to note that the COMSOL Multiphysics programming software in this project has seen many efforts to reduce instabilities and increase solution convergence, these include using interpolation functions for reaction rate (thermodynamically valid, but removes the hard-limits of the equilibrium constants) and diffusivities, with smoothening features, and removal of zeroes, as large differences in computed time-dependent variables is a major cause of efficient resolution issues. The values chosen in each regard were done so to balance the accuracy of the physics and chemistry with model stability, solution time, and efficiency.

3.1 Assumptions and Declarations of the Model

Below is a list of assumptions and declarations about the model surrounding the selective exclusion of certain real aspects of oxidation, in descending order of importance:

- Only internal oxidation of Fe/Al/Mn is considered, external oxidation is not
- Only a single phase of each oxide species is considered
- The surface is initially considered to be in equilibrium with the atmosphere. The initial oxygen concentration dissolved at the surface is defined by Sievert's law and the dissociation H_2O/H_2 equilibrium Equations 2.33 and 2.34.
- The surface oxygen Concentration boundary condition is subject to volume fraction of oxide relation using Maxwell's approach
- Grain boundary diffusion is a high-diffusivity pathway and the primary route of oxidant penetration
- The model volume is homogenised; therefore, no discrete particles exist, and microstructure ordering, and changes are not considered
- The inconsistencies of the diffusivity parameters of the solutes from literature are dwarfed by their difference from the diffusivity of oxygen
- The diffusion and self-diffusion of the base metal iron is not considered as it has such a large concentration that significant concentration gradients are unlikely to form
- All reactions are considered thermodynamically irreversible and therefore oxide dissociation is not considered
- Transformation from solute and interstitial oxygen to oxide molecule occurs according to the specified rate of reaction
- The Einstein–Smoluchowski relation of the diffusion of electrical charge carriers and the generation of electric fields is not considered as the incorporation of another field of physics to the model would serve little benefit whilst requiring an order of magnitude more computational resources
- The Kirkendall effect is not considered as the solutes are relatively dilute
- Effects that are not well understood are not included, such as: Cross-effects of diffusion and enhanced diffusion
- Dual phase steel grain boundary diffusivities are mean averages of Ferrite and Austenite grain boundaries diffusivities and grain concentrations

These assumptions do not invalidate the simulation, as whilst this is a sizable list of assumptions and declarations, it is necessary to define the limits of the model.

In relation to the assumptions on the diffusion of ions (Kirkendall, self-diffusion, diffusivity values), the results are not altered significantly, or the effects on four-component systems are not well known enough in order for an accurate incorporation, or the addition of such would add complexity to the model without a proportional benefit of computational load increase to simulation accuracy ratio.

3.2 Geometry

This section is where the shape of the model is discussed, involving how the module in COMSOL uses various polygons to create the desired structure.

Steels processing can produce a variety of grain sizes and structures [3], however a common $10\mu m^2$ has been used as the standard for testing in this project as this is within the range of the steels this model was aimed at stimulating. The different geometries of the model were initially adapted from the Fisher model with various iterations that ranged with problems from being too small to accurately portray the solute pool, to unnecessarily complicated instigating long simulation times that could be simplified by eliminating the symmetry. There existed three main geometries which saw many adaptations and further refinements over the course of the project whilst investigating the software limits. These three geometries are discussed:

3.2.1 Geometry 1

Based on the Fisher model, with a grain-boundary/grain (GB/G) volume ratio of 1/10, this simple geometry was the bedrock of testing that was necessary to discern the diffusion mechanisms that COMSOL incorporated, ensuring the legitimacy, which was confirmed by comparison to existing literature around the expected form of the concentration profile according to Fick's first law. This geometry was kept and used to test various changes across the span of the project for its small computational

demand and quick resolution time. The concentration profile for $D_{GB} > D_G$ is between Regime B and C diffusion.

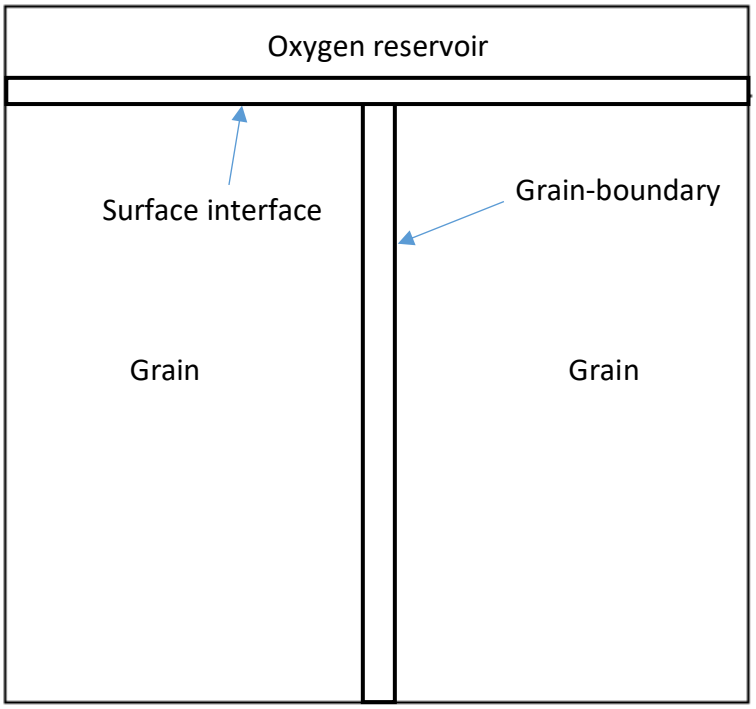

Figure 3.1 Early geometry schematic, homogenised grain structure, two grains, one grain boundary, surface oxygen reservoir, and a surface interface, 10μm in depth

Figure 3.1 shows an early model geometry, consisting of two grains separated by a grain-boundary, with an oxygen reservoir separated from the steel by a surface interface. The oxygen reservoir acted as a pool of oxygen whereby the diffusion of oxygen was subject to its concentration gradient into the model. This was used as a comparison to the other available boundary conditions "Concentration" and "Flux" which continually added material to the system via concentration and flux expressions, determining the superior method of oxygen addition was essential. The "Concentration" boundary condition was deemed to be most suitable for the purposes of this project as the oxygen reservoir was not consistent in oxygen contribution to the system. The "Surface interface" is an interface of the same steel composition and diffusivities of the grain-boundaries, between the "atmosphere" (surface oxygen boundary condition) and the steel subsurface; the surface interface

was used to act as the surface lateral transport medium which usually has a faster diffusion speed than grain boundaries [7, 53]. This iteration of the model was designed to start the model with a simple geometry to properly incorporate the reaction mechanisms, decreasing the chance of solution instability in the early stages of building the model.

3.2.2 Geometry 2

The next iteration of the geometry was similar to a horizontal brick wall section with larger than usual grain boundary widths to allow a large volume of oxygen to diffuse throughout the system to stress the Reactions mechanics, and further probe the consistency of the diffusion profile when a large portion of the model is fast-diffusions speed – which was shown, as expected, to be consistent with relevant general literature examples.

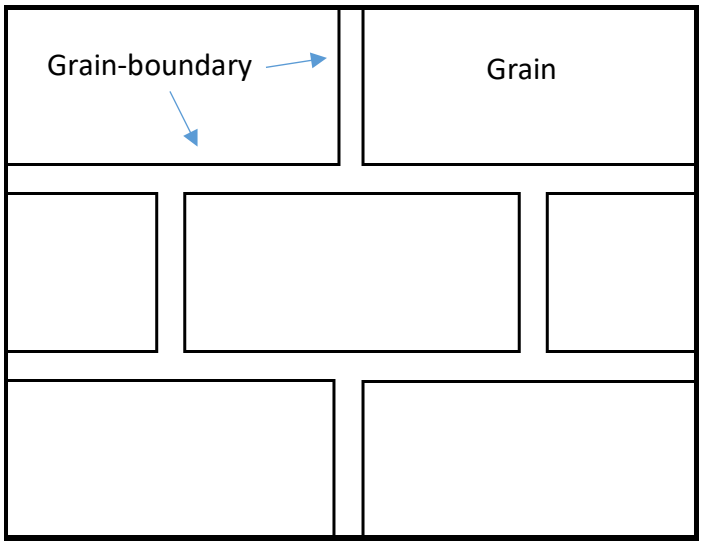

Figure 3.2 Brick-like geometry schematic, homogenised grain structure, very large grain boundary widths, four whole grains and two half grains, 35µm in depth

This geometry's purpose was served in the case of probing the limits of reaction of the software, where alumina formation occurred. Due to the simulations ran on this geometry under the high oxygen concentrations, it was found that there can exist a

negative concentration of a species. Obviously realistically false, this was partially rectified with the use of max (0, Y) functions in the reactions terms to prevent reactions when the concentration is zero or below. However, after these tests the geometry was deemed wasteful of computational resources due to the unnecessary symmetry and the inaccurate GB/G ratio, and was determined to be no longer sufficient.

3.2.3 Geometry 3

The next geometry was a vertical slither of a cross-section with much smaller grain boundary widths; it had several iterations which saw the development from a geometry of

X = 30µm, Y = 10µm (3 grains in depth) (Symmetry elimination)

X = 60µm, Y = 5µm (6 grains in depth) ("Solute reservoir" unnecessary)

X = 30µm, Y = 5µm (3 grains in depth)

The different versions of this geometry were investigated as the special considerations given to important parameters within the model were reclassified as specified above. The "solute reservoir" is in reference to the area of the model that functioned as a solute concentration boundary condition and was not to be oxidised, acting similar to the oxygen reservoir. The extra solute concentration was not found to significantly affect the solution and was deemed unnecessary, as the solute concentration is 5 orders of magnitude higher than the oxygen and unlikely to be depleted enough to significantly affect the results. As the geometry was 60µm in depth and the reactions were not instantaneous, the oxygen (in insignificant concentrations, but significant computationally) penetrated much farther than the reaction front resulting in the activation of the reactions terms for all the mesh elements of the model (which are incredibly dense), dramatically increasing the computational demand but without a significant impact on the solution. The simplification of the geometry was to eliminate half the depth as penetration beyond

30µm is very unlikely in the given time frame of the simulations and the concentration of the solutes was decided to be acceptable.

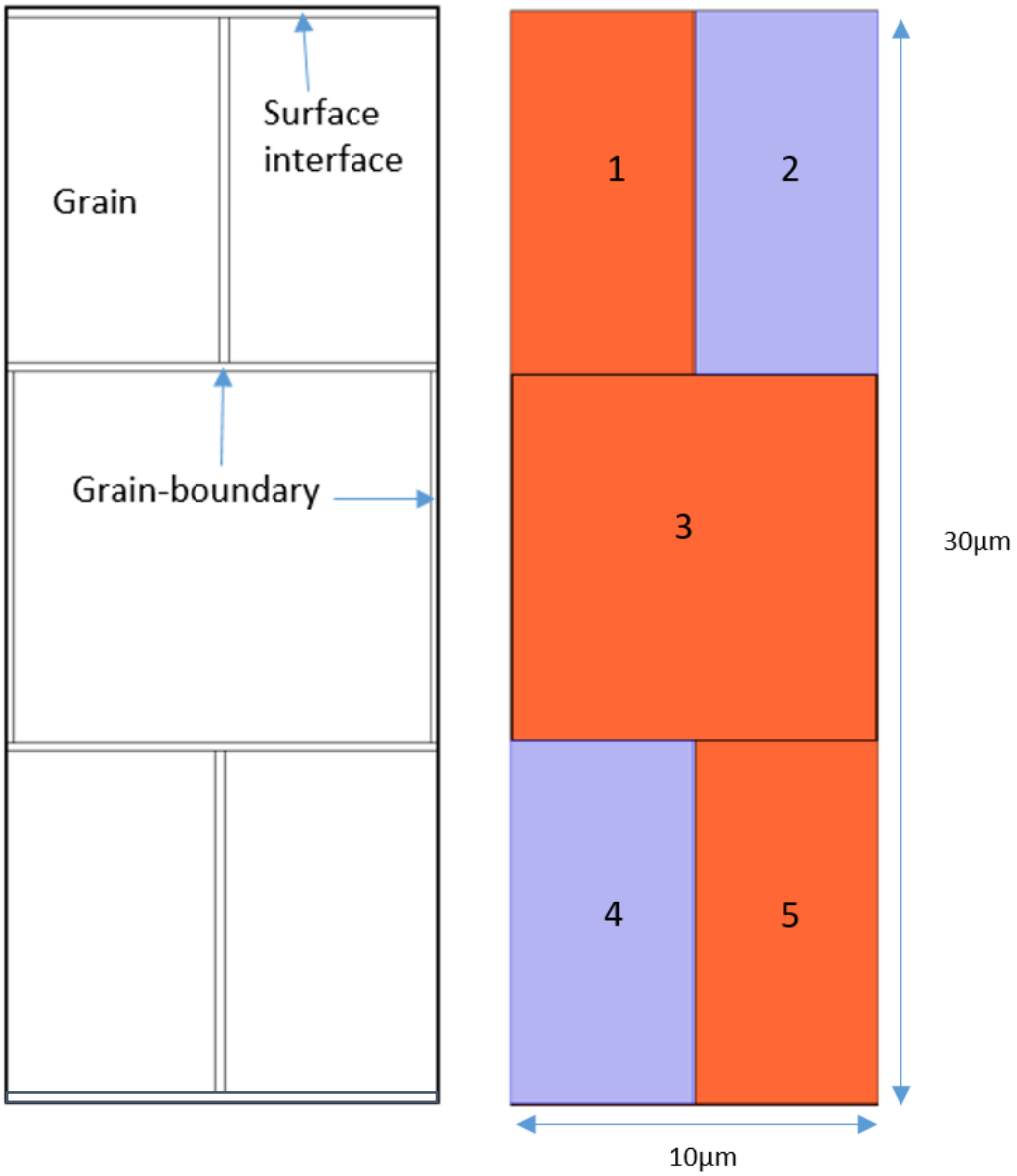

Figure 3.3 Left: Geometry schematic (not to scale), Right: COMSOL Geometry image (to scale). Final geometry of the model, dual phase steel, four half-grains (10µm x 5 µm) and one whole (10µm x 10µm), grain boundaries surround all grains except at the surface where a surface interface is present. Grains 1, 3, and 5 are "phase group 1" (orange), and Grains 2 and 4 are "phase group 2" (blue).

As seen in Figure 3.3, Steel phase groups 1 (Orange) and 2 (Blue) have customisable diffusivity and initial solute concentrations, for accurate steel grain phase equilibrium simulation.

The total elimination of symmetry was used for model mechanics verification and only valid for a single-phase steel. The simulation for dual phase steels in this project

which has a focus on adjacent grain contributions requires this geometry with parallel grains.

The user input values are the composition in wt.% and density of the steel, from these values the initial concentrations are calculated from the volume of the imaginary 3D sample. This imaginary 3D sample is a rectangular cuboid with a square base of dimensions X and Z, with the depth parameter Y, this is translated to the 2D model missing the Z dimension length Lz, but is included in the parameters. The definition of the model volume is used by the geometry section to automatically scale the various polygons without further refinement, this is also incorporated into the mesh size to streamline computation setups. The model has been found to be insufficient in the use of mesh elements due to the 1000 Grain/GB ratio, whilst realistic the connection of the grain-boundary mesh elements with the grain elements produces many times the amount of necessary mesh elements to accurately resolve the simulation, this was resolved by reducing the Grain/GB ratio to 200. The increased size of the GB is satisfactory as a 10 fold decrease in the total number of mesh elements results in a much faster resolution and far more stable model as there are fewer mesh elements to trigger the limiting conditions of the simulation. This increased model GB size is not very accurate for the initial steel grain-boundary, but the oxides created in the grain-boundary can go on to occupy a volume far greater than the initial GB volume. This mediates these stated negatives and adds greater accuracy during to the oxide formation as most of the simulation time involves oxides occupying the grain-boundaries.

3.2.1 Meshing

The mesh profile used in this model is a triangular based, with an equilateral triangle representing the desired perfection of mesh element quality. The model's meshes are set upon by the advice of the COMSOL support, where the recommended minimum number of mesh elements is five per diffusive length, to properly resolve the concentration gradients. There is a number of meshing expressions within the model, each has a significantly higher density of mesh elements in the grain-

boundary than the grains, as the fastest diffusion zones need a proportionate density according to the stated diffusive length.

The number of mesh elements has been drastically reduced by reducing the grain/grain boundary ratio from 1000 to 200 with 10µm x 10µm grains, this changed the simulation time from a variable simulation time of a more often two days to a consistent eight hours. There are 4 Mesh profiles total in the model (Mesh 1, 2, 3, 4), where the least and most dense meshes 1 (A + B) and 4 (C + D) respectively, are shown in Figures 3.4. Due to the same local scale the density of mesh elements makes it impossible see the grain boundary width through the blackness of mesh boundaries in A and C. The mesh profile parameters are adjusted according to the grain/grain boundary ratio and the necessary mesh elements per diffusive length. An increasing density of mesh elements increases the solution fidelity along with the solution time, therefore it is prudent to consider which is best for a given scenario; for example, a high surface oxygen concentration would require a larger amount of mesh elements to accurately and efficiently resolve the reaction mechanics and product concentrations.

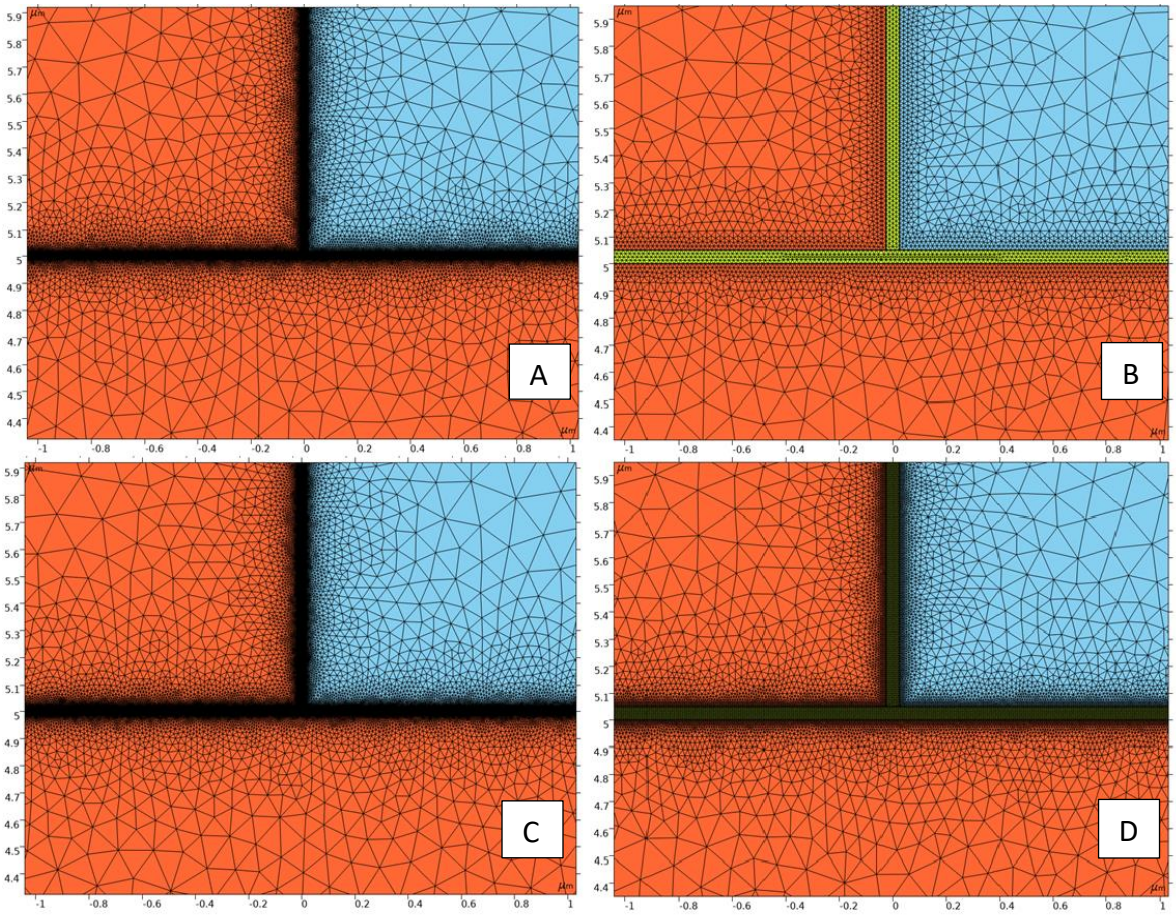

Figure 3.4 Final geometry, located to a grain boundary section. A + C) grain/grain boundary ratio = 1000, Total mesh elements: A (least dense) 750K elements, C (most dense) 2,800K elements. B + D) grain/grain boundary ratio of 200, B (least dense) 150K elements, D (most dense) 550K elements.

3.3 Parameters

This section presents the parameters that are used in every regard in the simulation setup which includes most of the equations, coefficients, and user input values. The parameters section of the software functions as a hub for these and can be called upon to be entered elsewhere into the model; it is also a convenient test bed for any of the various ideas to be implemented into the model as it doubles as a COMSOL-friendly calculator, which includes the solutions to the various functions used - to sample situations where the model could face difficulties.

The parameter list consists (left to right) of the given ***Name*** for the parameter which must be unique; the equation or input is called the parameter ***Expression*** (not included here, see appendix); ***Value*** is the output value of the expression; and ***Description*** is the user custom text field.

The parameters in this model follow a logic that can be mostly ascertained by the parameter name, for example, “D0fMnGB”:

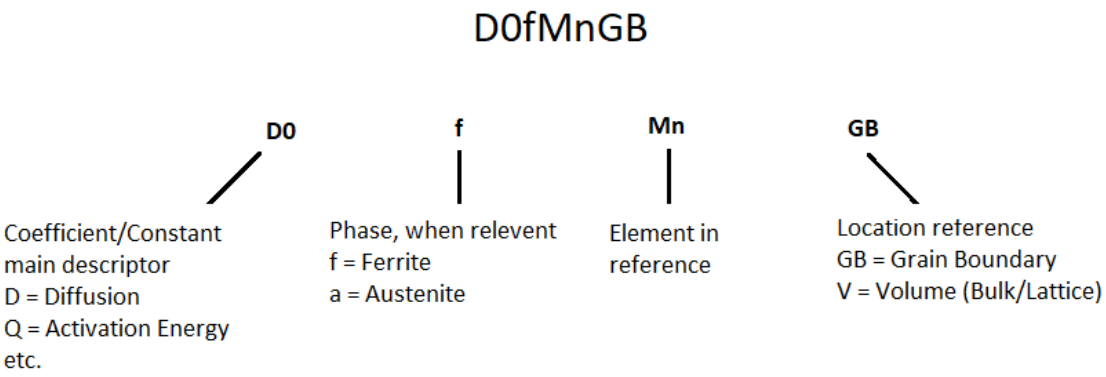

Figure 3.5 Key for the parameters list naming logic

The “ sign is used in the **description** to mean “same as above”, but with the small differences mentioned; also, a lowercase “cX” for species X is used as the instantaneous concentration, whereas an uppercase “CX” for species X is used as the initial concentration at t = 0 (user input); “instantaneous concentration” refers to the local concentration of a species at a certain mesh element and certain time-step where t > 0.

Table 3.1 Model diffusion and geometry parameters list

Name	***Value***	***Units***	***Description***
T	1123.15	K	Temperature
DFefV	1.38E-15	m^2/s	Fe in Ferrite Volume Diffusivity
DAlfV	4.39E-15	m^2/s	Al "
DMnfV	2.04E-15	m^2/s	Mn "
DOfV	6.80E-11	m^2/s	O "
DFeaV	4.99E-18	m^2/s	Fe in Austenite Volume Diffusivity
DAlaV	4.39E-15	m^2/s	Al "
DMnaV	1.08E-17	m^2/s	Mn "
DOaV	2.48E-12	m^2/s	O "
DFefGB	5.12E-08	m^2/s	Fe in Ferrite GB Diffusivity
DAlfGB	8.89E-08	m^2/s	Al "
DMnfGB	5.51E-08	m^2/s	Mn "
DOfGB	2.61E-06	m^2/s	O "
DFeaGB	9.48E-10	m^2/s	Fe in Austenite GB Diffusivity
DAlaGB	8.89E-08	m^2/s	Al "
DMnaGB	1.32E-09	m^2/s	Mn "
DOaGB	1.79E-06	m^2/s	O "
DOOx	1.16E-27	m^2/s	Oxygen Diffusivity in Oxides
p	6800	$kg*m^{-3}$	Avg density of LDS
GBrat	200		Grain/GB ratio factor
h_	10	µm	Model GB Height factor
GBw	0.05	µm	Average GB Width
Lx	10	µm	Base Length X (Horizontal)
Ly	30	µm	Base Length Y (Vertical) (Input)
Lyt	30.2	µm	Base Length Y (Vertical) (True Geometry Ly)
Lz	10	µm	Base Length Z (Depth (Dimensionalisation))
A_	3.02E-10	m^2	Area of Model
V_	3.02E-15	m^3	Volume of Model with Depth = Lz
MM	2.05E-11	kg	Initial Mass of Model, with Volume V_

Table 3.2 Model compositions, solubility, and oxide dissociation concentrations parameters list

Name	***Value***	***Units***	***Description***
AlWt	0.0475		Al Composition (Wt. % - From User)
MnWt	0.0485		Mn "
CWt	0.0016		C "
OthWt	0.0051		Other
FeWt	0.8873		Fe (Remainder)
CFef	110280	mol/m³	Fe Concentration in Ferrite Phase
CAlf	12578	mol/m³	Al "
CMnf	4878.8	mol/m³	Mn "
CCf	50.953	mol/m³	C "
CFea	106950	mol/m³	Fe Concentration in Ferrite Phase
CAla	10592	mol/m³	Al "
CMna	8562.8	mol/m³	Mn "
CCa	2842.1	mol/m³	C "
CFe	108610	mol/m³	Fe Conc. Ferrite – Austenite Average
CAl	11585	mol/m³	Al "
CMn	6719.8	mol/m³	Mn "
Nof	1.31E-06		Ferrite Oxygen Solubility [mole Fraction]
Noa	1.20E-06		Austenite "
COf	0.1665	mol/m³	Ferrite solubility [mol/m^3]
COa	0.1533	mol/m³	Austenite "
CsO	0.095331	mol/m³	Oxygen Surface Conc.
NOs	7.48E-07		Oxygen Surface Mole Fraction
pH2OpH2	0.1		Ratio of pH2O/pH2
cOox_Al2O3	4.19E-53	mol/m³	Al2O3 oxygen Dissociation Concentration
cOox_MnO	1.32E-18	mol/m³	MnO "
cOox_MnAl2O4	1.28E-23	mol/m³	MnAl2O4 "
cOox_FeOf	1.19E-14	mol/m³	FeOf "
cOox_FeOa	1.15E-14	mol/m³	FeOa "
cOox_FeAl2O4f	2.21E-15	mol/m³	FeAl2O4f "
cOox_FeAl2O4a	2.14E-15	mol/m³	FeAl2O4a "

Tables 3.1 and 3.2 are the most relevant parameters with many data values and variables such as diffusion Arrhenius coefficients and activation energies, molar mass, compound density, and thermodynamic data, along with a range of constants being omitted, for brevity and legal reasons. The full list of parameters can be found in the appendix.

3.4 Diffusion Module

The Transport of Diluted Species (tds*) module was decided to be the most suitable for the purposes of this project as the solutes in the steel are considered dilute, and this module does not implement unnecessary terms that come into play in the Transport of Concentrated Species (tcs*) like convection, as the module is not limited to solution based models.

As stated in the Geometry section, the initial phases of the model's construction involved the testing of the diffusion rate to assure their agreement with Fick's Laws of Diffusion, which they *were* determined to.

The specific species as identified in the software are not considered as related even when in consideration of their reaction; this means that all species type, such as Al and Al_2O_3 are subject to only their own individual species concentration gradients, meaning that although in reality Al is chemically a part of Al_2O_3, the software considers them separate as species "A" and "B", with names "Al" and "Al_2O_3". The unfortunate result of this is that in fast-diffusing/reacting scenarios the model will allow a reactant species to diffuse to an area of supposed highly concentrated product if the mesh size is insufficient. For example, manganese is in area 1 and 2, oxygen diffuses into area 1, producing MnO, therefore the model considers area 1to be depleted of Mn creating a concentration gradient and the subsequent diffusion of Mn from area 2 to 1 to continue the consumption and reaction of oxygen, leading to an potentially unlimited creation of MnO. This effect can be seen below in Figure 3.7 where the concentration of Al_2O_3 sometimes reached 2-3 orders of magnitude greater than the initial Al concentration, and up to 50 times the standard state

density of corundum after only 10 seconds, which is thermodynamically impossible even in an already high-concentration of Al-steel (10 wt.%).

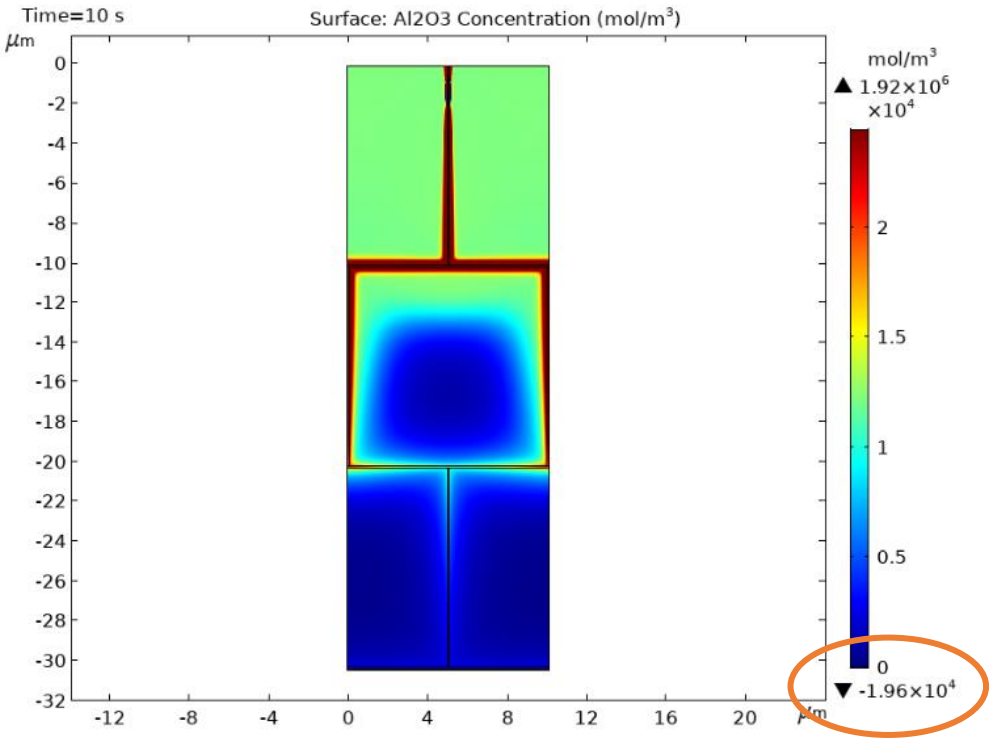

Figure 3.6 Al_2O_3 concentration with unrestricted diffusivity with high reaction rate, showing some negative concentrations, and an unrealistic solute enrichment. Initial conditions: 900°C (isothermal) Fe-10wt.%Al, using a high oxygen concentration of 20-30 mol/m³, at t = 10s. Orange ring showing most negative value

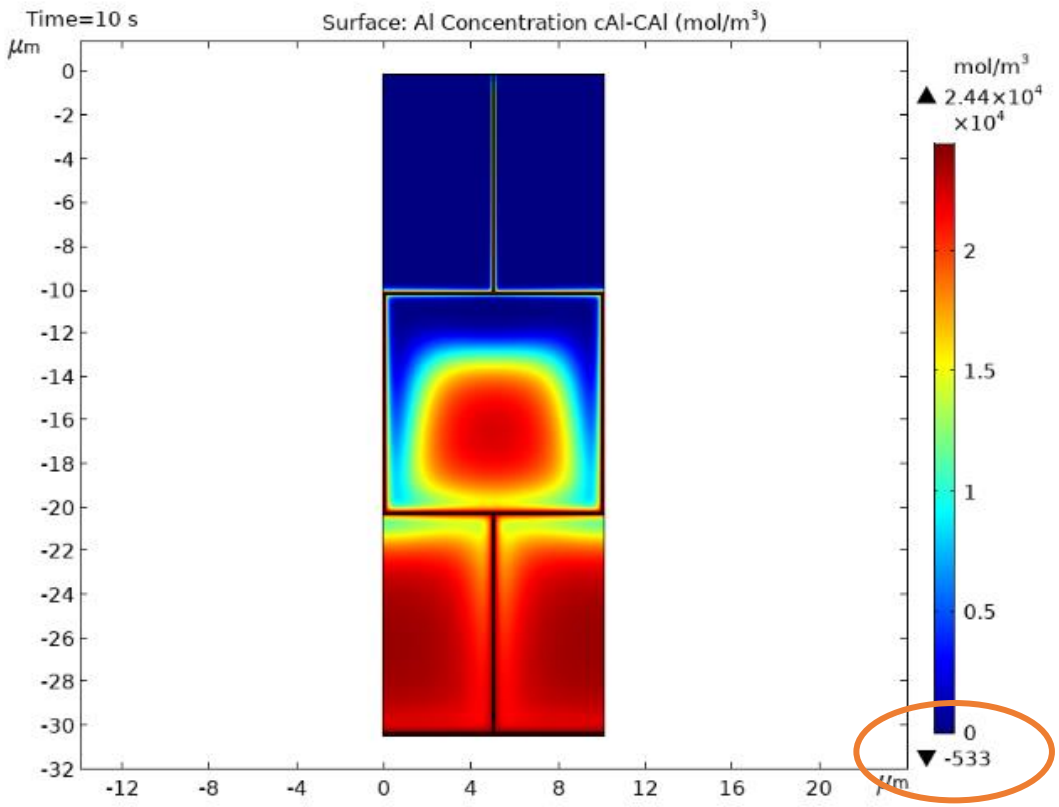

Figure 3.7 Aluminium concentration with unrestricted diffusivity, showing some negative concentrations, and an unrealistic solute enrichment. Initial conditions: 900°C (isothermal) Fe-10wt.%Al, using a high oxygen concentration of 20-30 mol/m³, at t = 10 s

This was also found to be partially due to the high reaction rate of the alumina formation and the insufficient mesh density, which contributed to the significant – and impossible – negative concentration seen in Figures 3.7 and 3.8 (highlighted on the scale, orange ring).

This situation was not totally resolved with the adjustment of the reaction rate and mesh refinements, therefore a pseudo-hard upper-limit for the concentration of a species was required in the form of the Solute Enrichment factor (α), which is also an interpolation function of negative relation shown in the next section. Interpolation functions are created using coordinates to define a graph commanding the behaviour of the related expression. Due to the complexity of the model's interpolation functions, smoothing was extremely necessary to retain an efficient resolution time.

3.4.1 Functions and Interpolation Coefficients of the Diffusion Module

The diffusivity inputs as stated before are subject to functions related factors like solute enrichment and volume fraction of oxide, these are implemented into the model via the Transport Properties physics interface. The interpolation relations are functions with unique names (e.g. intABC(T)) relating the user input variable (T) to the desired function in the physics user input field through either linear, piecewise cubic, or cubic spline relations. The interpolation relations are represented by plots and are presented in this section.

3.4.1.1 Effective Diffusivity

Effective Diffusivity as used in this project relates to the decrease in a species diffusivity due to the presence of oxides, however, this relation does not take into consideration the geometry of the oxide particles and their occupation of the local site. The usage of this parameter is defined by the flux unity of the oxygen and solute, although its purpose is for the consideration of a macroscopic area with volume fraction, it is viable for usage in this model because of the lack of discrete particles produced in the simulation as COMSOL considers each mesh element as having concentrations of each species with no consideration for the discrete nature of the oxide particles.

The lack of discrete particles means that there cannot be a consideration of the displaced atoms or developed internal stresses. Due to this the disproportionate concentration of the matrix iron and the very low likelihood of reaction, iron is not considered in the volume fraction of oxide expressions. The oxygen diffusivity D_{cO} expression in the model is a function of the initial oxygen diffusivity coefficient *DOfV* multiplied by the interpolation function of the volume fraction of oxide, where the initial concentration of the solute in the denominator is relative to its original phase (below is the expression using volume diffusion in ferritic grains as an example):

$$D_{cO} = DOfV * \left(intDO(f_v)\right)$$

Equation 3.1

Where f_v is the volume fraction of oxide:

$$f_v = \frac{(\sum(cX_{ox} * VmX_{ox}))}{\left((\sum(cX_{ox} * VmX_{ox})) + (\sum(cX_m * VmX_m))\right)}$$

Equation 3.2

Where *DOfV* is the volume diffusion of oxygen coefficient in ferrite, cX_{ox} is the instantaneous local concentration of oxide species X, VmX_{ox} is the molar volume of the same oxide species X.

In the model, to reduce the chance of negative concentrations and other instabilities a max operator is used, *(max(X, Y))*, where *X* is the lower limit of the max function usually set to zero, and *Y* is the active function in its full form. In COMSOL's programming language the max function sets a lower limit on the functions or dependant variables specified and is used in this project to prevent any value below zero of a species concentration which is necessary to almost completely eliminate the (physically impossible) negative concentrations resulting from the high rates of reaction in the Chemistry module:

Below is the interpolation function (*intDO*) plot for the oxygen diffusivity input field which relates the Effective Diffusivity of Oxygen with the volume fraction of oxide:

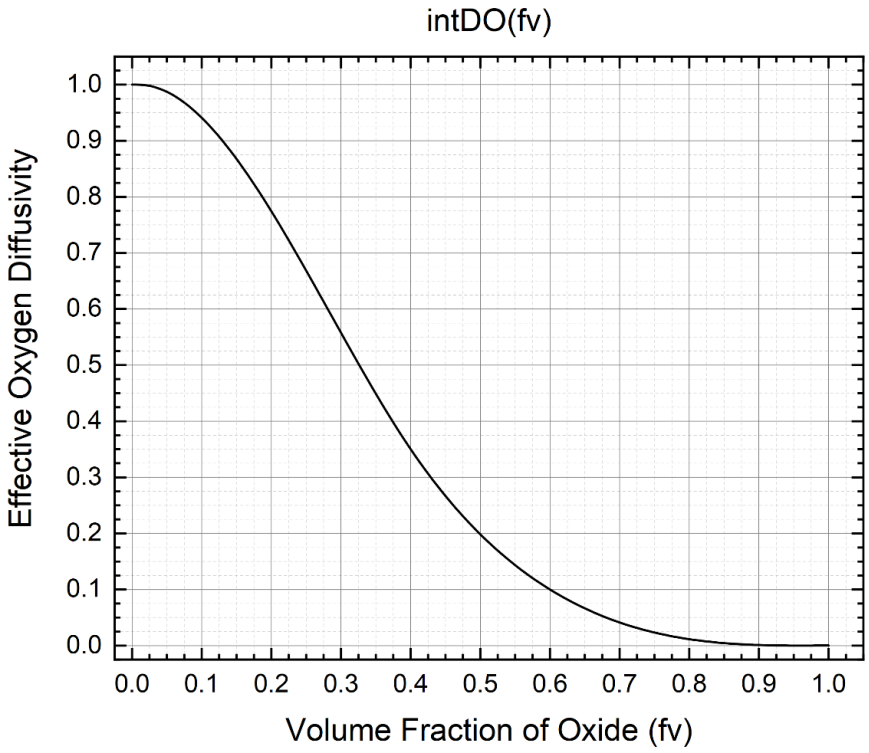

Figure 3.8 Interpolation function (intDO) plot of the local volume fraction of oxide (fv) affecting the Effective Oxygen Diffusivity

The diffusivities of the solutes are subject to the solute enrichment of the IOZ, implemented in the model by the diffusion speed reduced to 10% at 150% of the initial solute concentration of a species in any mesh element, further reduced to 1% at 175%, and effectively stopped at 200%. This is a relation of the local area subject only to the ratio of instantaneous-to-initial solute concentrations and which sees the density of the precipitates approaching the stoichiometric standard state crystal density through verification (seen in the results section).

An expression is given for the volume diffusivity of aluminium in ferrite multiplied by the interpolation relation as a function of the solute enrichment factor (α):

$$D_{cAl} = DAlfV * \left(intDAlMn(\alpha)\right)$$

Equation 3.3

Where the solute enrichment is given by:

$$\alpha = \frac{\left(x * cM_xO_y\right) + (cM)}{(CM)}$$

Equation 3.4

Where cM_xO_y is the instantaneous local oxide concentration of a species, with metal and oxygen stoichiometric coefficients *x* and *y*. *cM* is the instantaneous local concentration of the free metal species, and *CM* is the initial free metal species concentration. The plot of the interpolation function for solute enrichment relation is below:

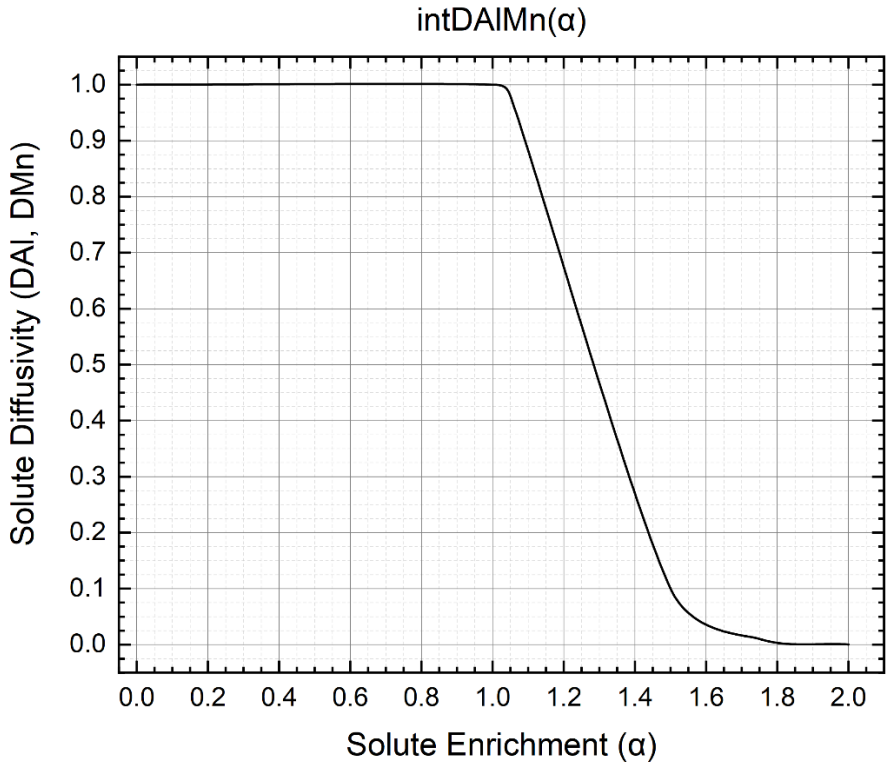

Figure 3.9 Interpolation function (intDAlMn) plot of the local Solute Enrichment (α) affecting the Solute Diffusivity (DAl, DMn)

3.4.1.2 Concentration Boundary Conditions

The Concentration boundary condition is responsible for the input at the selected boundary of the selected species. The boundary condition is altered according to a simple relation of the local volume fraction of oxide, which is an interpolation function (*intOxC*) related to the volume fraction of oxide set with a minimum limit of 10% in accordance with the worst-case-scenario logic where oxygen concentration does not cease. The concentration boundary condition is initially set by the surface oxygen equilibrium relation at the surface set by Sievert's Law defining the oxygen concentration (*CsO*).

$$c_O = \left(CsO - \left(CsO * intOxC(f_v)\right)\right) \quad CsO > 0.1$$

Equation 3.5

$$c_O = (CsO * 0.1) \qquad CsO < 0.1$$

Equation 3.6

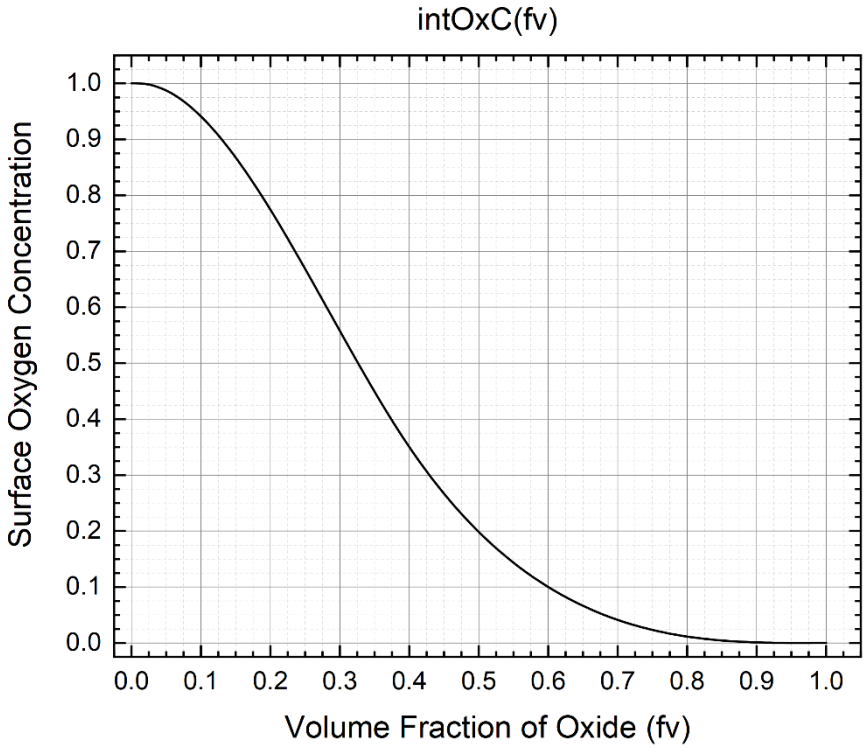

Figure 3.10 Interpolation function (intOxC) plot of the volume fraction of oxide (fv) affecting the surface oxygen concentration reduction

3.5 Chemistry Module

This COMSOL module involves the calculation of the reactant concentrations and reaction rates (user defined) to determine the product concentration in individual mesh elements. The initial reactions take place with the initial solute values (input defined), coupled with the tds* module to calculate the succeeding reactions.

3.5.1 Reaction Functions and Interpolation Relations of the Chemistry Module

The Oxide – Oxygen formation concentrations can be derived from the Gibbs Energy of Formation from the FactSage database, related through the Equilibrium constant by Equation 2.11:

Table 3.3 FactSage Oxide - Oxygen formation concentrations

Name	***Value***	***Units***	***Description***
cOox_Al2O3	4.19E-53	mol/m^3	Al_2O_3 O Formation Concentration
cOox_MnO	1.32E-18	mol/m^3	MnO “
cOox_MnAl2O4	1.28E-23	mol/m^3	$MnAl_2O_4$ “
cOox_FeOf	1.20E-14	mol/m^3	FeO formed from ferrite “
cOox_FeOa	1.16E-14	mol/m^3	FeO formed from austenite “
cOox_FeAl2O4f	2.22E-15	mol/m^3	$FeAl_2O_4$f “
cOox_FeAl2O4a	2.16E-15	mol/m^3	$FeAl_2O_4$a “

FactSage equilibrium calculations are presented from a perfect mixture, allowing all the reactants to have the possibility to react with every other participant over an infinite timeframe, which differs with the model (and reality) as the reactions will only occur in the local area with the constituent reactants present (limited to mesh element boundary), subject to their flux and the available time. However, the equilibrium constants do not provide a viable start condition for the Chemistry module as they are incredibly low compared to the concentration of the metals.

The non-instantaneous reaction rate and the lack of discrete oxide particles effects on diffusion mean that minute quantities of oxygen penetrate further into the model

than the alumina formation constant would realistically allow - activating most mesh elements and increasing computation times massively. Due to this reason along with the concentration values for the formation concentrations of oxides being incredibly low - therefore forming insignificant oxide concentrations - the reaction rates were set as high as possible whilst retaining simulation stability and an interpolation function was used to couple the depletion of the more stable oxide-forming metal to the subsequent reaction rate, e.g. aluminium depletion in the local area will trigger $MnAl_2O_4$ formation in excess oxygen via intSp.

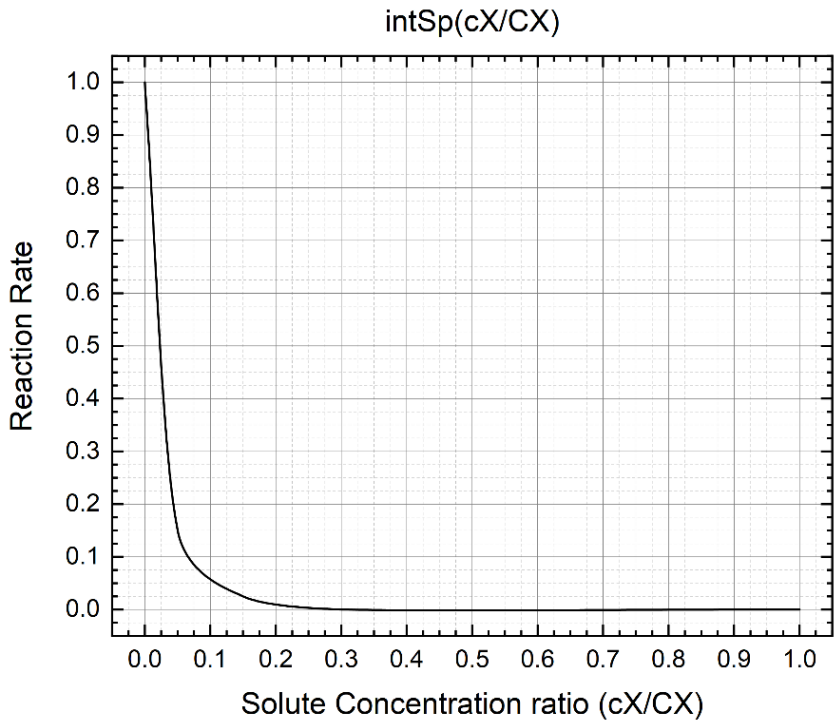

Figure 3.11 Interpolation function (intSp) plot of the Solute concentration ratio (local instantaneous/initial) affecting the Reaction rate expression by dictating the subsequent reaction start condition: Depletion of the previous more stable oxide-forming metal concentration close to zero

3.5.1.1 Thermodynamic Equilibrium Stability Sequence

Stability diagrams give a good representation of the composition of a system, however in multi-component systems there exists many non-stoichiometric phases in addition to stable stoichiometric compounds. This presents difficulties in modelling

reactions as the simulation runs with greater efficiency when the number of species in consideration is minimised. Following the diagrams in Chapter 2 and the data from FactSage's "Equilib" module, an irreversible reaction sequence is seen as an ideal method of implementation:

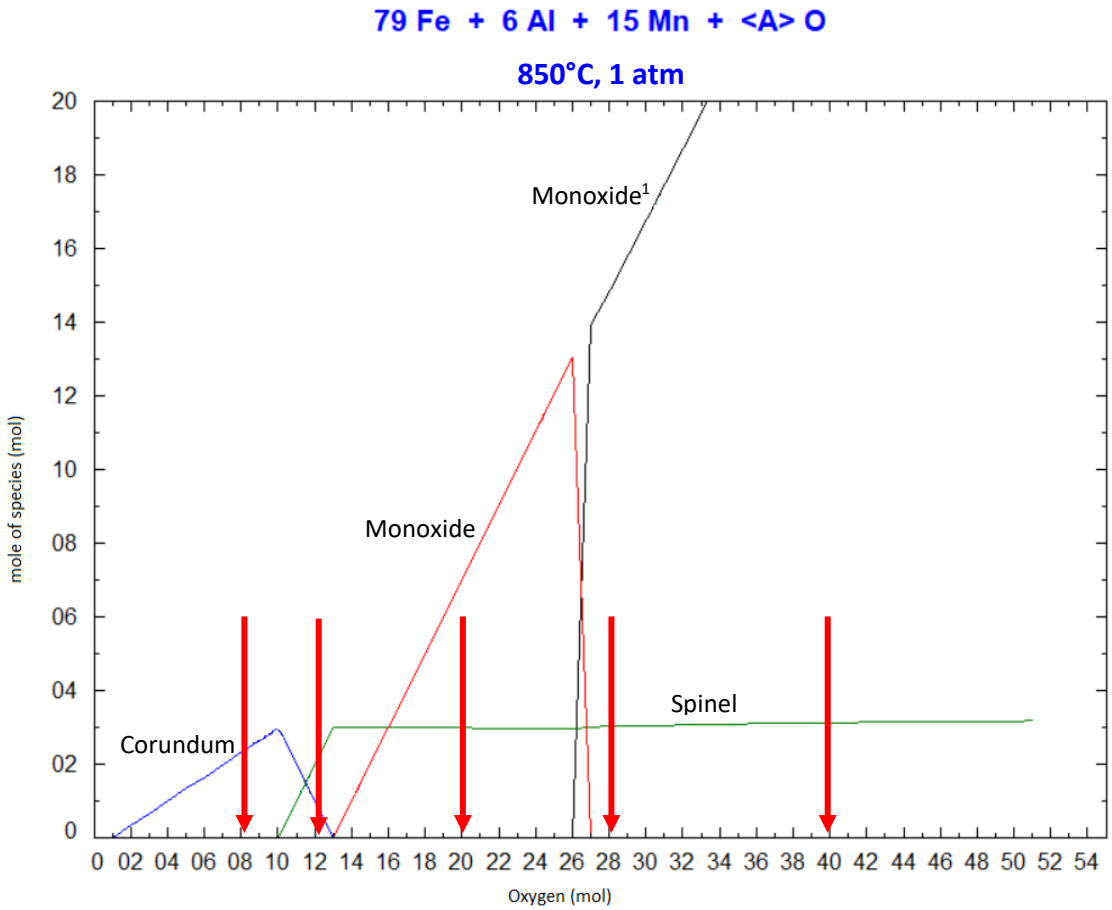

Figure 3.12 FactSage - Fe-6Al-15Mn steel oxygen stability diagram, 850C, 1 atm. Red arrows correspond to investiaged phase compositions. Monoxide is almost exclusively MnO, and Monoxide[1] is a mixture of MnO and FeO

Figure 3.13 is an oxygen stability diagram from FactSage with the Fe-6Al-15Mn steel composition, with Table 3.4 below showing the compositions at relevant points. "Corundum" is the most stable form of alumina (α-Al_2O_3); a spinel refers to the minerals consisting usually of general form AB_2X_4, in steel oxidation-relevant formulae A and B are metals (either different elements, or the same element with different valency) and X is oxygen [143], the most relevant spinels of this project are $MnAl_2O_4$ (manganese aluminate), and $FeAl_2O_4$ (hercynite); a monoxide is a phase consisting of one metal and one oxygen atom, the "Monoxide" phase in Figure 3.13

and Table 3.4 refers to an almost exclusive MnO (manganese oxide) composition, whilst Monoxide[1] is a phase consisting of both FeO (wüstite) and MnO. Al_2O_3

Table 3.4 FactSage - Fe-6Al-15Mn steel oxygen stability diagram table of notable values, 850°C, 1 atm

Oxygen (mol)	Name	Composition (%)	Amount (mol)
8	**Corundum**		2.67
	Al2O3	100%	
12	**Spinel**		3.00
	MnAl2O4	80.00	
	Al3O4+	13.00	
	Mn1Mn2O4 2-	5.97	
20	**Monoxide**		8.04
	MnO	99.70	
	Spinel		2.98
	MnAl2O4	80.00	
	Al3O4+	13.00	
	Mn1Mn2O4 2-	5.97	
28	**Monoxide1**		15.85
	MnO	80.31	
	FeO	19.69	
	Spinel		3.04
	MnAl2O4	63.46	
	FeAl2O4	13.68	
	Al3O4+	13.51	
40	**Monoxide1**		27.48
	FeO	51.31	
	MnO	48.69	
	Spinel		3.13
	MnAl2O4	43.29	
	FeAl2O4	29.70	
	Al3O4+	12.31	

The minimisation of the number of dependent variables is essential to a well-functioning model, as the additional species contribute exponentially to the resolution time of the simulation. The lack of kinetic considerations in the thermodynamic data also provides insight to the probability of forming manganese oxide and wüstite – which is low because the diffusion of aluminium and manganese to the local area will reduce these less stable oxides, especially for the iron oxides as it can be reduced by both diffusing solutes. Due to these reasons, a reaction sequence has been consolidated and simplified into the following:

In a Fe-Al-Mn-O system, free aluminium and oxygen form alumina (Al_2O_3, assumed α-phase); after aluminium depletion, free manganese and oxygen (Mn · O) are incorporated into the alumina, forming the spinel manganese aluminate ($MnAl_2O_4$); if Al_2O_3 is fully depleted via spinel formation in the presence of excess free manganese, manganese oxide (MnO) will form; after the depletion of free manganese, in the presence of iron and excess oxygen, the manganese will relinquish the aluminate to iron to oxidise in the form of manganese oxide and iron aluminate ($FeAl_2O_4$). As wüstite (FeO) is very unlikely to form internally [144], and that the concentration of oxygen required to oxidise through the sequence to its formation is very high for a short term annealing system, it is not considered in this model to also reduce the dependent variables.

3.5.2 The Reactions

The chemistry module has 6 irreversible equations which follow the order of the formation concentrations of oxide from Section 3.5.1.1; although the order is not totally indicative of the reactability ((for the range 800°C – 1000°C) Fe - Al -Mn + O).

The format for the representation of the Chemistry module reactions follows: Reaction Formula in standard stoichiometric format; Rate Expression consisting of the Forward rate constant (k_f^n), each species' reaction term (*chem.X*) with the stoichiometric coefficients, and solute depletion interpolation relation (*intSp(Y)*) where *Y* is the ratio of local instantaneous species concentration (*cX*) divided by the initial species concentration (*CX*); and Forward Rate Constant (k_f^n) value with [units]. There exist max functions on all chemical reaction terms of a species but have been removed here for clearer representation. The rate expressions are set by COMSOL's use of the law of mass action.

1. Al_2O_3 formation. Start condition: None - therefore always active

$$Al + \frac{3}{2}\bar{O} \rightarrow \frac{1}{2}Al_2O_3$$

Equation 3.7 Alumina production until consumption of local Al

$$rate = k_f^1 * \ chem.Al \ * \ chem.O^{1.5}$$

Equation 3.8 Rate expression for Al_2O_3 formation

Where, k_f^1 = 5 [1/s]

2. Intermediate hypothetical species Al_2O_4 formation. Start condition: Al depletion

$$Al_2O_3 + \bar{O} \rightarrow \ Al_2O_4$$

*Equation 3.9 Al_2O_3 conversion to the intermediate species Al_2O_4, which is a **hypothetical species**.*

$$rate = k_f^2 * \ chem.Al_2O_3 \ * \ chem.O * \ intSp\left(\frac{cAl}{CAl}\right)$$

Equation 3.10 Rate expression for Al_2O_4 formation

Where, k_f^2 = 0.5 [$m^3/(s \cdot mol)$]

3. $MnAl_2O_4$ formation. Start condition: Al depletion, free Mn presence

$$Al_2O_4 + Mn \rightarrow \ MnAl_2O_4$$

Equation 3.11 $MnAl_2O_4$ production occurs in the absence of free Al and presence of free Mn where formation occurs in presence of Al_2O_4

$$rate = k_f^4 * \ chem.Al_2O_4 \ * \ chem.Mn * \ intSp\left(\frac{cAl}{CAl}\right)$$

Equation 3.12 Rate expression for $MnAl_2O_4$ formation

k_f^4 = 0.1 [$m^3/(s \cdot mol)$]

4. MnO formation. Start condition – Al depletion, free Mn presence

$$Mn + \bar{O} \rightarrow \ MnO$$

Equation 3.13 If the concentration of Mn is too high to stoichiometrically consume the remaining Al_2O_4, free Mn is oxidised next

$$rate = k_f^3 * \ chem.O \ * \ chem.Mn * \ intSp\left(\frac{cAl}{CAl}\right) * intSp\left(\frac{cAl_2O_4}{CAl * 10^4}\right)$$

Equation 3.14 Rate expression for MnO

k_f^3 = 0.001 [m^3/(s · mol)]

The following two equations are related through two steps of transference of the intermediate species from Mn to Fe with the creation of manganese oxide.

5. Step 1: Mn transference from Al_2O_4 to free O. Start condition: Al + Mn depletion

$$MnAl_2O_4 + \bar{O} \rightarrow \ Al_2O_4 + MnO$$

Equation 3.15 Step 1: Mn transference from Al_2O_4 to O, to form MnO in the absence of free Al and Mn

$$rate = k_f^5 * \ chem.MnAl_2O_4 \ * \ chem.O * \ intSp\left(\frac{cAl}{CAl}\right) * intSp\left(\frac{cMn}{CMn}\right)$$

Equation 3.16 Rate expression for Mn transference

k_f^5 = 0.01 [m^3/(s · mol)]

6. Step 2: Fe combination with Al_2O_4. Start conditions: Al + Mn depletion

$$Al_2O_4 + Fe \rightarrow \ FeAl_2O_4$$

Equation 3.17

$$rate = k_f^6 * \ chem.Al_2O_4 \ * \ chem.Fe * \ intSp\left(\frac{cAl}{CAl}\right) * intSp\left(\frac{cMn}{CMn}\right)$$

Equation 3.18 Rate expression for Fe combination with Al_2O_4

k_f^6 = 0.01 [m^3/(s · mol)]

For the complete reaction (transference of the intermediate hypothetical species Al_2O_4 with MnO formation):

$$MnAl_2O_4 + \bar{O} + Fe \rightarrow \ FeAl_2O_4 + MnO$$

Equation 3.19

Splitting Equation 3.19 into two separate formulae is necessary to reduce to computational strain experienced by the solver as issues surface when three reactants are present.

The nature of high temperature oxidation means that the formation of oxides is quick when their respective oxygen formation concentrations has been reached. The reaction terms and start conditions represent this and has been implemented in the model as the more stable the oxide the faster the formation occurs. Optimisations are present to positively affect the model stability, and the considerations for the number of dependent variables and their interactions through the reactions. As the concentrations of the solutes Al and Mn are high, it is unlikely that they will be completely depleted locally in the oxidation times of this project. The irreversible nature of the reactions has not been seen to be an issue affecting the results of the simulation through a lack of oxide reduction – this is partially mediated by the lack of discrete particles effects on incoming solute flux. Formation of Fe-oxides (FeO, Fe_2O_3, and Fe_3O_4) are not implemented in the model as it is very unlikely to be formed given the solute flux and simulation conditions. The lack of Fe oxides (excluding spinel $FeAl_2O_4$) is justified by the previous statement, and has the positive effects by increasing the stability of the model greatly due to the lack of consideration of the extremely high Fe concentration compared to the solutes.

The justifications for these reactions being chosen as the basis for the Chemistry module include:

- The thermodynamic data from FactSage and the sequence of the reactions that the data suggests
- Addition of dependent variable species increases the computational load, limiting the number of reaction stages is critical. *Al_2O_4 was selected as a hypothetical intermediate species for this purpose*, as it is a main constituent of the reactions but also a relatively large molecule that does not require an

extra set of equations or reactants involved; Al_2O_3 is insufficient for this role as the reactions would need to incorporate a third reactant species, causing a large increase of computational resources.

3.5.3 Surface Oxidation

Surface Oxidation affects the dissolution kinetics of oxygen at the alloy surface. After the initial oxide formation at the surface various layers of oxides might exist, based on the alloy composition. The sample surface changes from an interface of metal – gas, to metal – oxide – gas, leading to a diminishing effect of oxygen penetration. The dissolution of oxygen at the surface in the presence of a scale has been investigated widely by many research groups, but the unique situation surrounding dual phase LDS brings a large area of unexpected results from the alumina and manganese oxide formation during and after the oxidant exposure as certain areas produce dense alumina oxides with no manganese oxide above, whilst others do, leading to heterogeneous surface oxidation on the same sample. Due to this reasoning, a simplified scale is considered using the same approach to volume fraction of oxide as the Effective Oxygen Diffusivity relation as specified before, based on Maxwell's approach [82, 144]; a surface interface boundary (with the properties of a GB in the model) acting similar to a scale - subject to a linear relation of volume fraction of oxide to effective flux, reduced by the concentration component – to reduce oxygen penetration.

3.5.4 Oxide Geometry

The implementation of oxide geometry does not easily fit within the scope of this modelling project as it involves many factors that greatly complicate the model for disproportionately small benefit (internal stress energy/crystal structure deformities, composition etc.), although, future endeavours could focus on this aspect especially the Al_2O_3 rods, potentially enhancing oxygen flux. However, due to the absence of discrete particles the microscopic diffusivity effects cannot be fully considered, such as the blocking feature. This means that the diffusivity through a certain region is

reduced, whereas in literature the formation of these particles would promote the diffusion around the particle, and when the particle is large enough, effectively block the diffusion; although, the diffusivity decrease used in the model remains valid from Maxwell's equation.

3.5.5 Solute Enrichment

Solute enrichment is a term referring to the local accumulation of a solute an oxidised area relative to the initial concentration. This factor is referenced the Effective Diffusivity subsection and is a limiting factor implemented in the model to prevent unlimited diffusion-reaction of the solutes.

3.6 Post-processing

The model involves SI units for its user-input fields, as such the initial values which are in the form of wt.% have to be converted to SI units after the simulation finishes, results are presented back in standard metallurgical terms (such as wt.%). This provides a standard for which most academics and researchers can commonly observe the results. As the species of the model are unique and do not themselves relate to one another, species are separated into individual species categories, with additional groupings where relevant, such as wt.% and at.%. These plots include:

- The presence of oxygen in all forms (all bound oxygen (vast majority) and free oxygen)
- Free base and solute metal concentrations (Fe, Al, Mn)
- Individual oxide concentrations (Al_2O_3, $MnAl_2O_4$, $FeAl_2O_4$, MnO)
- The plot parameters (plot scale and expressions) are automatically set to a scale determined by the COMSOL software, but this can and has been changed in certain circumstances to best represent the data. Below is a list of the different expression types and scale parameters of plots used:

- Instantaneous local concentration with open scale parameters (*cX*), the software automatically picks the scale based on maximum and minimum values of the results
- Instantaneous local concentration (*cX*) with initial concentration as scale parameters (0 – *CX*), any value over *CX* will be coloured the same as the maximum value
- Instantaneous local solute concentration divided by the Initial solute concentration - expression (*cX/CX*), with open scale parameters, to show the proportion of free un-bound solute remaining. This is different from plot type 2. as the full colour range of the scale is still used, both can be used and represent the results differently
- Instantaneous local oxide concentration divided by the respective initial solute constituents' concentration with appropriate stoichiometric coefficients factors ($(Y*cM_yO_z)/CX$), with open scale parameters
- Plots for all species in wt.%, at.%, and SI units [mol/m^3]
- Total Oxide concentration, all oxide concentrations in one plot, with open scale parameters
- Miscellaneous plots such as Mesh Quality, and crude diffusivity and reaction rates

Using several plots with different expressions and scale parameters is important when inspecting the results because very different pictures are presented, but also because a lot more information can be gathered. This is evident in the representation of a certain oxide relative to its metal's initial concentration, which allows the illustration of the Solute Enrichment Factor (α); or the volume fraction of oxide, allowing the inspection of the IOZ barrier effect.

4. Experimental Setup

The furnace used is an Infrared (IR) Furnace that houses an IR lamp as the main heating element and a vacuum sealed chamber. The infrared light is reflected with a gold-plated parabola chamber through a vertically orientated cylindrical Quartz rod. At the top of the Quartz rod inside the chamber a crucible, that is manufactured to absorb a maximum amount of the specific wavelength of infrared light, sits with the sample inside. It was chosen as it allows a fast heating rate (up to 100°C/min) for samples of decent size (10mm x 10mm) for surface oxidation (reducing any oxidation edge effects), and the ability to modify the input gas (including water vapour) without oxidising the chamber.

4.1 Sample Preparation

Each sample is cut from the material provided to about 10mm x 10mm, and mounted in KonductoMet. The samples are then ground with P800 SiC paper, then polished through the stages of polishing solutions 9µm, 3µm, to a final of 0.05µm Colloidal Silica with a mirror finish. Between each stage of polishing, the samples are briefly rinsed with cold water, and cleaned with Isopropanol and cotton wool.

The samples are then immediately transferred to the vacuum sample box (with added Silica for moisture control) and brought to a vacuum between 0.018 – 0.044 Torr; this is to prevent the establishment of a thin oxide film on the surface of the samples, which is more prominent the higher the Al content of the steel. This stage was previously not accounted for and saw some very different results, necessitating the inclusion of a vacuum storage stage; the samples are kept within this vacuum for no longer than 3 days before re-polishing the surface from the 9µm stage.

Surface grinding is used to eliminate oxides, any decarburisation zone, and generally to return the steel to a pristine, flat, initial state. The initial phase consists of grinding the surface with silicon carbide (SiC) paper with water to reduce the surface by 50 - 100µm.

1. P180 SiC, t = until flat
2. P800 SiC, t = 20 seconds

The polishing phase consists of specialised polishing pads and the corresponding diamond polishing solutions respectively, with the samples at each stage being polished in both directions Contra./Comp. to ensure surface consistency.

1. 9µm Micropad pad and 9µm MetaDi Supreme Diamond solution,

   4 minutes per direction

2. 3µm Trident pad and 3µm MetaDi Supreme Diamond solution,

   3 minutes per direction

3. 0.05µm Chemomet pad and 0.05µm Colloidal Silica Mastermet solution,

   2 minutes per direction

Samples are briefly rinsed with water, washed with a Propanol-laced swab then dried between each polishing phase. Once the samples were fully prepared, they were immediately transferred to a vacuum sample box and the atmosphere evacuated and kept in this state until ready to be used, which would be no more than 3 days before having the surface reset again.

4.2 Heat Exposure

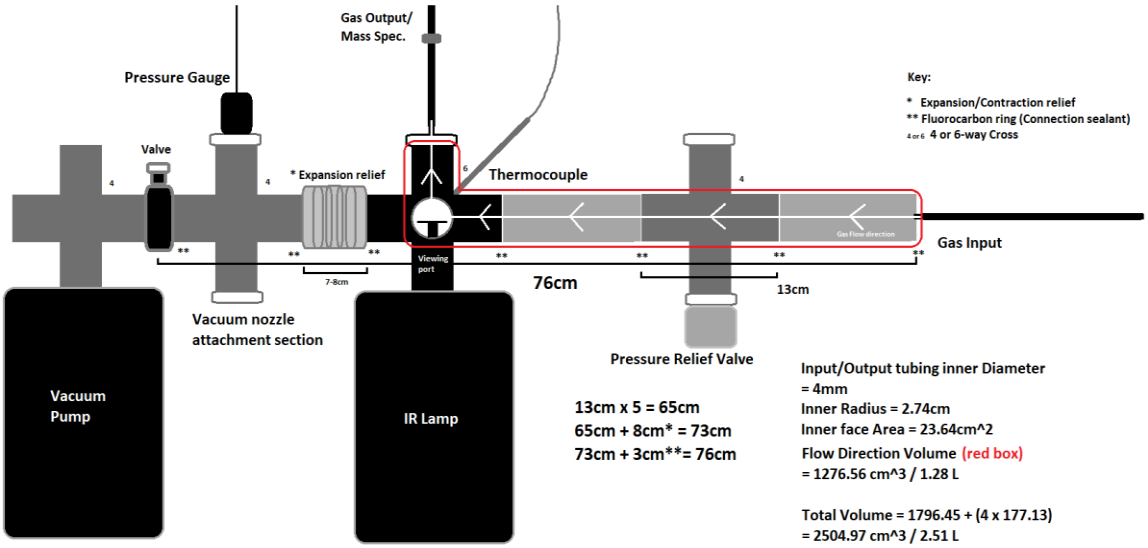

Figure 4.1 Infrared Furnace Schematic for high temperature oxidation in annealing atmospheres, white arrows showing flow direction of input gas, with additional information of dimensions

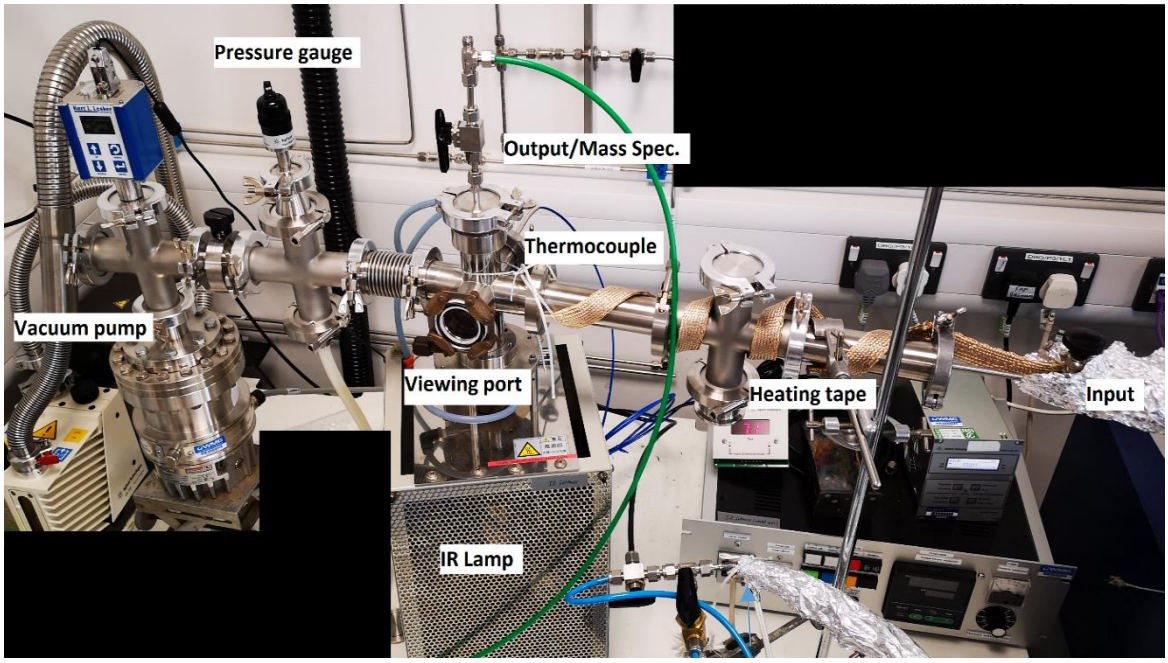

Figure 4.2 Infrared Furnace picture for high temperature oxidation in annealing atmospheres

The inside of the furnace has a total volume of roughly 2.5 L (1.28 L ahead of the crucible with respect to the gas flow direction), with the gas input on the far right, and the exit being directly above the crucible. The argon gas used has a purity of N5 and is sent (tubing 4mm diameter, and Flow Rate: 0.86 L/min Ar (converted from an N_2 gas flow meter of 1 L/min) through a round-bottomed water flask (hereon referred to as a humidifier) at temperatures: 0^{o}C and 20^{o}C, which is then sent to the chamber.

The metal tubing (between the humidifier and chamber), and the initial portion of the chamber are wrapped with thermal heating tape, set to a temperature of 60^{o}C with insulation high temperature glass wool and aluminium foil. This chamber-heating and insulation is to reduce the chance of water vapour condensing inside the chamber and affecting the results from an inaccurate reading of Ar - H_2O content from the Mass Spectrometer (Mass Spec.), and thereby the available oxygen to the steel surface.

The exit of the furnace is a tube, the same specifications of that which leads to the Humidifier, attached to the Mass Spec. that sucks in a small portion of the gas of volume 16 mL/min from the exit tubing which is forced as an exit by a pressure gradient from the chamber. The Mass Spec. is set to identify compounds and not radical species; therefore, it is set to measure argon (Ar), water vapour (H_2O), hydrogen (H_2), oxygen (O_2), carbon Dioxide (CO_2), and nitrogen (N_2). Hydrogen is included to measure the amount of oxygen that is penetrating the steel surface - from the dissociation of H_2O; carbon dioxide and nitrogen are included to measure any decarburisation, and as a set-point for where laboratory air is involved, respectively.

The Mass Spec. quadrupole is at a very low vacuum and in order to prevent damage the furnace chamber cannot be at vacuum when linked to the Mass Spec., so the stages of the experiment where the furnace chamber is in vacuum (and therefore no out-flow of the chamber gas) the Mass Spec. will take a sample from the laboratory atmosphere. This has the negative effect of making the transition readings unreliable for a small amount of time (10-30 seconds) as there is still a small portion of the

atmosphere from the chamber inside the exit tubing which will be mixed with the laboratory atmosphere. To combat this and ensure as close as possible accuracy, at 30 seconds to go until the furnace is at temperature, the chamber is filled with argon-only gas at a higher atmospheric pressure than standard laboratory atmosphere. This slight over-pressure forces out the contaminants in the exit tubing through a pressure gradient ensuring there is no backflow of laboratory atmosphere into the chamber. In the results section, these transition periods might be slightly altered, to the value proceeding the transition, as the anomalies can be great. Unaltered results are available on request where any modified results will be highlighted.

The oxidised samples' surfaces are imaged using a standard optical microscope. The samples are then mounted with the cross-section being the focus. The width of the sample (area originally $1cm^2$) is ground down between 0.3 and 0.5cm to observe the centre of the sample, eliminating edge effects - polished with the same preparation as before, and stored in the vacuum storage box. The samples are imaged using a scanning electron microscope (SEM), more information on this is presented in Section 4.4.

- Experiments were conducted throughout the lifetime of this project leading to the change in furnaces used, the refinement of the investigated parameters, and furnaces alterations – the conclusions from those preliminary experiments are:
- The size of the sample is important, with samples of area $1cm^2$ occupying a size where there is sufficient distance to separate sample edge oxidation effects from the centre to characterise the correct phenomena more accurately
- The chamber gas input valve must be positioned far enough away from the sample, so the gas does not directly cool the sample
- Oxidation of the steel grade Fe-10Al is of lower priority than the others, due to the high aluminium content and fully ferritic phase composition, external oxidation is mostly guaranteed at any surface oxygen partial pressure – which

can be seen below (and in works by Bott [106]) for a sample oxidised in ambient air at 900°C for 10mins, where internal and external oxidation is minimal due to the establishment of a dense nanometre-scale external oxidation layer.

-

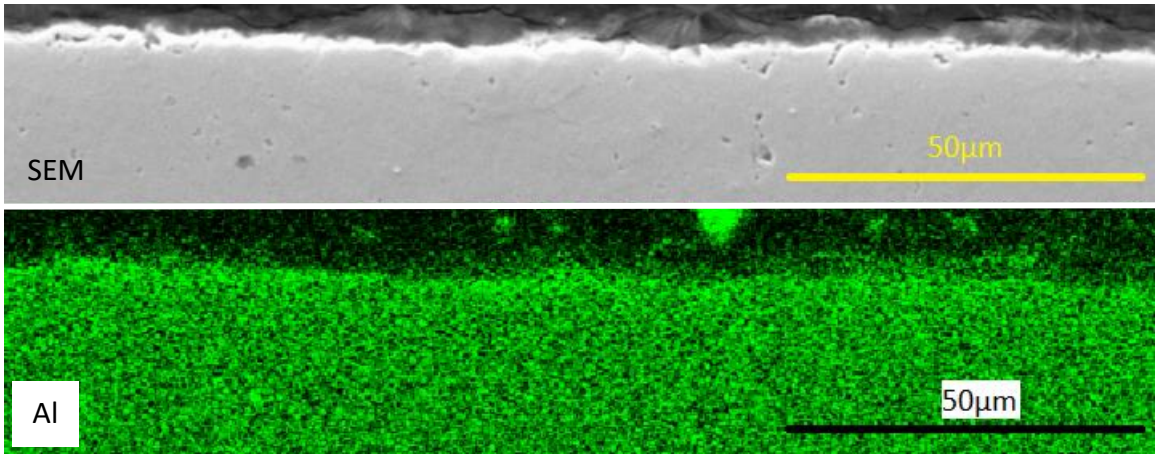

Figure 4.3 Fe-10Al steel grade, oxidised in ambient air for 10mins with isothermal oxidation stage of 900°C. Top: SEM image Bottom: aluminium composition

- Due to the significant aluminium contents of the steel grades, absolute control of sample exposure between initial preparation and final imaging is necessary. Otherwise, a surface passivation layer can develop between initial preparation and oxidation experiments; and after oxidation experiments samples can continually oxidise, eliminating the validity of the subsequent observations.
- A chamber vacuum stage at the isothermal temperature does not significantly affect the results. Below with Figure 4.4, shows the sample Fe-3Al-5Mn oxidised at 900°C with humidifier at 20°C, where #2 is the standard temperature profile of Figure 4.5 with 5mins of Ar - H_2O, and #1 is extended with a vacuum stage of 5mins for a final 10mins at isothermal temperature.

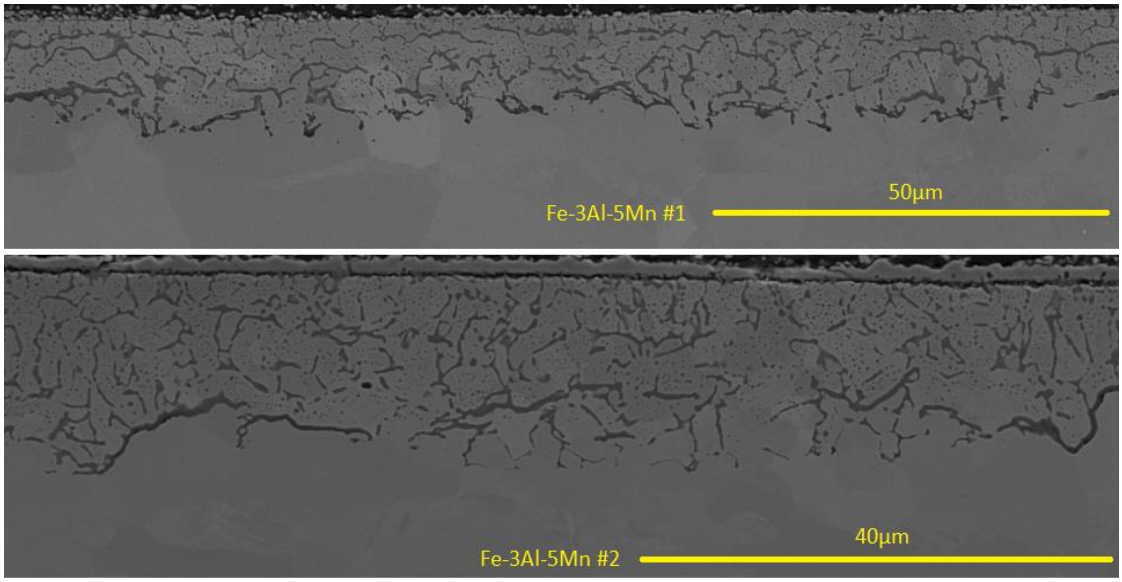

Figure 4.4 Fe-3Al-5Mn steel grade oxidised at isothermal temperature 900°C with Ar - H_2O humidifier at 20°C. Top: 10mins isothermal oxidation: 5mins Ar - H_2O + 5mins vacuum. Bottom: 5mins isothermal oxidation: 5mins Ar – H_2O

There was only an apparent small effect of aluminium reducing the oxides at the IOZ bottom; with the decision that there is not a significant effect of this vacuum stage on the internal oxidation of Fe-Al-Mn dual phase steels under these conditions.

Temperature ramping in vacuum is necessary as several minutes of temperature ramping in an argon atmosphere is somewhat significant in regard to the small amount of porous nanometre-scale surface oxidation due to impurities in the gas.

4.3 Ideal Temperature Profile

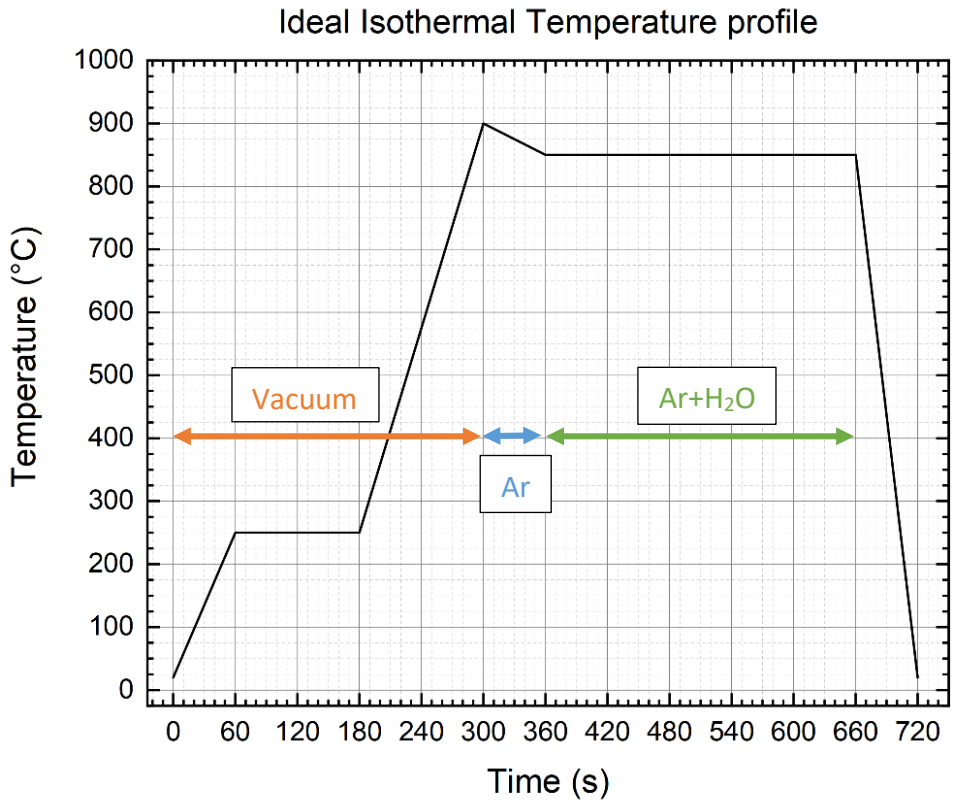

Figure 4.5 Ideal project experimental 5min isothermal oxidation annealing temperature profile for Infrared Furnace, adapted from industrial 5min annealing temperature profile

As this project is based around annealing, the isothermal oxidation temperature of 850°C was used, with oxidation times of 20-30sec, 2:30mins, 5mins, and 10mins. Initially, the samples are taken from the vacuum sample box and placed into the chamber at which point the chamber is brought to vacuum. Immediately after a sample has finished quenching at the end of the experiment, the sample is switched with the next from the vacuum sample box and the reaction chamber is brought to vacuum again.

This ideal isothermal temperature profile was chosen to keep the sample unoxidised for as long as possible to ensure accurate isothermal oxidation conditions, to be a valid comparison to the model (also isothermal). Due to the chamber being in

vacuum initially then preliminarily filled with pure argon when nearing the isothermal temperature, there is a large decrease in the sample temperature as the chamber is filled, this is compensated by the heating to 900°C and allowing the incoming pure argon to reduce to sample temperature near to 850°C and awaiting stabilisation which takes between 20 - 60 seconds. There were preliminary tests conducted on the introduction of the atmosphere to the chamber which found that the Vacuum to argon transition resulted in 50 -70°C decrease, whereas the argon to argon + water vapour transition did not significantly affect the sample temperature. Therefore, compensation measures were not included for the water vapour introduction to the reaction chamber.

4.4 Scanning Electron Microscope Usage

The scanning electron microscope (SEM) Zeiss Sigma FE-SEM [146] was used to view the samples produced in the following experiments, and compatible software AZtec 4.2 by Oxford Instruments [147] was used to capture images and data from the SEM, including elemental mappings through Energy Dispersive Spectroscopy on the SEM (EDS-SEM). An accelerating voltage of 10.00 kV was used with the SE input signal at a working distance of roughly 10mm with zero tilt, the standard electron images were acquired using 10 - 20µs dwell times, whilst the EDS-SEM images were completed with a 600µs dwell time. The point analysis spectra were acquired using the X-MaxN 80 detector.

The Aztec software provides accurate measurement tools within the software and these were used to analyse the cross-section grain sizes of the samples, the width and volume fraction of internal oxides, and the thickness of the external oxides (scale). The SEM was used in place of other measurement techniques due to the precise imaging performance provided and the seamless comparison with data provided by the EDS-SEM, along with time constraints surrounding the availability of resources and the prioritisation of available time.

5. Experimental Data

The ideal experimental iterations for this project consisted of a range of humidifier temperatures, isothermal oxidation times, and their repeats.

- **Ideal Experimental iterations:**
    - Humidifier 0°C, 10°C, and 20°C
    - 20-30sec, 2:30mins, 5:00mins, 10:00mins
    - All 4 steel grades
    - 2 additional runs of each condition iteration (3 each total)

Priority was given to the experimental conditions that would allow for the sufficient collection of data to characterise the internal oxidation of Fe-Al-Mn dual phase steels. As such the dual phase steels Fe-3Al-5Mn and Fe-5Al-5Mn; humidifier temperatures of 0°C and 20°C; and isothermal times of 20-30sec, 2:30mins, and 5mins - were given priority. The annealing phase times were chosen because the oxidation behaviour differences between 5mins and 10mins isothermal oxidation times were not considered to be significant compared to the differences between the other oxidations times – also the sanctity of the IR furnace was damaged by the longer isothermal oxidation times; the humidifier temperature extremes better represent the difference in oxidation behaviour as the difference of water vapour pressure of dew points 0 - 10°C, and 10 - 20°C is not large as can be seen below, showing the relation between Water Vapour Content (%) and Temperature (°C):

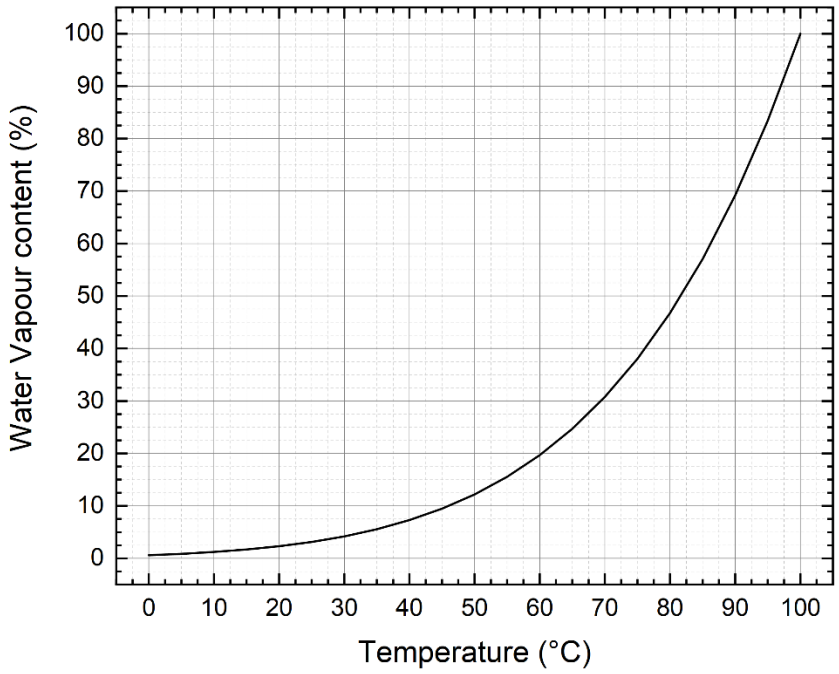

Figure 5.1 Diagram showing the relationship between Water Vapour Content (%) and Temperature (°C) [145]

Due to time constrains, not all the ideal experiment iterations could be completed; however, the majority of the prioritised iterations were.

- **Actual Experiment iterations:**
    - Both dual phase steels oxidised at humidifier temperatures 0°C and 20°C with 20-30sec, 2:30mins, and 5:00mins oxidation times
    - Austenitic sample oxidised at humidifier temperature 20°C with 20-30sec, 2:30mins, and 5:00mins oxidation times
    - 1 repeat of the experiments of the dual phase steels at humidifier temperature 0°C

Some additional points should be considered:

- Argon was sent through the humidifier and out the humidifier bypass exit (not through the furnace chamber) at all times when not in use in the chamber, this was to keep the small atmosphere within the humidifier saturated with water vapour, ready to be sent to the furnace chamber making the atmosphere Mass Spec. reading more accurate
- The initial isothermal temperature was intended to be 900°C, but due to limitations of the IR furnace and the effect of the introduction of near room temperature argon to a very hot furnace naturally caused some surface cooling on the sample. Therefore, the isothermal temperature was altered to be 850°C, with the initial temperature reaching between 880 - 910°C at vacuum, when the argon is introduced. After the chamber stabilised around 840 - 860°C, Ar - H_2O was introduced and the annealing oxidation phase began
- One limitation of the IR furnace was that an error occurred with the current controller, leading to a deviation between the temperature displayed and the actual. This was verified as an issue using two separate data loggers + thermocouples, however, time for fixing the controller was not available. This led to the recording of the temperature by hand to couple the readings with the displayed Mass. Spec. timings.
- During the experiments, the atmospheric pressure gauge reading at the oxidation phase was consistently between 40 and 70 Torr.
- The thermocouple was set in a small divot - drilled into the surface at a corner
- The humidifier temperature was used as the metric not Dew Point, as the introduction of Ar - H_2O led to the atmosphere's conversion from pure N5 Argon to the equilibrium water vapour in argon content over time.
- As the usage of the equipment was all manual, only some things could be prioritised for recording at certain points, as such the maximum vacuum temperature (~900°C) was not recorded.
- The Mass Spec. timings are not consistent nor determine the points of experimentation, as such a timer was used, linked to a certain time-point on the Mass Spec., this means that the start times given in the raw data are

accurate, but the end times are not always related to a specific time given by the mass spec as the experiment was ended according to the timer.

- The thermocouple reading fluctuated due to the gas flow over the surface as well as other reasons - because of this, at the specific time point on the record from the Mass Spec. the instantaneous value on the data logger was recorded
- Abbreviations are used for humidifier temperatures low and high humidity 0°C (H-0C) and 20°C (H-20C)

Considerations on Mass Spectrometer usage:

Immediately after the end of the isothermal oxidation time, the vacuum pump was enabled to drastically reduce the oxidising potential of the atmosphere before argon cooling. The Mass Spec. takes a sample of the atmosphere, to then analyse in its chamber which has a small delay of 10-30 seconds, which shows an offset with other recorded data; also, as proper use of the Mass Spec. prohibits sampling from a vacuum, when the chamber was at vacuum the Mass Spec. would sample from the laboratory atmosphere through a bypass tubing. As this is how the Mass Spec. functions, there is also not an immediate accurate reading, but it is subject to the composition of the atmosphere in the chamber, leading to large anomalous results when the various atmosphere changes occur, these have been mediated in the results below by copying the data from 1 - 3 cells below the anomaly so that all 2 - 4 cells have the same values. Some results for the 20-30seconds iterations were not adjusted due to the very small window of data. The graphs below show these adjusted results, the unedited versions of the data can be provided on request.

5.1 Recorded Temperature Profiles

The temperature profiles below are the data recorded manually from the experiments; they are normalised around the origin which signified the start of the annealing oxidation time. The negative values of time are therefore the time between the IR furnace activation for temperature increase where the chamber was at vacuum and the introduction of the water vapour at time = 0. There are different heating rates due to the manual control nature of the experiment, as well as the control of the atmosphere and temperature stabilisation in N5 Argon before the introduction of the Ar - H_2O.

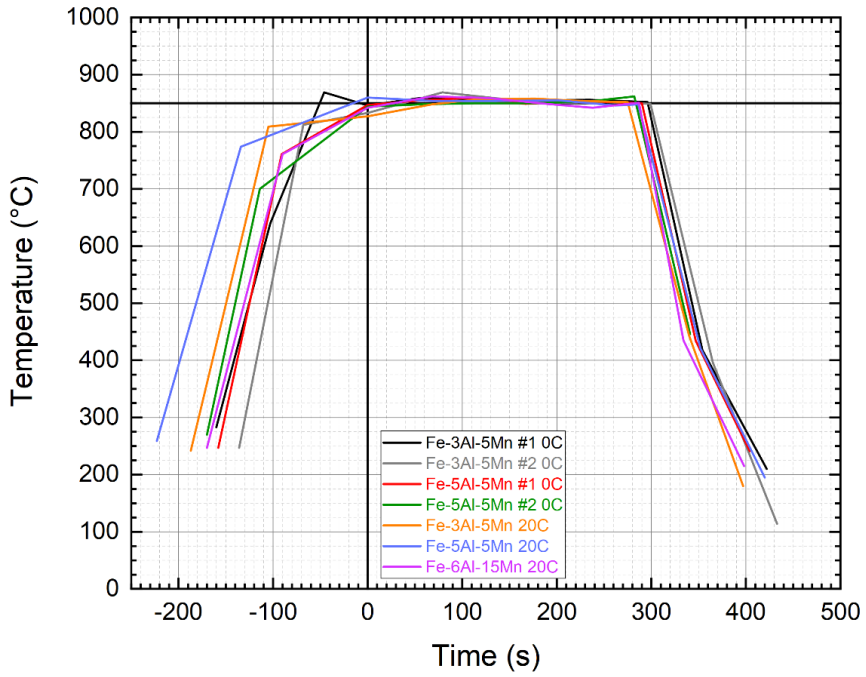

Figure 5.2 5mins oxidation time recorded Temperature Profile for humidifier temperature 0°C (run #1 and #2) and 20°C, normalised to oxidation start at time = 0

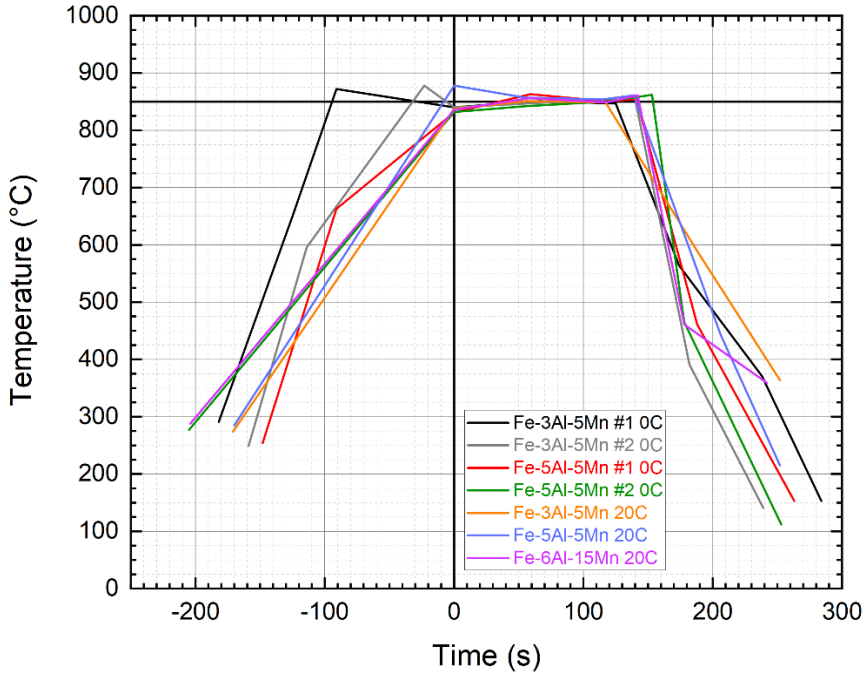

Figure 5.3 2:30mins oxidation time recorded Temperature Profile for humidifier temperature 0°C (#1 and #2) and 20°C, normalised to oxidation start at time = 0

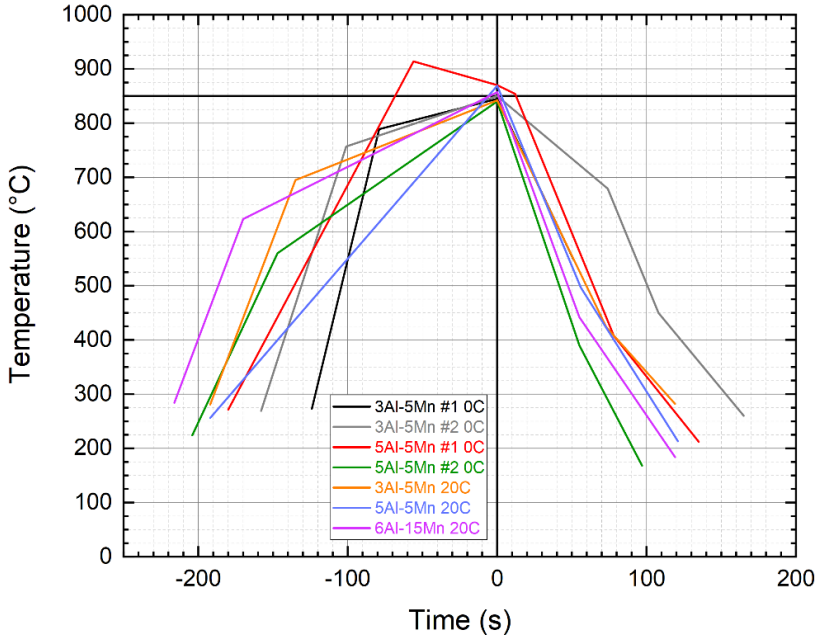

Figure 5.4 20-30sec oxidation time recorded Temperature Profile for humidifier temperature 0°C (#1 and #2) and 20°C, normalised to oxidation start at time = 0

The temperature profiles display two main areas of note: the initial temperature ramp, and the isothermal oxidation temperature zone.

The IR furnace was partially selected due to the fast heating rate to simulate industrial conditions. As the operation of the IR bulb emits a certain infrared light density (number of photons per cm^2) with a fixed crucible size, variations in the sample dimensions can amplify the heat rate differences with larger and thicker samples requiring longer to conduct the heat. However, once the desired temperature has been reached, there is a good consistency at 850°C shown by the 5mins and 2:30mins oxidation time temperature profiles. The very small window of oxidation time of the 20-30sec temperature profile does not present a good metric of comparison between samples.

5.2 Experimental Results and Data

Experimental Results and Data Contents

- 5.2.1 Microstructure analysis and comparison

- 5.2.2 Experimental Results with Mass Spectrometer data

Fe-3Al-5Mn

- 5:00mins
    - Humidifier Temperatures: 0°C (Run #1 + #2) and 20°C
- 2:30mins
    - Humidifier Temperatures: 0°C (Run #1 + #2) and 20°C
- 20-30sec
    - Humidifier Temperatures: 0°C (Run #1 + #2) and 20°C

Fe-5Al-5Mn

- 5:00mins
    - Humidifier Temperatures: 0°C (Run #1 + #2) and 20°C
- 2:30mins
    - Humidifier Temperatures: 0°C (Run #1 + #2) and 20°C
- 20-30sec
    - Humidifier Temperatures: 0°C (Run #1 + #2) and 20°C

Fe-6Al-15Mn

- 5:00mins
    - Humidifier Temperature: 20°C
- 2:30mins
    - Humidifier Temperature: 20°C
- 20-30sec
    - Humidifier Temperature: 20°C

5.2.1 Microstructure Comparison

5.2.1.1 Base Steel

Images were delivered from the Tata Steel industrial partners collaborating with this project and are presented below for comparison with the results of this study. These samples are considered to represent a comparable microstructure of the dual phase steels at the start of the isothermal annealing stage due to the relatively similar heat treatment and interrupted annealing stage constituting minimal isothermal annealing for the dual phase steels, and hereby referred to as the Base Steel.

The dual phase Fe-3Al-5Mn and Fe-5Al-5Mn steels, and the austenitic Fe-6Al-15Mn steel were quickly heated at a rate of 15°C/s then held at the isothermal temperature 850°C for 30 – 50 seconds then directly cooled to room temperature at a rate of 30°C/s. The dual phase samples were etched with Klemm etching agent for 90 seconds, and the austenitic Fe-6Al-15Mn sample was etched with the Viella etching agent for 40 seconds. The cold worked nature of the steel and short annealing treatment imparts a horizontal axis for the microstructure typically referred to as banding structure, this banding structure does not always have clear boundaries and so shall be considered separate from non-band grains during classification. Due to this property and the non-spherical shape of a large portion of grains, the definitions of the orientation of the grain measurements are listed as D = Longest diameter, and when relevant H = Height (vertical height of band), the phase in question is also specified with γ = retained austenite and bainite/martensite and α = ferrite. Where arrows would be impractical to signify very small sizes boxes have been used with the specified dimension. Due to the dual phase nature of the steels categorising the average grain size has been done with individual measurements and not the line length divided by intersections method. The images are in agreement with what can be expected given the data in Table 2.1.

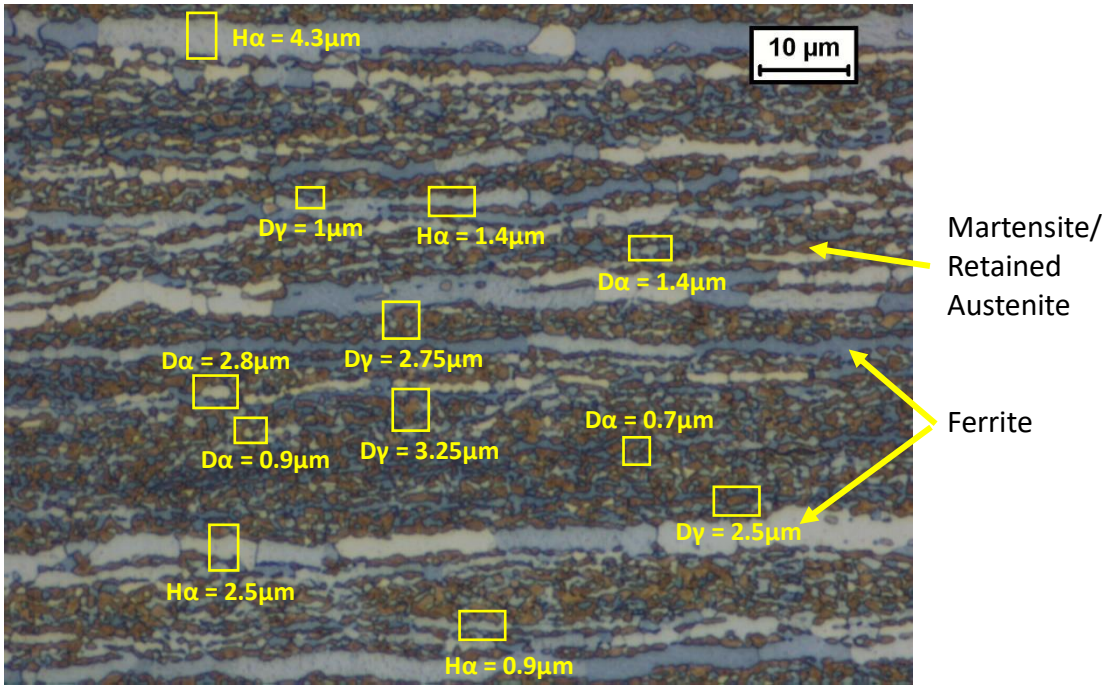

Figure 5.5 Etched Fe-3Al-5Mn steel grade after short annealing heat treatment, microstructure analysis showing mostly ferrite bands with intermediate ferrite and martensite/retained austenite bands between. Image at quarter depth - 0.25mm from surface

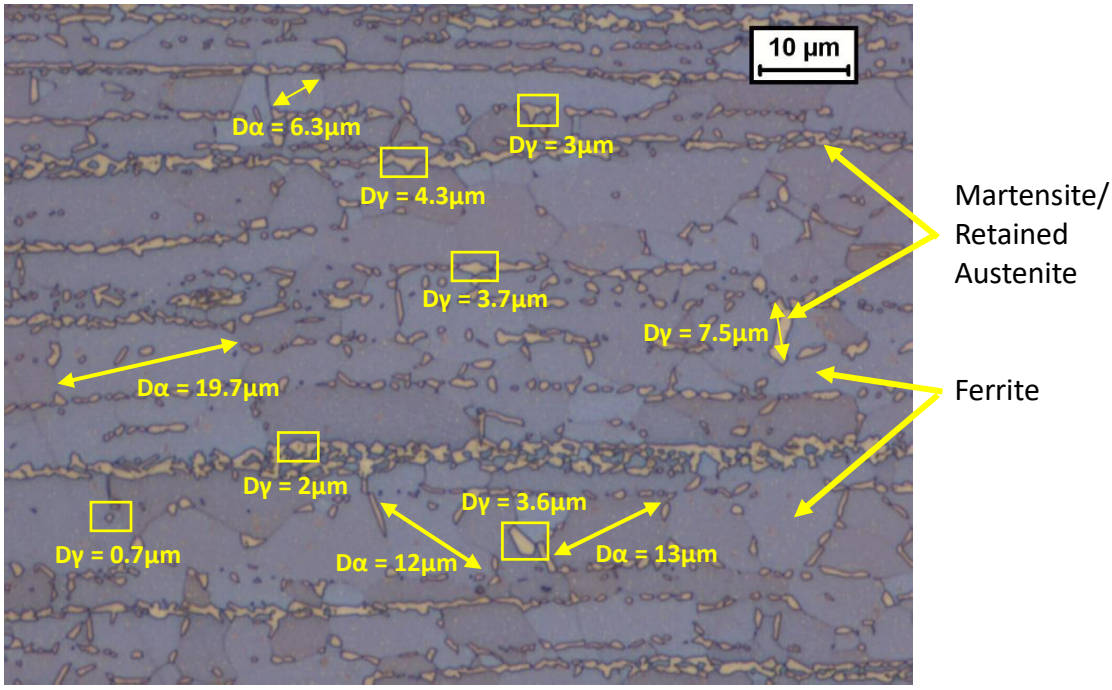

Figure 5.6 Etched Fe-5Al-5Mn steel grade after short annealing heat treatment, microstructure analysis showing larger ferrite grains with intermediate martensite/retained austenite at the ferrite grain boundaries with some retained austenite/martensite banding. Image at quarter depth - 0.25mm from surface

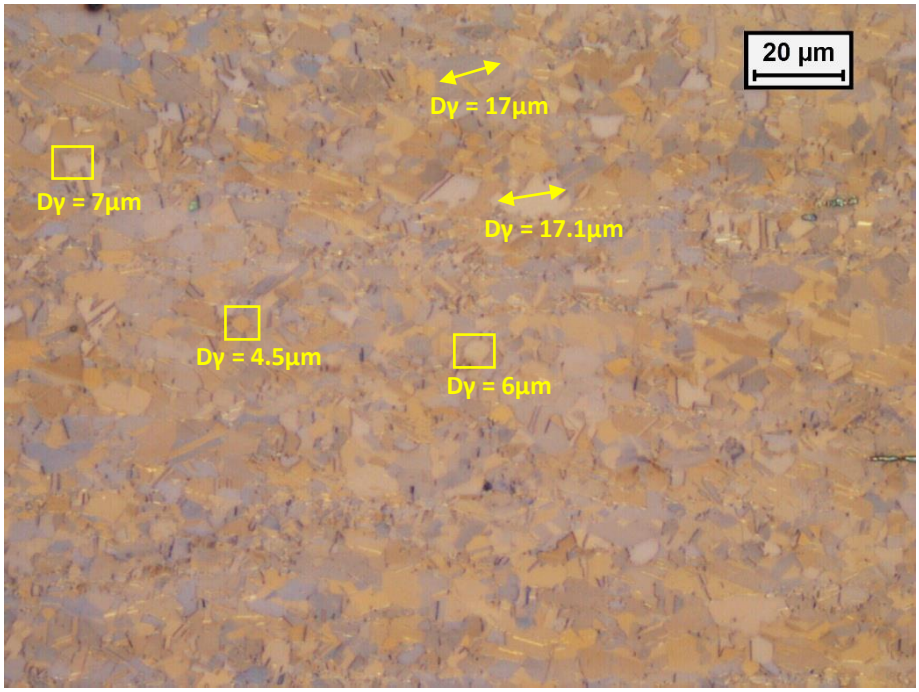

Figure 5.7 Etched Fe-6Al-15Mn steel grade after short annealing heat treatment, microstructure analysis showing austenitic and martensitic microstructure. Image at sample centre - 0.5mm from surface. Image contrast modified for clarity

The banding nature provides complex information about the microstructure and the separation of the bands and non-band grains is a somewhat effective method in categorising this because the ferrite bands of Fe-3Al-5Mn are long and extend great distances of which the endpoints are not clear and visible. Between the ferrite bands of the same sample are ferrite-austenite dual phase microstructure of small grain sizes. The Fe-5Al-5Mn sample produced a microstructure that is mostly ferritic with some minor austenitic banding and with additional small deposits of austenite along the ferrite grain boundaries. The Fe-6Al-15Mn sample shows a fully austenitic/martensitic microstructure with no banding present. The microstructure seen in Figures 5.5 and 5.6 shows mostly small/thin grains in both dual phase steels with larger ferritic areas seen in Fe-5Al-5Mn, associated with the higher aluminium content as shown in Table 2.1. There are two different scales of heterogeneous zones for consideration in Fe-3Al-5Mn; main components of the system are the banding structure that consists of long horizontal ferritic bands and an intermediate zone of very small ferrite and austenite/martensite/bainite grains. This region of very small grains provides a large grain boundary to grain ratio, whereas the ferritic band is the

opposite. This provides a very complex oxidation system as either of the horizontally aligned regions could be at the surface depending on the amount of surface grinding during the preparation phase. As the preparation phase of the experiments requires resetting the samples to an oxide-free surface and keeping them unexposed to oxygen in the air, this also mostly prevents pre-analysis of the samples due to the transfer between vacuum storage and analysis equipment oxidising the surface and any surface resetting will modify the microstructure which was the reason for the analysis in the first place or modify the surface composition though corrosion or other means.

The Fe-5Al-5Mn steel's microstructure was less complex than the steel named Fe-3Al-5Mn, the mostly ferritic phase composition provides a clearer avenue for oxidation. However, there is a significant amount of small austenitic grains that appear in minor horizontal bands and along the grain boundaries of the larger ferritic grains. This steel grade also has the same issue of microstructure differences related to depth that could affect the oxidation behaviour, although to a lesser degree.

The fully austenitic Fe-6Al-15Mn steel has a relatively consistent microstructure which can provide a stable comparison for the dual phase steels.

The table below shows the data taken from the above sample images provided by the industrial partners of this project.

Table 5.1 Grain size analysis of Tata Steel images of the steels used in this project

Diameter [µm]					
Tata Steel		Fe-3Al-5Mn (band, H)	Fe-3Al-5Mn (grain, D)	Fe-5Al-5Mn	Fe-6Al-15Mn
Ferrite	Range	H = 0.9 - 4.3	D = 0.7 - 2.8	D = 6.3 - 19.7	-
	Mean	H = 2.3	D = 1.45	D = 13.1	-
Austenite	Range	-	D = 1.0 - 3.25	D = 0.7 - 3.6	D = 4.5 - 17.1
	Mean	-	D = 2.55	D = 3.6	D = 10.3

5.2.1.2 Post-oxidation Samples

The microstructure of the samples that underwent oxidation during this experiment produced a microstructure profile that was significantly different from those shown above due to the longer annealing durations allowing more time for recrystallisation. Grain size analysis and partial phase characterisation has occurred on the SEM images gathered during sample analysis, presenting microstructure of ferritic, bainite/martensitic, and retained austenite. The SE and EDX - SEM analysis methods of this project allowed the categorisation of bainite/martensitic phases due to the characteristic appearance from ferrite and austenite. The prioritisation of a clean oxide-free sample surface and the available resources prevent an effective interrogation of an individual location's phase composition coupled to the pre- and post-oxidation microstructure. There are methods available such as gold sputtering, but the oxidation during the sample transfer that these extra steps would impart was deemed unacceptable, and the etching of the sample post-oxidation would greatly disrupt the oxides. The complex effects of the annealing on the dual phase microstructure during oxygen exposure provides a number of parameters that cannot be isolated easily with the current prioritisations. Of the non-bainitic/martensitic phases, ferrite will dominate if austenite can be retained, and the bainite/martensite will compromise the majority of the non-ferritic phases due to the relatively low austenite-stabilising elements' ability to retain the austenite when cooling down from the isothermal 850°C. This stability of the austenitic phase during cooling can be shown in Continuous Cooling Transformation (CCT) diagrams, which predict the phases present during sample cooling related to the temperature gradient. Shown below are the CCT diagrams obtained using JMatPro [59] for both dual phase steels used in this project:

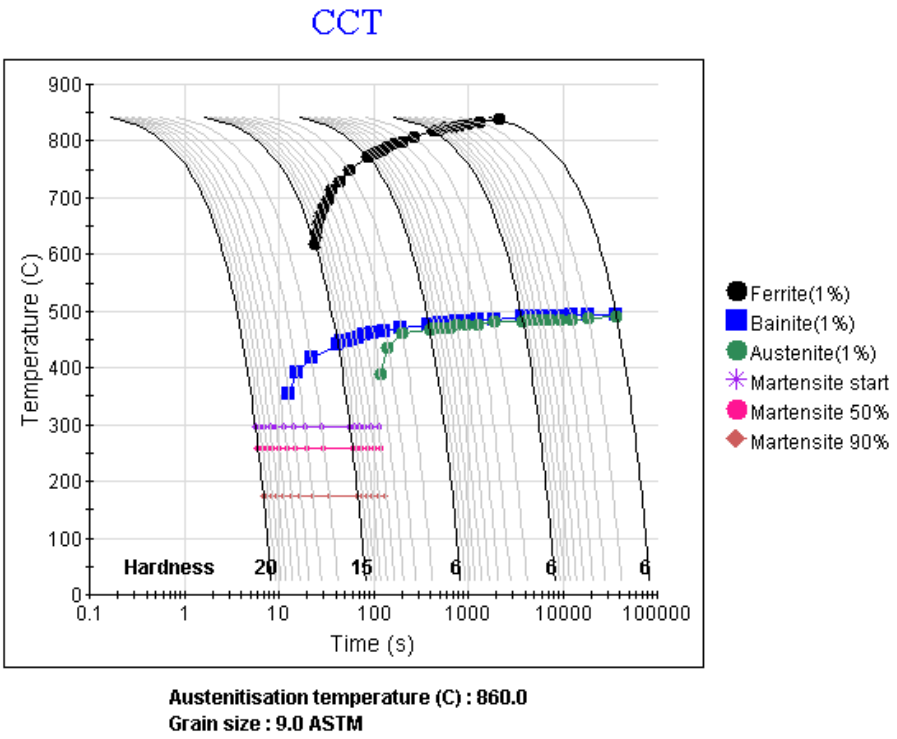

Figure 5.8 CCT diagram of Fe-3Al5Mn dual phase steel produced using JMatPro, representing the austenitic phase transformation during cooling, with ferrite not included here

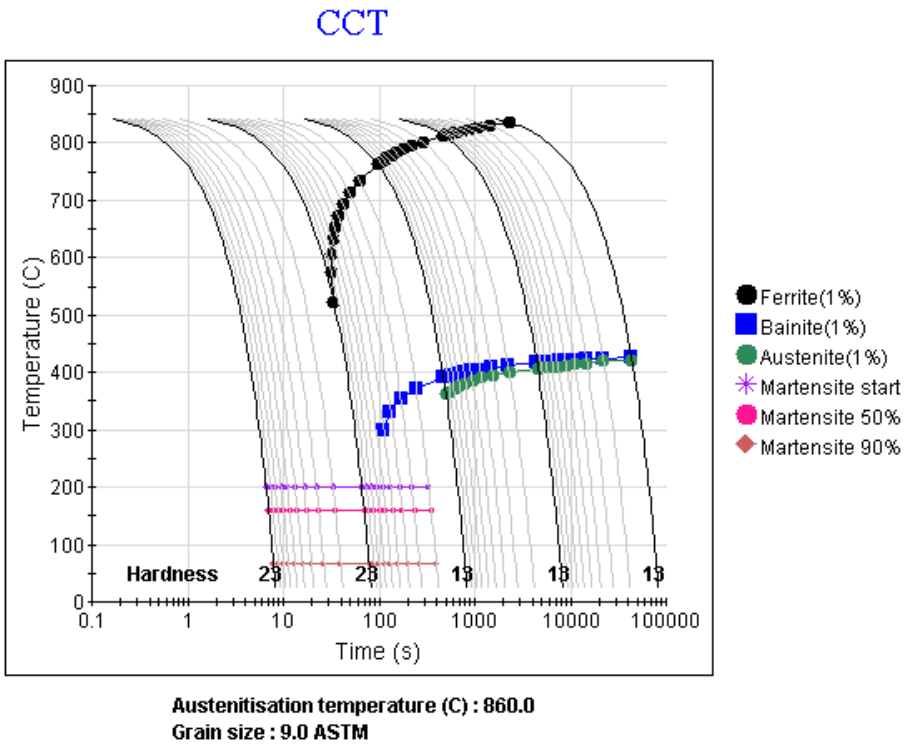

Figure 5.9 CCT diagram of Fe-5Al5Mn dual phase steel produced using JMatPro, representing the austenitic phase transformation during cooling, with ferrite not included here

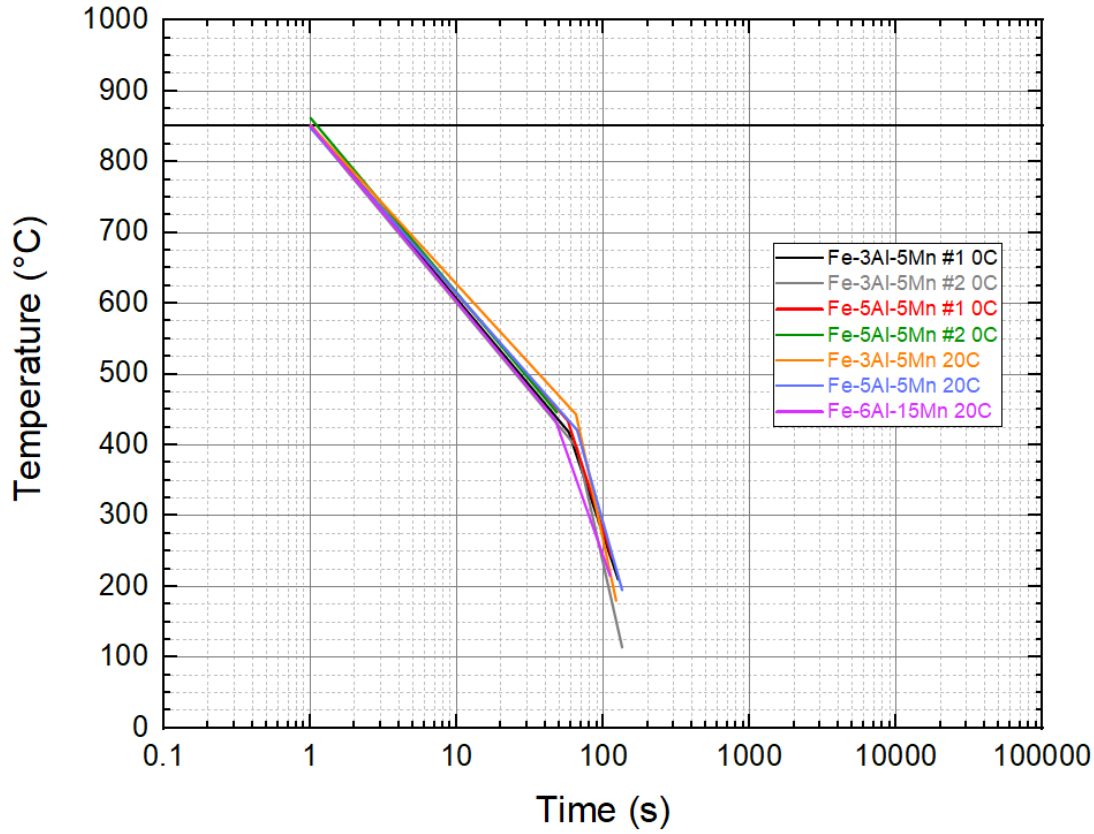

Figure 5.10 5mins, H-0C and H-20C, Fe-3Al-5Mn, Fe-5Al-5Mn, and Fe-6Al-15Mn steels cooling rates for comparison with CCT diagrams

Figures 5.8 and 5.9 refer to the phase fraction of austenite at the 850°C isothermal temperature, where the phase fraction of ferrite is retained to room temperature and is not a part of these diagrams. The samples of the experiments had temperature profiles that were conducted with an argon quenching after the isothermal stage, with an average temperature reached after 2 minutes of 203°C, subsequent air cooling with the reaction chamber exposed to the laboratory atmosphere occurred to a safe temperature to handle the sample and subsequent transfer to the vacuum storage box. For more information on the temperature profile, refer to Section 5.1. The air cooling stage provided a much larger cooling affect due to the volume of air flow.

There is a major presence of bainite/martensite in the Fe-3Al-5Mn steel grade, with a significantly less proportion in the Fe-5Al-5Mn grade, the high proportion of manganese in the Fe-6Al-15Mn grade prevented the majority of austenite from transforming during cooling and retained the vast majority of the microstructure.

The microstructure statistical analysis of the post-oxidation samples used in this project is presented below with a table of condensed information of the range and mean grain sizes. Due to a lack of available time surrounding the events of this project further microstructure analysis was unable to be performed, therefore ferrite and austenite are coupled as under one parameter due to the lack of means to interrogate the difference, unlike the bainite/martensitic phase which is categorised separately due to the characteristic appearance.

Table 5.2 Data of the range and mean average diameter in microns of the microstructure of the steels annealed in this project

Diameter [µm]			Ferrite / Retained Austenite		Bainite / Martensite	
			Range	Mean	Range	Mean
3Al-5Mn	5mins	0°C	5.30 - 19.70	11.61	6.70 - 22.20	12.93
		20°C	4.60 - 36.20	16.53	9.50 - 20.60	11.75
	2:30mins	0°C	5.6 - 32	13.63	8.10 - 14.10	10.24
		20°C	2.80 - 26.60	10.68	2.90 - 6.10	5.03
	20-30sec	0°C	3.6 - 23.4	10.55	4.60 - 28.10	17.58
		20°C	2.20 - 10.70	5.74	5.70 - 14.60	10.15
5Al-5Mn	5mins	0°C	5.90 - 79.00	30.38	5.50 - 14.50	8.68
		20°C	40.60 - 159.00	77.96	5.80 - 14.50	10.15
	2:30mins	0°C	6.60 - 22.70	12.09	7.16 - 40.10	21.31
		20°C	7.70 - 42.90	18.26	7.50 - 33.00	13.90
	20-30sec	0°C	6.70 - 34.20	17.18	8.00 - 28.40	18.43
		20°C	19.00 37.20	25.40	5.00 - 28.30	18.95
6Al-15Mn	5mins	20°C	28.70 - 72.00	51.60	-	6.60
	2:30mins	20°C	14.40 - 42.80	29.06	22.30 - 24.80	23.55
	20-30sec	20°C	17.10 - 60	27.68	-	-

Fe-3Al-5Mn Dual Phase Microstructure

Humidifier 0°C Run #1

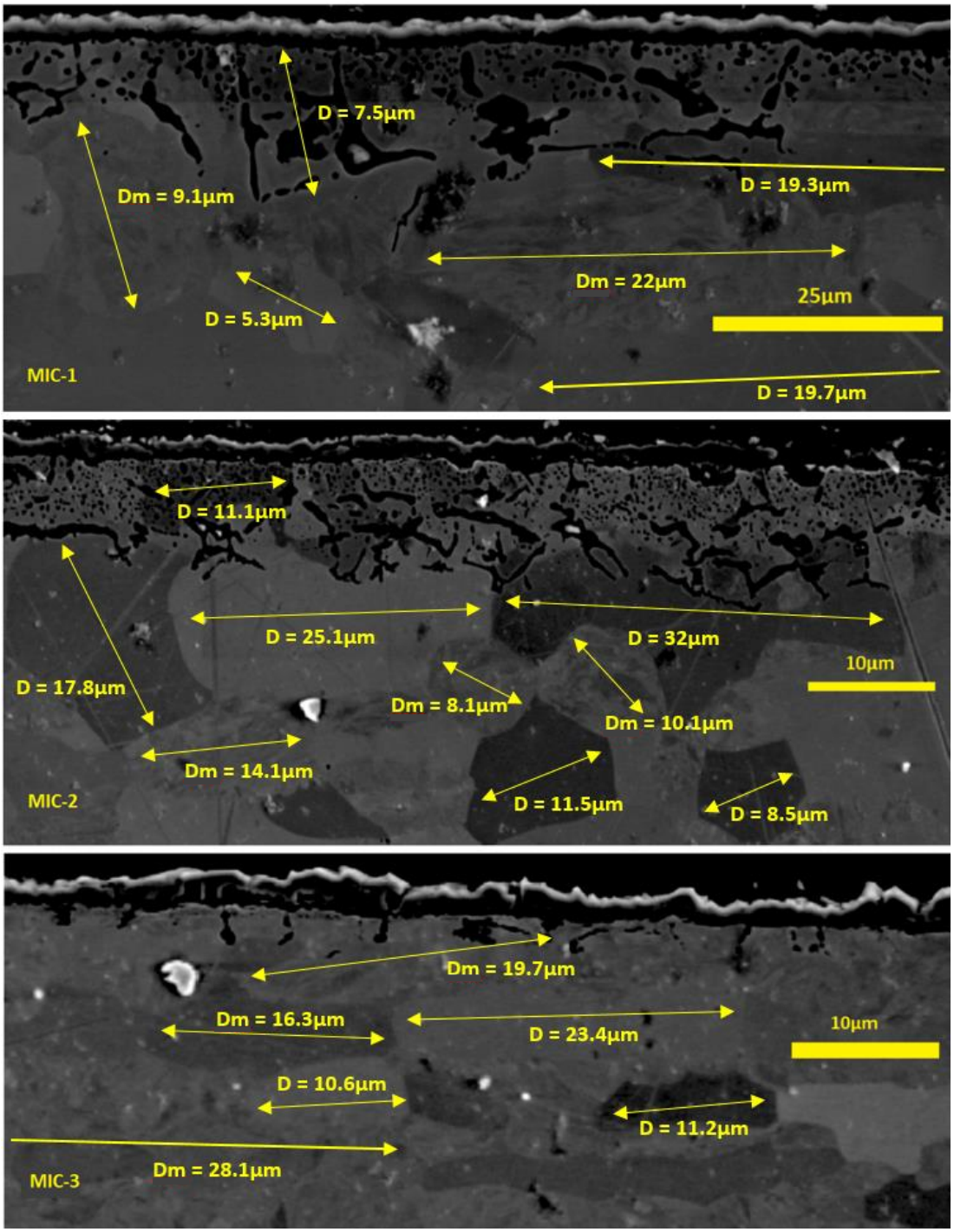

Figure 5.11 Fe-3Al-5Mn steel grade after H-0C Run #1 oxidation experimental annealing heat treatment, microstructure analysis showing grain growth occurred during annealing. Ferrite and bainite/martensite grains exist without apparent large banding structure, although ferrite grains remain mostly long and thin. MIC-1: 5mins, MIC-2: 2:30mins, MIC-3: 20-30sec.

Humidifier 0°C Run #2

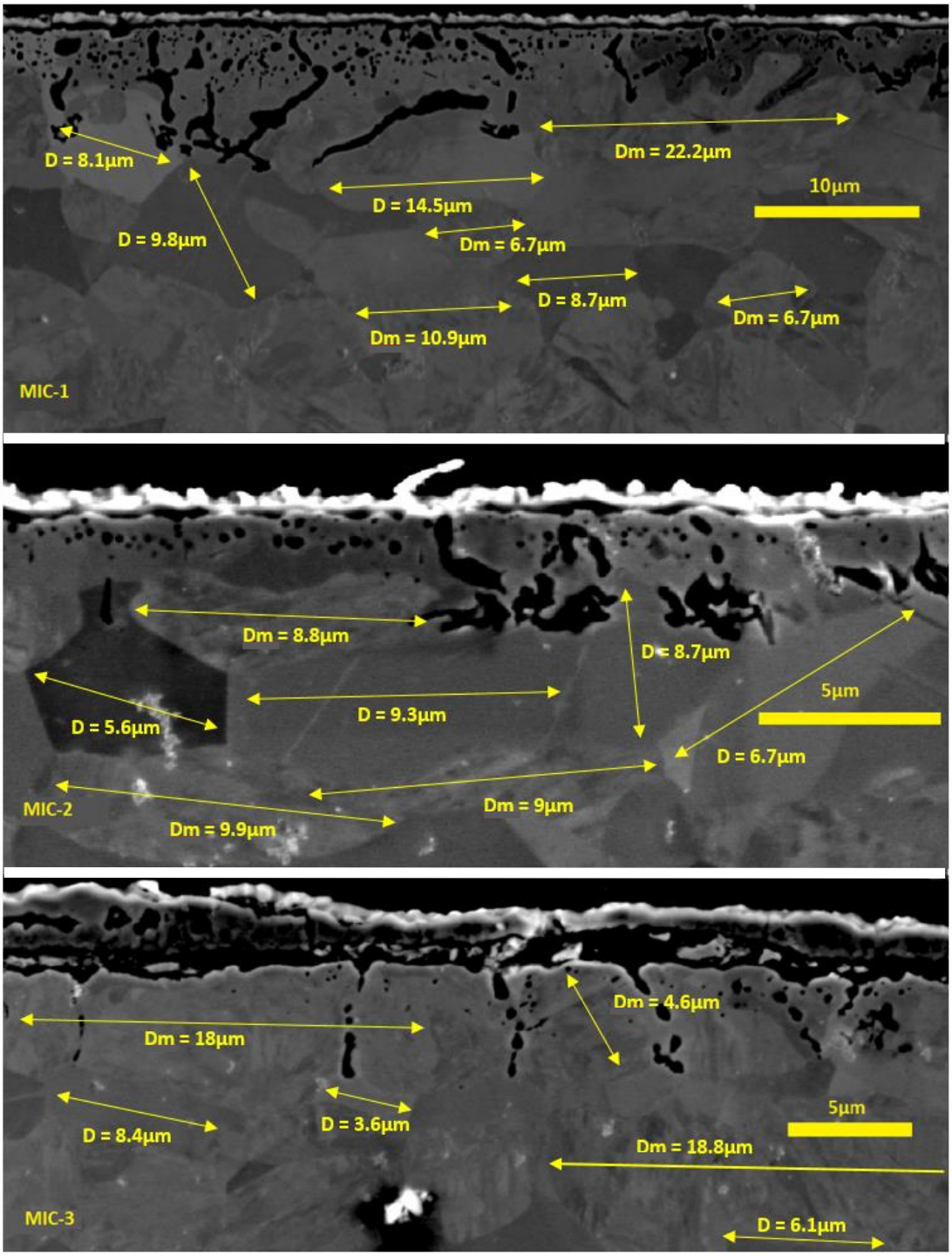

Figure 5.12 Fe-3Al-5Mn steel grade after H-0C Run #2 oxidation experimental annealing heat treatment, microstructure analysis showing grain growth occurred during annealing. Ferrite and bainite/martensite grains exist without apparent large banding structure, evidence of long and thin ferrite grains exists. MIC-1: 5mins, MIC-2: 2:30mins, MIC-3: 20-30sec.

Humidifier 20°C

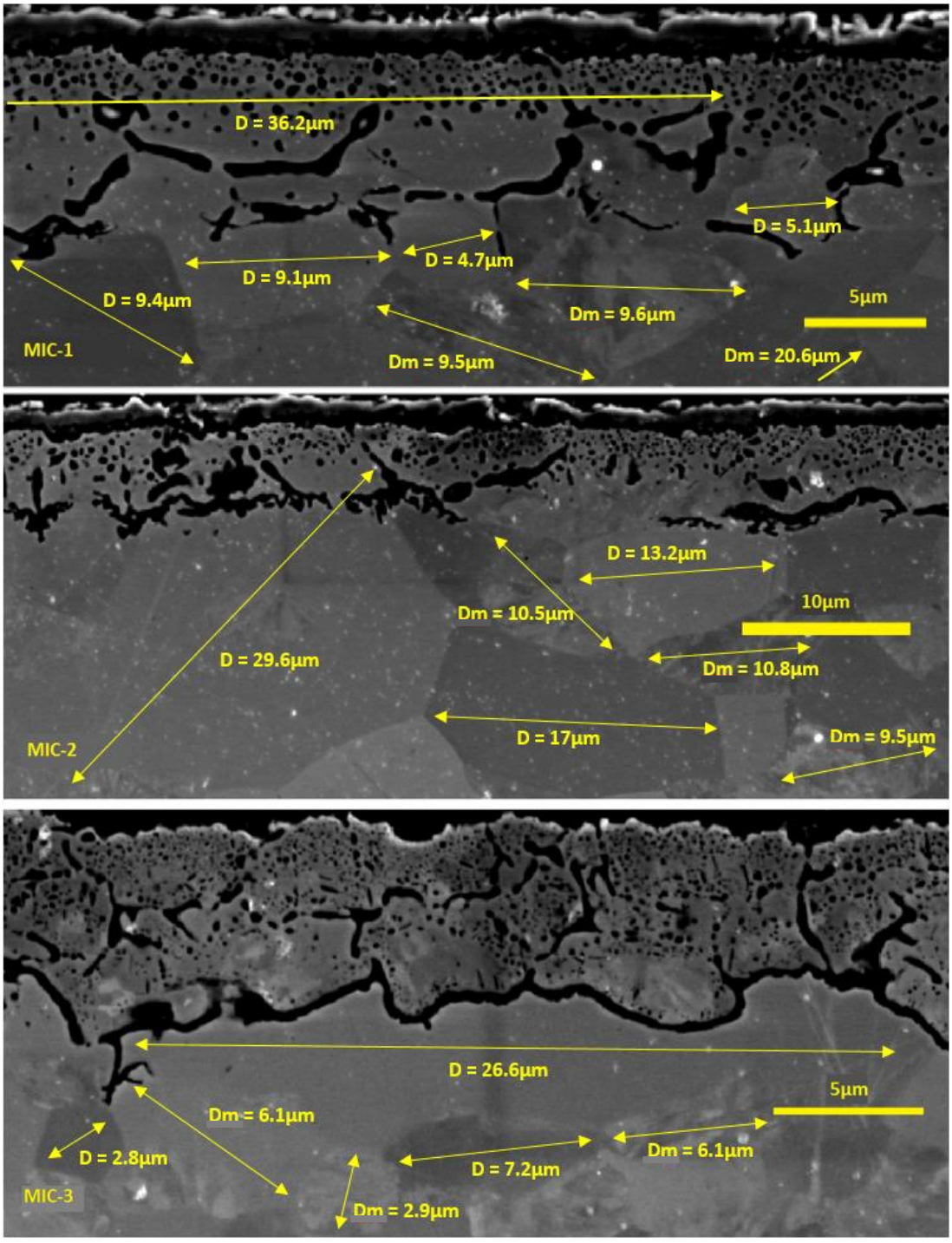

Figure 5.13 Fe-3Al-5Mn steel grade after H-20C oxidation experimental annealing heat treatment, microstructure analysis showing grain growth occurred during annealing. Ferrite and bainite/martensite grains exist without apparent large banding structure, evidence of long and thin ferrite grains exists. MIC-1: 5mins, MIC-2: 2:30mins Site 1, MIC-3: 2:30mins Site 2.

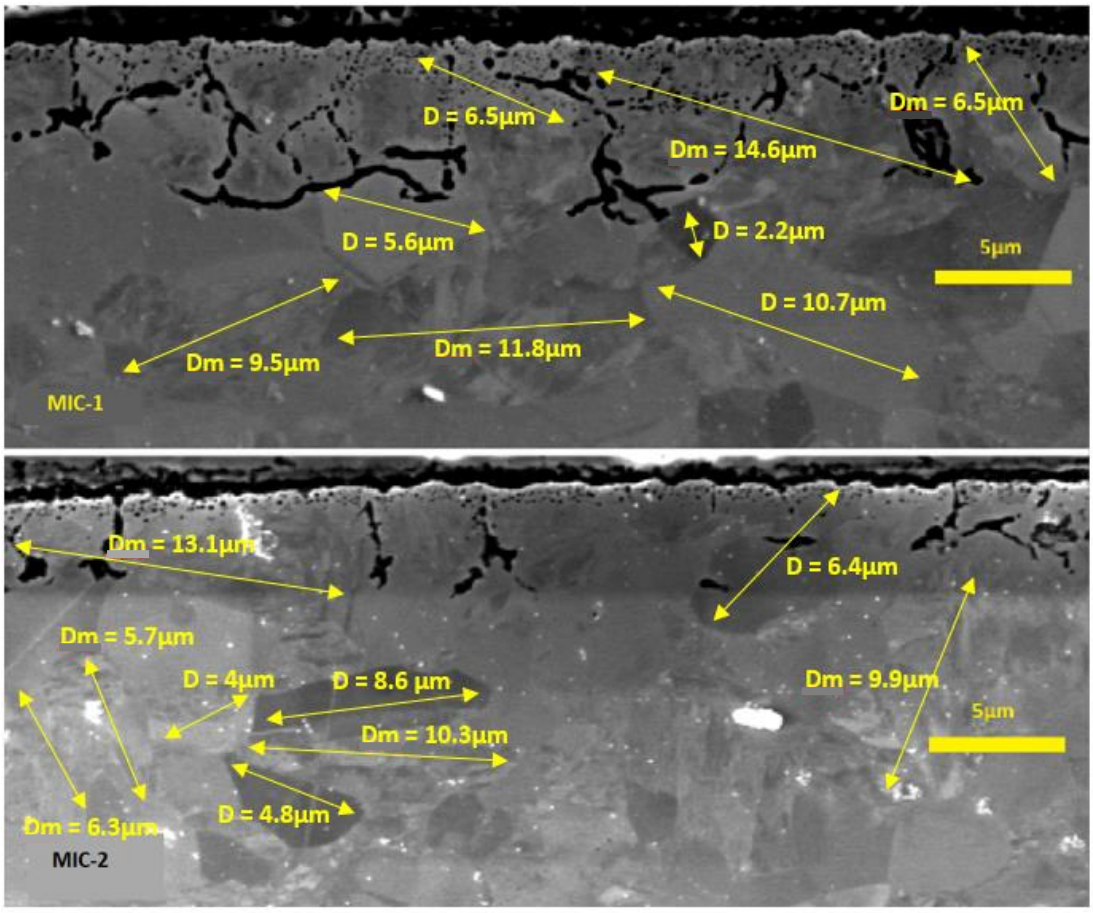

Figure 5.14 Fe-3Al-5Mn steel grade after H-20C oxidation experimental annealing heat treatment, microstructure analysis showing grain growth occurred during annealing. Ferrite and bainite/martensite grains exist without apparent large banding structure, although ferrite grains remain mostly long and thin. MIC-1: 20-30sec Site 1, MIC-2: 20-30sec Site 2,

Fe-5Al-5Mn Microstructure

Humidifier 0°C Run #1

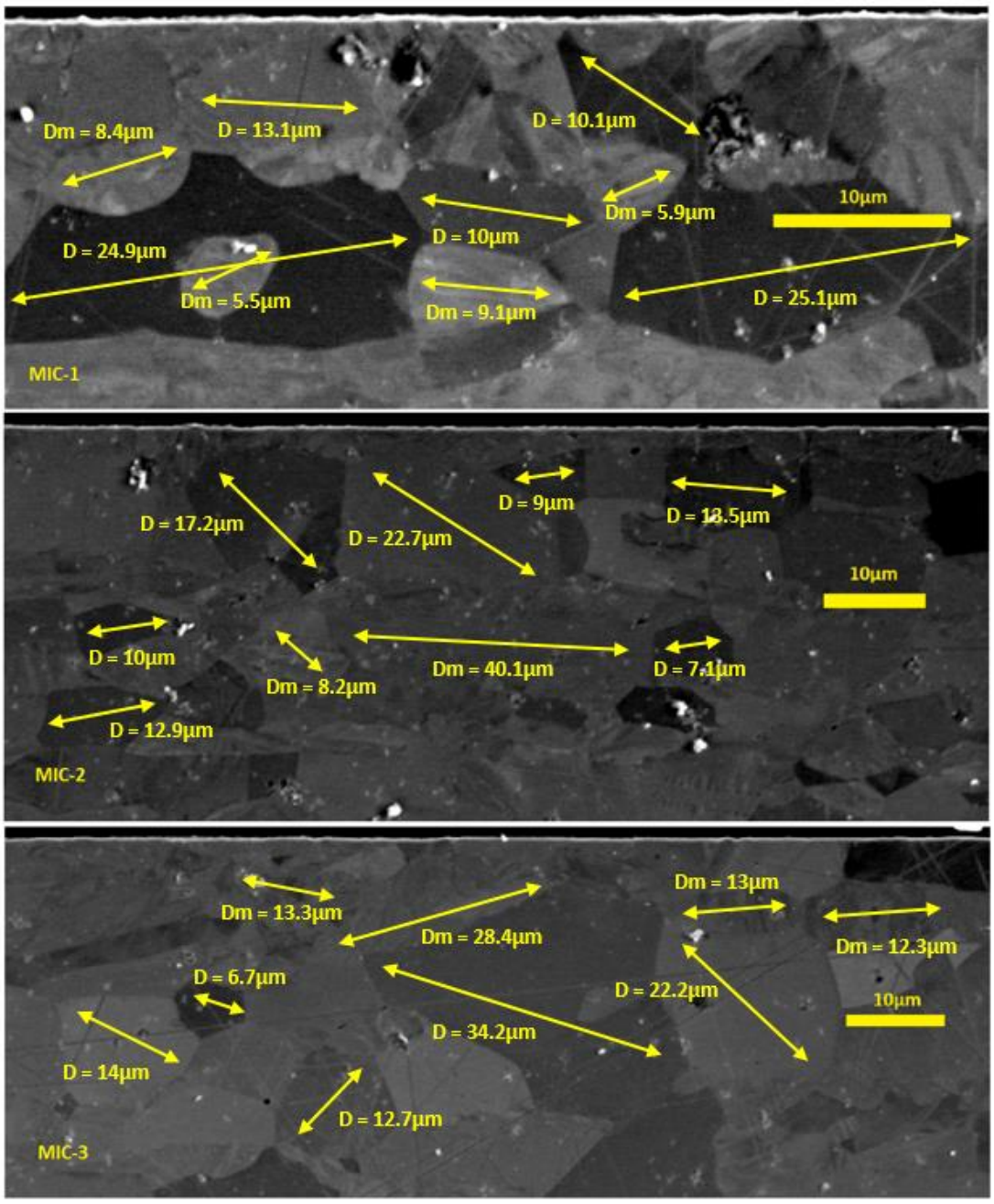

Figure 5.15 Fe-5Al-5Mn steel grade after H-0C Run #1 oxidation experimental annealing heat treatment, microstructure analysis showing grain growth occurred during annealing. Ferrite and bainite/martensite grains exist without apparent large banding structure. MIC-1: 5mins, MIC-2: 2:30mins, MIC-3: 20-30sec

Humidifier 0°C Run #2

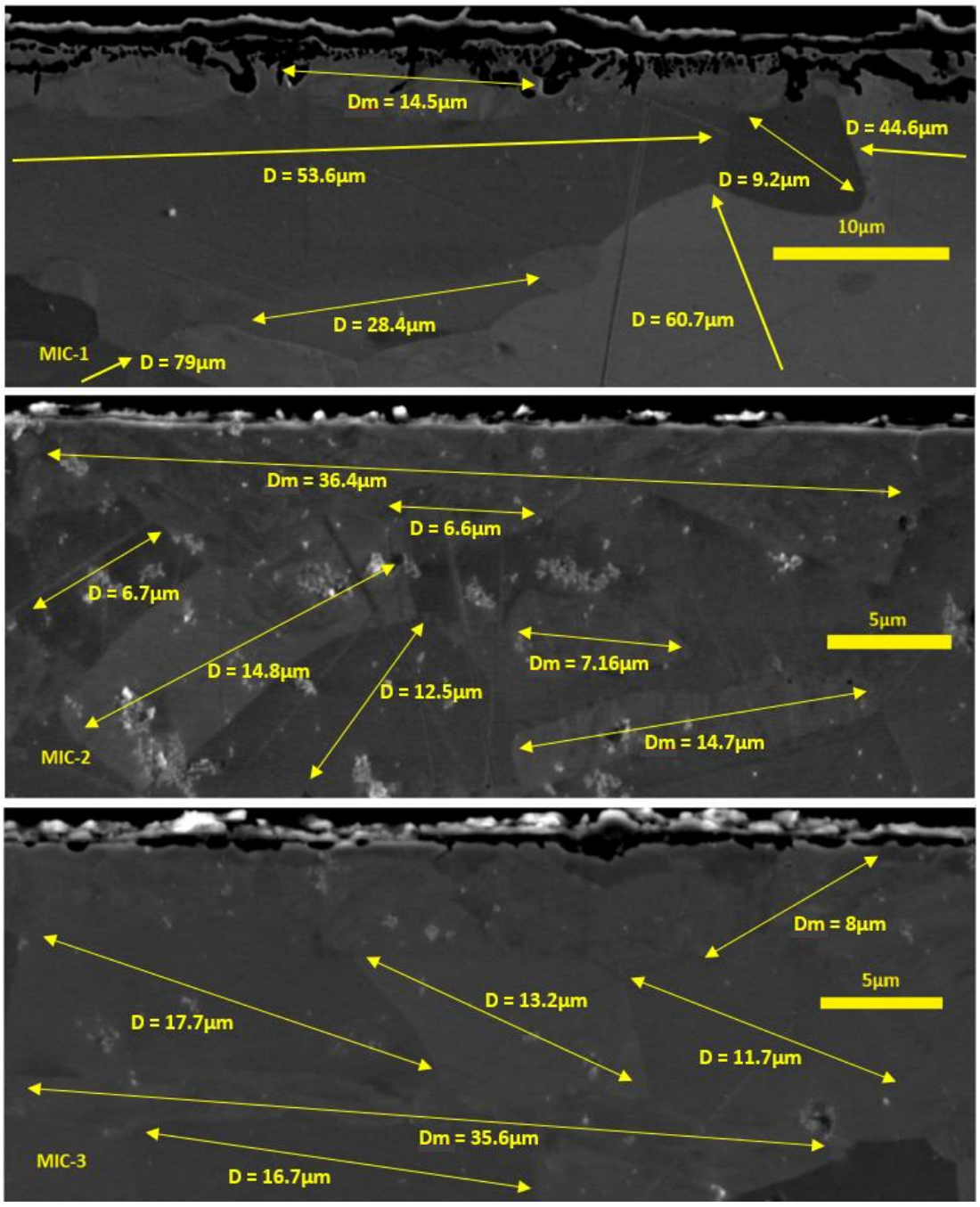

Figure 5.16 Fe-5Al-5Mn steel grade after H-0C Run #2 oxidation experimental annealing heat treatment, microstructure analysis showing grain growth occurred during annealing. Ferrite and bainite/martensite grains exist without apparent large banding structure. MIC-1: 5mins, MIC-2: 2:30mins, MIC-3: 20-30sec

Humidifier 20°C

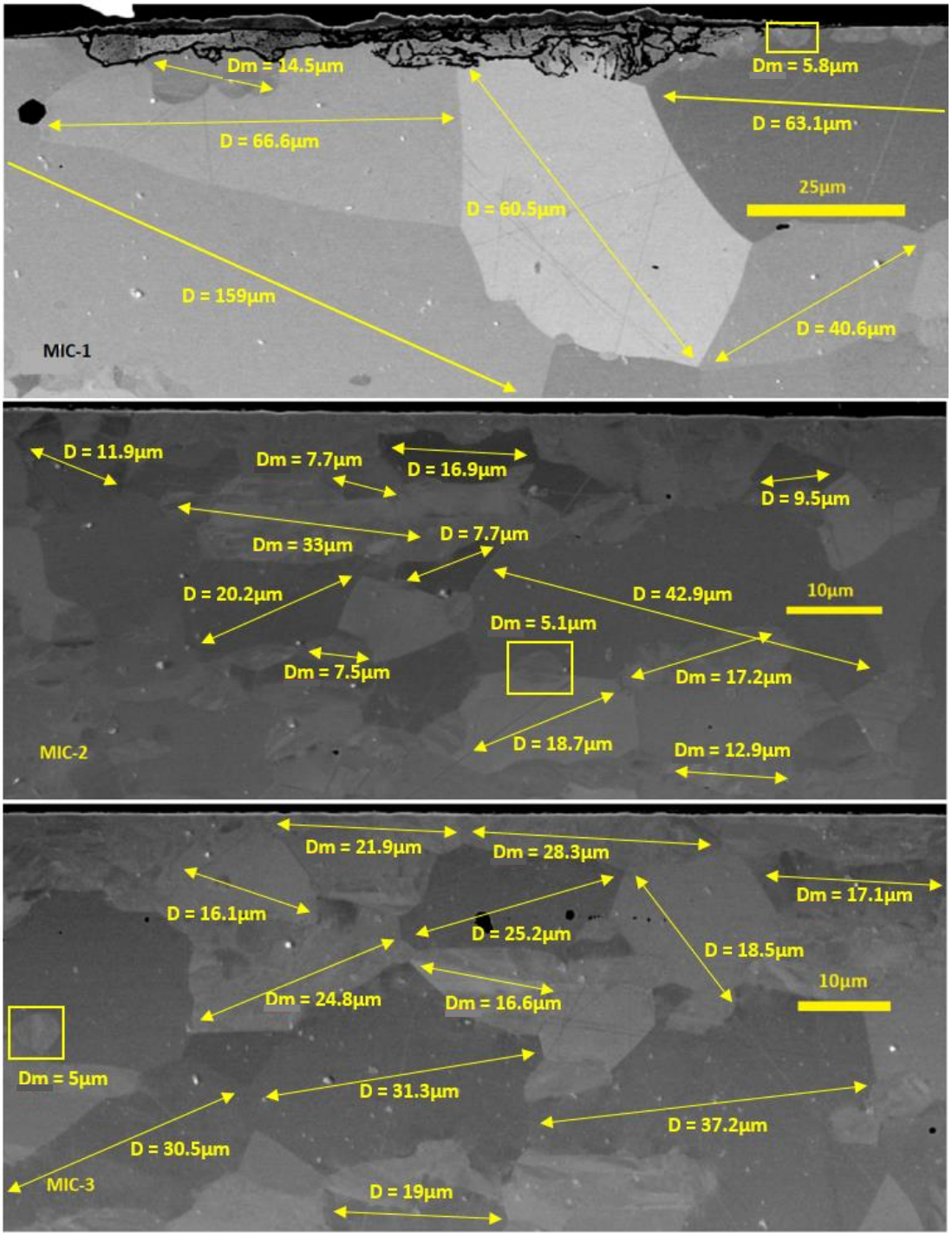

Figure 5.17 Fe-5Al-5Mn steel grade after H-20C oxidation experimental annealing heat treatment, microstructure analysis showing grain growth occurred during annealing. Ferrite and bainite/martensite grains exist without apparent large banding structure. MIC-1: 5mins showing very large grain sizes, MIC-2: 2:30mins, MIC-3: 20-30sec

Fe-6Al-15Mn Austenitic Microstructure

Humidifier 20°C

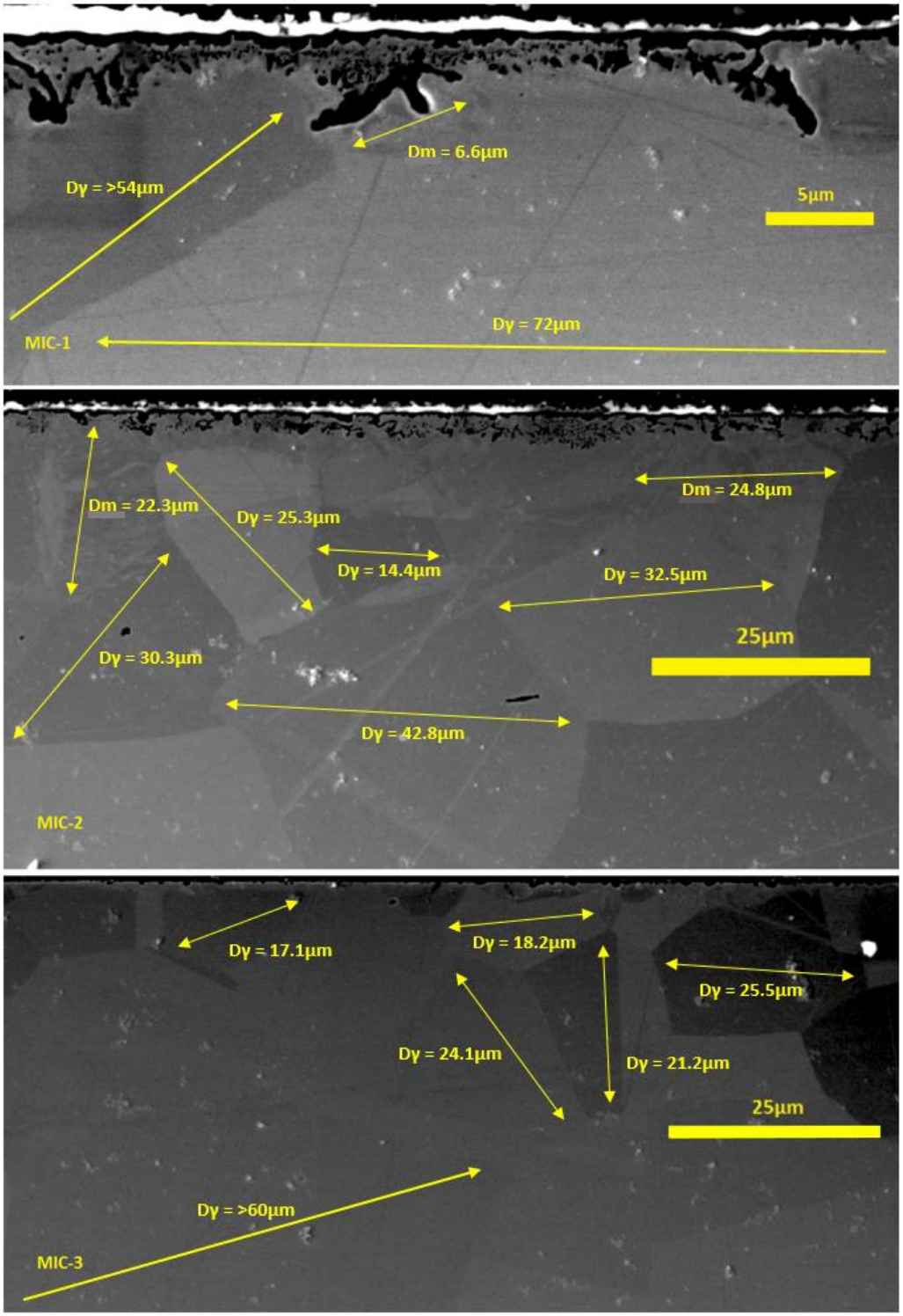

Figure 5.18 Fe-6Al-15Mn steel grade after H-20C oxidation experimental annealing heat treatment, microstructure analysis showing grain growth occurred during annealing. Contains bainite/martensite and austenite grains. MIC-1: 5mins, MIC-2: 2:30mins, MIC-3: 20-30sec

5.2.2 EDS-SEM Analysis with Mass Spectrometer Data

5.2.2.1 Fe-3Al-5Mn (Dual Phase)

5mins Isothermal Oxidation Time

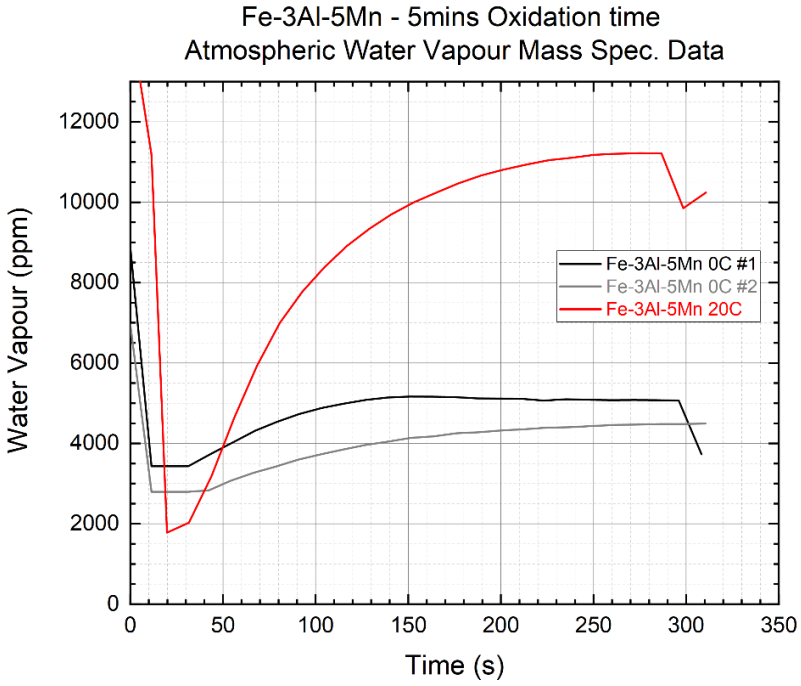

Figure 5.19 Fe-3Al-5Mn 5mins Oxidation time, Mass Spec. readings of chamber gas - Water vapour content (ppm)

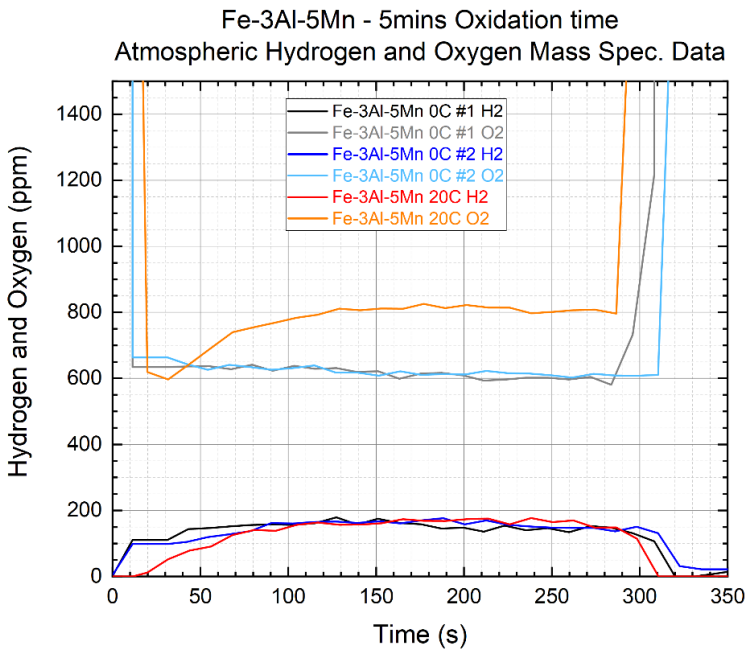

Figure 5.20 Fe-3Al-5Mn 5mins Oxidation time, Mass Spec. readings of chamber gas - Oxygen and Hydrogen content (ppm)

Humidifier Temperature 0°C

Run #1

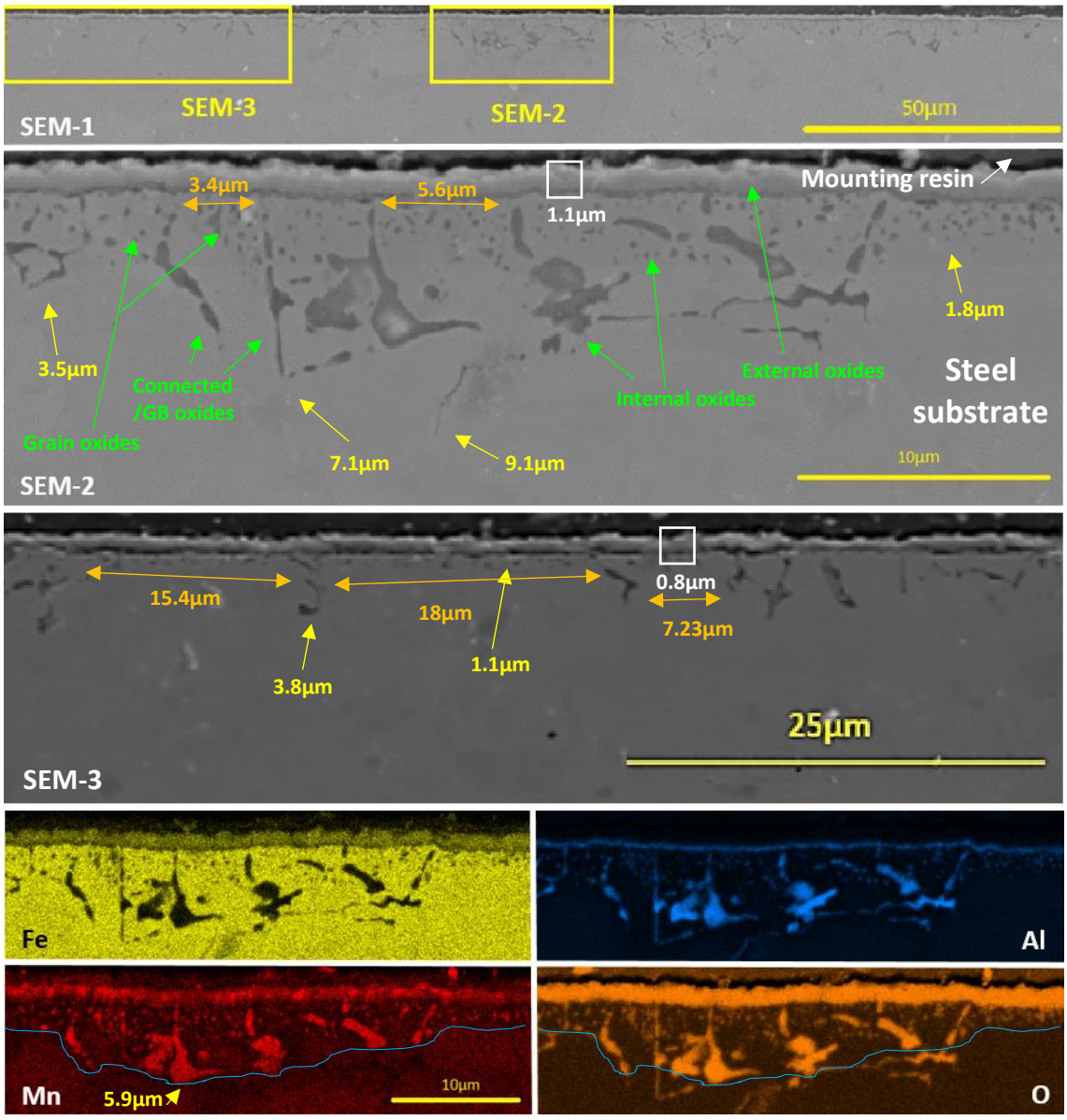

Figure 5.21 Fe-3Al-5Mn, Humidifier 0°C, 5mins first run. SEM images of IOZ: SEM-1 - 50µm scale view, SEM-2 - 10µm scale view - showing an area of higher than average internal oxidation, SEM-3 25µm scale view - showing an area of lower than average internal oxidation (sharpness and contrast increased 25%). EDS Composition mappings of SEM-2 with 10µm scale view for iron, aluminium, manganese, and oxygen. The green arrows are representing where you can expect to find certain oxides, usually as dark grey lines on the images for internal oxides, with yellow arrows depicting oxide depths, orange arrows depicting distances between GB/connected oxides, and blue lines showing the boundary between alumina and manganese aluminate, mean average GB/connected oxide width = 0.55µm, and grain oxide width = 0.19µm

SEM-1 shows a range of oxide depths (1.8 - 9.1µm), with some regions having minimal oxide formation, whilst other regions have large oxides grown and thickened

likely by a near flux equality between oxygen and aluminium. As seen in SEM-1, SEM-2 is an image of greater-than average oxidation, with more connected and thicker oxides, this could be due to a higher initial fraction of austenite. The significant differences in oxidation depths along with the oxide growth suggests that the solute flux is not far off what is required for Wagner's Criterion, this can be seen in SEM-3 where the thin dark layer (alumina) at lowest portion of the scale is slightly thicker where less internal oxidation occurs, which is expected as a thicker surface alumina layer will reduce the inward oxygen flux to a greater degree than most other oxides [5, 7, 76, 91]. The connected oxides generally appear to start very near the sample surface. The presence of this thicker alumina layer is likely due to a higher fraction of ferrite in the local area at the start of the isothermal oxidation. The size of the individual oxide particles of the grain seem to remain relatively stable, coupled with the numerous connected oxides along the grain-boundaries that increase in thickness with depth, it can be suggested that the oxygen flux is not significantly higher than the solute flux, due to the solute concentration component. The mean average grain size of Fe-3Al-5Mn 5mins 0°C is around 12µm, with a range of roughly 5 – 20µm, shown in Table 5.2, the connected oxides that are indicative of grain boundary oxidation are shown to be of a similar range and mean average shown in SEM-2 and SEM-3. With an initial heat rate constituting a duration of pre-isothermal oxidation heat exposure of around 3 minutes, the samples had a significant amount of time to recrystallise, and the microstructure at the point of initial oxidation was most likely constituting a mean average grain size larger than those presented in the Base Steel. This suggests a viable reason for the correlation between the connected GB oxides and the mean average grain size. The blue line in the manganese and oxygen elemental map images shows the depth of the formation concentration of manganese aluminate, this is likely due to the reduced oxygen flux which has three potential causes that are not necessarily mutually exclusive: as the rate of extension of the IOZ is reduced and as the flux competition starts to favour aluminium, there is a prevention of the formation of the spinel through an abundance of free aluminium arriving at the reaction zone; the reduction in oxygen flux correlates with a local concentration insufficient to fully oxidise the present aluminium, not regarding

additional aluminium that which might diffuse to the reaction zone, therefore the local oxygen concentration does not meet the manganese aluminate oxygen formation concentration; finally, the experiment was ended before sufficient oxygen concentration arrived to the area to further the formation of the spinel. Experiments that were conducted previously (Figure 4.4) to analyse the difference, these oxidation phenomena show subtle differences and present effects that are difficult to separate with the current resources available. Complex in-situ cross-section analysis during high temperature isothermal oxidation is likely required.

Run #2

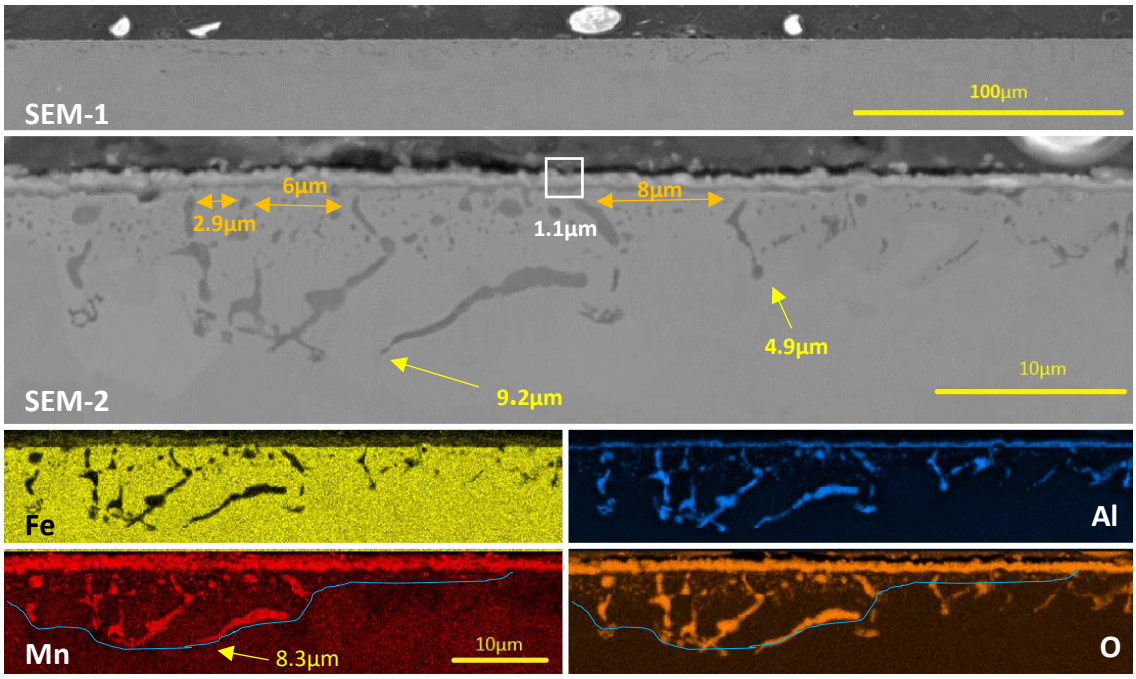

Figure 5.22 Fe-3Al-5Mn, Humidifier 0°C, 5mins second run. SEM images of IOZ: SEM-1 - 100µm scale view, SEM-2 - 10µm scale view. EDS Composition mappings of SEM-2 with 10µm scale view for iron, aluminium, manganese, and oxygen. Dark grey on the images are internal oxides, with yellow arrows depicting oxide depths, orange arrows depicting distances between GB/connected oxides, and blue lines showing boundary between alumina and manganese aluminate, mean average GB/connected oxide width = 0.66µm, and grain oxide width = 0.29µm

Fe-3Al-5Mn Run #2 shows a similar range of oxide depths as Run #1. The thin surface alumina layer is also relatively consistent. Similar to Run #1, the numerous spherical

oxides of the grain and the long connected oxides of the grain-boundary (GB) suggest the steel presents mostly Regime B diffusion. As with Run #1, Run #2 presents connected oxides at a greater depth, likely due to the reduction in oxygen flux shifting to favour aluminium, consequently oxide growth is more prevalent over nucleation.

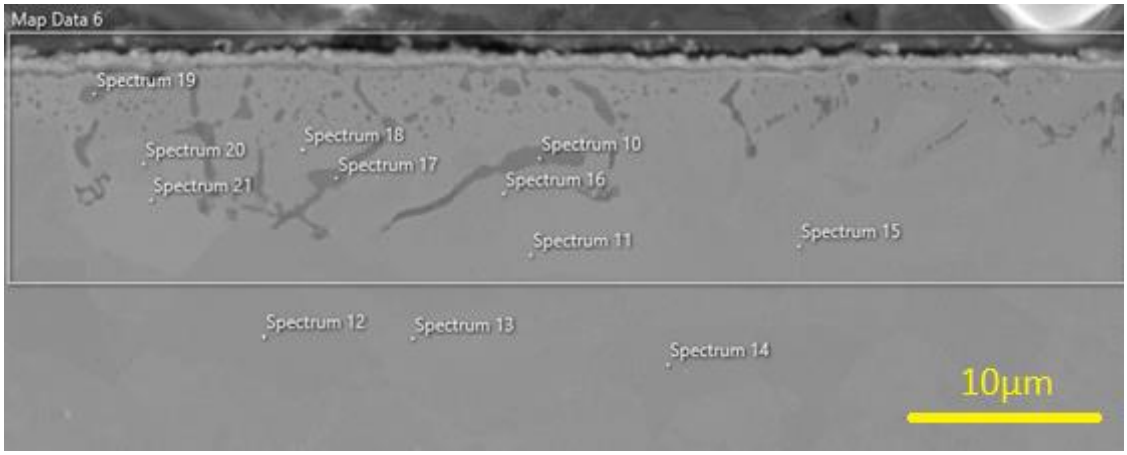

Figure 5.23 Fe-3Al-5Mn, Humidifier 0°C, 5mins second run. SEM image of IOZ 10µm scale view, with spectra analysis

Table 5.3 Fe-3Al-5Mn, Humidifier 0°C, 5mins, run two. SEM spectra analysis results, with ThermoCalc volume fraction of oxide calculations for spectra involving oxides

Spectrum #	Element Wt.%						TC Volume % Oxide
	Fe	Al	Mn	O	Si	C	
10	5.7	26.2	33.3	32.0	2.8	0.0	92.13
11	92.5	2.1	3.3	0.5	0.5	1.2	-
12	91.6	2.3	3.9	0.5	0.5	1.1	-
13	91.4	2.4	4.0	0.5	0.5	1.1	-
14	91.0	2.5	4.5	0.5	0.5	1.0	-
15	91.1	2.4	4.2	0.5	0.5	1.2	-
16	93.5	1.2	3.2	0.5	0.4	1.2	-
17	10.6	26.0	30.7	30.4	2.0	0.2	89.39
18	91.7	1.2	4.7	0.5	0.4	0.4	-
19	13.6	20.4	31.6	29.8	4.3	0.3	89.35
20	93.0	1.1	3.6	0.6	0.4	0.4	-
21	94.1	1.4	2.1	0.6	0.5	0.5	-

ThermoCalc data was used to identify the most likely oxide candidates for the oxide compositions and composited as TC internal volume % oxide in the spectra tables presented in this section. The volume fraction of oxide shows almost total oxide composition, manganese aluminate spinel taking the lion's share of notable spectra

10, 17, and 19. Spectra 14 and 15 represent the standard steel composition with minimal depletion due to their distance from the IOZ and position within the grain compared with 11 which experienced a small amount of depletion, suggesting that due to the big differences in grain-boundary volume and grain volume the grains can act as solute reservoirs but due to their slow diffusion speed each grain is unlikely to contribute significantly more material than any other grain in the local area.

Humidifier Temperature 20°C

Site 1

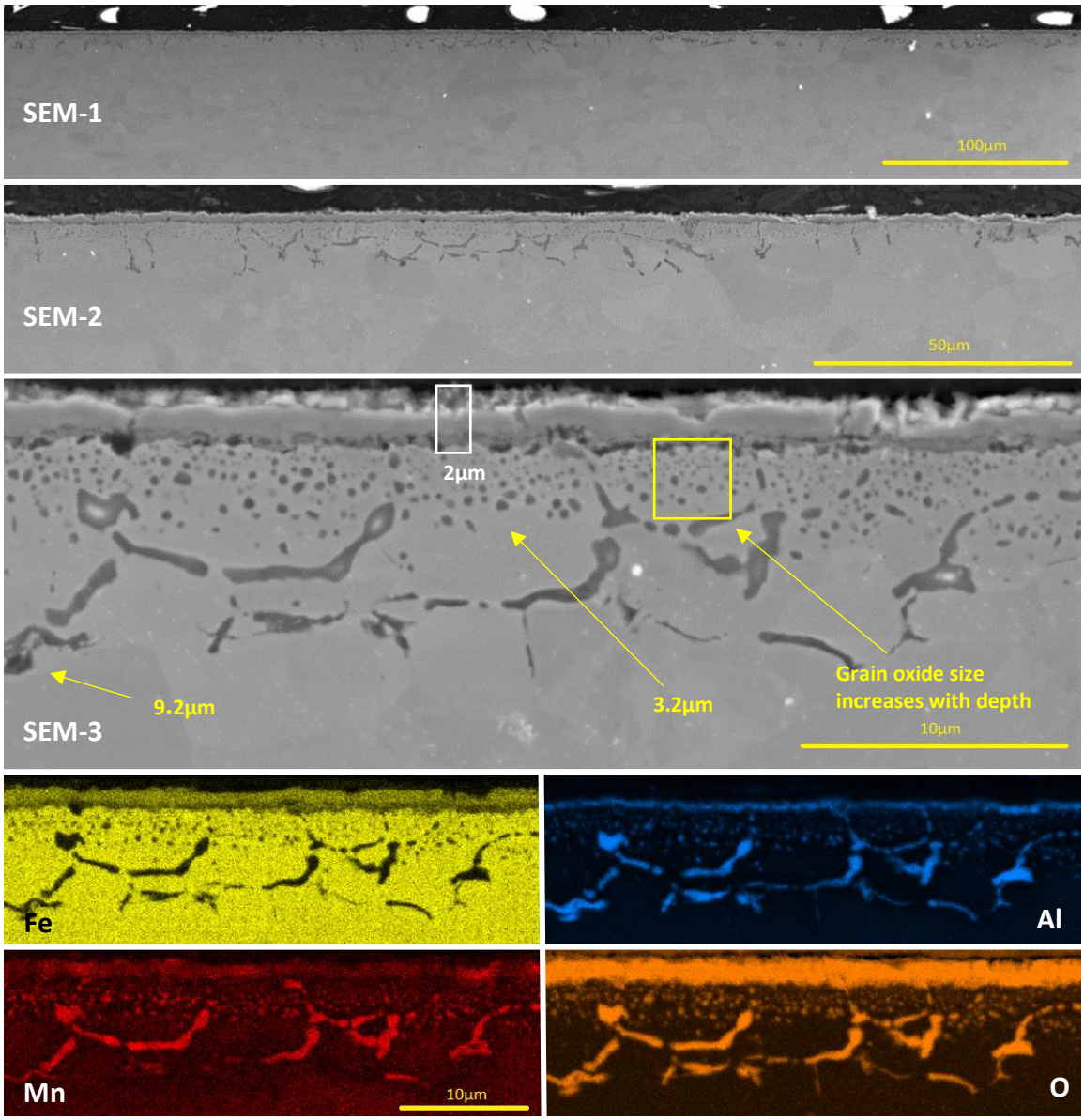

Figure 5.24 Fe-3Al-5Mn, Humidifier 20°C, 5mins. SEM images of IOZ Site 1: SEM-1 - 100µm scale view, SEM-2 - 50µm scale view, SEM-3 (Site 1) - 10µm scale view. EDS Composition mappings of SEM-3 (Site 1) with 10µm scale view for iron, aluminium, manganese, and oxygen. Dark grey on the images are internal oxides, with yellow arrows depicting oxide depths, mean average GB/connected oxide width = 0.68µm, and grain oxide width = 0.29µm

Figure 5.24 shows mostly individual oxide particles near the surface with connected oxides signifying grain-boundaries as can be seen by their relation to an image of

microstructure. The abundance of mostly individual oxides near the surface is due to the favour of the nucleation of oxides where oxygen permeability is higher than the solutes resulting in their small size; however, in SEM-3 very small oxide particles can be seen directly underneath the scale and from there increase in size to a certain point where all oxides are connected, a consistent depth of this effect can be seen across the sample. This indicates a decrease in the effective diffusivity of oxygen, but also that the flux of aluminium is still significant, although initially low compared to oxygen. Also, there are many thin GB/connected oxides at the greatest depth of the IOZ, suggesting that flux equality had not yet been reached. Compared to the Humidifier 0°C condition the connected GB oxides appear at a greater depth from the surface, this is most likely due to the increased oxygen flux in comparison creating a greater oxygen concentration gradient and completely oxidising the shallow-subsurface region before additional solute material can diffuse to the area, this is also supported by the very small oxide particles nearest the surface that decrease in number but increase in size with depth.

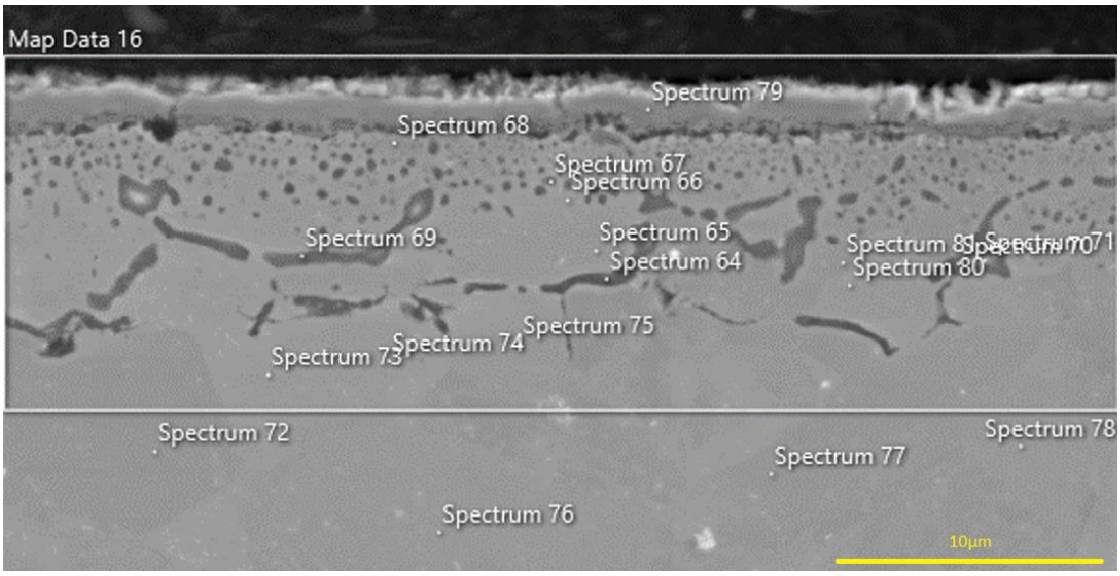

Figure 5.25 Fe-3Al-5Mn, Humidifier 20°C, 5mins. SEM image 10µm scale view, with spectra analysis

Table 5.4 Fe-3Al-5Mn, Humidifier 20°C, 5mins. SEM spectra analysis results, with ThermoCalc volume fraction of oxide calculations for spectra involving oxides

Spectrum #	Element Wt%						TC Volume % Oxide
	Fe	Al	Mn	O	Si	C	
64	14.2	15.7	29.7	28.6	10.3	1.5	81.84
65	95.7	0.6	1.6	0.2	0.4	1.4	-
66	96.0	0.3	1.7	0.4	0.2	1.5	-
67	65.2	7.0	14.2	10.1	2.0	1.5	43.59
68	95.5	0.7	0.8	1.4	0.1	1.6	-
69	30.5	10.3	33.6	19.5	4.9	1.4	68.26
70	9.0	32.9	24.0	31.8	1.0	1.4	85.01
71	4.6	41.8	11.0	39.6	1.5	1.5	92.79
72	92.9	1.9	3.3	0.3	0.5	1.0	-
73	93.8	1.7	2.3	0.2	0.5	1.5	-
74	93.8	1.6	2.3	0.2	0.5	1.6	-
75	94.9	1.0	1.8	0.2	0.4	1.7	-
76	91.1	2.3	4.7	0.2	0.6	1.1	-
77	91.8	2.2	4.0	0.2	0.6	1.2	-
78	92.9	1.9	3.2	0.3	0.5	1.2	-
79	68.3	0.9	6.0	23.0	0.1	1.7	-
80	92.8	1.2	3.8	0.2	0.4	1.5	-
81	94.3	0.8	3.0	0.2	0.3	1.4	-

Spectra 72 - 75 show a significant depletion of aluminium and manganese, but not more than half the initial value has been depleted, which is noteworthy considering the proximity to the IOZ; this relatively low level of depletion near the IOZ suggests that the flux of the solutes is comprised of material from many other grains, therefore adjacent grains likely do not have a majority effect on the local oxide formation in the grain boundary due to the high diffusivity. Spectra 76 and 77 both have slight depletion, but 77 more so than 76, likely due to the positioning of the point analyses, 76 is deep within a grain, and 77 is nearer the grain-boundary. Notable spectra are 64 - 67, showing the differences between the bulk compositions (65 and 66) and the adjacent oxides (64 and 67). Spectra 67 and 69 show significantly less volume fraction of oxide than other spectra, this is likely due to the positioning of the point analysis at near the oxide edge.

Site 2

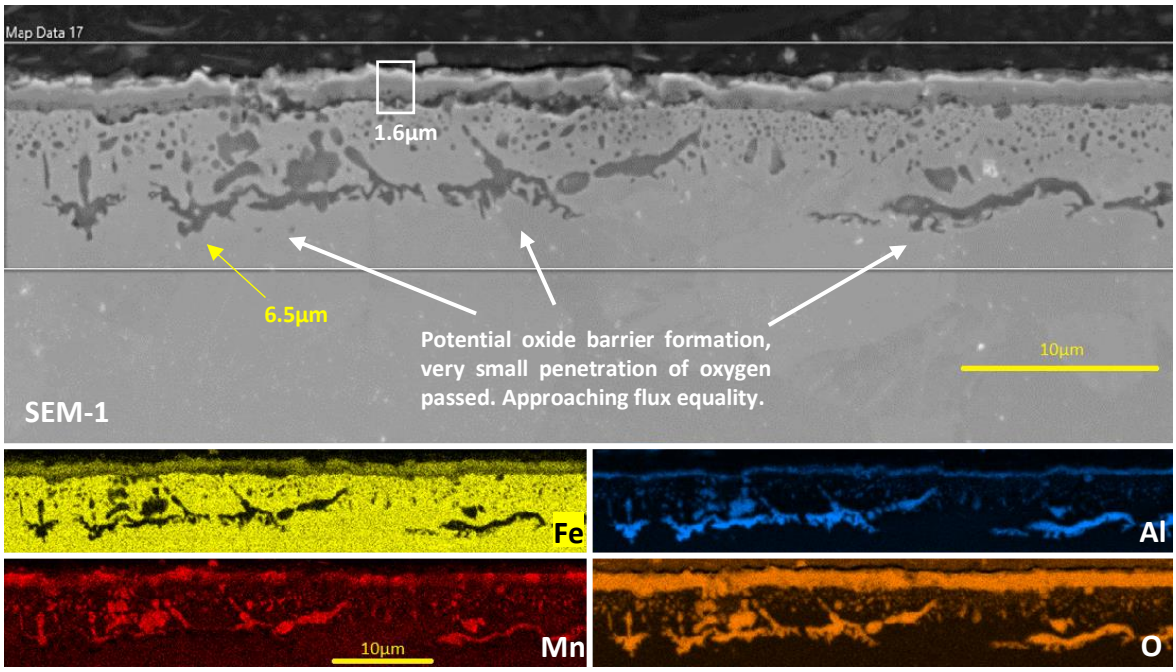

Figure 5.26 Fe-3Al-5Mn, Humidifier 20°C, 5mins. SEM images of IOZ Site 2: SEM-1 - 10µm scale view. EDS Composition mappings of SEM-1 with 10µm scale view for iron, aluminium, manganese, and oxygen. Dark grey on the images are internal oxides, with yellow arrows depicting oxide depths, mean average GB/connected oxide width = 0.89µm, and grain oxide width = 0.28µm

Figure 5.26, showing Site 2, offers a section of the sample with a large amount of connected oxides which appear to have grown in conditions close to flux equality. As stated before, for Site 1 - oxide particles closest to the scale are very small, increasing in size (up to a point) with depth, an expected phenomenon due to the nature of oxide growth coupled with effective diffusivity. Oxides at the lowest section of the IOZ are absent of manganese, suggesting the quantity of aluminium in the area or the additional flux to was sufficient to prevent manganese aluminate forming, or the experiment was not conducted over a duration to afford that local area the appropriate build-up of oxygen for the formation of manganese aluminate. The greater abundance of connected oxides suggests the local microstructure had a higher proportion of ferrite or a larger volume fraction of grain boundaries than Site 1. The former could be reasoned as the aluminium atoms benefit more so than the

oxygen atoms from the ferritic crystal structure compared to the austenitic crystal structure [111, 120]. There are some possible reasons for this:

- Lattice atoms distance: The change in the ratio of the size of oxygen atoms to the size of the iron parent lattice atoms, and the ratio of the size of the aluminium atoms to the size of the iron parent lattice atoms, and the effect this has on the activation energy of both diffusing atoms is more favourable for aluminium.
- Solubility: BCC lattices contain more numerous octahedral interstices than FCC lattices but of a much smaller volume [7], a BCC unit cell contains 6 octahedral and 12 tetrahedral sites, whilst a FCC unit cell contains 4 octahedral and 8 tetrahedral sites [64]. This correlates to a higher solubility of oxygen in ferrite than austenite [5], therefore perhaps whilst the diffusion speed of oxygen in ferrite is higher than austenite, the oxygen content in ferrite is higher for the same surface oxygen partial pressure but the average distance across the lattice that an oxygen atom travels in one jump is less because of the greater number of interstitial sites in ferrite that are available, producing a higher concentration gradient over a smaller distance. An analogy can be described as when you have a waterfall filling up a series of pools, if the pools are larger or more numerous, the last pool will be filled up at a later time.
- The increased aluminium concentration in ferrite is more significant to the total aluminium flux than the ratio of diffusivity increases.

How this relates to the grain boundary atomic structure is also currently unknown as the atomic structure and density of grain boundaries is subject to the adjacent crystal phases and how this is affected in dual phase steels not heavily investigated, further clarification is needed. Regardless, the ferritic phases of LDS see less oxidation and the IOZ depth is minimised compared to austenite [95-101, 103, 105, 107, 111, 119-122]

Comparison Discussion (Fe-3Al-5Mn 5mins)

The difference in oxygen flux between the humidifier 0°C (H-0C) and 20°C (H-20C) temperatures is significant, showing more oxidation in H-20C conditions mainly by more numerous connected oxides of a greater thickness from oxide growth where flux equality with aluminium is closer due to the increased GB oxide widths, which is expected. Internal oxides consist of mainly $MnAl_2O_4$ stoichiometry with the very bottom portion of the IOZ strictly Al_2O_3; the scale is composed of a thin alumina layer under a thick single layer of Fe-Mn oxides ($MnO \cdot FeO$).

As the isothermal oxidation temperature keeps diffusion speeds constant, the lack of a significant difference in IOZ depth likely rests on the concentration component of the flux term. This is due to the higher oxygen concentration leading to greater internal (GB oxide width average: H-0C = 0.61µm, H-20C = 0.77µm) and external oxide formation (scale thickness average: H-0C = 1.1µm, H-20C = 1.8µm), thereby reducing oxygen diffusivity to a greater extent than with lower oxygen concentrations [89]. However, the increased oxygen flux lead to the exacerbation of grain oxidation where the oxygen was transported to the solute for reaction, suggesting that the growth of the grain-boundary oxides is due to the solute flux from other areas of the bulk compared to the near-surface substrate. This implies that solute content of individual grains are less significant than the larger area's total contribution to flux via high-diffusivity pathways. Furthermore, this demonstrates that an adjacent different-phase grains' compositions in dual phase steels do not necessarily affect the immediate local grain-boundary oxidation behaviour to a significant degree when the oxygen permeability is much higher than the solute permeability when the grain sizes are relatively small (5 - 20µm).

The Fe-3Al-5Mn steel grade produces oxides of individual particles along the grain boundaries, increasing in size with depth, this is apparent in both humidity scenarios although the growth vs nucleation dynamic shifts to growth at an earlier stage in the lower oxygen concentrations as the flux equality is reached sooner, this is evident by the position of the connected GB oxides from the surface, with the H-20C condition producing oxides that connect at a greater consistent depth than in the H-0C scenario.

2:30 minutes Isothermal Oxidation Time

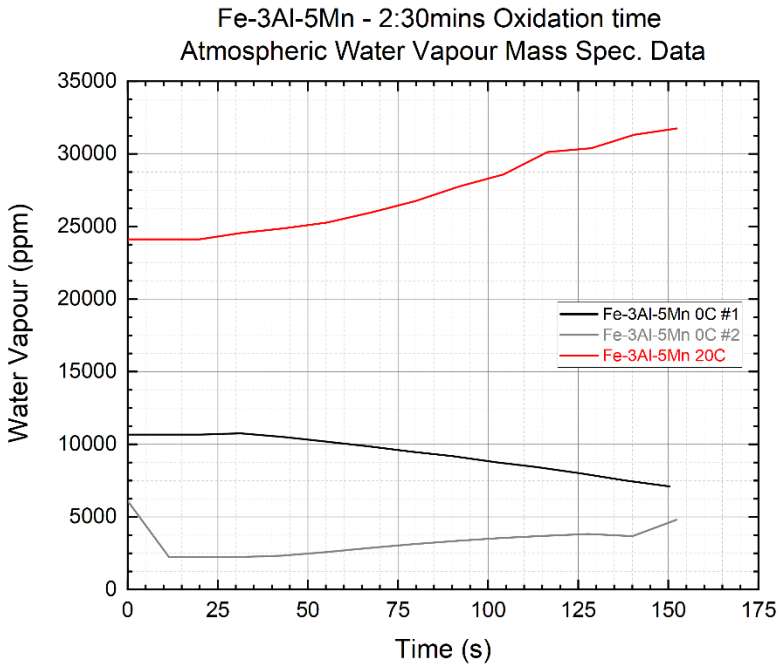

Figure 5.27 Fe-3Al-5Mn 2:30mins Oxidation time, Mass Spec. readings of chamber gas - Water vapour content (ppm)

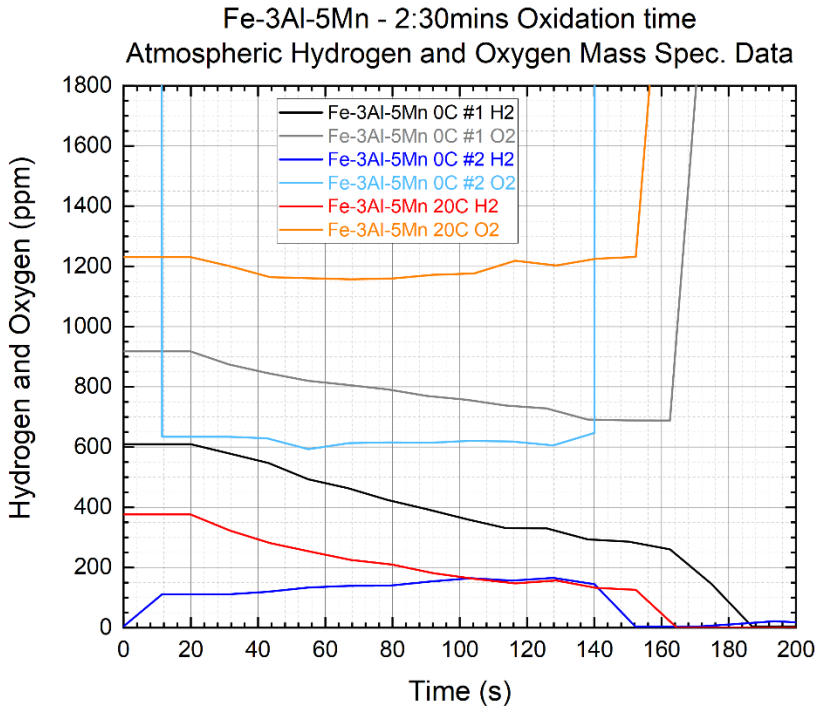

Figure 5.28 Fe-3Al-5Mn 2:30mins Oxidation time, Mass Spec. readings of chamber gas – Hydrogen and Oxygen content (ppm)

Humidifier Temperature 0°C

Run #1

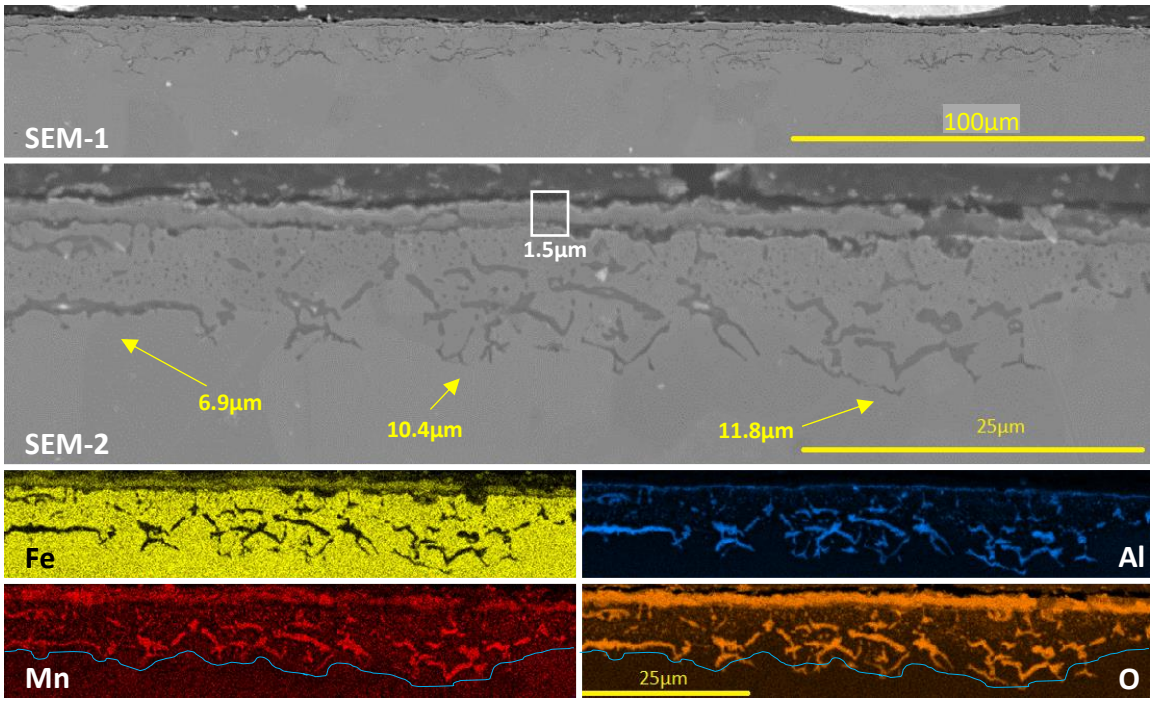

Figure 5.29 Fe-3Al-5Mn, Humidifier 0°C, 2:30mins first run. SEM images of IOZ: SEM-1 - 100µm scale view, SEM-2 - 10µm scale view. EDS Composition mappings of SEM-2 with 25µm scale view for iron, aluminium, manganese, and oxygen. Dark grey on the images are internal oxides, with yellow arrows depicting oxide depths, mean average GB/connected oxide width = 0.75µm, and grain oxide width = 0.28µm

Seen in Figure 5.29, this Run #1 sample underwent oxidation with a much larger water vapour content than Run #2, which is similar to the H-20C water content of the 5mins oxidation times. This shows a very large amount of oxidation, as can be seen by the Hydrogen Mass Spec. atmospheric readings in Figure 5.28, which is a result of the dissociation of water. Oxide growth becoming prevalent over oxide nucleation occurs at a similar depth as the 5mins sample. The formation of thick internal oxides at the bottom of the IOZ shows how effective diffusivity of oxygen is reduced, this is because the distance between the manganese aluminate reaction and the bottom of the alumina reaction is very small as the oxygen content in the local area is high enough to reach that oxide oxygen formation concentration everywhere but the very bottom. This is likely due to the very across the thick internal oxides and the flux of

aluminium to the local area making the spinel formation not thermodynamically likely.

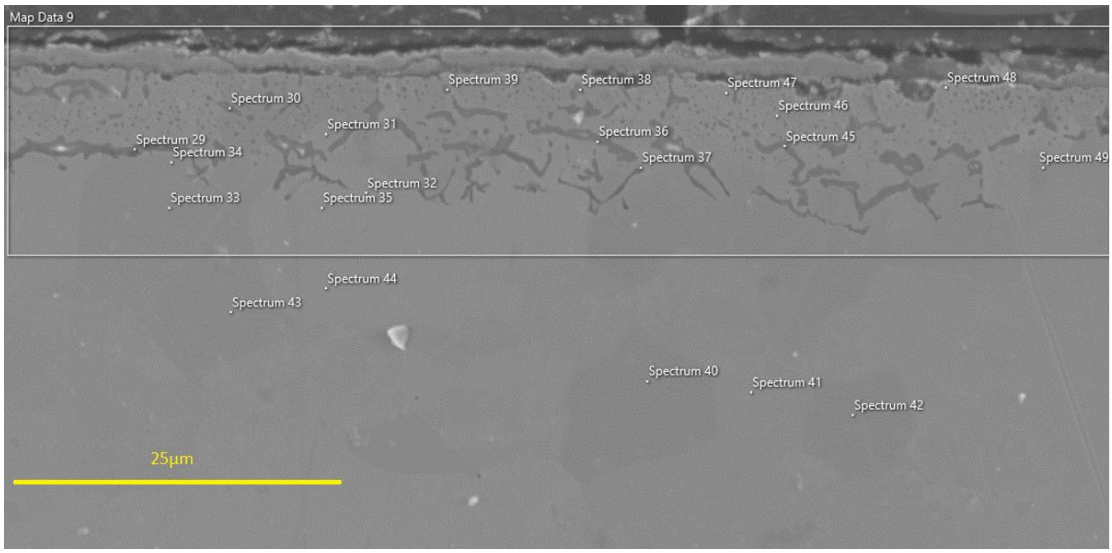

Figure 5.30 Fe-3Al-5Mn, Humidifier 0°C, 2:30mins first run. SEM image of IOZ 25µm scale view, with spectra analysis

Table 5.5 Fe-3Al-5Mn, Humidifier 0°C, 2:30mins. SEM spectra analysis results, with ThermoCalc volume fraction of oxide calculations for spectra involving oxides

Spectrum #	Element Wt.%						TC Volume % Oxide
	Fe	Al	Mn	O	Si	C	
29	6.8	40.5	13.2	37.4	2.0	0.1	91.55
30	27.1	22.4	22.7	25.9	1.2	0.7	81.76
31	94.5	0.6	2.8	0.5	0.4	1.2	-
32	93.7	1.3	2.8	0.5	0.5	1.3	-
33	94.0	1.4	2.4	0.5	0.5	1.2	-
34	95.0	0.9	1.6	0.9	0.5	1.2	-
35	94.5	1.2	2.1	0.5	0.5	1.2	-
36	14.9	22.9	32.1	27.3	0.5	0.6	85.21
37	69.8	8.4	10.0	9.7	2.2	1.4	41.45
38	58.2	10.1	13.6	14.5	2.4	1.2	56.73
39	75.4	2.0	12.0	7.3	2.4	0.9	35.14
40	90.6	2.4	4.9	0.5	0.5	1.2	-
41	90.6	1.9	5.3	0.5	0.5	1.3	-
42	90.5	2.4	4.9	0.5	0.5	1.2	-
43	91.9	2.0	4.0	0.5	0.5	1.1	-
44	92.0	1.9	3.9	0.5	0.5	0.5	-
45	11.8	21.1	35.8	27.7	2.9	0.7	85.25
46	91.1	1.4	3.2	2.7	0.4	1.4	-
47	96.3	0.3	0.7	1.2	0.2	1.3	-
48	89.6	2.2	2.3	3.8	0.5	1.6	-
49	90.9	2.0	5.0	0.4	0.5	1.3	-

Run #2

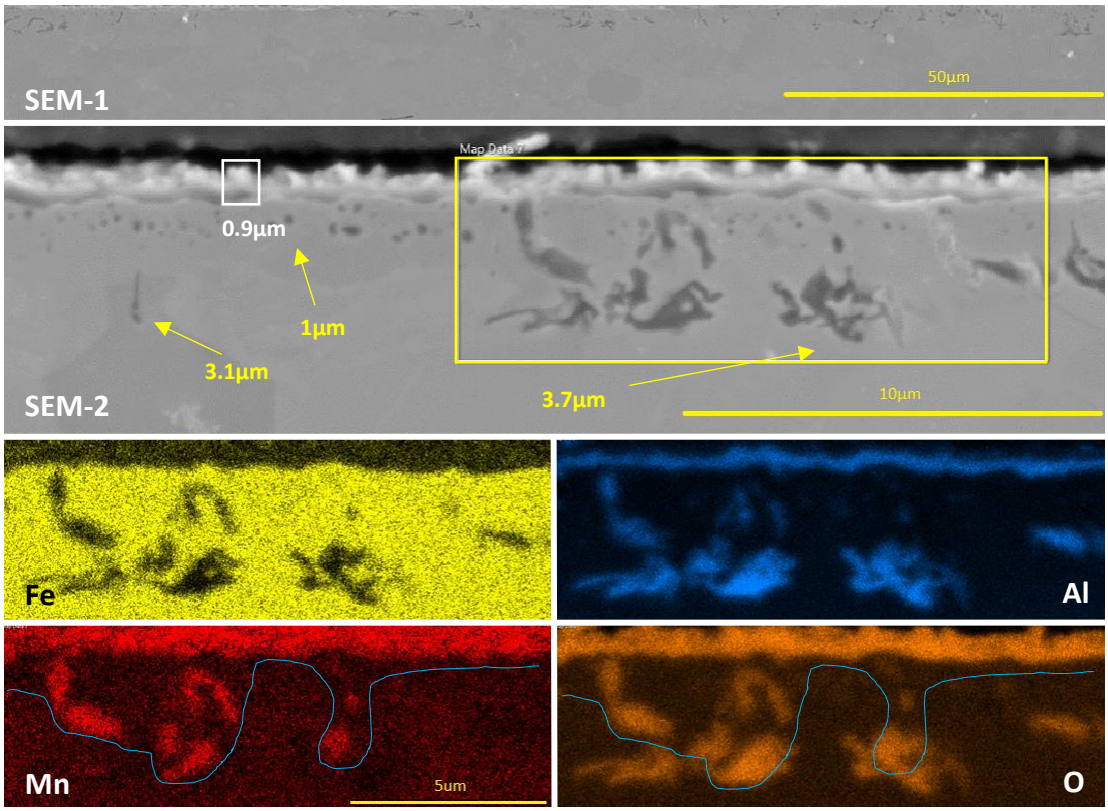

Figure 5.31 Fe-3Al-5Mn, Humidifier 0°C, 2:30mins second run. SEM images of IOZ: SEM-1 - 50µm scale view, SEM-2 - 10µm scale view with map data area shown (yellow box). EDS Composition mappings of SEM-2 with 5µm scale view for iron, aluminium, manganese, and oxygen. Dark grey on the images are internal oxides, with yellow arrows depicting oxide depths, and blue lines showing boundary between alumina and manganese aluminate, mean average GB/connected oxide width = 0.36µm, and grain oxide width = 0.15µm

This Run #2 iteration is more comparable as a better representation of the 2:30mins iteration due to the water vapour content being consistent with the expected water vapour pressure of H-0C, although comparisons to Run #1 are possible. With a lower surface oxygen partial pressure and shorter time to oxidise over, the IOZ is substantially smaller. The growth vs nucleation dynamic appears to favour growth at a similar depth to the 5mins sample which is expected given the point during the experiment at which this occurs – the beginning. Regime B diffusion is apparent with the advancing reaction front visible shown in a similar shape via the oxide positions relative to their compositions: the small individual oxide particles consisting of aluminium oxide and the GB oxides consisting of manganese aluminate; and the aluminium-rich lower portion of the IOZ. This sample along with the 5mins iteration

establishes evidence that the reaction front of Fe-3Al-5Mn occurs by inward discrete oxide growth initially along a grain-boundary, with the nucleation of grain oxides and subsequent occurring sequentially. The GB connected oxides do not always appear to neatly follow the path of the grain boundary when the flux competition between oxygen and aluminium is approaching equality - this could be due to various reasons, which are not necessarily mutually exclusive:

- Subsequent growth of the initial GB oxides does generally continue down from the surface into the sample but does not have an discrete and specific direction
- The oxide-steel interface created by the initial GB oxidation provides a high diffusivity pathway that bypasses the low diffusivity oxide and steel grain mediums, this would create a reaction zone on the perimeter of the GB oxide
- The connected GB oxides with no clear direction are actually the connection of grain and grain-boundary oxides due to the redirection of oxygen atoms into the adjacent grains due to the oxides occupying the grain-boundary creating a slower diffusivity zone than said grains

Each of the above possibilities can be attributed partially to the oxidation behaviour in Figure 5.31, attention is paid to the blue line on the manganese and oxygen elemental maps showing the manganese aluminate oxygen formation concentration zone. This zone appears to stem from a central core of oxidation which branches laterally. Due to the short duration of annealing and oxygen exposure coupled with the parameters governing these experiments, there are few pieces of literature to compare these results to and confirm a likeliest reason for this behaviour. [95-101, 103, 105, 107, 111, 119-122].

Humidifier Temperature 20°C

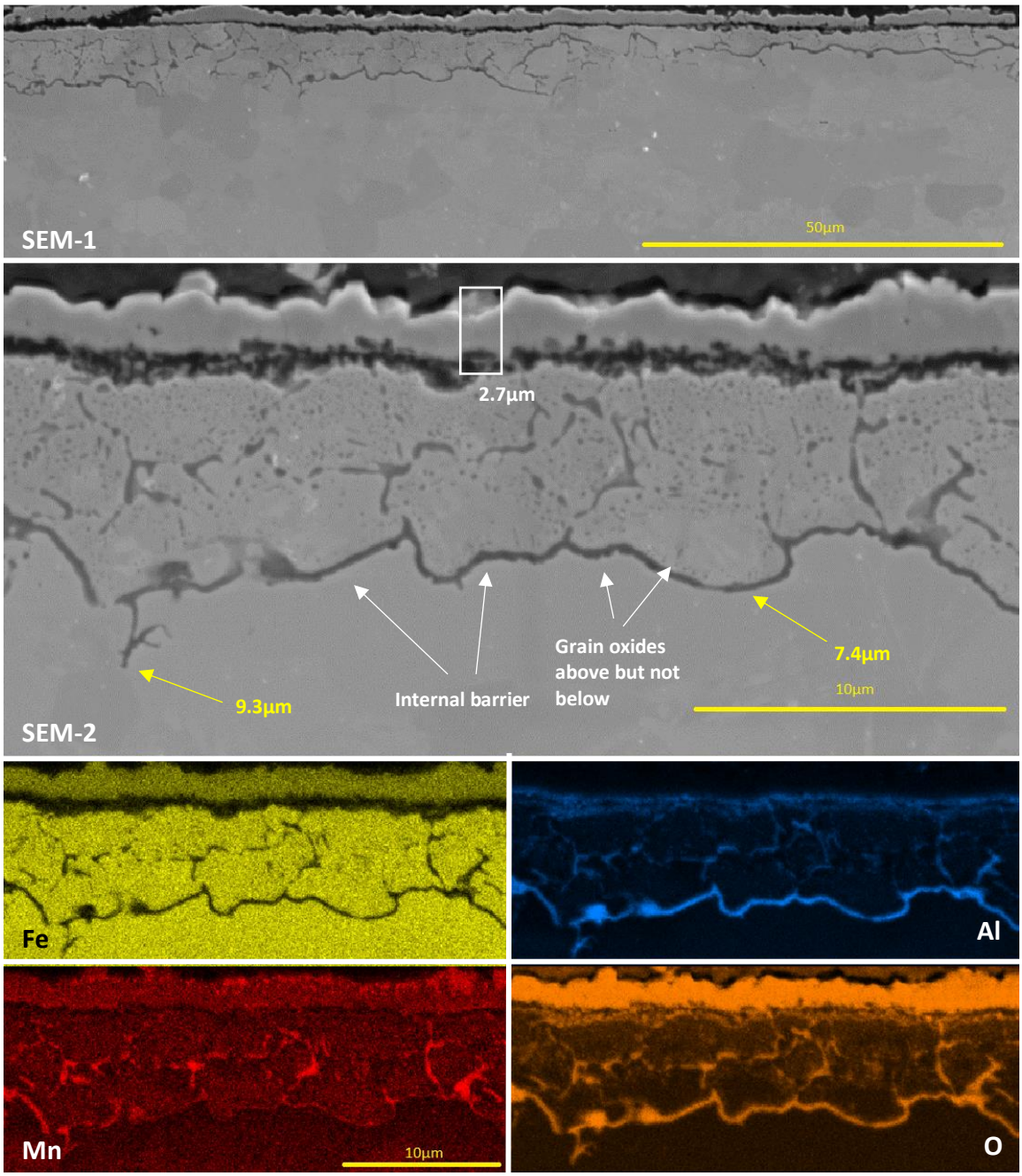

Figure 5.32 Fe-3Al-5Mn, Humidifier 20°C, 2:30mins. SEM images of IOZ: SEM-1 - 50µm scale view, SEM-2 - 10µm scale view. EDS Composition mappings of SEM-2 with 10µm scale view for iron, aluminium, manganese, and oxygen. Dark grey on the images are internal oxides, with yellow arrows depicting oxide depths, mean average GB/connected oxide width = 0.24µm, and grain oxide width = 0.14µm

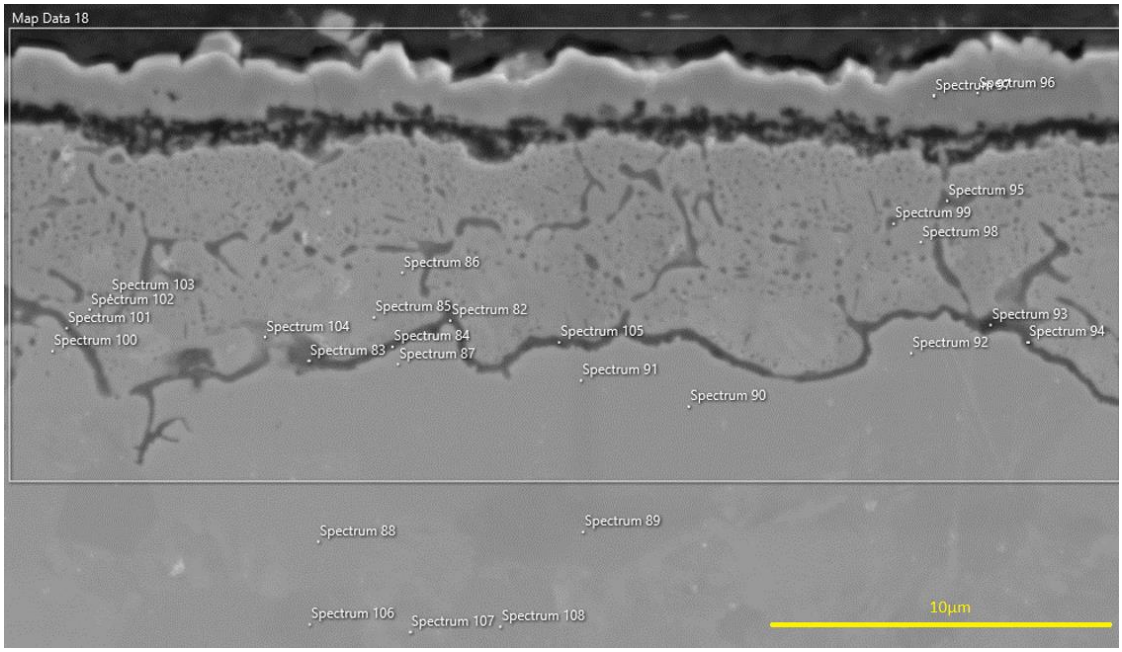

Figure 5.33 Fe-3Al-5Mn, Humidifier 20°C, 2:30mins. SEM image 10µm scale view, with spectra analysis

Table 5.6 Fe-3Al-5Mn, Humidifier 20°C, 2:30mins. SEM spectra analysis results, with ThermoCalc volume fraction of oxide calculations for spectra involving oxides

Spectrum #	Element Wt.%						TC Volume % Oxide
	Fe	Al	Mn	O	Si	C	
82	44.2	24.6	6.2	21.3	1.8	1.9	65.85
83	23.8	26.8	18.1	26.8	2.7	1.8	77.76
84	44.0	27.0	5.3	20.9	1.0	1.8	64.48
85	90.9	1.6	5.2	0.2	0.4	1.6	-
86	97.0	0.4	0.6	0.3	0.3	1.5	-
87	95.9	0.8	0.8	0.4	0.5	1.6	-
88	91.7	2.1	4.4	0.2	0.5	1.1	-
89	91.7	2.1	4.5	0.2	0.5	1.1	-
90	94.0	1.3	2.3	0.2	0.5	1.5	-
91	94.8	1.2	1.5	0.1	0.5	1.8	-
92	96.2	0.8	0.7	0.2	0.5	1.6	-
93	33.0	27.6	4.4	26.9	6.1	2.1	73.77
94	89.3	4.4	0.7	3.3	0.6	1.8	15.99
95	55.8	7.7	19.4	13.0	2.2	1.8	52.91
96	65.7	1.0	9.3	22.2	0.1	1.6	92.91
97	64.6	1.1	9.0	23.4	0.2	1.7	95.24
98	95.3	0.4	1.8	0.7	0.1	1.7	-
99	81.1	4.3	6.3	5.8	0.7	1.8	27.87
100	96.7	0.2	0.6	0.5	0.3	1.8	-
101	93.6	1.2	1.5	1.7	0.3	1.7	-
102	94.2	0.9	2.0	1.0	0.2	1.7	-
103	83.6	4.1	5.6	4.5	0.5	1.7	22.20
104	84.9	1.8	7.0	3.4	1.2	1.8	17.25
105	69.6	14.2	2.4	10.9	1.0	1.9	42.19
106	91.5	2.5	4.1	0.2	0.6	1.1	-
107	90.8	2.0	5.1	0.3	0.5	1.3	-
108	91.3	2.4	4.4	0.2	0.5	1.2	-

This sample underwent oxidation in a very high water vapour content atmosphere, this can be seen by the interspersed surface alumina layer, unable to effectively reduce the oxygen penetration subsequently forming a thicker manganese-rich scale than usual at 2.7µm. It is not possible here to determine whether the internal volume expansion of the substrate oxidation or the increased surface oxygen partial pressure is the cause or their individual contributions to the increased manganese content at the surface in the form of external oxides [114-118]. The oxygen penetrated the grains and formed a very large number of small oxides, smaller in size than easily and usually

seen, this is due to the much higher oxygen flux than the aluminium flux through the higher oxygen concentration gradient as if the fluxes were closer to equality the oxide formation would be less in favour of nucleation with fewer individual particles forming. The appearance of the internal boundary not seen on Fe-3Al-5Mn as distinctly in other iterations, this is likely due to the much higher oxygen content than other H-20C iterations, as seen in comparison of Figures 5.24 and 5.32, this increased oxygen content is likely the cause of its early formation as compared to the 5mins iteration. In Figure 5.32 at the white arrows labels "Grain oxides above but not below" it can be seen that oxygen penetration of the grains occurred above the barrier and not below – hinting at the effectiveness of the barrier at preventing oxygen penetration via oxide density. It is also clear here that the oxygen penetrated the grain from the grain boundary. As the diffusion of oxygen is substantially lower (several orders of magnitudes [76]) in the grains than the grain-boundaries, the significant formation of these grain oxides suggests that the internal barrier formed at a time significantly before the end of the isothermal experiment. In can be reasoned that as the initial oxygen concentration gradient was high the depth at which the volume fraction of oxide necessary to laterally extend the oxides was further into the substrate [106, 148-150]. The sizes of the grains appear to also affect the oxidation behaviour, this could be due to a higher grain boundary volume increasing both the relative oxygen and aluminium fluxes, forming oxides with increased density via decreased defect concentration. Evidence of this comes from the dense and thick aluminium-rich internal barrier, where in Figure 5.24 it can be seen that there is an unusual absence of manganese which is usually present; the reason for this is probably that the alumina is dense enough to prevent any flux through it thereby inhibiting its further oxidation by manganese. This can be seen by the formation of small grain oxides above the internal barrier which would not have formed if the oxygen could penetrate the barrier, due to its density.

20-30 seconds Isothermal Oxidation Time

Humidifier Temperature 0°C

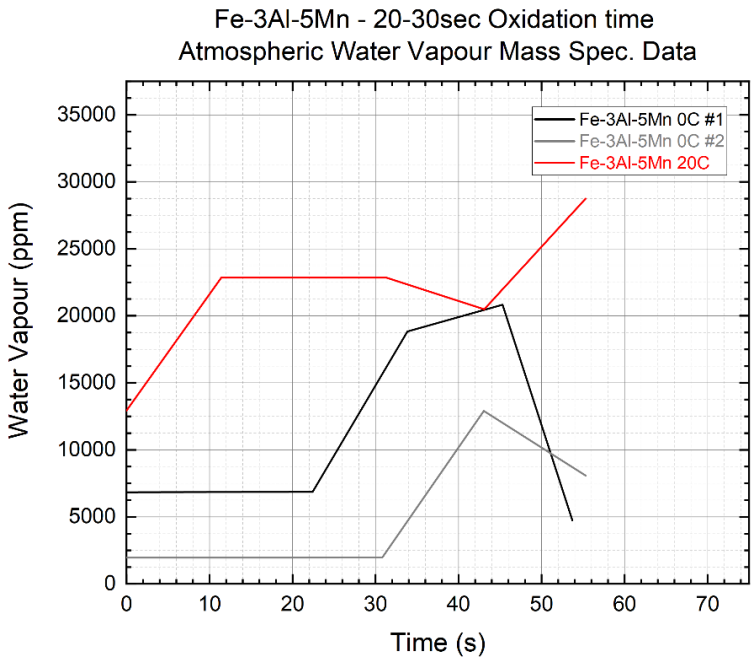

Figure 5.34 Fe-3Al-5Mn 2:30mins Oxidation time, Mass Spec. readings of chamber gas - Water vapour content (ppm)

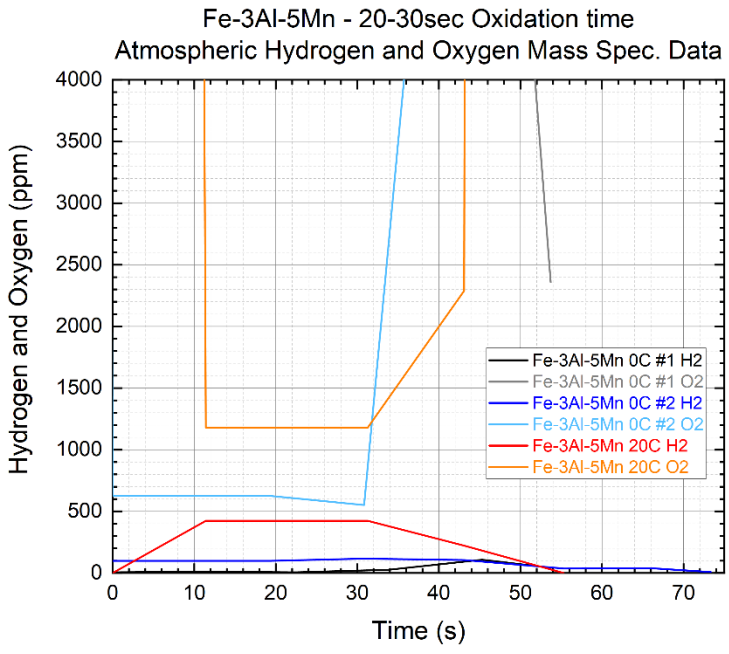

Figure 5.35 Fe-3Al-5Mn 2:30mins Oxidation time, Mass Spec. readings of chamber gas – Hydrogen and Oxygen content (ppm)

Run #1

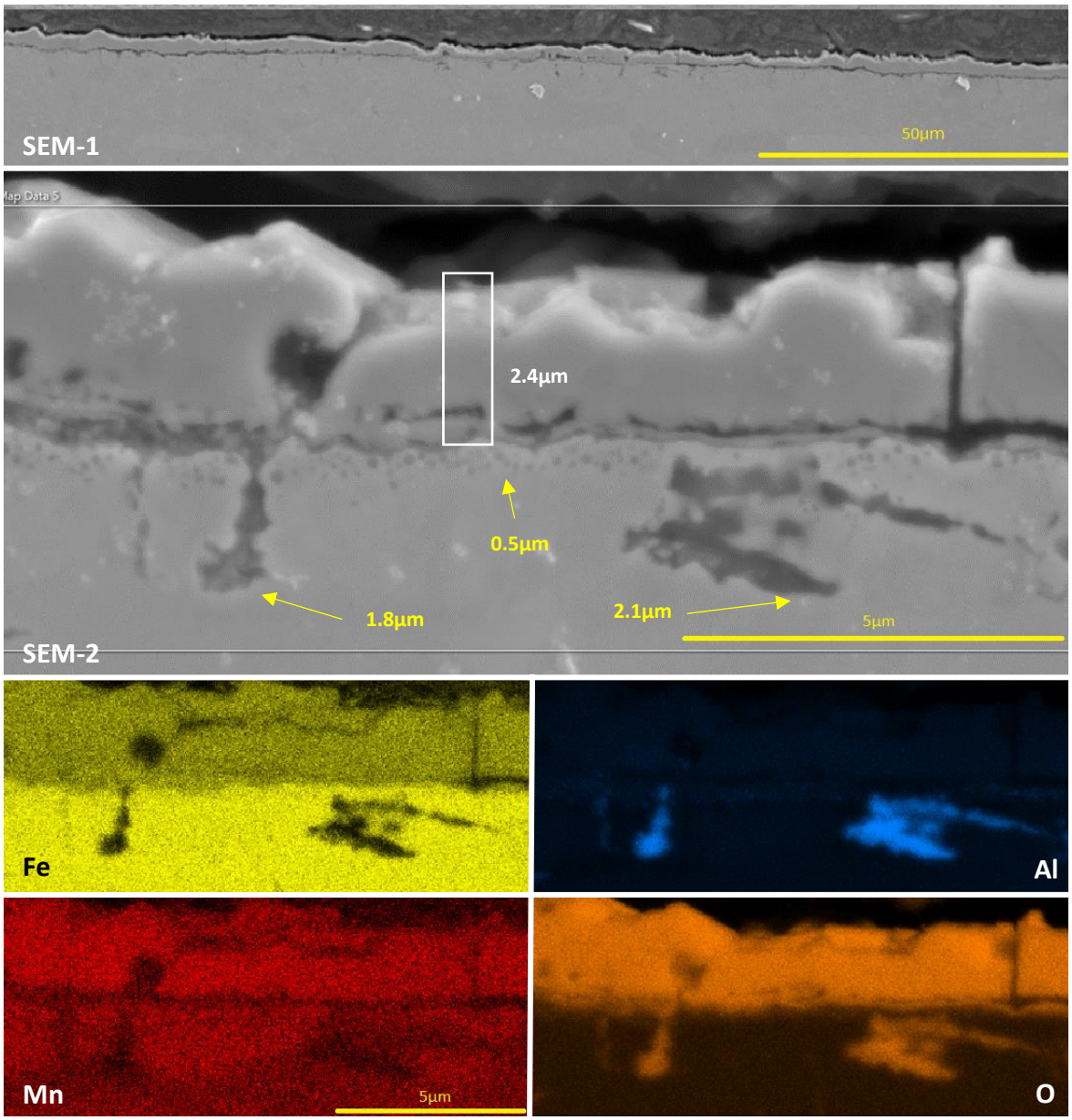

Figure 5.36 Fe-3Al-5Mn, Humidifier 0°C, 20-30sec first run. SEM images of IOZ: SEM-1 - 50µm scale view, SEM-2 - 5µm scale view. EDS Composition mappings of SEM-2 with 5µm scale view for iron, aluminium, manganese, and oxygen. Dark grey on the images are internal oxides, with yellow arrows depicting oxide depths, mean average GB/connected oxide width = 0.31µm, and grain oxide width = 0.09µm

Run #2

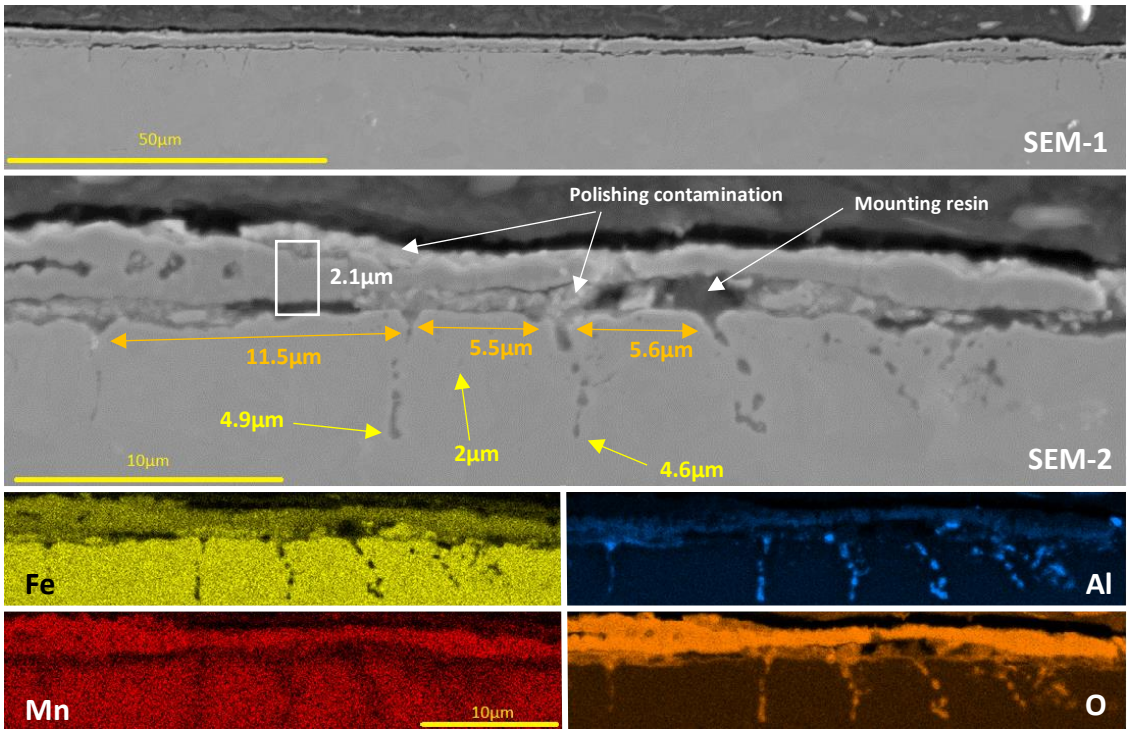

Figure 5.37 Fe-3Al-5Mn, Humidifier 0°C, 20-30sec first run. SEM images of IOZ: SEM-1 - 50µm scale view, SEM-2 - 10µm scale view. EDS Composition mappings of SEM-2 with 10µm scale view for iron, aluminium, manganese, and oxygen. Dark grey on the images are internal oxides, with yellow arrows depicting oxide depths, orange arrows depicting distances between GB/connected oxides, mean average GB/connected oxide width = 0.29µm, and grain oxide width = 0.10µm

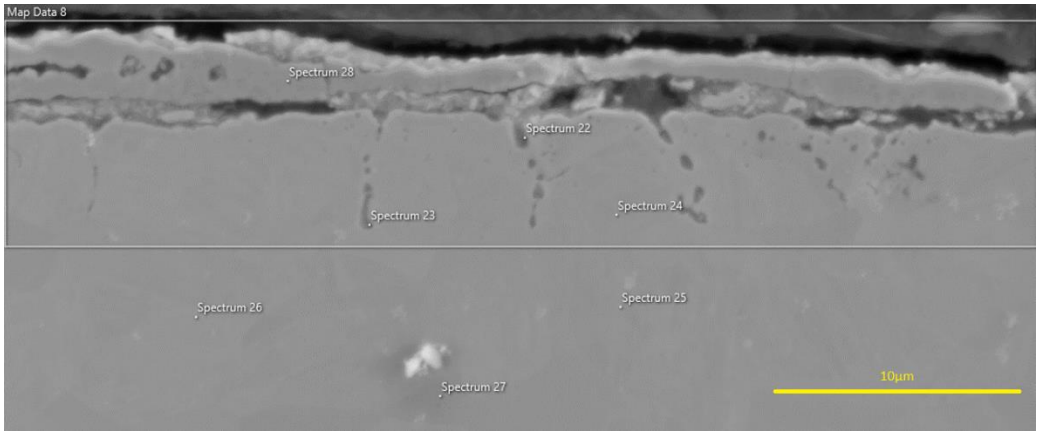

Figure 5.38 Fe-3Al-5Mn, Humidifier 0°C, 20-30sec second run. SEM image 10µm scale view, with spectra analysis

Table 5.7 Fe-3Al-5Mn, Humidifier 0°C, 2:30mins. SEM spectra analysis results, with ThermoCalc volume fraction of oxide calculations for spectra involving oxides

Spectrum #	Element Wt.%						TC Volume % Oxide
	Fe	Al	Mn	O	Si	C	
22	40.1	21.3	2.6	26.5	9.3	0.2	75.36
23	68.3	15.3	2.7	11.7	1.2	0.7	45.59
24	91.2	1.9	4.7	0.5	0.5	1.3	-
25	90.3	2.2	5.2	0.5	0.5	1.2	-
26	90.6	2.2	5.0	0.5	0.5	1.2	-
27	90.1	3.0	4.4	0.6	0.7	1.3	-
28	67.0	1.4	9.6	20.5	0.5	0.9	88.36

Humidifier Temperature 20°C

Site 1

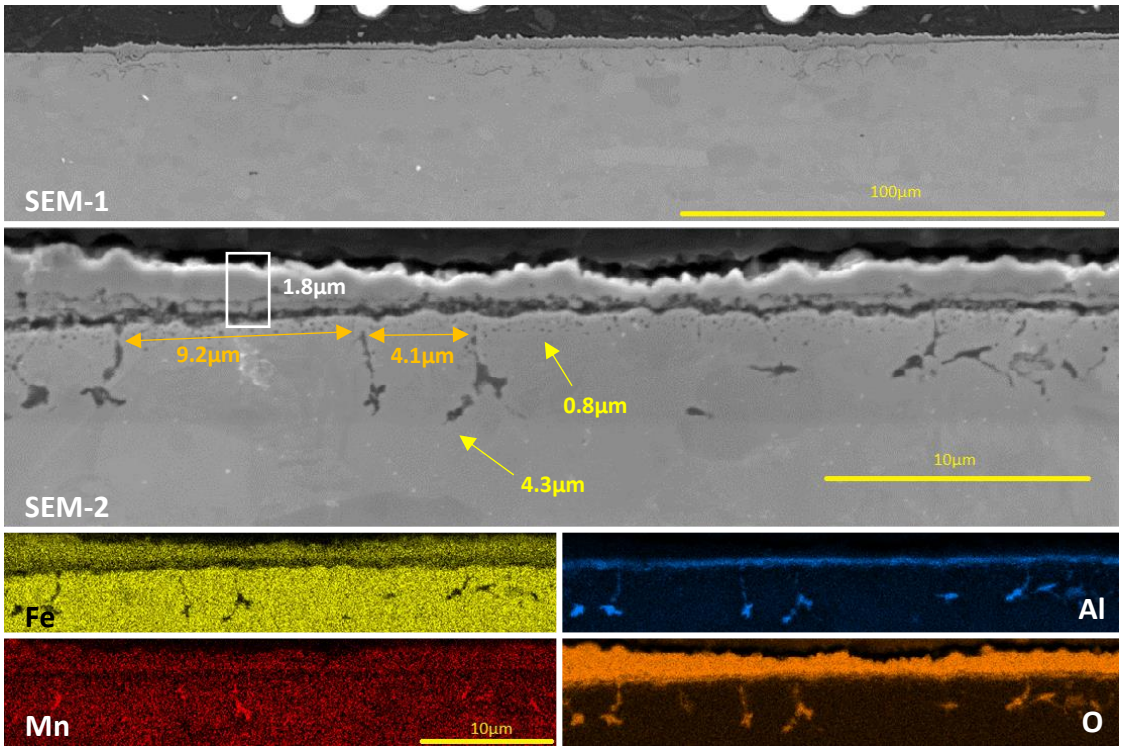

Figure 5.39 Fe-3Al-5Mn, Humidifier 20°C, 20-30sec. SEM images of IOZ: SEM-1 - 100µm scale view, SEM-2 - 10µm scale view. EDS Composition mappings of SEM-2 with 10µm scale view for iron, aluminium, manganese, and oxygen. Dark grey on the images are internal oxides with yellow arrows depicting oxide depths, orange arrows depicting distances between GB/connected oxides, mean average GB/connected oxide width = 0.30µm, and grain oxide width = 0.10µm

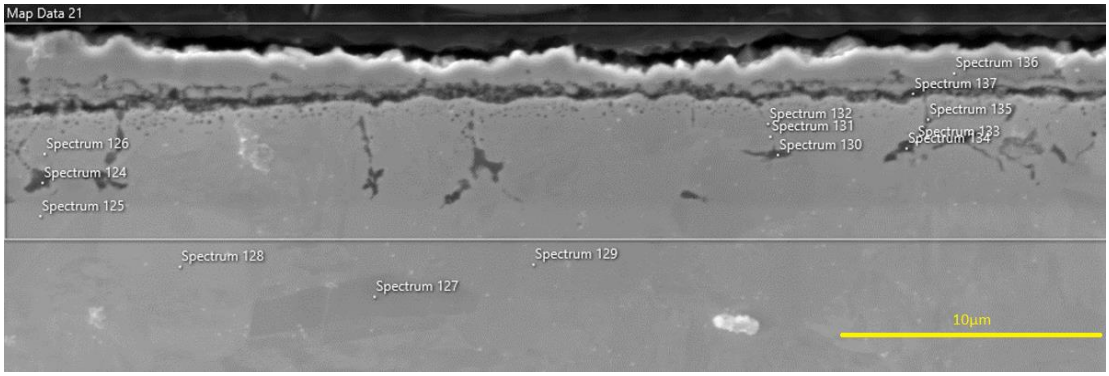

Figure 5.40 Fe-3Al-5Mn, Humidifier 20°C, 20-30sec. SEM image 10µm scale view, with spectra analysis

Table 5.8 Fe-3Al-5Mn, Humidifier 0°C, 2:30mins. SEM spectra analysis results, with ThermoCalc volume fraction of oxide calculations for spectra involving oxides

Spectrum #	Element Wt.%						TC Volume % Oxide
	Fe	Al	Mn	O	Si	C	
124	17.5	34.8	10.2	32	2.3	3.2	81.10
125	93	1.8	2.8	0.2	0.5	1.7	-
126	91	1.8	4.5	0.3	0.5	1.9	-
127	91.4	2.4	3.9	0.3	0.5	1.4	-
128	92.1	2.2	3.8	0.2	0.5	1.3	-
129	91.1	2.5	4.1	0.2	0.5	1.5	-
130	71.7	13.3	1.8	10.3	0.6	2.3	40.24
131	93.8	0.9	2.6	0.5	0.4	1.7	-
132	93.9	0.8	2.3	0.8	0.3	1.9	-
133	75.8	5.5	8	7.5	1.4	1.7	34.25
134	26.3	29.1	9.5	28.1	3.7	3.3	75.32
135	75.1	6.4	9.2	7.3	0.5	1.6	33.72
136	66.8	1.7	6.4	23.1	0.1	1.9	93.80
137	43.9	15.6	4.2	29.8	3.3	3.1	89.08

Site 2

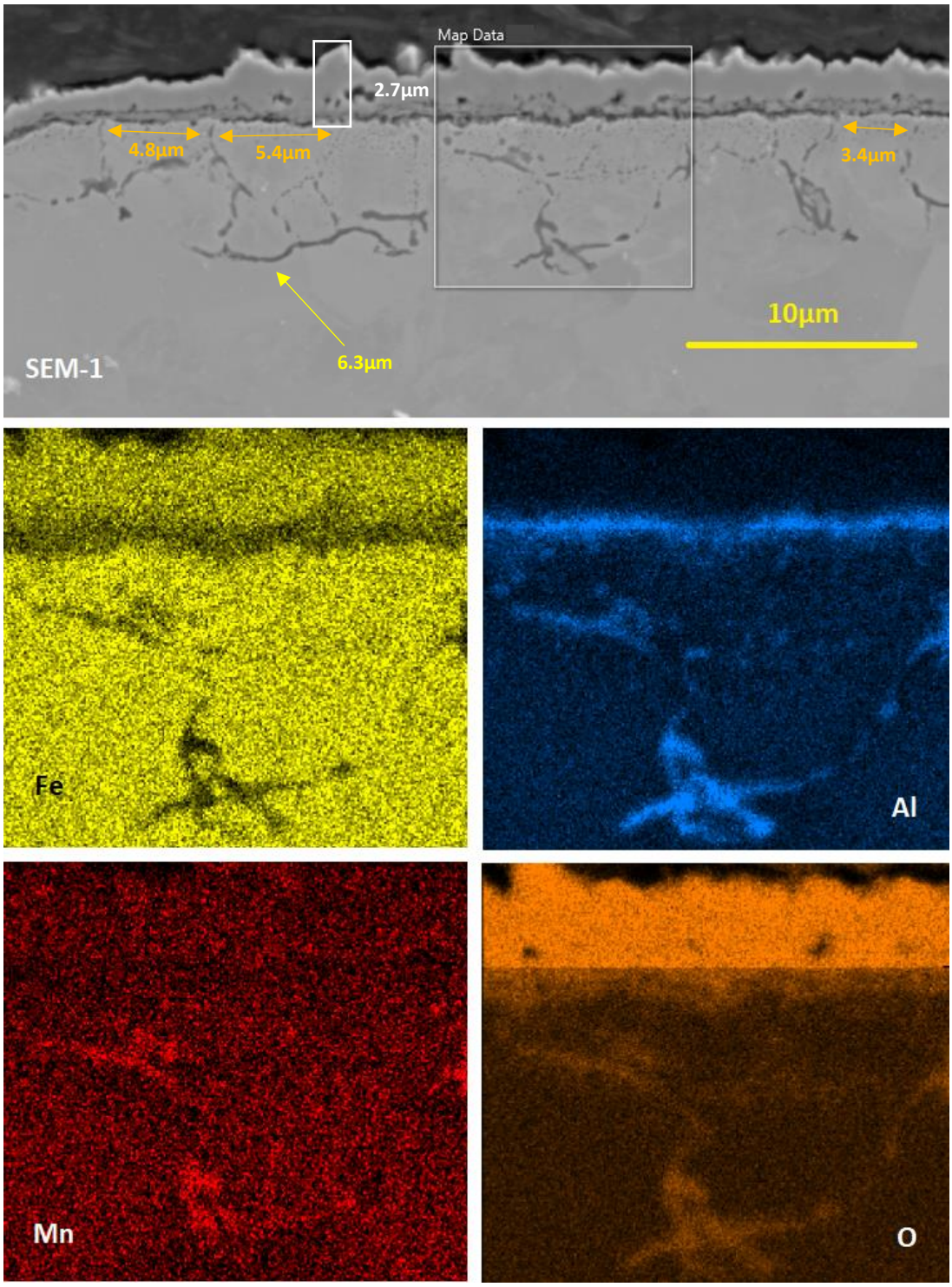

Figure 5.41 Fe-3Al-5Mn, Humidifier 20°C, 20-30sec. SEM images of IOZ: SEM-1 - 100µm scale view, SEM-2 - 10µm scale view. EDS Composition mappings of SEM-2 with 10µm scale view for iron, aluminium, manganese, and oxygen. Dark grey on the images are internal oxides with yellow arrows depicting oxide depths, orange arrows depicting distances between GB/connected oxides, mean average GB/connected oxide width = 0.15µm, and grain oxide width = 0.10µm

Comparison Discussion (Fe-3Al-5Mn 20-30sec)

Due to the short time of this oxidation iteration there is minimal grain oxidation, with very small particles forming directly beneath the scale. Comparisons of the grain-boundary oxidation at the different humidity conditions displays the first formation is of discrete particles and the eventual connection via oxide growth, with other instances of long and thin grain boundary oxides forming likely by very small discrete grain-boundary oxides growing and connecting. This demonstrates that the reaction front is relatively large, and the difference between it and the internal oxidation zone is small, where the reactions occur throughout with the slow penetration of the grains at the lower humidity, and the faster oxidation with the higher humidity results in the faster depletion of solute and the reaction front moving on. This is expected, however due to the internal barrier formation, the reaction kinetics are slowed considerably and will not fully abide common parabolic and linear rates across the full duration of isothermal annealing, it is possible that it follows a logarithmic rate law which is characterised by a high initial reaction rate, reducing to a very low rate [151].

The apparent exclusive internal formation of aluminium oxide is clear that standard thermodynamics is at play with the aluminium oxidising internally where the oxygen concentration is lowest, thus preventing its significant outward diffusion, whereas the manganese atoms diffuse to the surface where the oxygen potential is higher and seemingly sufficient to form the manganese oxide. Comparisons to similar literature are scarce as the very short annealing times are not commonly researched; H. Wang et al. [103] used a mostly ferritic steel under the most similar conditions in the literature closest to this project, with an annealing duration of 1 minute. The samples that underwent the highest oxygen exposure exhibited recrystallised ferrite below the external oxides, and internal oxides both within this zone and below it. The authors do not mention where the images of the samples were taken so it is unclear what to compare, although the most likely scenario is within a grain because of the relatively homogeneous oxidation and the small image size (up to 3µm x 3µm, with oxides extending 1.2µm). The oxides below the ferrite recrystallised zone extend inward linearly, this is somewhat comparable to this sample and conditions discussed here in this subsection as the grain oxides extend inward fed by the adjacent grain boundary.

5.2.2.2 Fe-5Al-5Mn (Dual Phase)

5:00 minutes Isothermal Oxidation Time

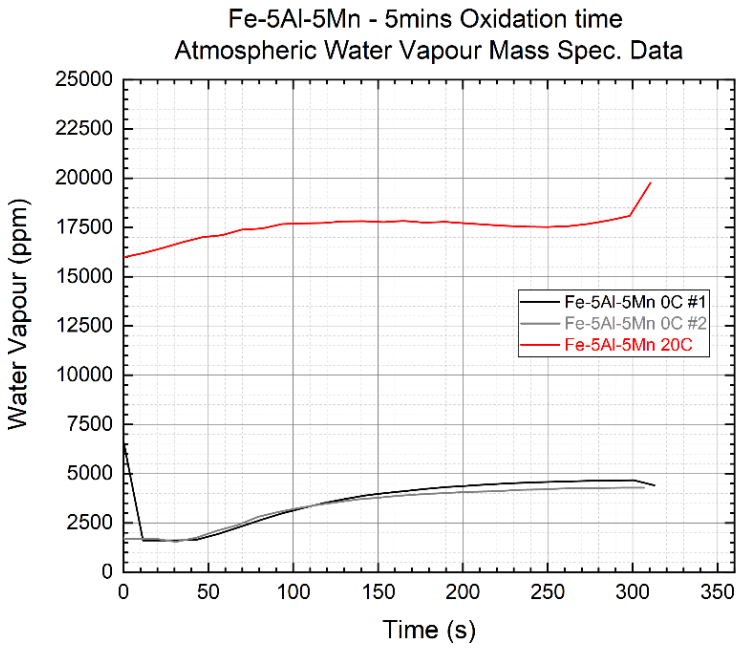

Figure 5.42 Fe-5Al-5Mn 5mins Oxidation time, Mass Spec. readings of chamber gas - Water vapour content (ppm)

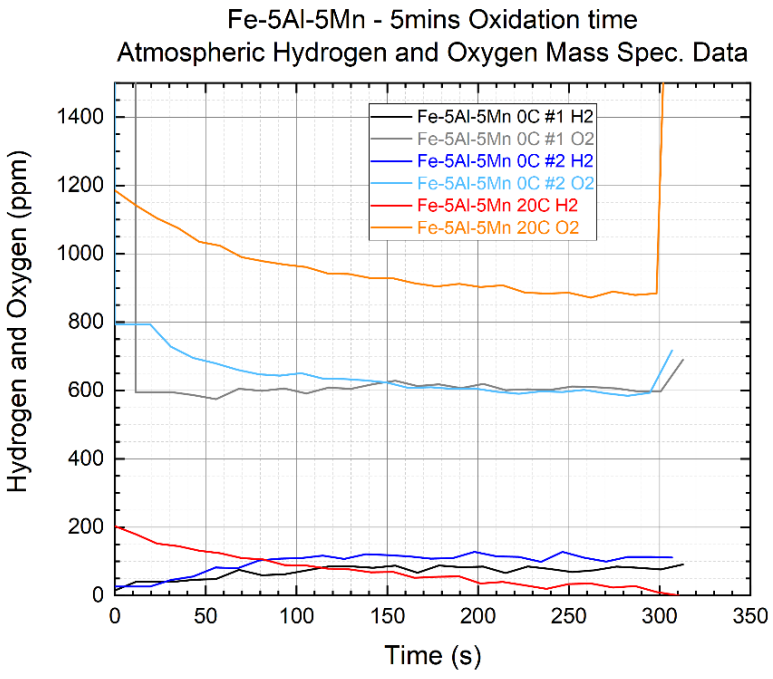

Figure 5.43 Fe-5Al-5Mn 5mins Oxidation time, Mass Spec. readings of chamber gas – Hydrogen and Oxygen content (ppm)

Humidifier Temperature 0°C

Run #1

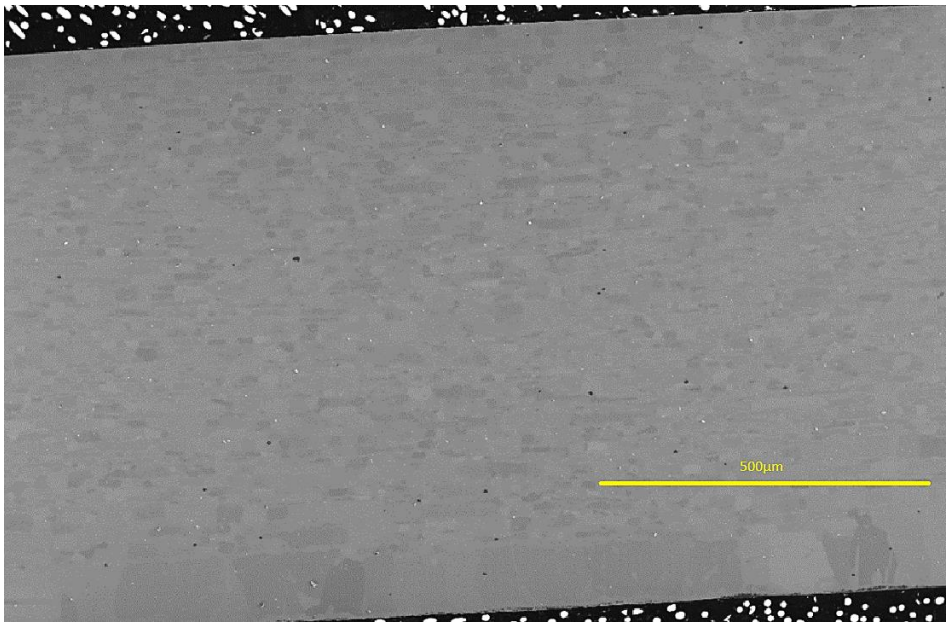

Figure 5.44 Fe-5Al-5Mn, Humidifier 0°C, 5mins first run. SEM image 500µm scale view. (Sharpness and contrast increased – 20%)

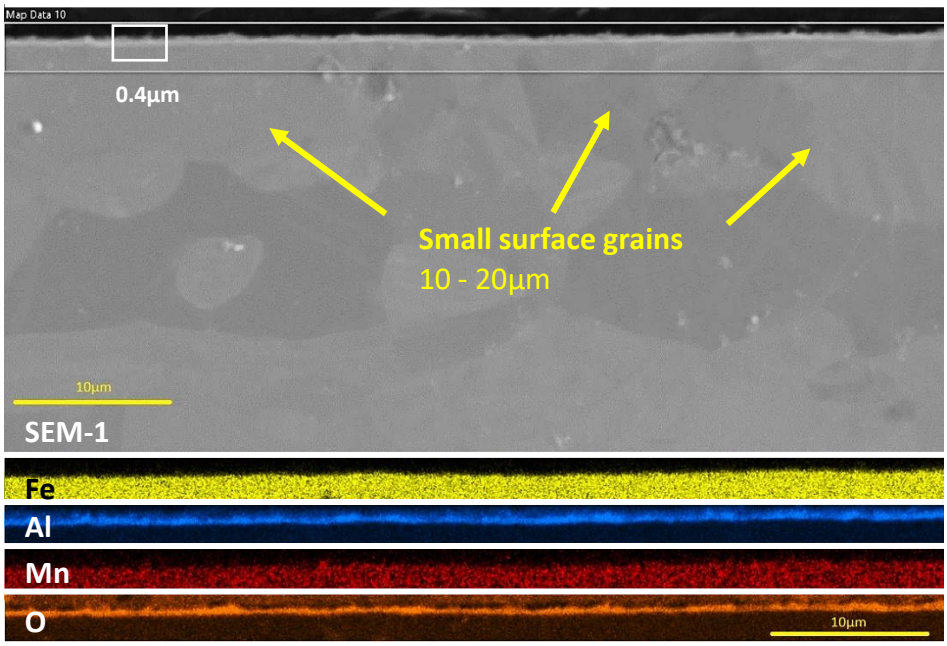

Figure 5.45 Fe-5Al-5Mn, Humidifier 0°C, 5mins first run. SEM images of IOZ: SEM-1 - 10µm scale view with map data area shown (yellow box). EDS Composition mappings of SEM-1 with 10µm scale view for iron, aluminium, manganese, and oxygen.

Run #2

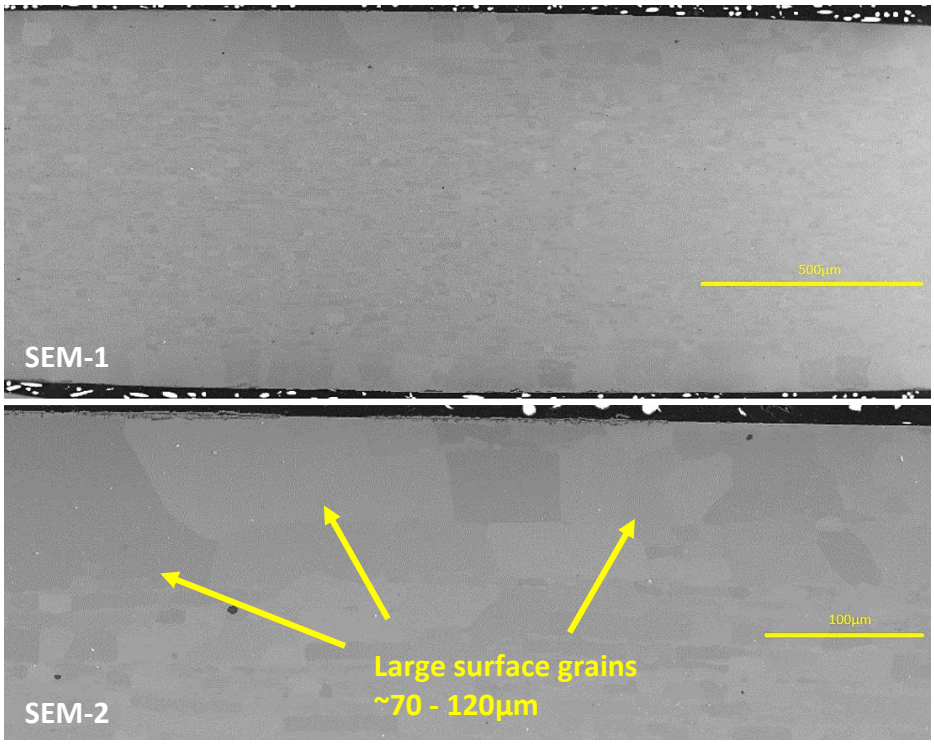

Figure 5.46 Fe-5Al-5Mn, Humidifier 0°C, 5mins second run. SEM images - comparison of grain sizes: SEM-1 - 500µm scale view, SEM-2 - 100µm scale view. (Sharpness and contrast increased- 20%)

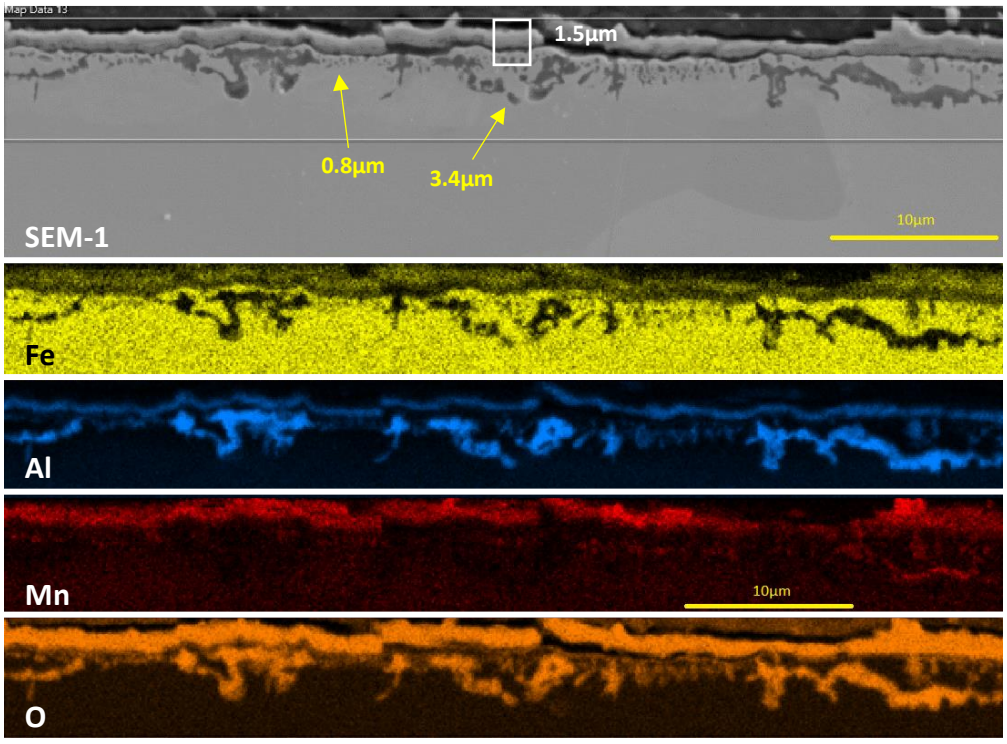

Figure 5.47 Fe-5Al-5Mn, Humidifier 0°C, 5mins first run. SEM images of IOZ: SEM-1 - 10µm scale view. EDS Composition mappings of SEM-1 with 10µm scale view for iron, aluminium, manganese, and oxygen.

Comparison of Fe-5Al-5Mn H-0C shows stark differences, Run #1 forms an exclusive protective alumina scale with no internal oxidation; whereas Run #2 does form the alumina scale but it is not protective and internal oxidation results. The atmospheric water vapour contents were consistent; therefore the only difference is the microstructure as shown with the labels. The differences presented here are a good example of the effect of grain size on internal oxidation as the Fe-5Al-5Mn steel grade has shown it is able to form the protective alumina layer, therefore the flux of the solute must be affected whereby large grains have a reduced volume of high-diffusivity pathways, subsequently reducing the aluminium flux to the surface.

Humidifier Temperature 20°C

Site 1

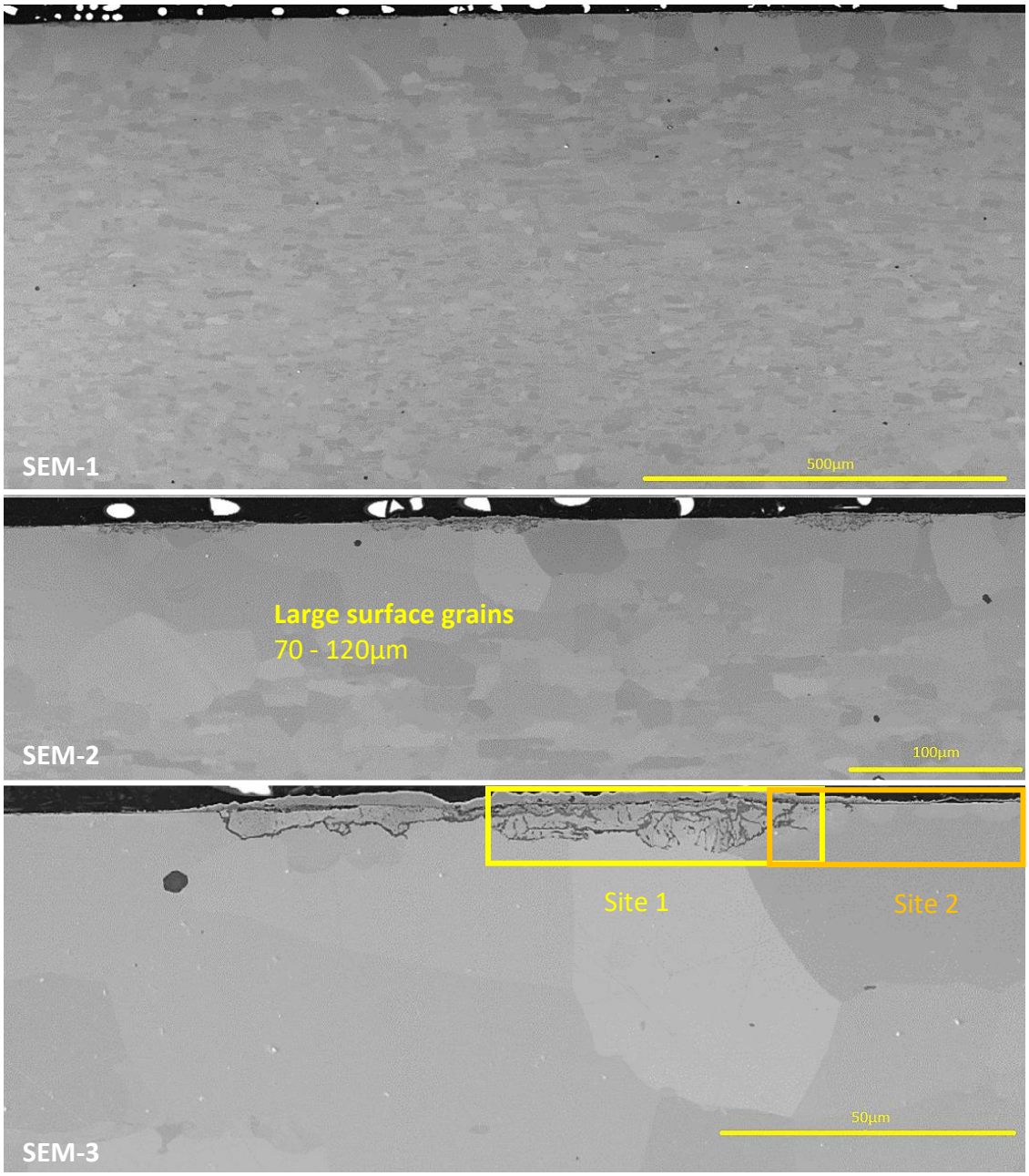

Figure 5.48 Fe-5Al-5Mn, Humidifier 20°C, 5mins. SEM images showing oxidation behaviour at different scales on large grain sizes: SEM-1 - 500µm scale view, SEM-2 - 100µm scale view, SEM-3 - 50µm scale view with labels showing, large surface grains, and Site 1 (yellow box) and Site 2 (orange box). (Sharpness and contrast increased 20%)

Site 1

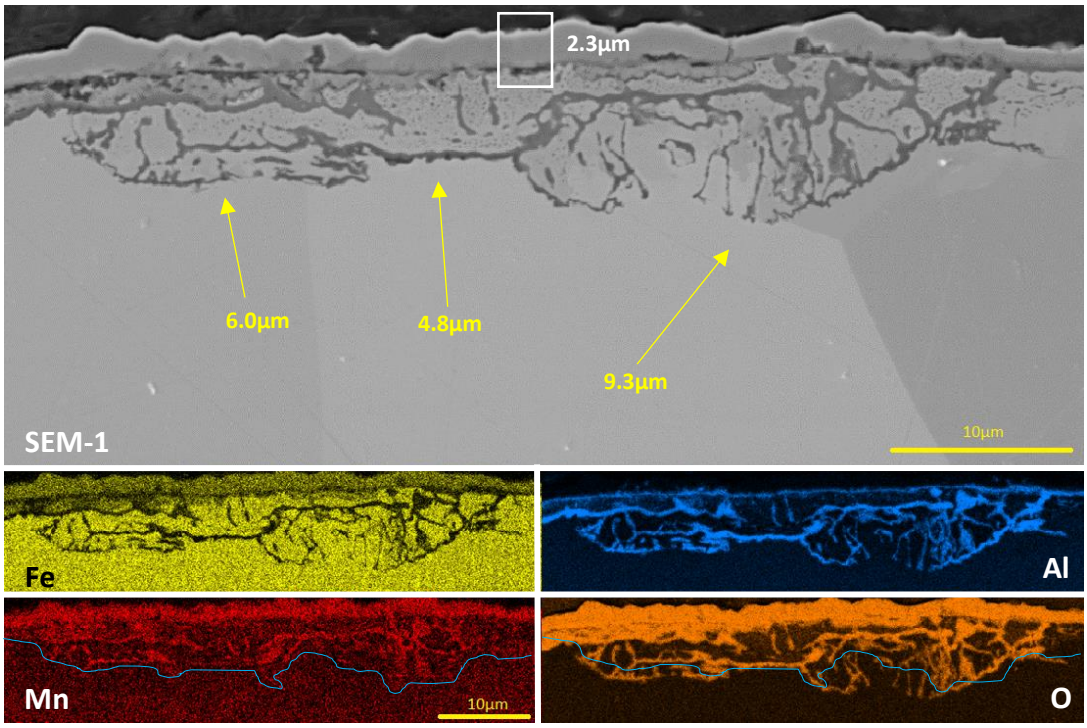

Figure 5.49 Fe-5Al-5Mn, Humidifier 20°C, 5mins, Site 1. SEM images of IOZ: SEM-1 - 10µm scale view. EDS Composition mappings of SEM-1 with 10µm scale view for iron, aluminium, manganese, and oxygen. Dark grey on the images are internal oxides with yellow arrows depicting oxide depths, orange arrows depicting distances between GB/connected oxides, and blue lines showing boundary between alumina and manganese aluminate, mean average GB/connected oxide width = 0.40µm, and grain oxide width = 0.15µm

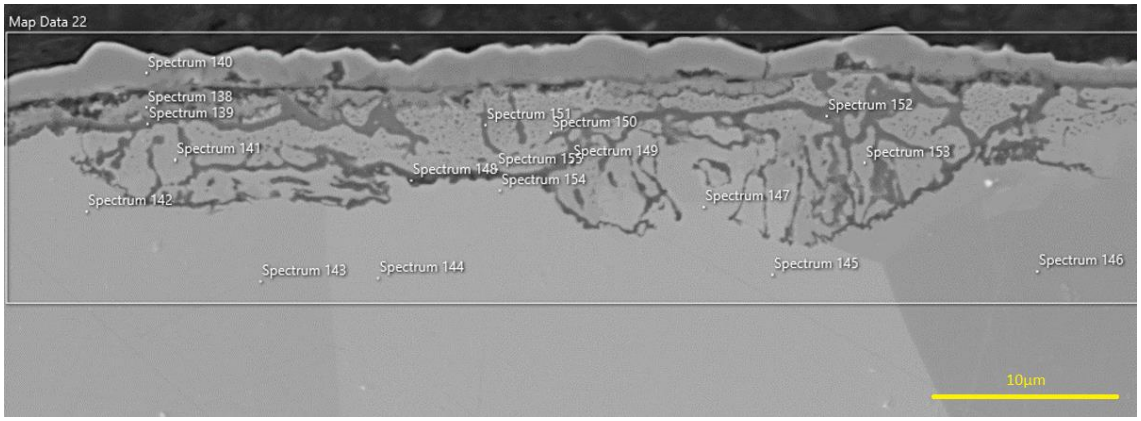

Figure 5.50 Fe-5Al-5Mn, Humidifier 20°C, 5mins, Site 1. SEM image 10µm scale view, with spectra analysis

Table 5.9 Fe-5Al-5Mn, Humidifier 20°C, 5mins. SEM spectra analysis results, with ThermoCalc volume fraction of oxide calculations for spectra involving oxides

Spectrum #	Element Wt.%						TC Volume % Oxide
	Fe	Al	Mn	O	Si	C	
138	55.7	5.9	11.1	25.0	0.6	1.7	93.63
139	23.5	25.4	18.8	29.7	1.2	1.6	85.70
140	56.9	0.3	17.4	23.7	0.1	1.6	95.51
141	95.4	0.8	1.7	0.3	0.2	1.5	-
142	92.5	2.6	2.5	0.3	0.5	1.6	-
143	91.2	3.0	3.5	0.3	0.5	1.5	-
144	91.4	3.0	3.4	0.3	0.5	1.4	-
145	91.8	2.8	2.9	0.3	0.5	1.7	-
146	90.7	3.4	3.7	0.3	0.5	1.4	-
147	92.8	1.7	2.3	0.4	0.4	2.5	-
148	86.7	5.8	1.4	3.8	0.6	1.6	18.10
149	13.4	28.4	22.8	31.7	2.2	1.6	88.00
150	84.7	3.7	4.8	4.7	0.5	1.6	23.34
151	91.0	1.7	2.2	3.3	0.3	1.5	17.61
152	19.0	28.3	18.6	30.7	1.9	1.5	85.55
153	89.5	3.0	1.6	3.8	0.3	1.7	19.15
154	93.2	2.5	2.0	0.3	0.5	1.5	-
155	87.9	3.1	3.0	4.0	0.3	1.6	20.19

Site 2

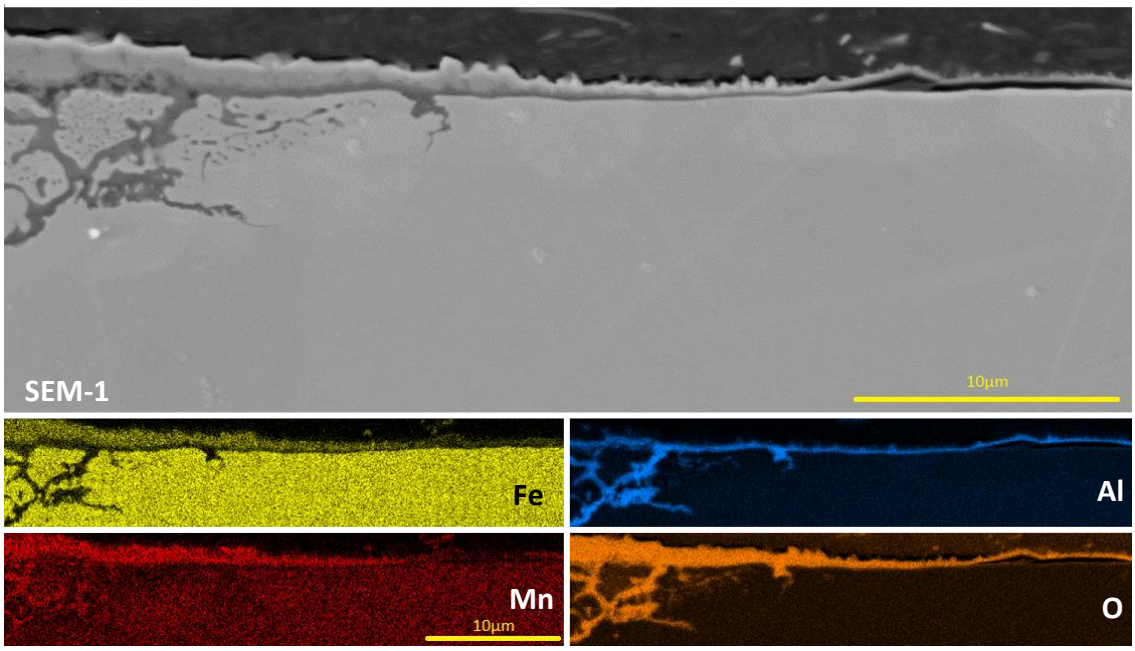

Figure 5.51 Fe-5Al-5Mn, Humidifier 20°C, 5mins, Site 2. SEM images of IOZ: SEM-1 - 10µm scale view. EDS Composition mappings of SEM-1 with 10µm scale view for iron, aluminium, manganese, and oxygen. Dark grey on the images are internal oxides.

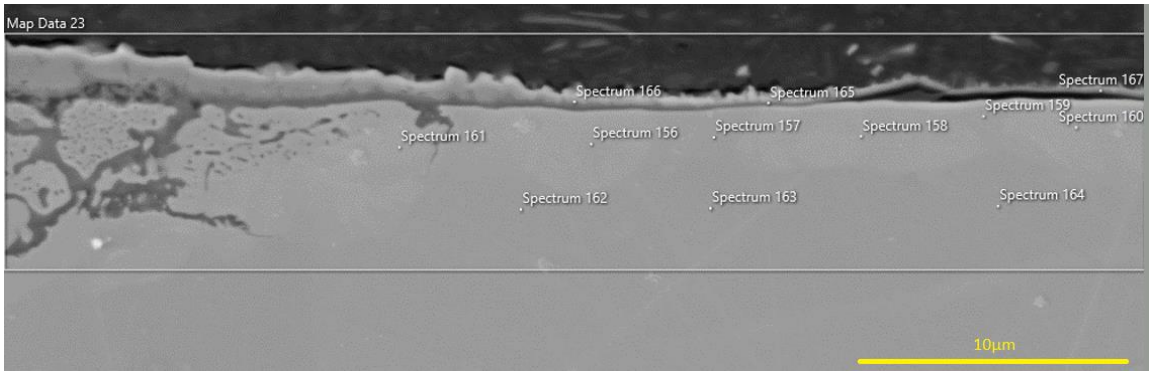

Figure 5.52 Fe-5Al-5Mn, Humidifier 20°C, 5mins, Site 2. SEM image 10µm scale view, with spectra analysis

Table 5.10 Fe-5Al-5Mn, Humidifier 20°C, 5mins, Site 2. SEM spectra analysis results

Spectrum #	Element Wt.%						TC Volume % Oxide
	Fe	Al	Mn	O	Si	C	
156	88.6	3.1	5.2	0.2	0.5	2.4	-
157	90.3	3.5	4.1	0.2	0.5	1.4	-
158	88.6	2.9	5.4	0.2	0.5	2.4	-
159	89.9	3.7	4.1	0.2	0.6	1.5	-
160	89.4	3.0	4.7	0.2	0.5	2.2	-
161	90.1	2.6	4.3	0.2	0.5	2.3	-
162	90.6	3.3	3.8	0.2	0.5	1.5	-
163	89.8	3.8	4.0	0.2	0.5	1.6	-
164	89.0	3.9	4.7	0.2	0.6	1.6	-
165	37.3	16.3	13.3	24.6	0.2	8.2	72.62
166	42.5	11.0	17.3	25.4	0.2	3.7	86.24
167	45.7	16.8	8.2	16.5	0.4	12.4	44.74

Comparison Discussion (Fe-5Al-5Mn 5mins)

The main differences between the iterations of Fe-5Al-5Mn for the 5mins oxidation duration are the grain sizes, with larger grains and a subsequent reduction in the volume of high-diffusivity pathways connected to the surface the sample fails to produce a protective alumina scale. The samples that are oxidised internally exhibit few discrete oxides with most of the solute flux contributing to the growth of the existing particles which occurs near the surface surrounding the grain-boundary. This is interesting as it could imply that the oxygen-to-aluminium diffusivity ratio in the

grain-boundary being greater than the oxygen-to-aluminium diffusivity ratio in the grain if not other effect is present.

The difference between the humidity conditions provides a good representation of internal oxidation which is similar to results seen by Bott [106] for Fe-Al steels, showing the higher oxygen flux of H-20C leading to greater oxygen penetration and the position of the internal barrier is altered accordingly, as expected. However, the oxides form with an unusual shape which appears to form without any specific direction and not specifically following the grain-boundaries - likely due to the homogenous nature of the crystal exhibiting few defects and minute localised thermodynamic conditions promoting nucleation and growth, displaying random internal oxide growth from a macroscopic perspective.

H-20C Site 1 (Figure 5.49) shows isolated internal oxidation sites separated by regions of protective scales without internal oxidation, seemingly the regions of protective scales have a higher proportion of grain-boundaries, as can be seen in SEM-2.

2:30 minutes Isothermal Oxidation Time

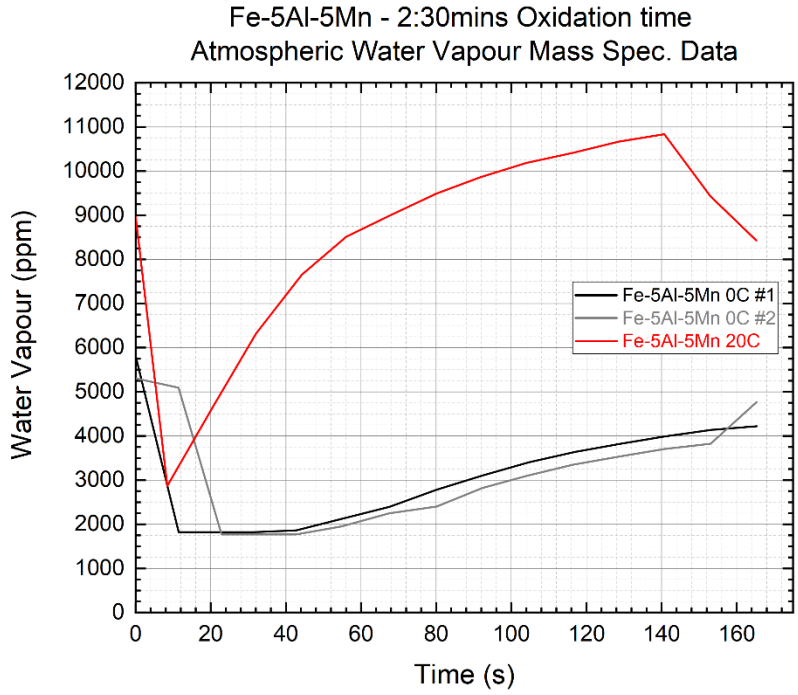

Figure 5.53 Fe-5Al-5Mn 2:30mins Oxidation time, Mass Spec. readings of chamber gas - Water vapour content (ppm)

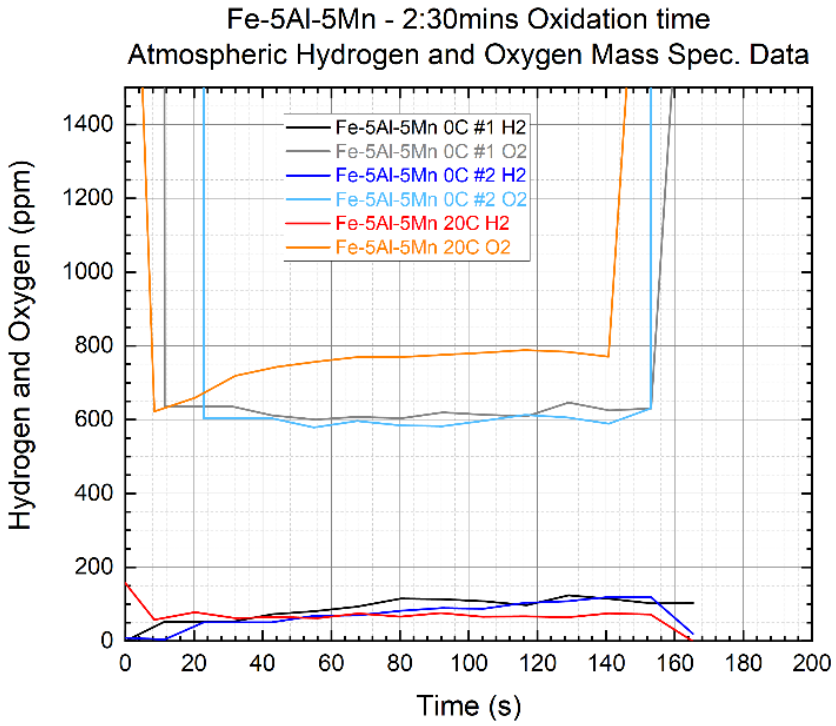

Figure 5.54 Fe-5Al-5Mn 5mins Oxidation time, Mass Spec. readings of chamber gas – Hydrogen and Oxygen (ppm)

Humidifier Temperature 0°C

Run #1

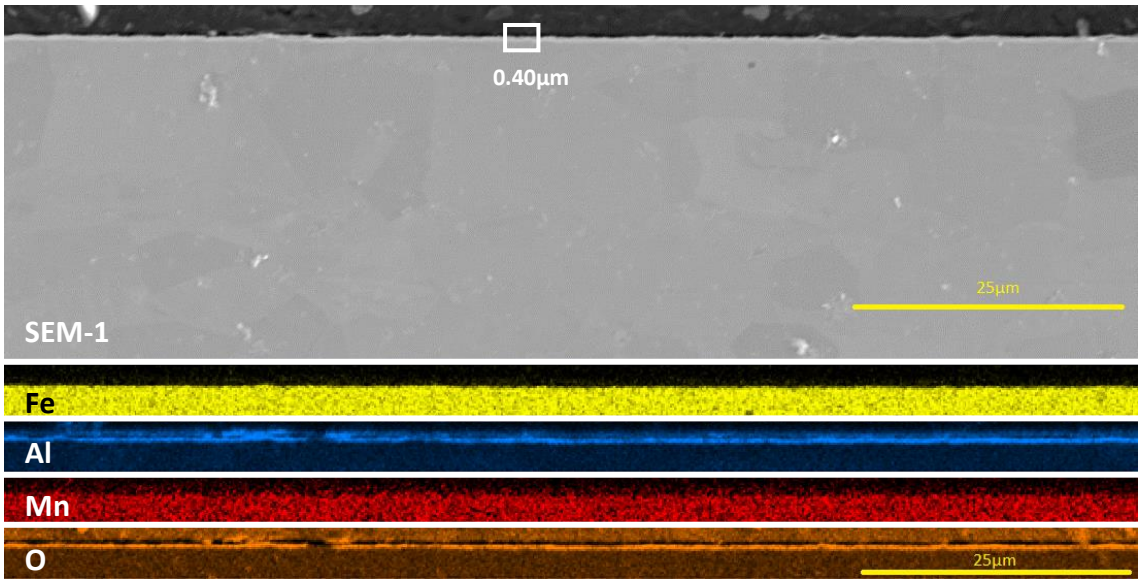

Figure 5.55 Fe-5Al-5Mn, Humidifier 0°C, 2:30mins first run. SEM images of IOZ: SEM-1 - 25µm scale view. EDS Composition mappings of SEM-1 with 25µm scale view for iron, aluminium, manganese, and oxygen

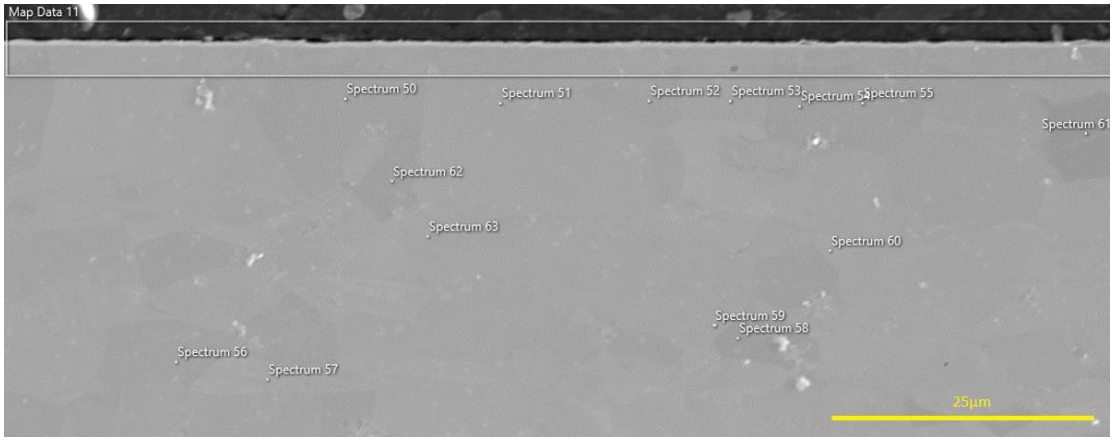

Figure 5.56 Fe-3Al-5Mn, Humidifier 0°C, 20-30sec second run. SEM image 10µm scale view, with spectra analysis

Table 5.11 Fe-5Al-5Mn, Humidifier 0°C, 20-30sec second run. SEM spectra analysis results

Spectrum #	Element Wt.%						TC Volume % Oxide
	Fe	Al	Mn	O	Si	C	
50	89.1	4.0	4.7	0.4	0.6	1.1	-
51	89.1	4.0	4.7	0.6	0.6	1.0	-
52	89.2	4.1	4.4	0.6	0.6	1.1	-
53	89.6	4.0	4.5	0.5	0.5	0.9	-
54	88.8	4.1	5.0	0.4	0.6	1.1	-
55	88.9	4.0	4.9	0.5	0.7	1.1	-
56	89.6	4.0	4.5	0.5	0.6	0.9	-
57	88.1	3.4	6.0	0.4	0.5	1.7	-
58	88.6	4.1	5.1	0.4	0.6	1.2	-
59	88.3	3.4	5.7	0.4	0.5	1.8	-
60	88.5	3.4	5.5	0.5	0.5	1.7	-
61	90.3	4.1	3.8	0.2	0.6	1.0	-
62	88.7	4.2	4.7	0.4	0.7	1.3	-
63	88.4	3.5	5.5	0.4	0.7	1.6	-

Run #2

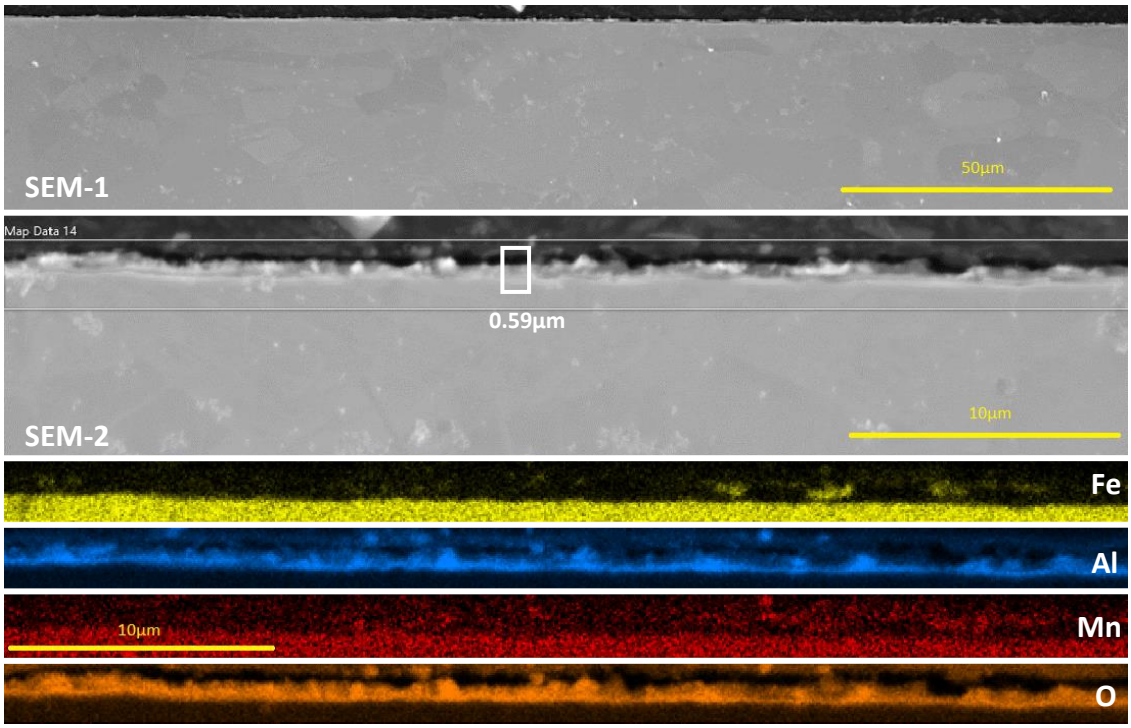

Figure 5.57 Fe-5Al-5Mn, Humidifier 0°C, 2:30mins second run. SEM images of IOZ: SEM-1 - 50µm scale view, SEM-2 - 10µm scale view. EDS Composition mappings of SEM-2 with 10µm scale view for iron, aluminium, manganese, and oxygen

Humidifier Temperature 20°C

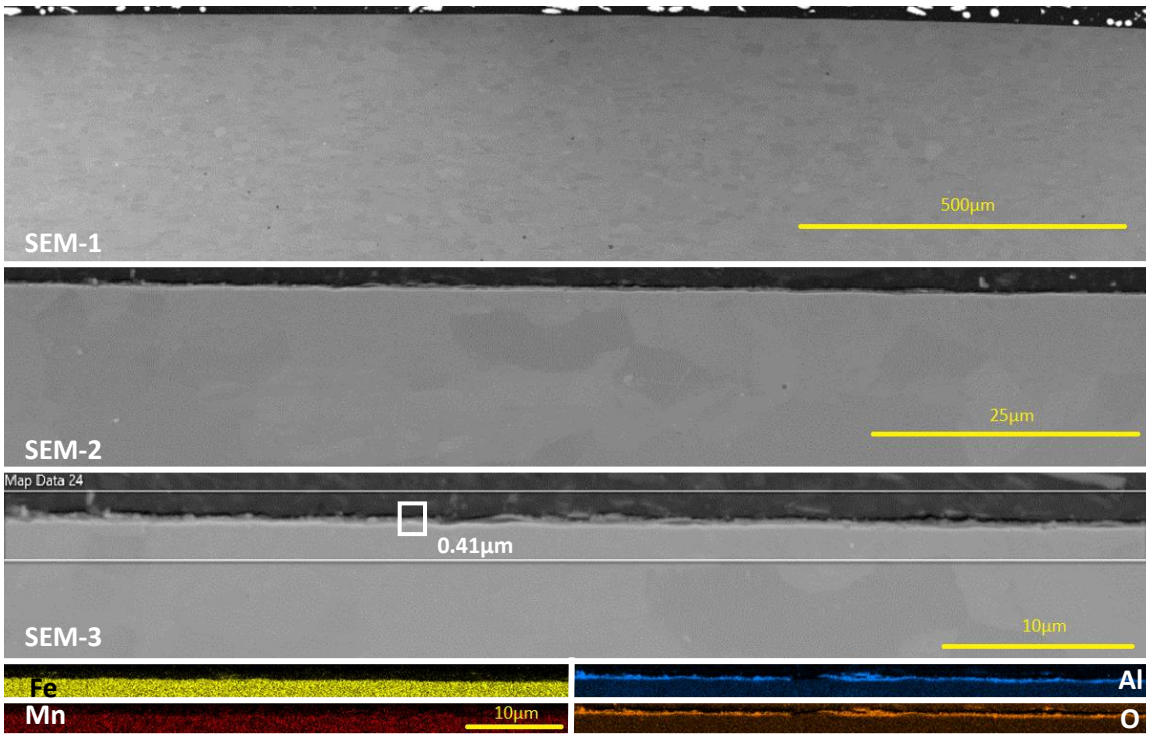

Figure 5.58 Fe-5Al-5Mn, Humidifier 20°C, 2:30mins. SEM images of IOZ: SEM-1 - 500µm scale view, SEM-2 - 25µm, SEM-3 - 10µm. EDS Composition mappings of SEM-3 with 10µm scale view for iron, aluminium, manganese, and oxygen

Comparison Discussion (Fe-5Al-5Mn 2:30mins)

All iterations of the Fe-5Al-5Mn 2:30mins conditions formed exclusive alumina scales that were dense enough to prevent internal oxidation, likely due to the relatively high volume of grain-boundaries (small grain sizes: 10 - 20µm) supplying a flux of aluminium at or above Wagner's Criterion for both humidity conditions. It is interesting to note that the differences between the diffusivities and compositions of the phases of the dual phase steel (ferrite and austenite) are less significant than the grain-boundary volume ratio which sees the differing oxygen fluxes resulting in the very similar protective alumina scales. This could be due to a certain grain's diffusivities and its solute concentrations influence is a minority portion of the conglomeration of the larger area's total flux, as the diffusivity of the grain-boundary is orders of magnitude higher than the grain. For example, an aluminium atom occupying a grain-boundary site at a depth of 50µm would reach the surface before

an aluminium atom 10µm into a grain; as grains are much larger than grain-boundaries and act as reservoirs, the larger area's total flux is a compilation and less dependent on any local individual crystal's phase; which is also important when considering two or more adjacent phases close to the surface, as the solute flux from the bulk would be more important than the intergranular solute composition and the oxidation of adjacent different phase grains would be more visible at much lower solute concentrations.

20-30 seconds Isothermal Oxidation Time

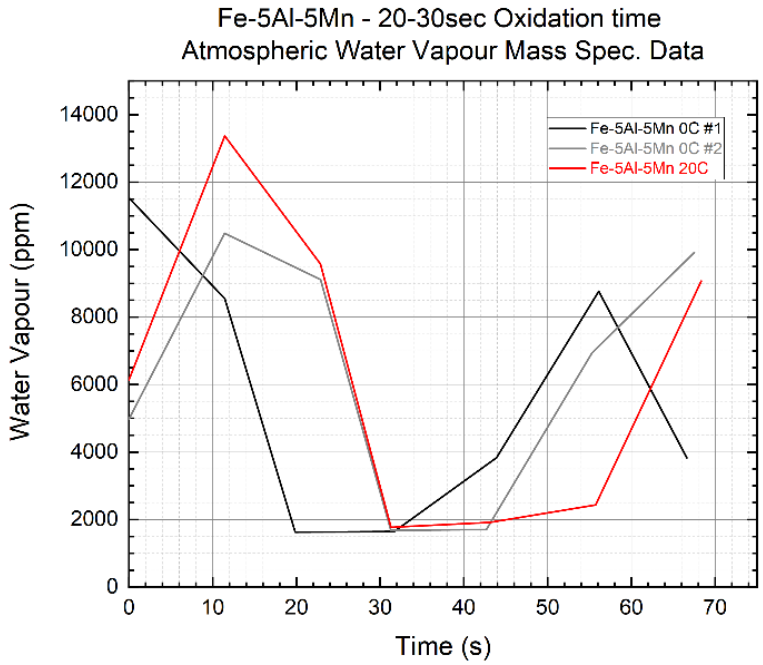

Figure 5.59 Fe-5Al-5Mn 2:30mins Oxidation time, Mass Spec. readings of chamber gas - Water vapour content (ppm)

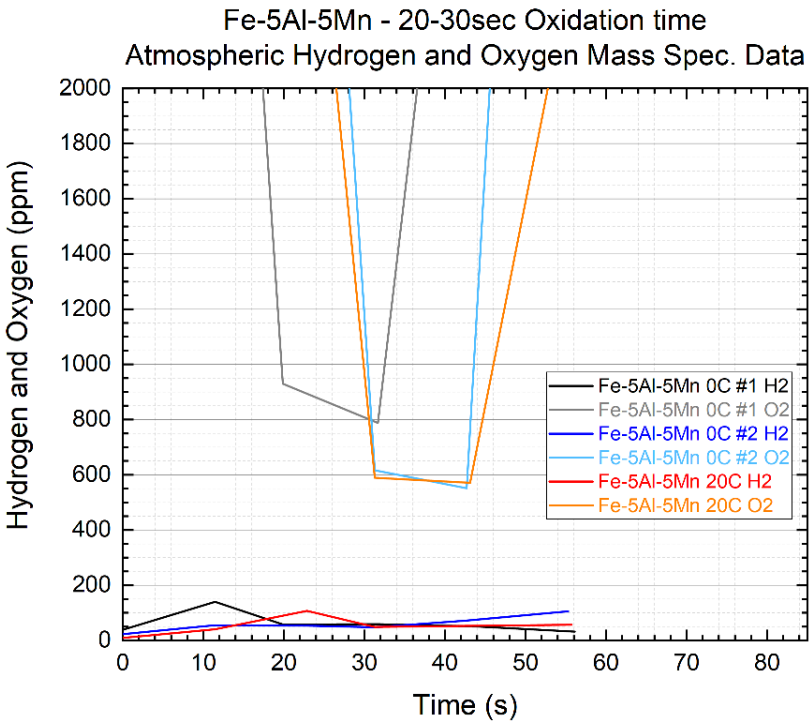

Figure 5.60 Fe-5Al-5Mn 2:30mins Oxidation time, Mass Spec. readings of chamber gas – Hydrogen and Oxygen content (ppm)

Humidifier Temperature 0°C

Run #1

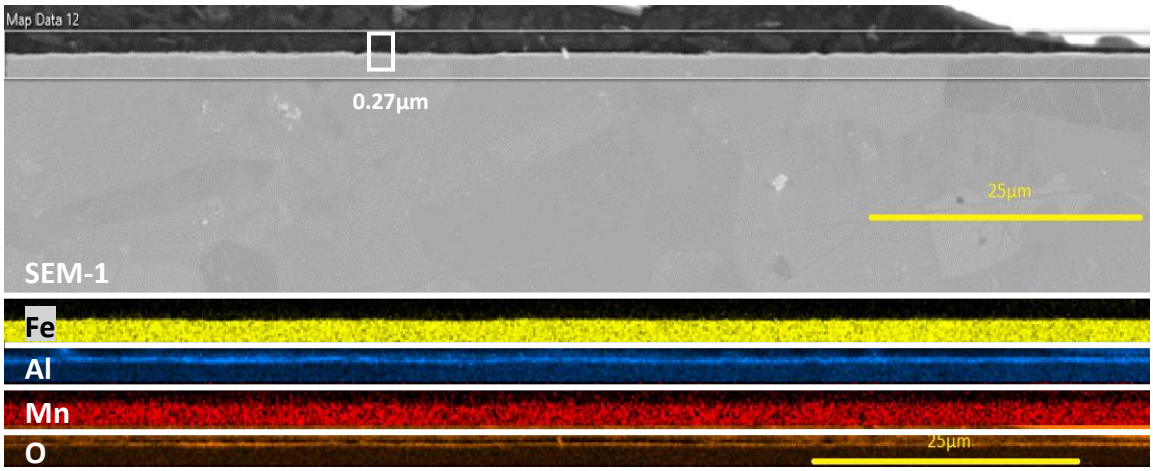

Figure 5.61 Fe-5Al-5Mn, Humidifier 0°C, 20-30sec first run. SEM images of IOZ: SEM-1 - 25µm scale view. EDS Composition mappings of SEM-1 with 25µm scale view for iron, aluminium, manganese, and oxygen

Run #2

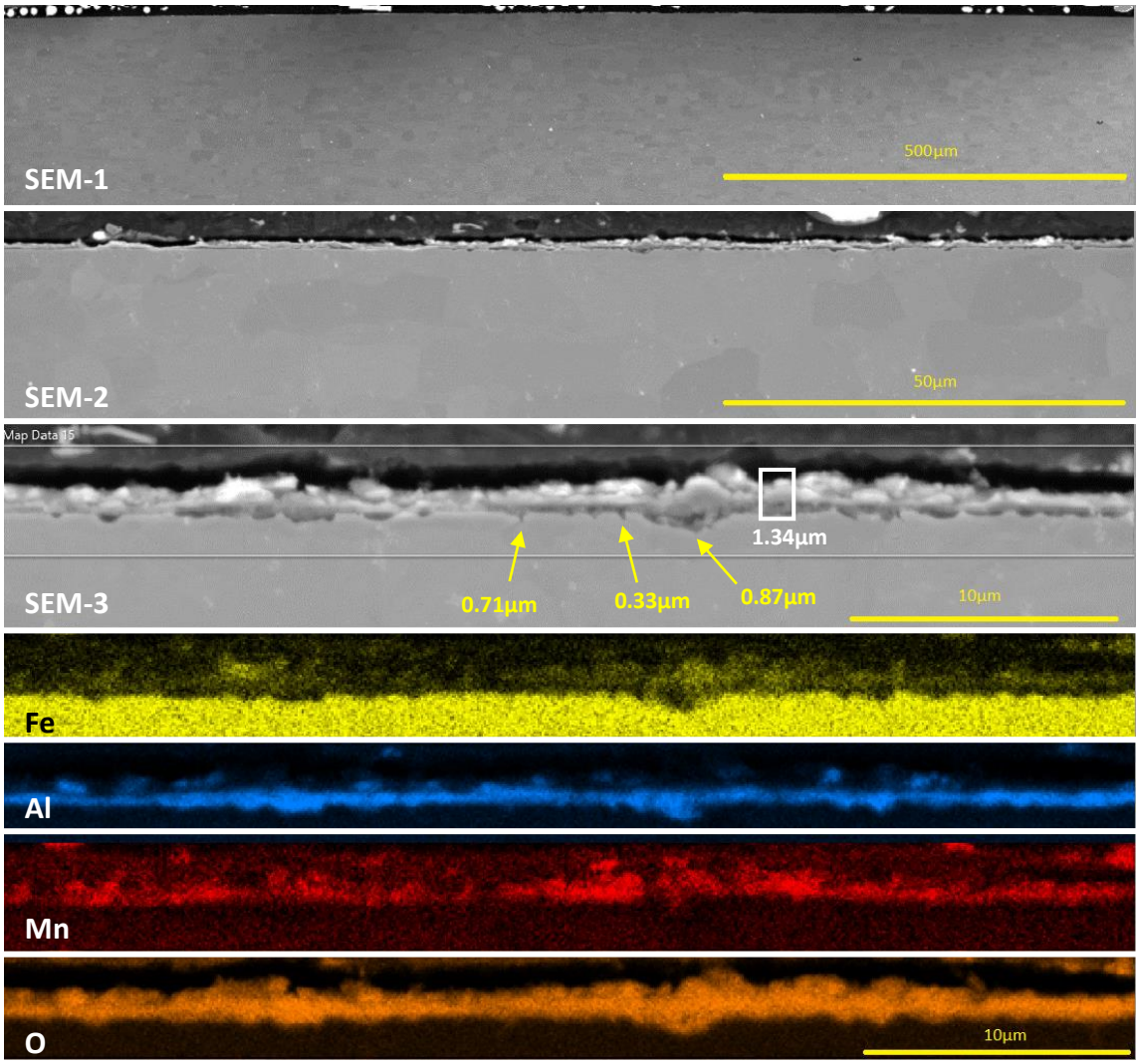

Figure 5.62 Fe-5Al-5Mn, Humidifier 0°C, 20-30sec second run. SEM images of IOZ: SEM-1 - 500µm scale view, SEM-2 - 50µm scale view, SEM-3 - 10µm scale view. EDS Composition mappings of SEM-3 with 10µm scale view for iron, aluminium, manganese, and oxygen. Yellow arrows depict oxide depths

Humidifier Temperature 20°C

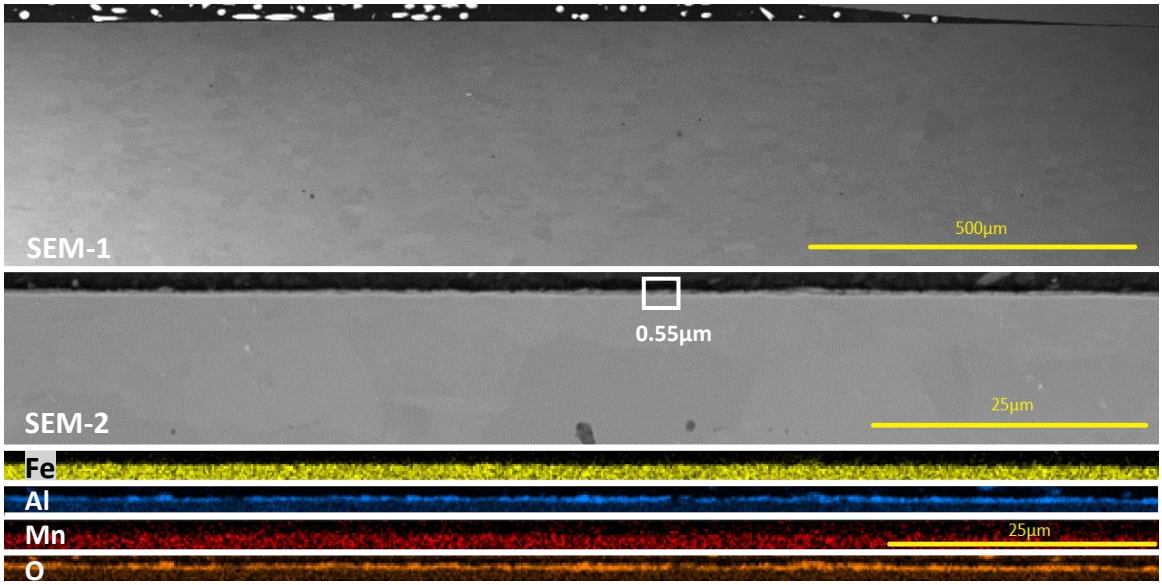

Figure 5.63 Fe-5Al-5Mn, Humidifier 20°C, 20-30sec. SEM images of IOZ: SEM-1 - 500µm scale view, SEM-2 - 25µm. EDS Composition mappings of SEM-2 with 25µm scale view for iron, aluminium, manganese, and oxygen

Comparison Discussion (Fe-5Al-5Mn 20-30sec)

Small grains (10-20µm) at the surface have resulted in protective alumina scales with a complete absence of internal oxides in all samples. However, H-0C Run #2 is not an exclusive alumina scale, with some manganese oxides above indicating that the flux of the solutes is sufficient at these small grain sizes to adhere to Wagner's criterion but not always exclusively form the alumina scale.

5.2.2.3 Fe-6Al-15Mn (Austenite)

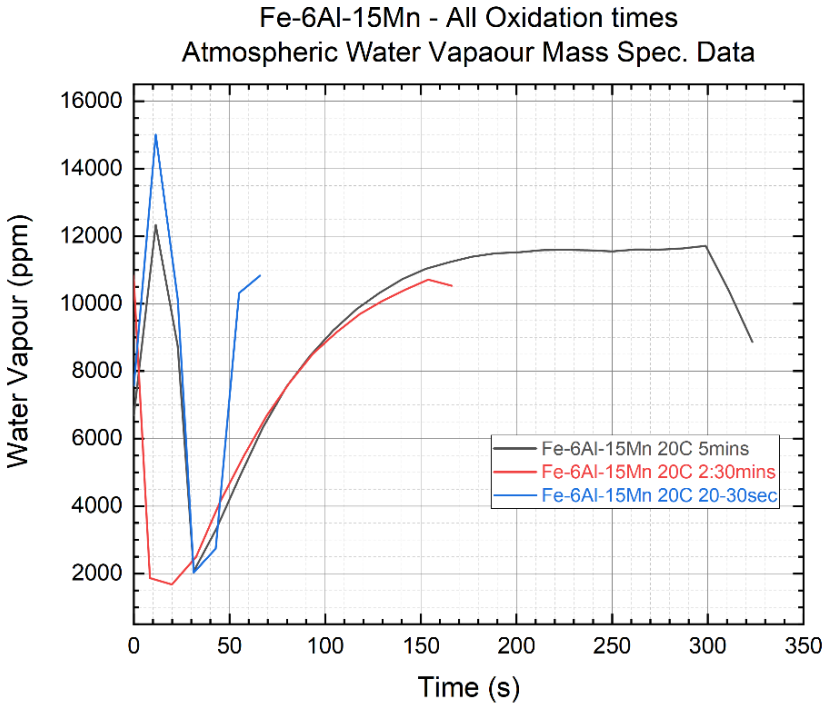

Figure 5.64 Fe-6Al-15Mn 5mins Oxidation time, Mass Spec. readings of chamber gas - Water vapour content (ppm)

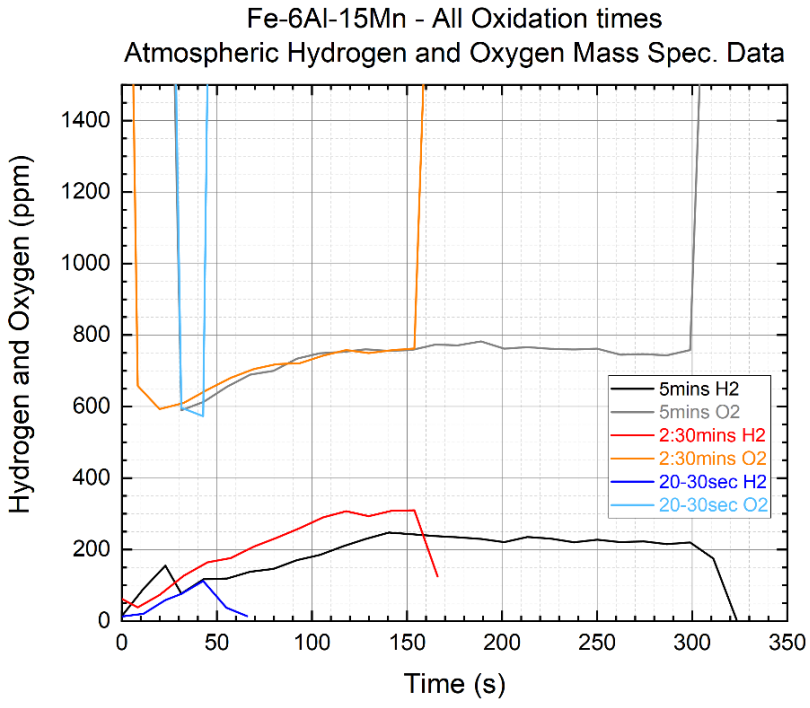

Figure 5.65 Fe-6Al-15Mn 5mins Oxidation time, Mass Spec. readings of chamber gas - Hydrogen and Oxygen content (ppm)

5 minutes Isothermal Oxidation Time

Humidifier Temperature 20°C:

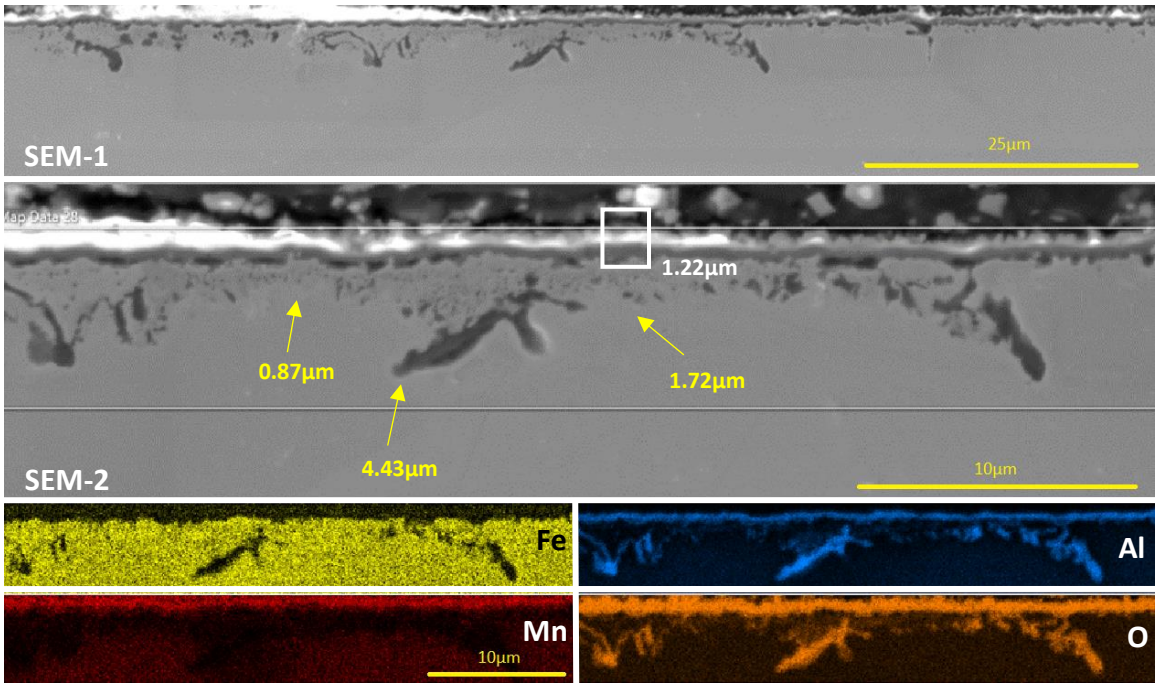

Figure 5.66 Fe-6Al-15Mn, Humidifier 20°C, 5mins. SEM images of IOZ: SEM-1 - 25µm scale view, SEM-2 - 10µm. EDS Composition mappings of SEM-2 with 10µm scale view for iron, aluminium, manganese, and oxygen. Dark grey on the images are internal oxides, with yellow arrows depicting oxide depths, mean average GB/connected oxide width = 0.52µm, and grain oxide width = 0.12µm

2:30 minutes Isothermal Oxidation Time

Humidifier Temperature 20°C:

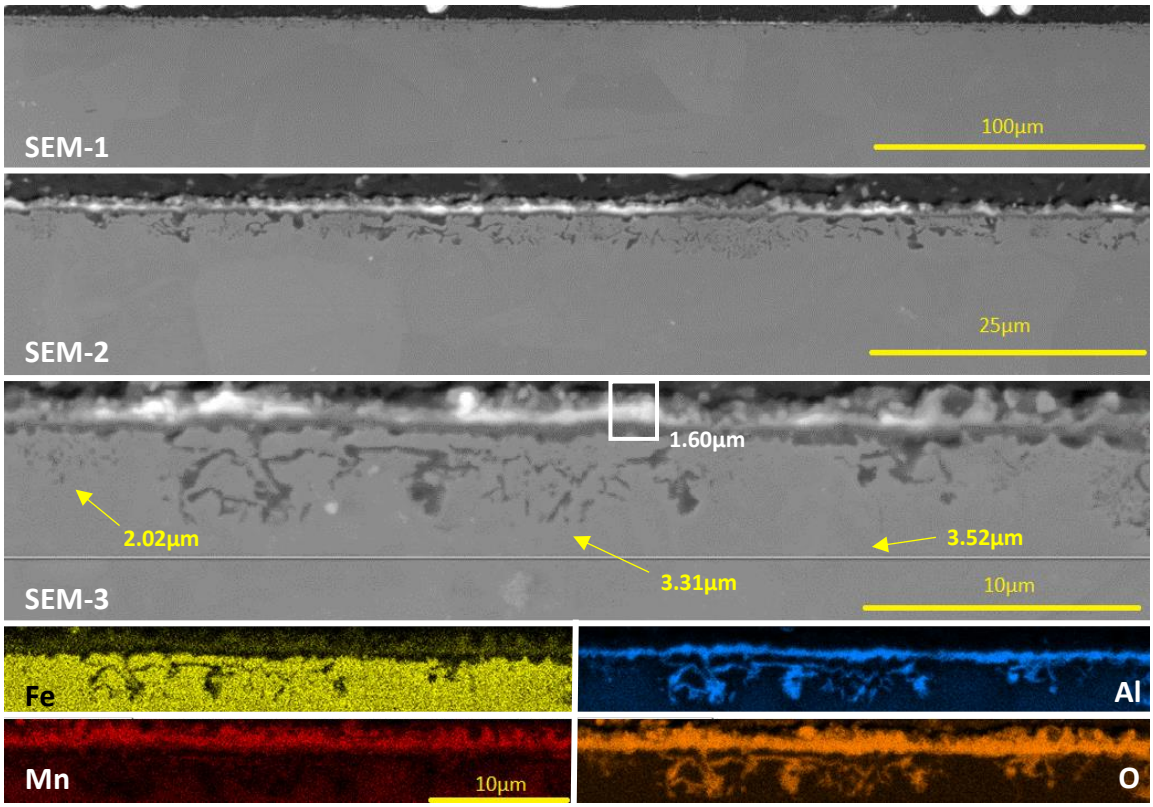

Figure 5.67 Fe-6Al-15Mn, Humidifier 20°C, 2:30mins. SEM images of IOZ: SEM-1 - 100µm scale view, SEM-2 - 25µm, SEM-3 - 10µm. EDS Composition mappings of SEM-3 with 25µm scale view for iron, aluminium, manganese, and oxygen. Dark grey on the images are internal oxides, with yellow arrows depicting oxide depths, mean average GB/connected oxide width = 0.31µm, and grain oxide width = 0.13µm

20-30 seconds Isothermal Oxidation Time

Humidifier Temperature 20°C:

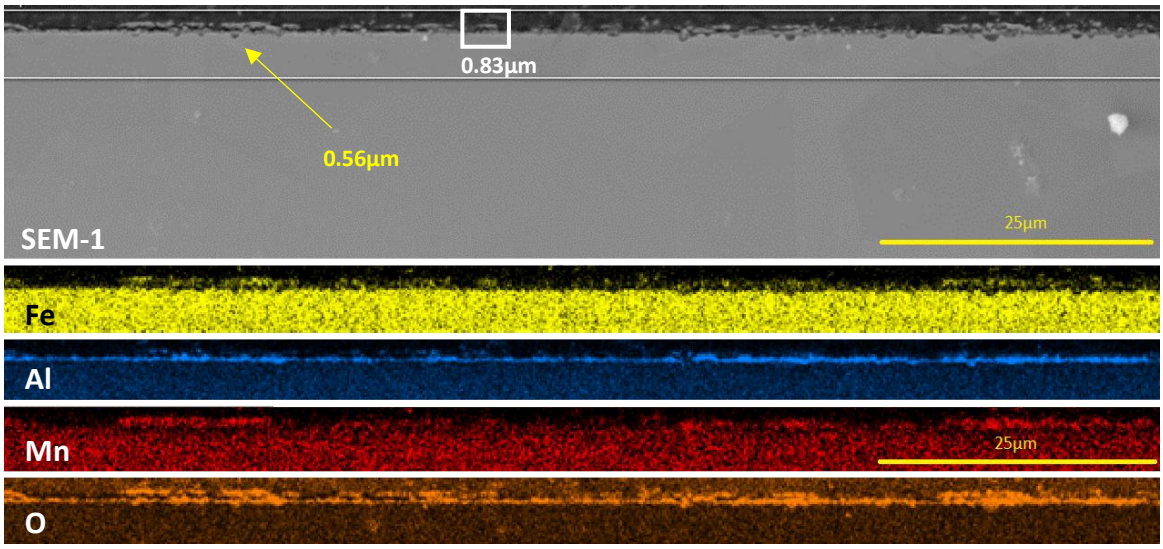

Figure 5.68 Fe-6Al-15Mn, Humidifier 20°C, 20-30sec. SEM images of IOZ: SEM-1 - 25µm scale view. EDS Composition mappings of SEM-1 with 25µm scale view for iron, aluminium, manganese, and oxygen. Dark grey on the images are internal oxides, with yellow arrows depicting oxide depths, mean average internal oxide size = 0.40µm

Comparison Discussion (Fe-6Al-15Mn All Oxidation Times)

As this austenitic steel grade was oxidised only at a humidifier setting of 20°C, this comparison section focusses on the difference in oxidation time. Also, consideration is given for the spallation of surface oxides on this Fe-6Al-15Mn steel grade that consistently occurred.

This steel grade formed a layered manganese and alumina scale which is comparatively less protective [112] than an exclusive alumina scale because of the increased stoichiometric and structural defects, exposing the substrate to oxygen penetration. The formation of the scale occurs first via alumina's fast formation with manganese oxide forming above, with the formation of internal alumina occurring with the growth of precipitated particles and subsequent connection, this can be seen in Figure 5.66 where there is extensive internal oxidation, there is also many very small grain oxide particles surrounding the large grain boundary oxides, occurring as seen before due to the difference in grain and grain-boundary diffusivities. The grain-boundary oxides are grown from the flux of aluminium to the site which is of higher concentration than the dual phase steels. Due to the absence of the ferritic grains in this austenitic steels compared to the dual phase steels, the grain-boundary diffusion speeds are likely lower due to the packing density of the atoms in the crystals subsequently affecting the grain-boundary packing density which could explain the lack of the protective scale in kinetic terms.

5.3 Experimental Data Discussion

This section focusses on the discussion of the experimental data along with the theories mentioned before in Section 2. The investigation into the internal oxidation of low density dual phase Fe-Al-Mn-C steels is the main objective of this project, with many different individual variables present that can inflict significant changes to the oxidation behaviour, this discussion is for the consideration of the reader to the difficulties in isolating these variables during internal oxidation and the further complications in comparing results with the limited relevant published literature.

5.3.1 Fe-3Al-5Mn

Connecting grain boundary oxides are common in this steel's IOZ, with many smaller particles spread throughout the grains, although the oxides do not always neatly follow the grain boundary which could be due to almost equal aluminium and oxygen fluxes [87]. The thermodynamic stabilities of the internal oxides forming alumina (Al_2O_3) first, then oxidising further with manganese to form manganese aluminate ($MnAl_2O_4$) can be seen in most of the different iterations of experimentation on the Fe-3Al-5Mn sample, only in the 20-30 seconds isothermal oxidation times did the manganese aluminate not always form as the concentration of oxygen within the IOZ had not yet passed the formation concentration. These initial stages of Fe-3Al-5Mn oxidation show that the grain-boundary oxidation starts with discrete particles that combine as they grow - suggesting that the oxygen permeability at this stage is significantly larger than the solute's [5, 7, 87]. The effective diffusivity of oxygen can be seen in this sample's condition iterations, where the reduction in diffusion speed eventually leads to the formation of the internal oxide barrier [89]. Although this internal oxide barrier appears to form and prevent oxygen penetrating the substrate further, it could be growing inwards towards the bulk, like an external oxide scale can slowly grow inwards [5]. The depth of the internal barrier appears to vary slightly with surface oxygen concentration, although the local phase fraction will also play a role and this is not a concrete conclusion on internal barrier depth.

5.3.2 Fe-5Al-5Mn

When internal oxidation did occur in the Fe-5Al-5Mn sample with small grains near the surface, there was not a clear orientation suggesting similar aluminium and oxygen flux [87, 89] from the lateral growth of the particles. The formed oxides were largely absent of manganese, from a thermodynamic standpoint this means that the concentration of aluminium was high enough to appropriate all the available oxygen and not reach the manganese aluminate formation concentration, as this sample had an increased aluminium concentration this is expected. The differences in this steel grade's surface grain sizes suggests that the aluminium concentration is sufficient to form protective alumina scale but the increased size of the grains leads to a lower high-diffusivity pathway volume and the effective flux of aluminium is reduced, unable to form a dense enough scale [7, 152, 153]. Also, with large grains the internal oxidation consisted of mainly $MnAl_2O_4$ stoichiometry, indicating the lack of fast-diffusivity pathways also allowed depletion of aluminium in the IOZ.

This sample had an increased proportion of ferrite when compared to Fe-3Al-5Mn which likely supported the high aluminium flux [47-52, 125-135]. This bring into question again the role of the packing efficiency on the diffusion of oxygen and aluminium and which element's diffusion speed benefits most, this will be discussed further below.

5.3.3 Fe-6Al-15Mn

The Fe-6Al-15Mn sample also shows a lack of internal manganese aluminate, due to the formation of obstructive oxides produced by the high concentration of aluminium and the higher flux of aluminium itself compared to Fe-3Al-5Mn and Fe-5Al-5Mn; this is supported by the unusually thick morphology of the oxides and their position close to the surface that do not extend far into the bulk.

The fully austenitic microstructure is thought to be the kinetic determining factor in the formation of a relatively thick manganese oxide layer compared to Fe-5Al-5Mn where both formed the thin alumina scale even at slightly lower aluminium concentrations. The thermodynamic determining factor is believed to be a porous layer of alumina and subsequent oxygen penetration that depletes the surface region

below the scale of aluminium, and the diffusion of manganese occurs across the scale to the higher oxygen potential without aluminium present. This porosity [125-135] or lack of density of the alumina scale could be due to the relatively slow diffusion speed of austenite. Perhaps at the surface the high manganese content prevents a coherent alumina scale from forming due to minute manganese oxide formation, with additional aluminium material not diffusing to the surface and not reducing the manganese oxide thereby creating a scale of an increased stoichiometric window [5] and higher porosity. This stoichiometric window can also be affected by the ratio of metal atoms to oxygen and the volume available to occupy. Manganese oxide (MnO) has one metal atom to one oxygen atom, whilst alumina (Al_2O_3) has an oxygen-metal ratio of 1.5, so aluminium is able to consume more oxygen for the same initial lattice volume.

5.3.4 Grain Size and Internal Oxidation

The preparation method for all the samples were the same, however there exists certain anomalies in the samples that due to time constraints could not be rectified, one of which is the grinding of the surface to remove the decarburisation zone. Although the samples were prepared at the same time some differences evidently arose.

When carbon (which has a significantly faster diffusivity compared to metal atoms) content in a steel phase is reduced it is less able to support the stabilisation of the austenitic structure [8, 12, 13], along with larger grains forming at the surface [3, 4, 8], and the pinning of grain boundaries [121] by internal oxides during annealing, this can lead to increased grain sizes close to the surface and possibly transformation to ferrite if decarburisation is severe, amongst other phenomena [3, 7]. The larger grain sizes have been labelled where appropriate, seen mostly on the Fe-5Al-5Mn sample where the surface was likely insufficiently ground.

This increased grain size leads to the effective separation of the grain boundary and the centre of the grain-surface interface except from the surface diffusion of the solute after reaching the surface elsewhere [7, 53]. This separation means that when

the fast diffusion pathways cannot supply the requisite material to form the protective scale over the grain and if the solute flux in the grain is insufficient to do so as well the surface oxidation behaviour will be heterogeneous with internal oxidation more likely.

The iterations of Fe-5Al-5Mn with small grains sizes (up to 10µm) clearly show a protective scale formation, with a clearly defined exclusive alumina layer in the Humidifier 0°C iteration; in the Humidifier 20°C iteration it can be seen again with a small amount of manganese oxide above. Whereas where the grain sizes are relatively large (~50µm), internal oxide formation is prevalent. Suggesting a relation between Wagner's Criterion [87] and a factor containing the grain – grain boundary volume ratio and the respective diffusivities [152, 153].

5.3.5 Effective Diffusivity and Internal Oxidation Zone Depth

In literature [72, 89] the idea of a consistently advancing oxidation front has been presented in the estimation of the IOZ depth; these results suggest that a new consideration must be given to whether the system is capable of creating horizontally forming oxides when the flux of the solute to the oxidation zone is enough to eventually sufficiently reduce the oxygen permeability to flux equality. On the approach towards flux equality the relationship of oxide particle growth vs new particle nucleation skews towards growth.

In a system with an atmosphere of very high oxygen partial pressure, this flux equality in the IOZ after the reduction in oxygen diffusion speed creating the horizontally-growing oxides, and eventually an internal barrier, would seemingly logically lead to the complete oxidation of the enclosed zone through the sequence of formation concentrations to end in a Fe-Al-Mn spinel - from the increasing internal oxygen concentration. But this is not evident in the experiments conducted as where this enclosed zone did occur there is still a small concentration of solute in the surrounding steel. This suggests that the primary reason is that the respective oxidation times were not long enough to bring about the total oxidation. This information presents a useful tool in terms of a time limit on which oxides, although

thermodynamically possible given the composition, are unlikely to form. Therefore, future experiments should focus on longer oxidation times to categorise this more effectively.

The diffusivity decrease [89] is due to the increasing volume fraction of oxide of the IOZ, this can be seen throughout the sample iterations of Fe-3Al-5Mn, where the decrease in oxygen diffusivity leads to the growth of oxide particles being favoured when approaching flux equality, with horizontal oxide formation and the enclosure of a section of the IOZ is possible if this phenomenon is pervasive.

If an infinite time is given to oxidise an infinitely deep sample with consistent oxygen surface penetration and not enacting higher oxides' formation concentrations (which reduces oxygen flux to the reaction front), flux equality will always occur eventually.

The above statement relies on the assumption of constant oxygen surface dissolution, which only incorporates one part of the equation for flux, the other being concentration. The initial formation of the alumina scale leads to a constant reduction in the dissolved oxygen concentration compared to an unoxidised surface, therefore the differences between the reduced surface oxygen penetration and the IOZ volume fraction of oxide contributions to the total flux and subsequent flux equality establishment should be investigated further as it is beyond the scope of this project as it would involve the categorisation of the surface oxidation phenomena on LDS Fe-Al-Mn steels to be more conclusive than it is currently.

5.3.6 Thermodynamic vs. Kinetic Considerations

The flux of aluminium to the IOZ is where the thermodynamics and their coupling to kinetics needs further attention. The preference of aluminium to bond with oxygen means that it is difficult to discern where the aluminium oxidation front ends and where the alumina formed from the reduction of manganese aluminate is [80] because when flux equality occurs the lower portion of the oxides created at that site will always remain alumina due to the abundance of aluminium. Similarly, with oxygen transport, solute transport through an oxide is many magnitudes slower,

therefore if an internal oxide barrier is sufficiently dense the aluminium will be slow to reduce the manganese aluminate even if thermodynamically viable. This may explain why the bottom of the internal oxide barrier is always rich in aluminium for the Fe-3Al-5Mn sample. The transport of aluminium to the IOZ also suggests that the Fe-5Al-5Mn and Fe-6Al-15Mn samples do not have a unitary discrete oxidation front.

5.3.7 Phase Packing Efficiency and Solubility

The difference between ferrite and austenite oxidation does not seem to be neatly described by the differences in diffusion speed and solute concentrations of these phases. The aluminium concentration differences between the two phases of both dual phase steels does not constitute more than 0.8 wt.%, hardly enough to have a profound effect such as that suggested by W. Peng et al [107, 111, 120] – perhaps diffusion could provide the additional variables. Ferrite has a less efficient packing structure than austenite creating a greater total volume of interstitial sites [8, 53, 145], oxygen is a diffusing atom that occupies these interstitial sites. Chemical diffusion occurs by chemical potential gradient with concentration gradient often within the same direction [5-8] , and the amount of available interstitial sites is related to the diffusion speed pre-exponent parameter [5-8] whereby the likelihood of a diffusive jump occurring is related to the possibility of an available destination site existing. The distance between the intervening atoms forms an energy barrier to the destination and has a great effect on the diffusivity, consisting of the numerator of the exponential function, with a tighter lattice requiring a greater amount of energy to surmount. With these in consideration it can be reasoned that ferrite diffusion supports both faster substitutional and interstitial diffusion, which it does and the evidence to support this fact is well documented. [5-8, 76]. However, whether the different lattice and interstitial diffusion mechanisms benefit equally from this decreased energy has not been studied at all, to the knowledge of this author. If the greater distance between host lattice atoms reduces the activation energy of metal solute lattice atoms to a greater degree than interstitial atoms, it might explain why ferrite can produce a higher solute flux than austenite. If there is no discrepancy between the ratio of diffusion speed increase from austenite to ferrite for both

oxygen and aluminium, then there might not be a significant difference in oxidation behaviour as the slight variance in concentration between the phase's elemental composition of the steels in this project would be unlikely to produce the differences seen by published authors [103, 105, 107, 111, 119-122]. There are valid arguments both for and against equal and unequal proportional increase of diffusivity, but until more research has been conducted into accurate and consistent diffusion speeds based on diffusing atom size relative to the host lattice atoms and their separation distance, this knowledge is unlikely to be generated soon.

If it is assumed that the increase in diffusivity of oxygen and aluminium is of equal proportion then perhaps the answer lies with the concentration component of flux and how the different lattice structures receive the oxygen. The term consisting of the diffusion parameters that are not related to the activation energy are combined into the common pre-exponent diffusivity term (D_0), and under the definition [5] of these given by D. Young there are no limits on which interstitials an atom can occupy (octahedral or tetrahedral). Within this lies a logical possibility of all interstitial sites having the equal and unhindered possibility of oxygen interstitial occupation. A BCC lattice has more numerous interstitial sites, but a FCC lattice has larger interstitial sites, an interstitial occupier atom might affect the lattice parameters depending on the ratio of the interstitial site volume compared to the atomic diameter, this is why carbon is more soluble in austenite than ferrite as it can occupy the larger interstitial sites of austenite without imparting as much strain on the lattice [8]. Hypothetically, as ferrite has more interstitial sites it can accommodate more oxygen atoms than austenite and for the same initial oxygen concentration at the surface with the same diffusion speed an individual oxygen atom is likely to travel farther in austenite than ferrite as the oxygen must fill up more numerous empty interstitial sites for a similar concentration gradient. To the knowledge of this author, there is little-to-no consideration for this aspect of flux in published literature, the magnitude of this affect could be significant, although the activation energy of the diffusion exponential term likely has the greatest effect on the total diffusivity even still.

The effects of the host lattice on the diffusion speed of atoms within are numerous and complex, the full scope of which is involved with the diffusion of oxygen and metal solutes during oxidation. Until investigation techniques become powerful enough to monitor in-situ diffusion of atoms through a lattice the questions that are posed during this discussion are unlikely to be answered soon.

5.3.8 Volume Expansion due to Internal Oxidation

Lattice strain energy can be imparted on a lattice for a number of reasons, more notably in the steel industry through deformation. However, during oxygen exposure and subsequent inward diffusion, the oxidation reaction can turn the dense steel lattice into a relatively less dense oxide lattice, dependent on the stoichiometry and flux of reactants. The lattice can contain a certain amount of lattice strain energy before a major consequence appears, in oxidation one observed consequence is the formation of surface pure metal nodules [102, 103]. Different forms of these surface nodules have appeared in oxidation literature [105, 114] as the description of the nodule is based on the relatively spherical shape and the surface location of the nodule rather than the composition or method of creation. When the pure metal nodules appear at the surface during internal oxidation it has been suggested that the increase in lattice strain energy from the formation of the internal oxides is the culprit due to the relative increase in volume. The theory goes that this volume expansion due to internal oxidation increases the lattice strain energy and this provides a driving force for diffusion on other atoms hosted by the lattice [95, 103, 126-129], most notably iron. In a system containing iron, aluminium, and manganese it can be logically inferred that when aluminium is oxidised internally that manganese would be the primary recipient of the additional flux increase. This is rationalised as manganese having a faster diffusion speed and higher oxidation potential than iron, so the net driving force required for diffusion of manganese is lower. This could contribute to the appearance of manganese at the surface along with the standard chemical potential driving force in highly oxidative atmospheres, such as those found in the experiments of this project. The diffusion of manganese partially due to the increase in lattice strain energy would decrease the lattice strain energy a similar amount

compared to iron as the difference between the atomic radii is very small [154], in some calculations manganese is the larger atom [155, 156], which could further reason for the manganese diffusion in place of iron. Of course if the lattice strain energy increased significantly the diffusion of both manganese and iron is possible, and in reality both are likely to occur regardless, if conditions allow. This is likely to be affected by the recrystallisation annealing of the microstructure.

5.3.9 Recrystallisation Annealing and Oxidation

"Recrystallisation is the formation of a new set of strain-free and equiaxed grains that have low dislocation densities and are characteristic of the precold-worked condition" [8]. This project focusses on the isothermal annealing stage of LDS production, in doing so the recrystallisation of the crystals should be considered by the reader, as at what stage the microstructure undergoes recrystallisation and the relation to the oxidation behaviour might need in-situ cross-section analysis. This aspect of annealing and the effect on Fe-Al-Mn-C oxidation are not well researched.

5.3.10 Dual Phase Nature

The dual phase (Ferritic and Austenitic) make-up of two of the steels experimented upon on do not appear to show a significant difference in the local oxidation behaviour between different adjacent oxide grain phases.

This can be explained as the grain/grain-boundary system being subject to a coupling of the very fast grain-boundary diffusion speed and the grain's large size acting as a large reservoir of solute supplying a very small volume which is constantly depleting; the slow diffusion speed of the grains results in the small contribution of solute from any individual grain, suggesting that the larger area's contribution is more significant than the local grain-GB-grain, as the grain-boundary diffusion speeds can transport atoms from significantly farther away before an atom at an appreciable distance within a grain, closer to the oxidation front, has diffused to the grain-boundary.

The oxidation behaviour must be partially characterised by the ratio between the oxygen and aluminium diffusion speeds in ferrite and austenite. For example, if this ratio is comparable, the depth at which the flux equality occurs in both crystals of ferrite and austenite can be similar due to the lower aluminium concentration and slower diffusion speed in austenite producing fewer oxide particles, thus reducing the effective oxygen diffusivity at a lower rate to a similar speed as ferrite; opposite to ferrite, where the faster diffusion speed of oxygen is coupled by the crystal's increase in aluminium concentration reducing the effective oxygen to at a greater rate. If the ratio of the diffusivities of the species in each phase is dissimilar, these differences will be most visible in the large grain sizes.

The consistent scale formation on Fe-5Al-5Mn is most likely due to the relatively large grain boundary volume supplying solute from the bulk. In the Fe-3Al-5Mn sample the internal oxidation zone appears relatively homogeneous, without any significant differences when examining the grains close to the surface. The relatively large volume of grain boundaries ensures that permeability of oxygen and aluminium remains high, and the differences in diffusivities between ferritic and austenitic crystal grains does not seem to have a significant affect, nor does the difference in grain solute composition.

This result can also be seen in the Fe-5Al-5Mn sample: when large grains occupy the subsurface region internal oxidation occurs (20°C, 5mins); however, this steel has the potential to meet Wagner's criterion as seen when the grain boundary access is high with small grains, an exclusive protective alumina scale forms. Therefore, the difference is likely down to two different considerations: the diffusivity of the grain having a significant role in the flux contribution due to larger grain size and fewer grain boundaries; and the decarburisation of the subsurface grains having a larger number of free interstitial sites, increasing the diffusion speed through available jump sites. The more significant role probably lies on the larger grain size as the interstitial sites are relatively free of occupiers regardless.

To properly characterise the effect of dual phase steel oxidation on the microstructure phase makeup, large grain sizes should be used.

5.4 Experimental Results Conclusions

Experiments have been conducted in a vacuum reaction chamber at an isothermal temperature of 850°C, with an average initial heat rate of 6°C/s up to 800°C, and 1°C/s from 800 - 850°C to allow for temperature stabilisation before isothermal oxidation. An argon-water vapour gaseous mixture was added to the reaction chamber upon the temperature stabilisation signifying the beginning of the isothermal oxidation duration, the argon flow was passed through a humidifier with water temperature set to 0°C and 20°C for different experimental iterations. The samples existed in a vacuum at several stages: in a vacuum storage box immediately after initial sample preparation until moved to the experimental reaction chamber (the storage container was then reset to vacuum), during the experimental heating ramp where the reaction chamber was brought to a vacuum, after the high temperature experiment the samples were again put in the vacuum storage container until sample preparation for SEM analysis, and within the SEM. Samples were analysed using EDS-SEM, oxidation behaviour was analysed with Fe, Al, Mn, C, O elemental mappings and spectra. From this, conclusions can be suggested based on the knowledge in Section 2 about internal oxidation phenomena:

- The results suggest that the dual phase nature of the microstructure is a minor component of the parameters affecting intergranular oxidation behaviour of Fe-Al-Mn-C steels with grain sizes up to 20µm

- The grain boundary metal solute flux contributions are significant and dominate the internal oxidation behaviour due to the very fast diffusion speeds of both oxygen and aluminium. Affected by differences in grain sizes, and therefore total grain-boundary volume, the oxidation behaviour is more so altered by grain boundary - to - grain volume ratio than the differences in composition and diffusivity of ferrite and austenite in dual phase Fe-Al-Mn-C steels as the larger microstructure local area is suspected to provide a larger cumulative role in metal solute flux than two adjacent crystals.

- Effective diffusivity is a major component of the internal oxidation of the systems in question, this can be seen by the increasing connectivity of the oxide particles, horizontal oxide formation and the eventual “barrier oxides” forming and preventing further oxygen penetration, with an “enclosed zone” forming.

6. Simulation Data

Four simulations were deemed to be necessary to validate the model and properly quantify the oxidation behaviour where the diffusion speeds and solute concentrations differ. These are 1. Fully Ferritic crystal phase, 2. Fully Austenitic crystal phase, 3. Dual Phase crystal make-up, homogeneous concentrations, 4. Dual Phase crystal make-up, heterogeneous concentrations.

The differences between 1, 2, and 3 provide a good distinction between the diffusion profiles of each species in the different phases whilst 4 represents the effect of local solute concentration on the oxide formation. The steel grade these four fundamental simulation types is Fe-5Al-5Mn as it provides a larger difference in the solute concentrations of the different ferritic and austenitic crystal phases and still share a relatively similar ferritic/austenitic phase fraction, seen in Table 2.1.

As stated in the Diffusion Module section, the Volume Fraction of Oxide was determined as a function of oxides volumes compared to the initial base metal volume, with the metal concentrations involving only the solute concentration, this is because in reality the formation of the discrete oxide molecule does not contain iron, and the vast concentration of iron in the calculations greatly reduces the limiting behaviour of the Effective Diffusivity until the iron is oxidises which is unlikely. This is also how the Volume Fraction of Oxide is represented in the results, without the consideration of the matrix iron.

The results are presented by COMSOL 2D Surface plots, where the surface refers to the geometry face presented to the viewer. The simulation plots are given for: the total volume fraction of oxide (%) which includes all oxides; Al_2O_3, and $MnAl_2O_4$ volume fraction of oxide; and unoxidised free aluminium, and manganese as relations of the ratio of instantaneous solute concentration (cAl, cMn) to the initial phase concentration (Ferrite (CAlf, CMnf), Austenite (CAla, CMna)). For the Dual Phase steels these involve both the homogeneous and heterogeneous solute simulations represented by the same ratio, but the denominator is the average solute concentration of ferrite and austenite (CAl, CMn).

These results are framed by the axis in micrometres, where the origin (0, 0) is the centre of the geometry; the scale on the right is the representation of the stated value, with the Maximum and Minimum values present at the top and bottom of the scale respectively representing the data values (accompanied by the black arrows), whereas the scale values are attached to the right. The scale limits are stated with the graphics, which are set to the most applicable values for the best representation of the data, the reader is advised to check the scale and the data value limits on each graphic. The real-time of the simulation is based on 300s isothermal oxidation and is shown in the top left corner of the graphics.

Simulation Results and Data Contents:

Four initial conditions were simulated for verifying the results of the model, these include changes to the diffusivities and grain solute concentrations.

- Initial Conditions

- Simulation Results

1. Ferrite
    - Homogeneous ferrite diffusivities and solute concentration

2. Austenite
    - Homogeneous austenite diffusivities and solute concentration

3. Dual Phase
    - Heterogeneous ferrite and austenite diffusivities, homogeneous solute concentrations

4. Dual Phase
    - Heterogeneous ferrite and austenite diffusivities, heterogeneous solute concentrations

- Simulation Discussion

- Simulation Conclusions

6.1 Initial Conditions

The initial conditions of the simulation results for Fe-5Al-5Mn include:

- Isothermal Temperature: 850°C, Isobaric pressure: 1 atm
- Model Dimensions (length refers to the hypothetical dimension Z, to couple real-world variables to the 2D model, an asterisk* marks its inclusion):
    - Width (Lx) = 10µm
    - Depth, including GB widths (Ly): 30.02µm,
    - Hypothetical Length* (Lz): 10µm
    - Total Area: 302 μm^2
    - Total Volume*: 3020 μm^3
- The surface oxygen concentration (based on pH_2O/pH_2 = 0.1): 7.48ppm
- Grain base metal iron and solutes aluminium and manganese concentrations for the dual phase ferritic and austenitic crystals, using ThermoCalc equilibrium data, are displayed in Figure 2.5.
- The GB metal concentrations are equal to the respective grain phase concentrations. However, for the heterogeneous dual phase concentration iterations, the GB metal concentration value is the average of the initial ferrite and austenite concentrations.

To aid the reader, a matrix table of the ratios of grain-boundary diffusivities - to grain diffusivities, and to grain-boundary diffusivities for ferrite and austenite has been compiled and presented below.

Table 6.1 Oxygen, aluminium, and manganese diffusivity matrix table of ratios of grain-boundary diffusivities - to grain diffusivities, and to grain-boundary diffusivities for ferrite and austenite at 850°C, blue cells are most relevant ratios, and grey are ratio to self = 1, based on values "Numerical Data and Functional Relationships in Science and Technology" [87]

850°C, 1 atm			Grain-boundary					
			Ferrite			Austenite		
			Oxygen	Aluminium	Manganese	Oxygen	Aluminium	Manganese
Grain	Ferrite	Oxygen	3.836E+04	1.308E+03	8.110E+02	2.641E+04	1.308E+03	1.934E+01
		Aluminium	5.938E+08	2.025E+07	1.255E+07	4.087E+08	2.025E+07	2.994E+05
		Manganese	1.279E+09	4.361E+07	2.704E+07	8.803E+08	4.361E+07	6.449E+05
	Austenite	Oxygen	1.053E+06	3.589E+04	2.225E+04	7.245E+05	3.589E+04	5.307E+02
		Aluminium	5.938E+08	2.025E+07	1.255E+07	4.087E+08	2.025E+07	2.994E+05
		Manganese	2.414E+11	8.232E+09	5.103E+09	1.662E+11	8.232E+09	1.217E+08
Grain-boundary	Ferrite	Oxygen	1.00	0.03	0.02	0.69	0.03	0.00
		Aluminium	29.32	1.00	0.62	20.19	1.00	0.01
		Manganese	47.30	1.61	1.00	32.56	1.61	0.02
	Austenite	Oxygen	1.45	0.05	0.03	1.00	0.05	0.00
		Aluminium	29.32	1.00	0.62	20.19	1.00	0.01
		Manganese	1983.11	67.63	41.93	1365.08	67.63	1.00

6.2 Fe-5Al-5Mn Simulation Results and Data

6.2.1 Ferrite - Homogeneous Ferrite Diffusivities and Solute Concentration

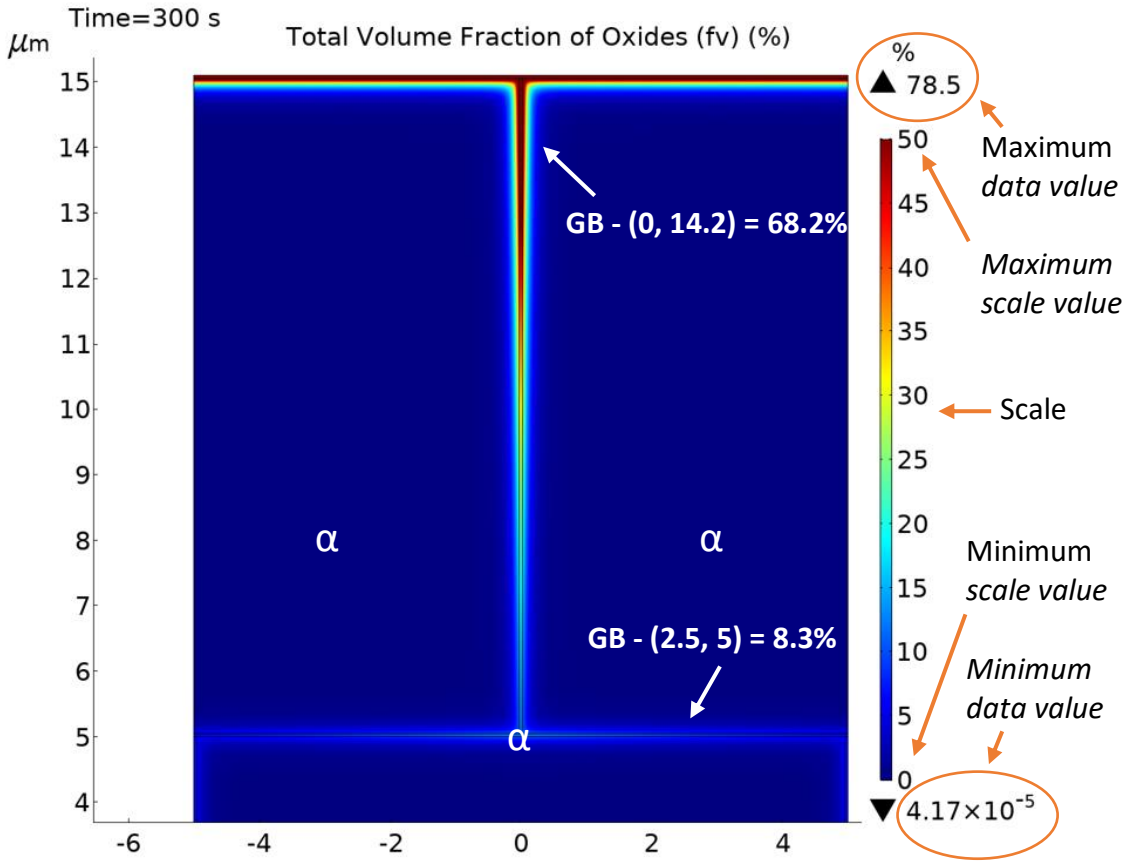

Figure 6.1 Fe-5Al-5Mn Steel fully ferritic grains simulated at an isothermal 850°C using COMSOL software for 300 seconds with a surface oxygen concentration of 7.5ppm. Total volume fraction of oxide graphic, surface grains view, this graphic's scale limits are equal to the data value limits

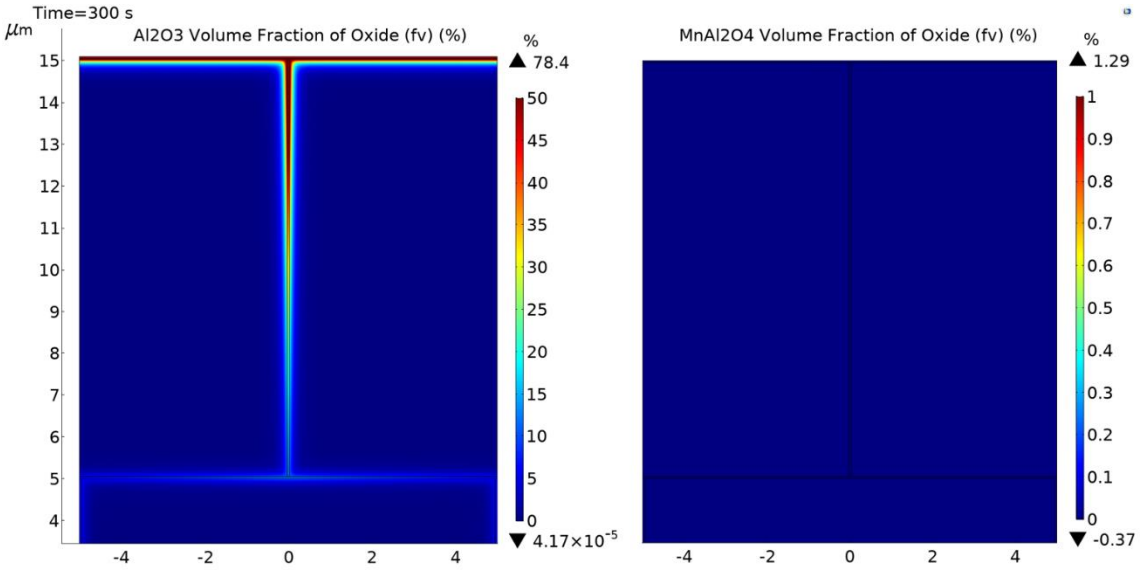

Figure 6.2 Fe-5Al-5Mn Steel fully ferritic grains simulated at an isothermal 850°C using COMSOL software for 300 seconds with a surface oxygen concentration of 7.5ppm. Al_2O_3 volume fraction of oxide graphic, surface grains view, relative scale limits: Al_2O_3 -lower: 0%, upper: 50%, $MnAl_2O_4$ – lower 0%, upper 1%

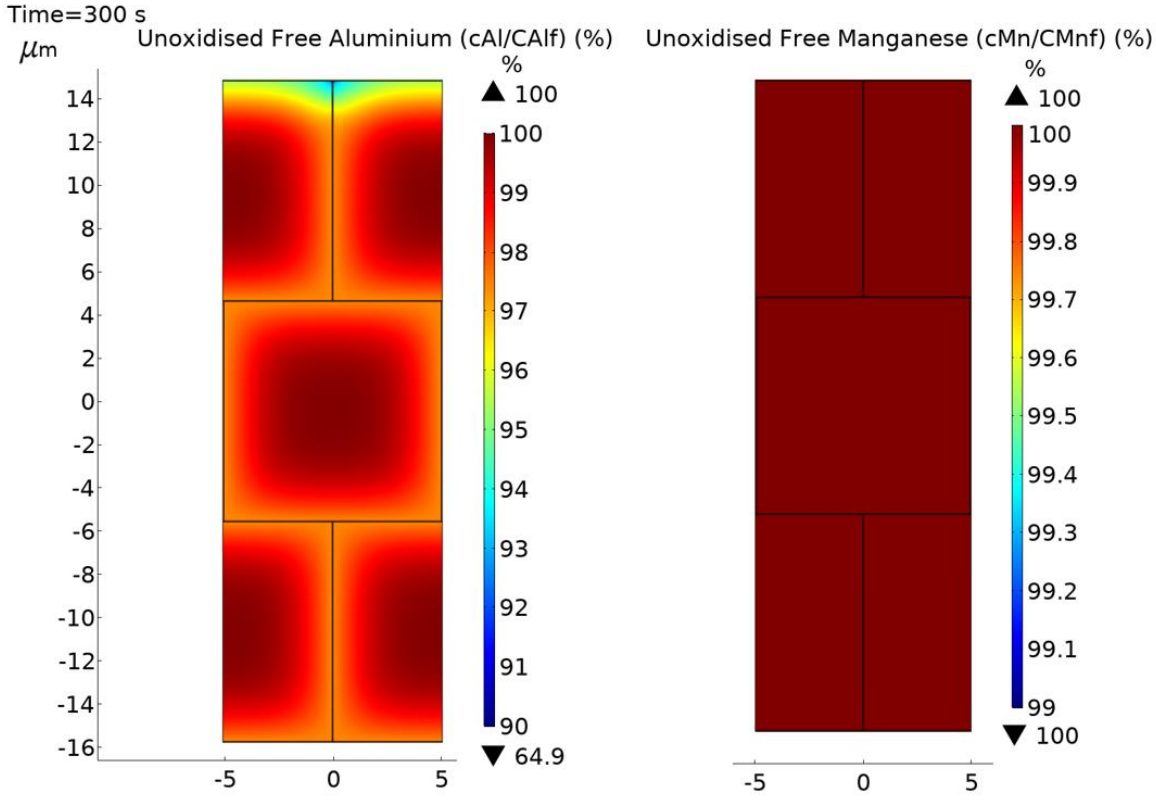

Figure 6.3 Fe-5Al-5Mn Steel fully ferritic grains simulated at an isothermal 850°C using COMSOL software for 300 seconds with a surface oxygen concentration of 7.5ppm. Aluminium and manganese concentration ratios to initial - graphic, full geometry view, scale limits: Al -lower: 90%, upper: 100%, Mn – lower 99%, upper 100%

The small grain sizes are coupled with a relatively large grain-boundary volume, leading to the flux contribution domination by the grain-boundaries; this is shown in the in the simulation results as the primary oxidation of the grain-boundary, with minimal grain oxidation observed.

With this project's ideal dual phase steel grain size simulated upon (up to 20μm), the domination of the grain-boundary flux means that the grain contribution is not significant, and solute atoms are transported from further into the geometry close to the grain/grain-boundary interface from numerous grains before solute in the grain reaches the grain-boundary; as stated above, this also works in the opposite with regard oxygen penetration.

As seen in Table 2.4, the Fe-5Al-5Mn steel grade ferritic phase contains high quantities of aluminium contributing to a high aluminium flux to the oxidation zone which helps the rapid formation of dense oxides. The only oxide that formed in this simulation was alumina, which is consistent with the small grain experimental results, where internal oxidation did occur, they only consisted of alumina. As this model relies on a worst-case-scenario where the oxygen penetration never stops and the lack of discrete oxides to completely block a site, the internal oxidation is expected and justified. There is also slight formation of oxides in the grains.

6.2.2 Austenite - Homogeneous Austenite Diffusivities and Solute Concentration

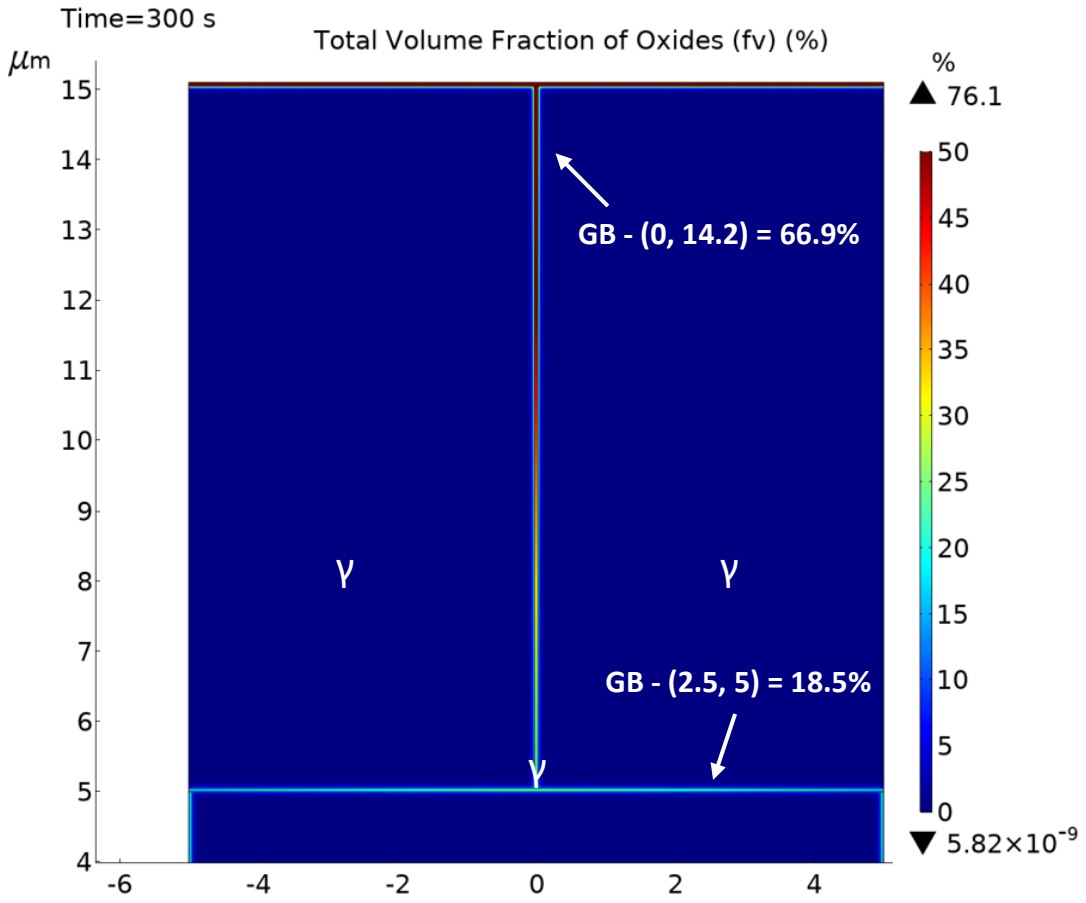

Figure 6.4 Fe-5Al-5Mn Steel fully austenitic grains simulated at an isothermal 850°C using COMSOL software for 300 seconds with a surface oxygen concentration of 7.5ppm. Total volume fraction of oxide graphic, surface grains view, this graphic's scale limits are equal to the data value limits

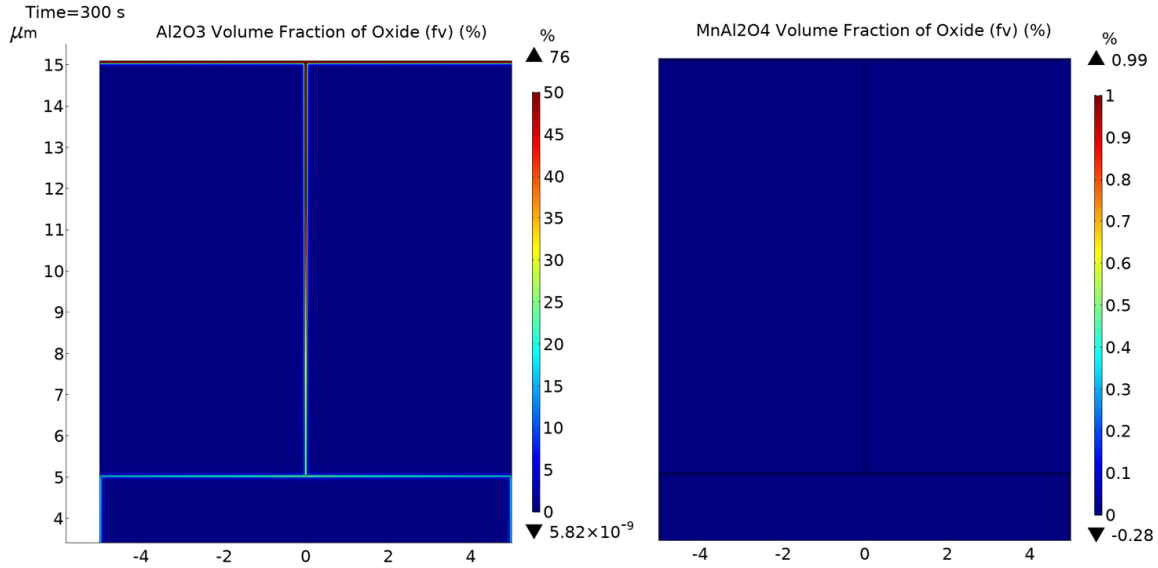

Figure 6.5 Fe-5Al-5Mn Steel fully austenitic grains simulated at an isothermal 850°C using COMSOL software for 300 seconds with a surface oxygen concentration of 7.5ppm. Al_2O_3 volume fraction of oxide graphic, surface grains view, relative scale limits: Al_2O_3 - lower: 0%, upper: 50%, $MnAl_2O_4$ - lower 0%, upper 1%

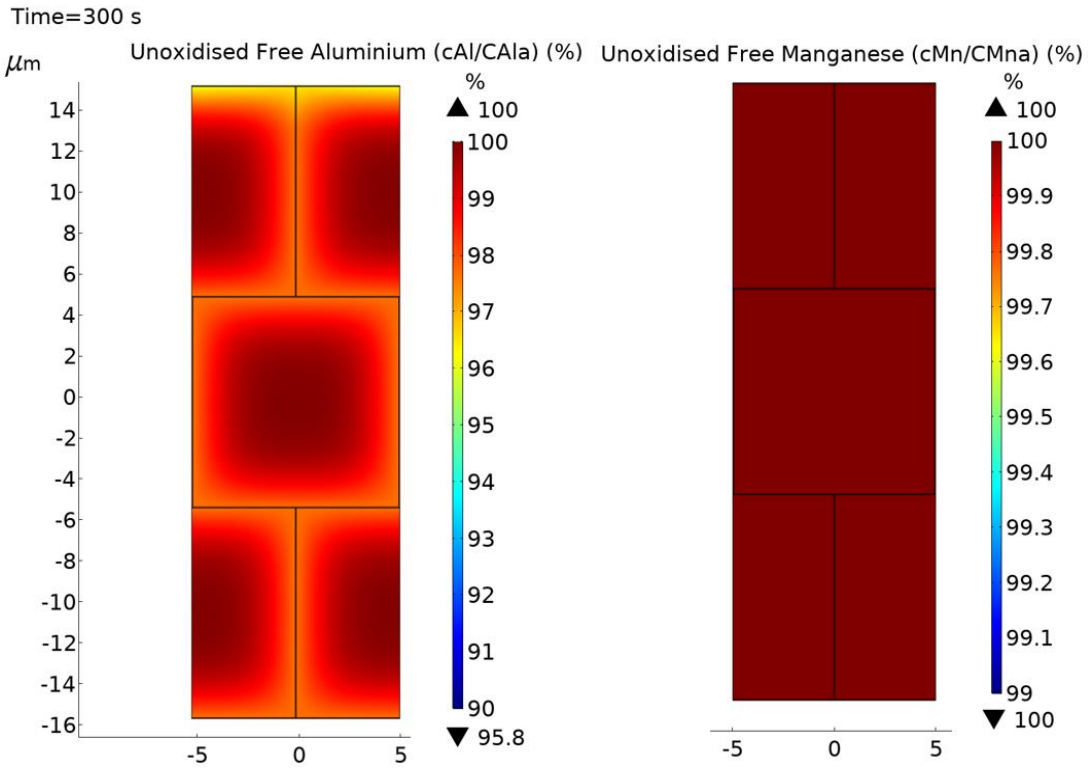

Figure 6.6 Fe-5Al-5Mn Steel fully austenitic grains simulated at an isothermal 850°C using COMSOL software for 300 seconds with a surface oxygen concentration of 7.5ppm. Aluminium and manganese concentration ratios to initial - graphic, full geometry view, scale limits: Al -lower: 90%, upper: 100%, Mn – lower 99%, upper 100%

Grain boundary domination of the flux contribution is also present in the fully austenitic simulation, which is not unexpected when considering the slower diffusivity. The slower austenitic diffusivities and lower concentrations lead to the delayed establishment of dense oxides diminishing the oxygen permeability less than the fully ferritic simulation, contributing to a larger amount of oxidation at a greater depth.

6.2.3 Dual Phase - Heterogeneous Ferrite and Austenite Diffusivities, Homogeneous Solute Concentrations

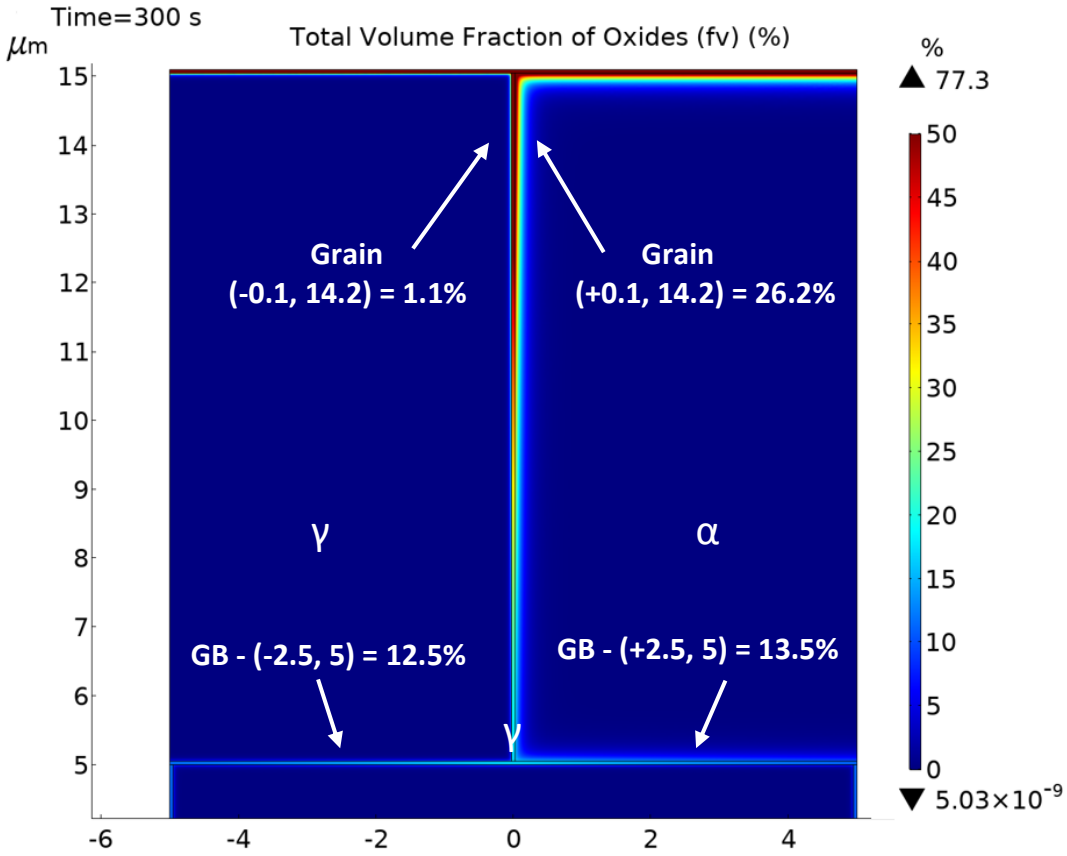

Figure 6.7 Fe-5Al-5Mn Steel dual phase homogeneous concentrations (ferrite – austenite average) grains, simulated at an isothermal 850°C using COMSOL software for 300 seconds with a surface oxygen concentration of 7.5ppm. Total volume fraction of oxide graphic, surface grains view, this graphic's scale limits – lower: 0%, upper: 50%, values shown with corresponding coordinates

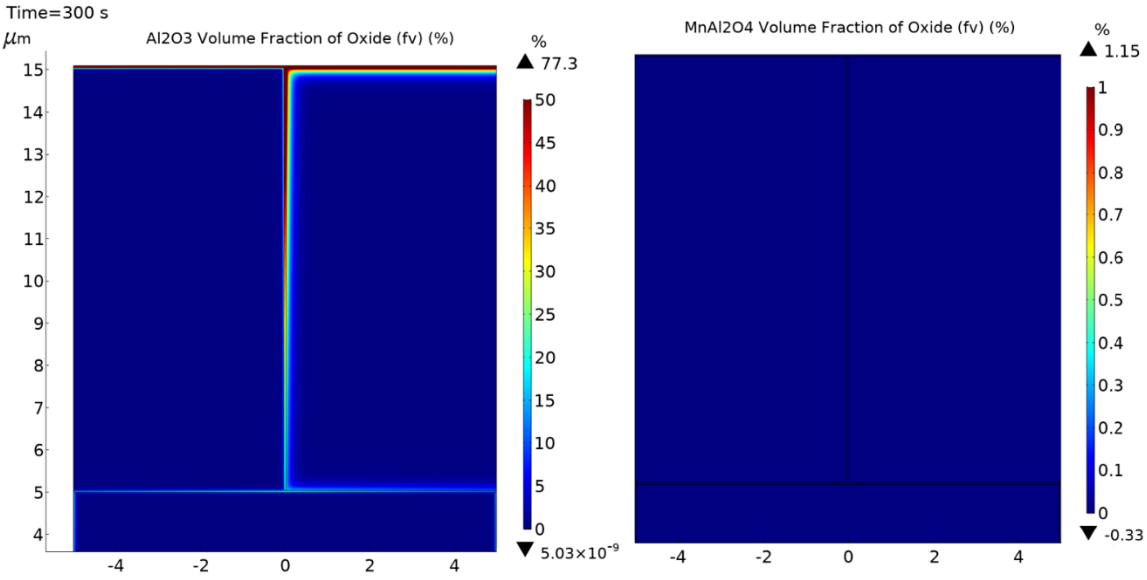

Figure 6.8 Fe-5Al-5Mn Steel dual phase homogeneous concentrations (ferrite – austenite average) grains, simulated at an isothermal 850°C using COMSOL software for 300 seconds with a surface oxygen concentration of 7.5ppm. Al_2O_3 volume fraction of oxide graphic, surface grains view, relative scale limits: Al_2O_3 - lower: 0%, upper: 50%, $MnAl_2O_4$ - lower 0%, upper 1%

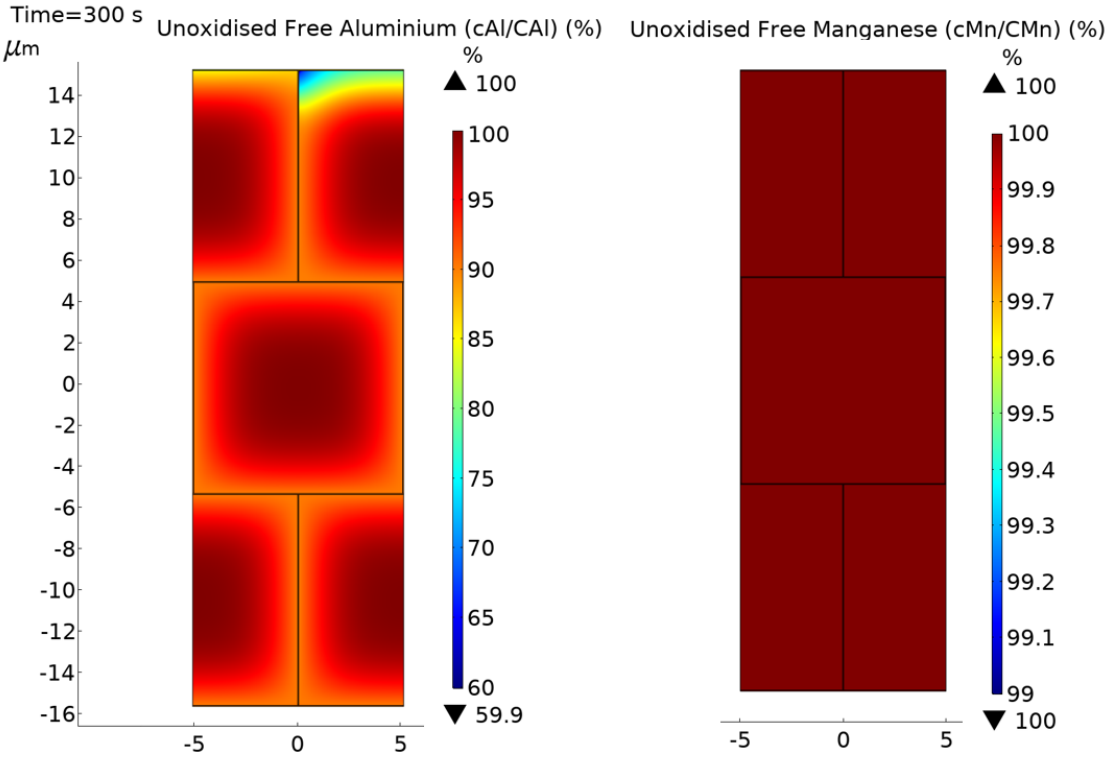

Figure 6.9 Fe-5Al-5Mn Steel dual phase homogeneous concentrations (ferrite – austenite average) grains, simulated at an isothermal 850°C using COMSOL software for 300 seconds with a surface oxygen concentration of 7.5ppm. Aluminium and manganese concentration ratios to initial - graphic, full geometry view, scale limits relative to ferrite – austenite solute average: Al -lower: 90%, upper: 100%, Mn – lower 99%, upper 100%

There is a small but significant difference in the oxidation behaviour seen in this dual phase homogeneous concentration iteration, the ferrite grain has a larger oxide penetration. This is not unexpected given the fully ferritic and austenitic simulations, however, there is a significant difference at the grain/grain-boundary interface as shown in Figure 6.7. These slight differences suggest that the dual phase nature of the steel does not greatly affect the inter-grain behaviour at the current grain sizes due to the dominance of the grain-boundary flux contribution; but the small differences could be better explored in a system where the total grain-boundary volume is altered via different grain sizes. These results suggest that if experiments are conducted on a large range of grain sizes, the grain flux contribution would become significant at a 'critical' grain size and the dual phase oxidation behaviour could be explored further.

6.2.4 Dual Phase - Heterogeneous Ferrite and Austenite Diffusivities, Heterogeneous Solute Concentrations

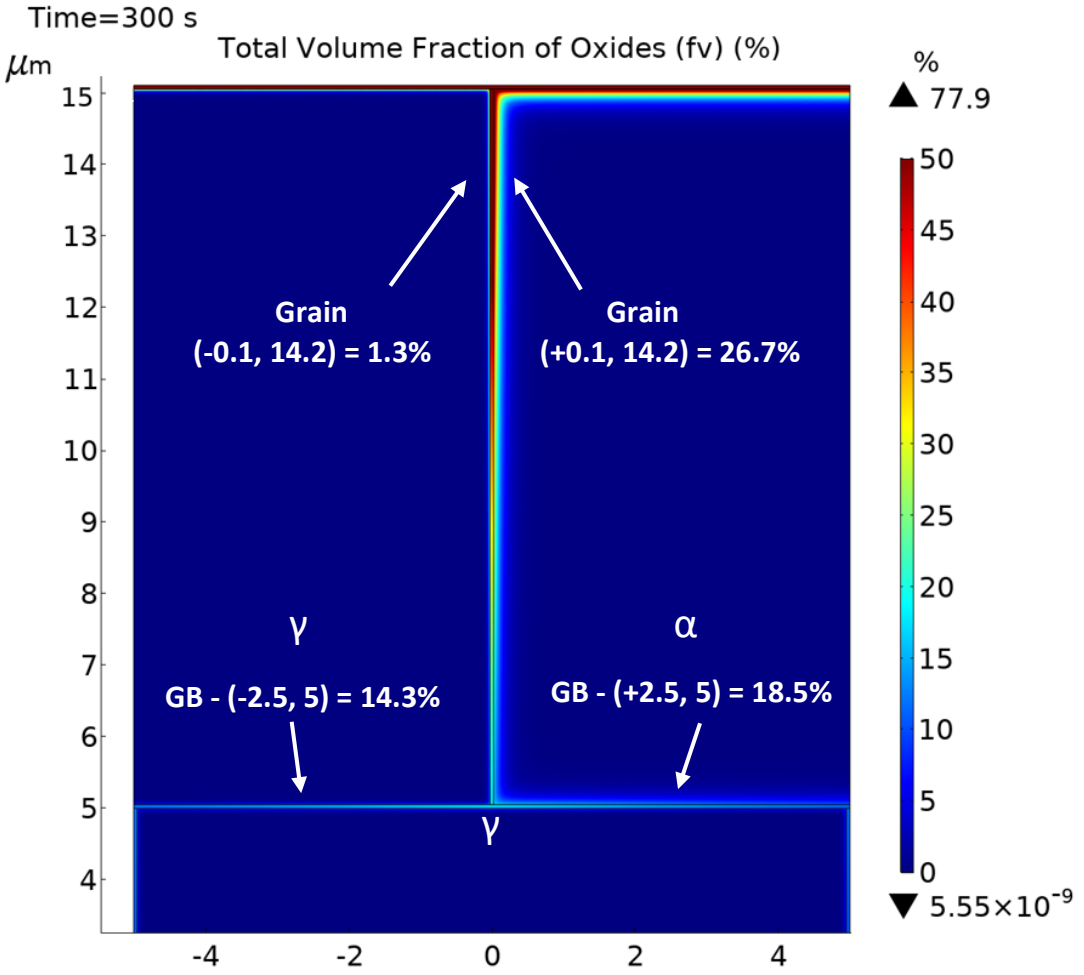

Figure 6.10 Fe-5Al-5Mn Steel dual phase heterogeneous concentrations (ferrite – austenite average) grains, simulated at an isothermal 850°C using COMSOL software for 300 seconds with a surface oxygen concentration of 7.5ppm. Total volume fraction of oxide graphic, surface grains view, this graphic's scale limits – lower: 0%, upper: 50%

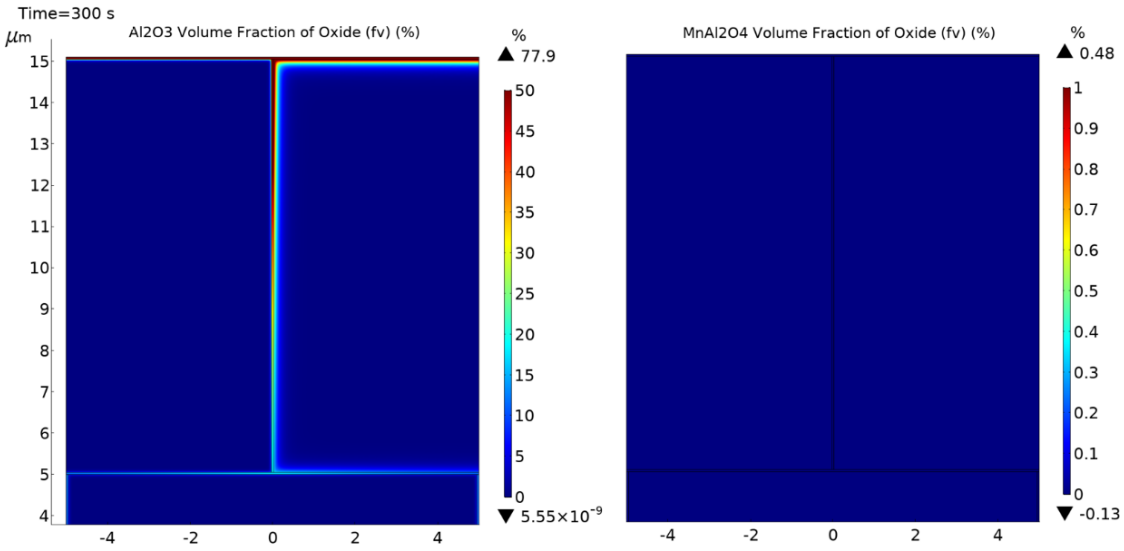

Figure 6.11 Fe-5Al-5Mn Steel dual phase homogeneous concentrations (ferrite – austenite average) grains, simulated at an isothermal 850°C using COMSOL software for 300 seconds with a surface oxygen concentration of 7.5ppm. Al_2O_3 volume fraction of oxide graphic, surface grains view, relative scale limits: Al_2O_3 - lower: 0%, upper: 50%, $MnAl_2O_4$ - lower 0%, upper 1%

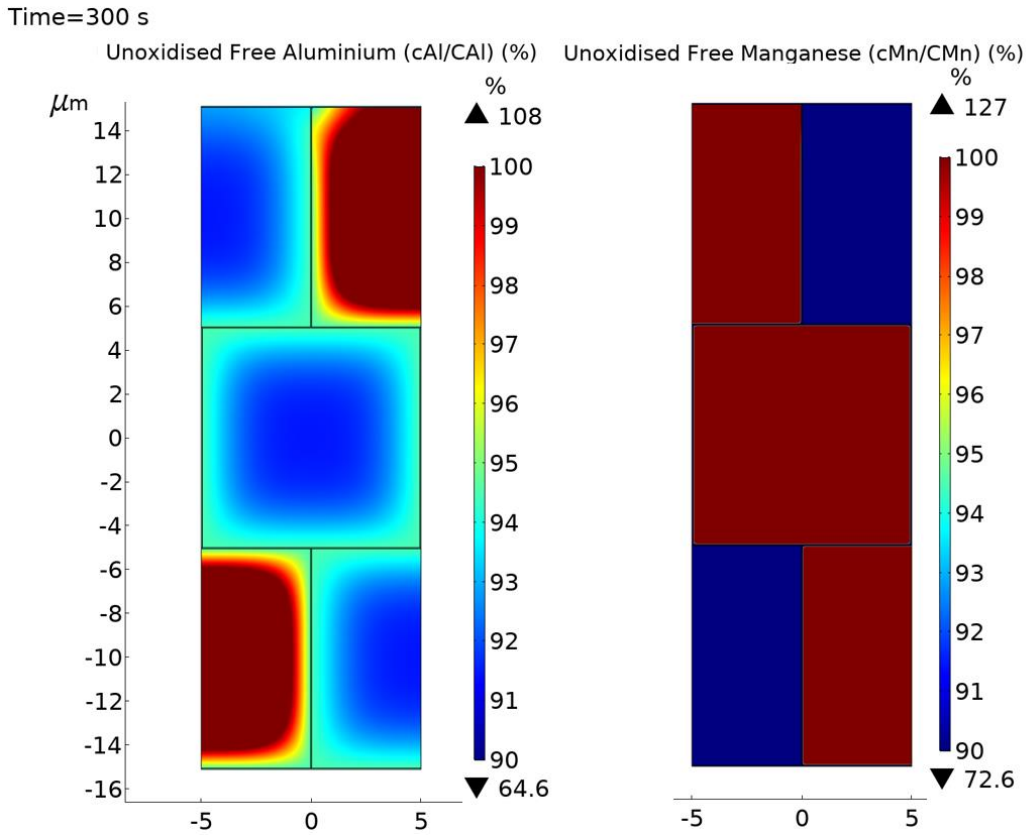

Figure 6.12 Fe-5Al-5Mn Steel dual phase heterogeneous concentrations (ferrite – austenite) grains, simulated at an isothermal 850°C using COMSOL software for 300 seconds with a surface oxygen concentration of 7.5ppm. Aluminium and manganese concentration ratios to initial - graphic, full geometry view, scale limits relative to ferrite – austenite solute average: Al - lower: 90%, upper: 100%, Mn - lower 90%, upper 100%

The flux of aluminium from the ferritic grain shows a slightly larger proportion of oxides at the surrounding boundary compared to the dual phase homogeneous concentrations iteration. Comparing, this small increase is not significantly different from the homogeneous concentrations, suggesting that the total geometry aluminium flux is controlled more significantly by the diffusion speed than the concentration component, which agrees with the assertion about the grain-boundary diffusion dominating the system.

The slightly increased oxidation depth and oxide concentration likely comes from the lower concentration of grain-boundary oxides formed near the surface reducing the incoming oxygen flux which is due to the lower average aluminium flux compared to the homogeneous simulation, because the initial concentrations were derived from the average of ferritic and austenitic solute concentrations.

6.3 Simulation Discussion

As can be seen in volume fraction of oxide measurements, the values approach full oxide volume, with values similar to those found in the experimental results with values of 35 - 50 Vol.% near the edge of oxide particles, reaching 70 - 90 Vol.% at the centre of oxide particles, suggesting good comparisons with the measurements in the simulation.

The large quantity of aluminium in the ferritic grains did not greatly alter the oxidation behaviour which is seen by the greater penetration of ferritic grains by the oxygen compared to the austenitic grains, this is due to the domination of the aluminium grain-boundary flux on the 10µm grains. This major difference in flux contributions can be seen in the similar, significant, depletion of aluminium from the grains at the deepest portion of the geometry.

The differences visible due to the dual phase microstructure in the simulations results are small and do not affect the adjacent grain-GB-grain oxidation greatly; however, their existence is significant because they are visible in spite of the grain-boundary flux domination. As there is evidence of a variance occurring it would be prudent to further explore the dual phase nature of these steels with less total grain-boundary volume.

As specified before, a limitation of the modelling software is the lack of inclusion of the space occupancy of atoms and molecules, namely the interactions between the species (oxides, oxygen, aluminium, and manganese), but also the blocking potential of the oxides. This was partially remedied through the use of the effective diffusivity interpolation function, although this does not divert the flow of atoms but slows the diffusion. This appears to be a major source of discrepancy with the experimental results.

The model created for this project is a representation of the conglomeration of the state-of-the-art internal oxidation theories, an optimised model based on the amount of available computing resources, the capabilities of state-of-the-art modelling software, and the necessary refinements for reasonable resolution. This

provides a good illustration of the current theories surrounding internal oxidation and what is lacking. There are comparisons to the experimental results that have been discussed, however, where the model fails due to certain limitations of both the current theories and the modelling software. Those limitations can be scrutinised and the possibility of ascertaining the future avenues of improvement for both the theories, experimental data, and modelling software are possible. Here shall be discussed the likely most beneficial avenues of potential improvement for modelling Fe-Al-Mn-C steels internal oxidation during annealing:

Spatial occupation of a species: The occupation of an individual location by any metal, oxide, or oxidant species should be enforced. Modelling software has limitations and an atomistic simulation in the macroscopic view would be incredibly resource-intensive, however there are potential avenues of implementation based on the volume fraction of a species relative to the stated initial concentration of each species but also the local cumulative concentration of all species, this can be subject to individual criteria based on input conditions provided by the researcher. This is in the opinion of this author the single biggest limitation with the modelling software capabilities for this project.

Consistent diffusion and solubility values: the lack of accurate and consistent grain and grain boundary diffusivity and solubility values for all the elements in the Fe-Al-Mn-C system severely prevents accurate oxide formation as the Fe-Al-Mn-C system is very complex and the conglomeration of many parameters are needed. A major discrepancy between the experimental and simulation results was the grain oxidation, limited by oxygen diffusion speed. The values for diffusion are based on many criteria, diffusivity values were taken based on the similarity of system composition (affects lattice parameters related to diffusion pre-exponent and activation energy), valid temperature range, and the author of the publication (to retain a consistent source, with similar experimental conditions). The continuation of diffusivity values research would depend largely on industrial attention, with the rise of low density Fe-Al-Mn-C steels, this might be more likely.

Clarification of the oxygen transport mechanism at the internal oxide-metal interface: alumina rods form from a potential mechanism of oxygen transport along the internal oxide-metal interface and this could be in play in any other situation but does not play such a significant role as to become obvious here. Discerning the role of this phenomenon would establish a much more unified internal oxidation theory.

Although the goal of model creation is to as accurately as possible simulate a certain system, the simulation results presented here allowed the discrete categorisation of the above improvement discussions through discrepancies to the experimental results. This is also an important aspect of modelling, similar to the significance of null results.

6.4 Simulation Conclusions

Internal oxidation simulations of Fe-3Al-5Mn and Fe-5Al-5Mn have been conducted, with respected diffusion values of oxygen, aluminium, and manganese used for the isothermal temperature profile of the model. The mathematical modelling investigation into the affect that the dual phase microstructure has on the internal oxidation of Fe-Al-Mn-C steels has been complete. The scientific knowledge of internal oxidation has been coupled with leading oxidation theories such as the concentration of oxygen penetrating the steel surface related to the atmospheric partial pressure of oxygen [85] and the effective diffusivity change dependant on the local volume fraction of oxide [89]. These have been added to produce a state-of-the art model which is highly optimised with worst-case-scenario and variable minimisation considerations. The model represents an assembly of up-to-date internal oxidation phenomena that has been widely supported in literature, other theories are coming to the fore but need further evidence and mathematical clarification in order to be cleared for accurate modelling representation of the industrial processing of LDS; this includes the oxygen transport along the oxide-metal interface.

Specific conclusions can be made from the simulation results when considering the input variables:

- The dual phase microstructure does affect the inter-granular oxidation behaviour

- The differences in internal oxidation behaviour of Fe-Al-Mn-C steels that the dual phase nature of the steel contribute to are dwarfed by the metal solute grain-boundary flux contribution

The limits on modelling are imposed by the data available and the software to implement them, further experimental analysis of oxygen, aluminium, and manganese diffusion in the grains and grain boundaries of Fe-Al-Mn-C steels. The state-of-the-art modelling software used in this project also imparted limitations on the simulation capabilities, namely the consideration of a species concentration is dependent on the initial values and interaction between species is minimised to chemical reactions alone.

Future modelling of internal oxidation should focus on software that can affirm the kinetic and spatial interactions between species.

7. Discussion

The experimental results of Fe-3Al-5Mn showed that the grain-boundary was the primary location of oxide formation, with the oxides initially growing from small particles and combining. This connection of oxides did not readily occur in the grains, due to the slow diffusion speed of the solutes compared to the oxygen. The numerous small oxide particles formed because the difference in oxygen and aluminium diffusivities caused the oxygen to diffuse to the aluminium which promoted particle nucleation rather than particle growth [5, 7, 53, 89], and the surrounding metal was quickly depleted and the reaction front moved on. The steel grade did not exhibit significant visible internal oxidation disparity due to the dual phase microstructure.

The effective diffusivity decrease of the oxygen is apparent in this sample, as the increased connectivity of the grain-boundary oxides often leads to an oxide barrier, although the barrier does not always form a distinguishable feature. The grain boundary oxides often grow laterally into the grains with no clear direction or morphology, likely due to the oxygen and aluminium grain boundary fluxes reaching equality [87]. The inconsistent morphology of the connected GB oxides that grow laterally into the grain could be due to instantaneous density gradients on the outside of the oxide particle causing a seemingly random location for growth with the arrival of oxygen and aluminium contributing some measure to the microscopic reactant gradient. The simulation of this growth mechanism alone would be very complex, involving asymmetric instantaneous reactant arrival and final oxide location.

This sample is unlike most of the dual phase steel short annealing conditions reviewed in Section 2.11, the equality of fluxes pertaining to a unique system that is rarely found in literature. The current understanding of internal oxidation does well to describe the situation.

The simulation results show metal solute flux contribution from many grains with the intergranular oxidation being less so affected by the phase of the immediate adjacent grains. This aspect is difficult to compare to the experimental results as the oxidation

of aluminium and manganese in the IOZ alters the microstructure through depletion of these phase stabiliser elements.

The Fe-5Al-5Mn dual phase steel when exhibiting the desired 10-20µm grain sizes produced an exclusive protective alumina scale. When the grain sizes were large, oxygen penetration of the grain was prevalent at the surface but differences in oxidation behaviour was not significantly visible due to the dual phase nature of the steel.

The experimental data suggests that the flux component of the solutes is a complex relation of the grain-boundary diffusion speed and the grain size which acts as a solute reservoir, with a small contribution by each individual grain, relying on the cumulative, larger area's solute flux contribution. This means that the grain-boundary diffusion is the dominant factor in the internal oxidation of these dual phase steels, and the oxidation behaviour differences due to the dual phase nature of the steel was likely dwarfed by these aspects.

The simulation results also support the grain-boundary diffusion dominating the total microstructure solute flux for this steel with small grain sizes (10µm), where significant partial solute depletion of all the grains occurs. The simulation results suggest the diffusion component of the flux term is a dominant factor in the oxidation behaviour, as the grain-boundary diffusion controls the dominant total flux component; the grain boundary oxidation is not governed significantly by the dual phase nature of the steel by difference in diffusivities and initial solute concentrations.

However, there is a very small visible effect in the simulation results due to the dual phase nature of the steel. This might suggest that the dual phase nature does not significantly affect the oxidation behaviour when the grain-boundary volume is high; however, as the grain-boundary flux dominates the total flux contribution whilst still

displaying this oxidation disparity indicates a potentially significant effect with larger grain sizes to increase its visibility.

7.1 Dual Phase Fe-Al-Mn Oxidation Phenomenon Discussion

The following discussion is an attempt to explain as fully as possible what occurs during internal oxidation of dual phase Fe-Al-Mn-C steels with high manganese and aluminium. Constructed from the combined knowledge of all the above presented literature from the well-sourced textbooks with established authors to those of the literature review section - this presents a complex scenario that is scientifically reasoned according to the thermodynamics of oxidation, flux competition, diffusion-medium diffusivity values, lattice structure, and oxide formation mechanics.

As a main factor determining whether an oxide will form is the oxide oxygen formation concentration there are some specifics compiled here that involve internal oxidation and need consideration to fully understand what the results of this study will mean. The main property of aluminium that sets it apart from iron and manganese in the system in question is the extremely high oxygen affinity, with most industrial oxygen partial pressures oxidation is almost guaranteed.

7.1.1 Exclusive External Oxidation, Fe-Al

As aluminium is the preferential oxidiser in the system, the oxidation behaviour is usually defined by the ability of aluminium and oxygen to reach each other and react. The aluminium flux will supply the requisite material to form an exclusive external oxide layer known as a scale, if the density of the scale is high enough then a protective oxide layer will form, effectively preventing oxygen penetration to the substrate and no internal oxidation will occur, as defined by Wagner's criterion. The formation of an exclusive external oxide layer does not posit the definite formation of a completely protective layer, as the reaction atmosphere to form the external

layer could be lower than what could be experienced at a later stage whereby the external oxide layer may now not be sufficiently dense to prevent penetration.

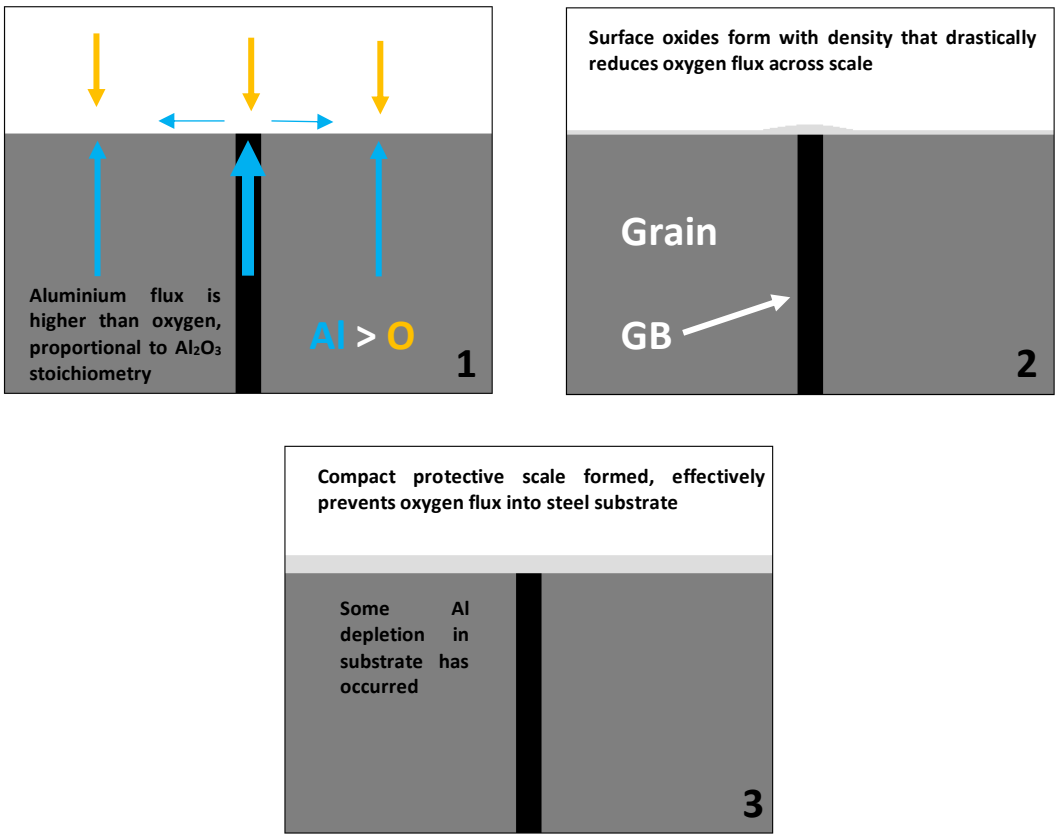

Figure 7.1 A nanoscopic schematic representing the formation of a protective surface oxide layer of alumina, when the aluminium flux is proportionally higher than oxygen for its formation. Image 1. Shows the oxygen dissolving at the specimen surface and the diffusion of the metal solute aluminium occurring in a chemical potential response with a larger flux of aluminium occurring at the grain boundary, lateral surface diffusion of aluminium also occurs at the surface via concentration gradient – indicated by horizontal arrows. Images 2 and 3 show the proceeding time-steps of external oxidation. Coloured arrows are related to the same element depicted, arrow size is proportional to flux magnitude when relevant

7.1.2 Internal Oxidation, Fe-Al

In this current scenario we consider a steel with significant aluminium quantity only. If this aluminium flux is insufficient to form the protective layer then some small measure of external aluminium oxidation will occur and internal oxidation will be prominent [87]. Wagner's criterion for this system is partially determined by the ratio of the fluxes of aluminium and oxygen, but one parameter that is not considered is the density of the established oxides and the position of formation, Wagner's

criterion is determined by the ratio of one metal solute to oxygen ratio, this therefore does not form a solution to a complex Fe-Al-Mn-C system.

As the diffusion of oxygen through an oxide is related to the stoichiometric window of the oxide and hence the density as compared to the pure form of the oxide [5], a decrease in the oxide density correlates to an increase of the amount of vacancies in the oxide lattice and will positively affect the oxygen flux across the scale [5-8, 53, 63, 90]. Different oxide species exhibit different oxygen diffusion speeds as the number of jump sites differs within the available stoichiometric window [5, 76]. Aluminium and chromium are known to produce oxides of sufficient density to produce the protective scale, whereas manganese and iron oxides do not produce oxides of sufficiently small stoichiometric window and subsequent density to effectively prevent oxygen diffusion [5, 89, 90, 91]. This is an effective description of oxides and how the relation of density and stoichiometry affect diffusion, however other factors such as the crystal structure of the oxide lattice, the charge of the lattice and vacancy sites etc. contribute to this phenomena. The inadequacy of manganese and iron to form the exclusive protective oxide scales suggests that if incorporated into an oxide that does, forming a spinel, the protective nature of the latter would be diminished by density reduction. Hence it can be reasoned that manganese and its oxides when incorporated into a protective alumina layer could allow the effective penetration of oxygen into the substrate. “Effective penetration” here refers to the significant flux of oxygen across the surface oxidation layer, as the increased density of an oxide reduces the flux but does not completely prevent the diffusion forever, as diffusion is a temperature-dependent phenomena and given enough time oxygen will reach the substrate even in a dense perfect oxide lattice [89, 105].

In a monocrystalline, or polycrystalline material with very large grain sizes, with an initial oxygen flux that is significantly higher than the aluminium flux then significant internal oxidation will occur producing an oxygen concentration gradient across the depth of the substrate with a maximum at the surface and minimum and the furthest penetrating oxygen atom, with oxides nucleating when the local oxygen concentration reaches the oxide oxygen formation concentration [69, 72, 106], at the RF.

This is where the relation between metal solute concentrations and oxide oxygen formation concentrations will be most delicate. The ratio of metal solutes concentrations and internal oxygen concentration will determine the location the metal solute of lesser oxidising potential will form, at the surface and subsurface, at the grain boundary, and in the grains.

If the main oxidising element aluminium is of low quantity whilst the oxygen concentration is high, aluminium oxide will form until all aluminium in the local area is oxidised and additional aluminium will diffuse to the high oxygen potential area and further the oxidation, the faster oxygen diffusion will extend the reaction front and IOZ. The formation of surface oxides will reduce the flux of oxygen into the steel, internal oxides will extend the low-diffusivity zone and reduce this further depending on oxide stoichiometry, the ratio of the aluminium and oxygen fluxes will tend towards equality with increasing depth and [89] volume fraction of oxide of the IOZ. If a semi-infinite pool of aluminium exists by a sufficiently thick sample of which to contribute the necessary metal solute concentration, eventually the oxygen flux will reduce to a similar value to the aluminium flux. As the oxygen flux value approaches the aluminium flux value, the nucleating oxidation mechanism will tend towards particle growth. Approaching flux equality even closer, the flux of reactants causes oxide formation to become even denser with formation possibly occurring in a fashion disorientated with the a seeming random direction possibly determined by the local reactant concentration gradients, eventually forming a dense internal oxide barrier/layer. When this dense internal oxide barrier is produced, the diffusion between the “enclosed zone” and the rest of the substrate will essentially cease, effectively preventing atomic diffusion across. The formation of this barrier with very large grains has been apparent in the Fe-5Al-5Mn sample with H-20C.

This dense internal oxide barrier could form before the complete oxidation of the enclosed zone due to the fast penetration along the grain boundaries of polycrystalline materials, if this is the case then oxygen will continue to penetrate the grains oxidising the remaining aluminium. When the aluminium is fully oxidised in the enclosed zone the internal oxygen concentration will increase up to the limit

corresponding to the amount able to be dissolved in the parent matrix, called the solubility [5, 7, 8]. The parent iron matrix has the potential to dissolve an amount of oxidising solute higher than the iron oxide oxygen formation concentration, however this has never been found because the iron and oxygen react to form the oxides before this solid state limit is known, and as such the solubility limit is usually defined up to the point of oxide oxygen formation concentration. If this current system in question *is* subject to a surface oxygen partial pressure contributing to a maximum internal oxygen concentration higher than this iron oxide oxygen formation concentration then the enclosed zone will form iron oxides that eventually incorporate the previously formed aluminium oxide into an iron aluminate spinel $(Fe)(Fe, Al)_2O_4$ known commonly as hercynite with stoichiometric formula $FeAl_2O_4$ [5, 90]. This will continue until all the iron within the enclosed zone is oxidised. Aluminium from further into the steel could diffuse to the base of the dense internal oxide barrier - as the diffusion of a species is reliant on a chemical potential gradient which is generally related to the concentration gradient of the species. Aluminium has the potential to react with the iron oxides, and the miniscule oxygen concentration available at the barrier by the very slow diffusion across the thick oxide barrier. The chemical potential as a driving force for the accumulation of aluminium at the base of the enclosed zone is not well understood and is speculative, perhaps the aluminium enrichment [5, 6] is merely in the form of the relatively dense aluminium oxide increasing with depth to the point of prevention of oxygen penetration which could occur over a few microns. A brief investigation was conducted into either possibility during this project with the introduction of a vacuum stage during annealing to retain high diffusion speeds but reduce the internal oxygen content, conclusions were drawn that suggest there is more to investigate but this is not under the scope of this project.

Surface oxides containing both aluminium and iron will form subject to the thermodynamic equilibrium where the less stable oxides will form nearer the top of the scale [5, 6, 136-138]. This will occur from the presence of aluminium in the initial steel, and iron diffusion in the proceeding time-step after the aluminium flux to the surface is effectively ceased and is preoccupied by reaction in the IOZ. The continued

formation of surface oxides will further reduce the oxygen flux [5-7, 53, 136-138] into the material with different oxides affecting the situation across a range of magnitudes, this in turn can reduce the greatest potential depth of the dense internal oxide layer.

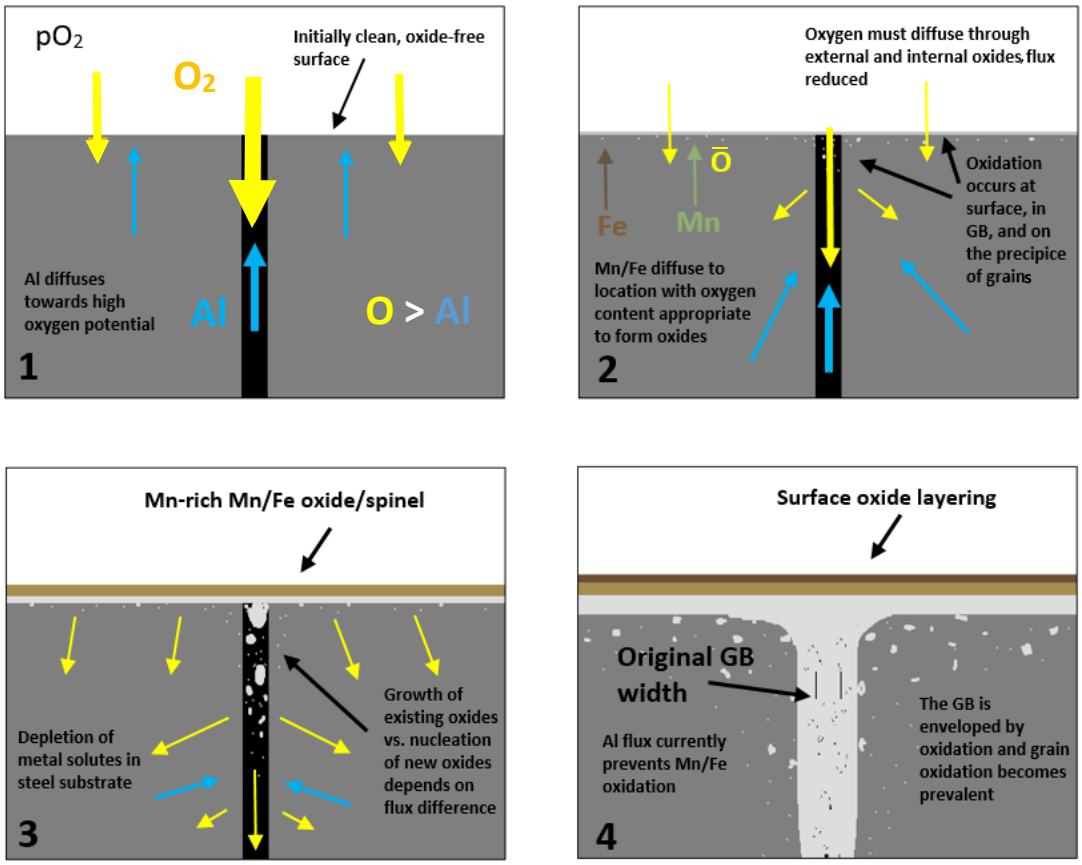

Figure 7.2 Nanoscopic schematic showing the initial stages of internal oxidation of Fe-Al-Mn-C steels when oxygen flux is higher than the metal solutes' flux. 1. A clean steel surface is exposed to an oxidant-containing atmosphere. 2. A thin surface aluminium oxide layer forms, oxygen penetrates the steel, mostly via the high diffusivity grain boundary causing more oxide nucleation there than the grain, aluminium flux is insufficient to form a dense protective oxide layer. 3. Oxygen transport through the grain boundary and grains continues with the extension of the reaction front. Surface oxidation of mostly manganese and some iron occurs. 4. The grain boundary oxidation extends laterally and becomes many times larger than the initial grain boundary width. Significant diffusion of manganese and iron to the surface has formed a relatively thick and layered scale.

7.1.3 Internal Oxidation, Single Phase Fe-Al-Mn

Restarting this scenario with a third component: manganese, the oxidation behaviour will follow a similar description but is subject to the additional oxide/spinel oxygen formation concentrations and the ratio of aluminium to manganese compared with

internal oxygen concentration. Oxygen penetrates the substrate reacting with aluminium in the local area with additional aluminium diffusing from elsewhere, the same as described before. The oxygen will continue to diffuse further into the steel, extending the internal oxidation zone. As the average depth of alumina IOZ is increasing, manganese oxide could diffuse to a location of suitable oxygen concentration, likely the surface if the internal oxygen concentration is being kept lower than the manganese oxide/spinel oxygen formation concentration due to alumina formation internally [107, 111, 120, 119]. Manganese can diffuse from the surrounding substrate and as the internal oxygen concentration increases due to continued exposure the manganese aluminate oxygen formation concentration will be reached and manganese oxide will form and be incorporated with alumina into the manganese aluminate spinel $(Mn)(Mn, Al)_2O_4$, commonly known as galaxite with stoichiometric formula $MnAl_2O_4$.

If the initial concentration of manganese is proportionally higher than the initial aluminium concentration for the total incorporation of the remaining aluminium oxide into the spinel, manganese oxide (MnO) will form where sufficient oxygen concentration exists, formed according to the usual oxygen gradient across the IOZ depth. The inclusion of manganese into the steel could have negative effects on the formation of the protective oxide layer, if manganese is incorporated into the scale the ability of the scale to protect the steel substrate from oxidation will be reduced from the maximum attributed to aluminium oxide alone; although there exists some uncertainty in misconstruing cause and effect as the evidence often associated with this could occur from when the penetration of oxygen into the steel prevents aluminium from reducing the surface manganese oxides and manganese is free to diffuse to the surface and react. Manganese oxide formation could reduce the IOZ depth as the formation of manganese oxides externally and internally will reduce the oxygen flux some measure via effective diffusivity decrease and chemical reaction; manganese inclusion in the steel could contribute to a reduced IOZ depth by this method and the subsequent formation of the dense internal oxide layer.

The formation of internal oxides can increase the lattice strain energy, providing a driving force for the diffusion for metal atoms. The volume expansion due to the internal oxide formation has been known to form pure iron nodules at the surface [103], this should be possible for manganese as it is a smaller atom and exhibits faster diffusion speed than iron in both FCC and BCC steel lattices. The net driving force for manganese diffusion to the surface could consist of both chemical potential and volume expansion components.

In these later stages of oxidation, as aluminium diffusion to the subsurface region is effectively stopped by reaction at the RF, higher oxide oxygen formation concentrations will be reached if the surface oxygen partial pressure is sufficient. Furthermore, if an enclosed zone is formed internally the oxide oxygen formation concentrations for all manganese and iron oxides will be reached, if sufficient surface oxygen partial pressure is applied, and the IOZ will consist of an iron-manganese aluminate spinel $(Fe, Mn, Al)_3O_4$. Depending on the partial pressure of oxygen at the surface and the magnitude of the volume expansion of oxides the surface will consist of iron and manganese oxides of a certain morphology.

7.1.4 Internal Oxidation, Dual Phase Fe-Al-Mn

Now considering a polycrystalline dual phase Fe-Al-Mn-C steel, the grain boundary defects must be considered. Overall, similar oxidation behaviour would occur in terms of effective diffusivity, thermodynamic reaction sequence, and scale growth – except with a high diffusivity pathway providing narrow corridors of extreme diffusivity values.

As discussed previously, a major factor in the diffusion speed of a species is the ability of an atom to translate to the next available vacancy, this incorporates the intermediate lattice and diffusing atoms sizes [5, 7, 53]. Larger atoms, both matrix atoms and the diffusing atom, will increase the energy requirements for diffusion as the space to move between is smaller, for this reason so too will the phase and

subsequently the density of the crystal affect the diffusion speed [5, 7, 53]. Austenite of FCC crystal structure has a higher crystal packing factor than ferrite of BCC crystal structure, as such austenite will require a diffusing atom to possess a higher energy than ferrite [76]. As the relevant crystal structure is the lowest energy form of the matrix atoms at the current system parameters they produce a crystal/grain with a near-perfect lattice structure, the matrix atoms are in a repeating order of units and are efficiently packed together, although this will be altered by any treatment the steel product is given such as cold working. Any other non-crystalline form of the same matrix atoms will by definition be less efficiently packed with the average distance between atoms being greater. This requires a diffusing atom to surmount a lower energy barrier on average thereby increasing the diffusivity of the species in that form - grain boundaries are such a defect as they are produced from the growth collision of multiple mismatched crystals [8].

Grain boundary diffusion is sensitive to impurities, adjacent crystal orientation, and temperature, etc. [157, 158]. The grain boundary is defined by its width, normally the grain boundary width is unknown, so values of 2 to 10 atom diameters are assumed [159, 160] with values used in literature ranging between 0.1 – 1 nm [7, 8, 65, 161]. Oxidation and corrosion attack generally occurs at the grain boundaries due to the faster diffusion speed, this is known as sensitisation and has been the subject of research for decades. The solute elements that do not easily inhabit the crystal segregate to the grain boundary during high temperature steel manufacturing, this has been studied extensively, and the segregation of the alloying elements is known to strongly affect the grain boundary diffusion rates [158, 159]. The relatively high proportion of additional metal solute elements in Fe-Al-Mn-C steels is believed to increase alloying element segregation [3] but the limits and common values are not well understood and have not been considered as a part of this present project. Any individual grain boundary's properties including element composition, atom packing efficiency, and width will be affected by the adjacent grains that produce it, e.g. two adjacent austenitic grains could produce a grain boundary of higher density than two adjacent ferritic grains. As the steels of this project exhibit a dual phase nature it is possible that the segregation is not homogeneous and any grain boundary could display any

given composition of aluminium, manganese, carbon, nitrogen, and silicon; this provides a complex system to investigate and mathematically model. Assumptions can be compensated for during model creation but the dual phase microstructure of the steels used in this project have likely lead to minor abnormalities in oxidation behaviour. The magnitude of the segregation effects on oxidation could be minor due to the miniscule size of grain boundaries, also the fast diffusion speed they provide could diminish this too through high contributions of metal solute flux from elsewhere. The scope of this project does not involve grain boundary segregation, the topic would have to involve k-carbide formation, a precipitate that is linked to higher aluminium content, above 2% [3], and many other mechanisms and parameters necessary to consider for such circumstances – although segregation of elements should be kept in mind by the reader.

The faster diffusion provided to atoms travelling through the grain boundaries, known as a fast diffusivity pathway, enables a more potent avenue of oxidation than the grain. The competition of metal solute and oxygen fluxes is given further treatment by C. Geers and I.Panas [162] to consider the role of high diffusivity pathways. Grain boundary contribution is dominant compared to the grain as the diffusivity ratio of grain boundary to grain can be several orders of magnitude. The size and shape of grains directly affect the oxidation behaviour that a material exhibits, with smaller grain sizes leading to a reduction in oxidation rate [107, 111,120,163]; as smaller grains are equivalent to more numerous grains for the same volume, more grains relates to more grain boundaries, therefore a higher proportion of high diffusivity pathways [164]. Although, there is a clear relation of grain size and oxidation rate, the grain boundaries operate as high diffusivity pathways for oxygen as well.

The above phenomenon seems to be more effective at increasing metal solute flux and there are three main rational possibilities for this, including but not limited to:

- Diffusivity: The increased average distance of atoms from grain to grain boundary, and the change in the ratio of the size of oxygen atoms to the size of the iron lattice atoms to the ratio of the size of the aluminium atoms to the size of the iron lattice atoms and the effect this has on the diffusivity pre-

exponent and activation energy of both diffusing atoms is more favourable for metal solute substitutional diffusion.

- Lattice solubility: BCC lattices contain more numerous octahedral interstices than FCC lattices but of a much smaller volume [7], a BCC unit cell contains 6 octahedral and 12 tetrahedral sites, whilst a FCC unit cell contains 4 octahedral and 8 tetrahedral sites [8, 64]. This correlates to a higher solubility of oxygen in ferrite than austenite [5], therefore perhaps whilst the diffusion speed of oxygen in ferrite is higher than austenite, the average oxygen gradient in ferrite than austenite is higher for the same surface oxygen partial pressure and the average distance across the lattice that an oxygen atom travels in one jump is less because of the greater number of interstitial sites in ferrite.

- Concentration: the increased aluminium concentration in ferrite is more significant to the total aluminium flux than the ratio of diffusivity increases.

The nanoscale size of grain boundaries means that their oxidising metal solute content is very low, this is provided by the adjacent grains acting as a reservoir of material due to their slow diffusivity as a medium and large comparative size. The concentration gradient across the grain will reach a homogenised state faster when the diffusion speed is faster and when the grain sizes are smaller, therefore in grains of slower diffusion speed such as austenite the concentration gradient will be narrower and on larger grains the concentration gradient will take longer to affect a significant proportion of the total material compared to a smaller grain. However, the overwhelming majority of metal solute inhabits the grains and even a small percentage of the whole is significant compared to the initial grain boundary concentration contribution. This relationship between grain/grain boundary

concentration contribution and kinetic properties can greatly affect the oxidation results and should be considered.

As the grains contribute the vast majority of total metal solute, a deviation between grain contents can affect the oxidation profile as well. Fe-Al-Mn-C dual phase steels have aluminium-rich ferrite and manganese-rich austenite grains at the industrial annealing temperatures, however both still retain a significant quantity of each minor component, e.g. the dual phase steel used in this project Fe-3Al-5Mn has ferritic (α) and austenitic (γ) compositions (wt.%), respectively: Al_{α} = 3.27, Mn_{α} = 3.39 and Al_{γ} = 2.51, Mn_{γ} = 6.17. Although the subsurface austenitic grains harbour less aluminium than the ferritic grains, the content is still appreciable and will provide a significant contribution in the total aluminium flux component via the grain boundaries. As the phase composition changes with temperature, and element composition through oxidation-related depletion, any transformation, recrystallization, and grain boundary pinning mechanics at play during the annealing process will affect the microstructure and subsequent total diffusivity ratio. Providing another mechanism by which the oxidation behaviour can be altered, any single heat treatment will impart a specific sequence of parameters and system conditions. Any number of these differences can also occur throughout the same specimen at individual points as the local microstructure varies.

The main parameters of the dual phase steel affecting oxidation are the adjacent grains' metal solute content and the crystal structure, this was expected to produce a heterogeneous surface oxide composition initially. This expectation of the initial surface oxidation is supported by the information and literature discussed so far [107, 111, 120], but the surface oxidation is coupled to the internal oxidation and this relationship is complex and the heterogeneity of the internal and external oxidation is seemingly minor.

The grain boundaries are the primary route of oxygen penetration into the steel and will be the site for oxide formation after the initial surface oxidation. The formation of external oxides will reduce the available surface oxygen dissolution sites and produce a medium of low oxygen diffusivity thereby decreasing the subsequent

maximum potential internal oxygen flux by both concentration and kinetic components. The parameters concerning element transport across growing scales are complex and the full scope is mostly beyond this project. The external oxides will continue to grow as metal solute atoms diffuse towards the surface, oxygen diffuses and reacts with the free metal solute atoms according to the local oxide formation concentration which can be located at several unique depths depending on the metal element, e.g. as aluminium has an incredibly high oxygen affinity it will react at the locations comprising any oxygen concentration in this system, as seen in Figure 2.1. Due to the very low aluminium oxide oxygen formation concentration the limit of the aluminium oxide formation reaction likely lies on other components such as the transport of material to the reaction site, hence the flux competition of aluminium and oxygen will provincially decide the depth of the internal oxidation zone.

As the formation of internal oxides is subject to the flux competition, the nature of oxidation can change according to the available material in the local area. Nucleation, the initial formation of a particle, is the main formation type of internal oxides when the oxygen diffusivity is high and will form many small particles; growth of existing particles becomes more prevalent as the flux of aluminium and oxygen tends towards equality. With a high surface partial pressure of oxygen and with the grain boundary diffusion speed of oxygen being many magnitudes higher than any metals', the oxygen will arrive at the local site of aluminium rather than aluminium being transported to the oxygen, this will nucleate an immobile oxide molecule [5, 6]. This can be expressed using the ratio of diffusive lengths seen in Equation 2.30 for oxygen to aluminium grain boundary diffusion which describes the distance an atom will diffuse in a 2D system over a specified duration, this ratio is 5.42. Oxygen will continue to diffuse internally along the grain boundaries primarily arriving at aluminium sites whilst the flux of aluminium to the high oxidation potential locations from the bulk steel will continue.

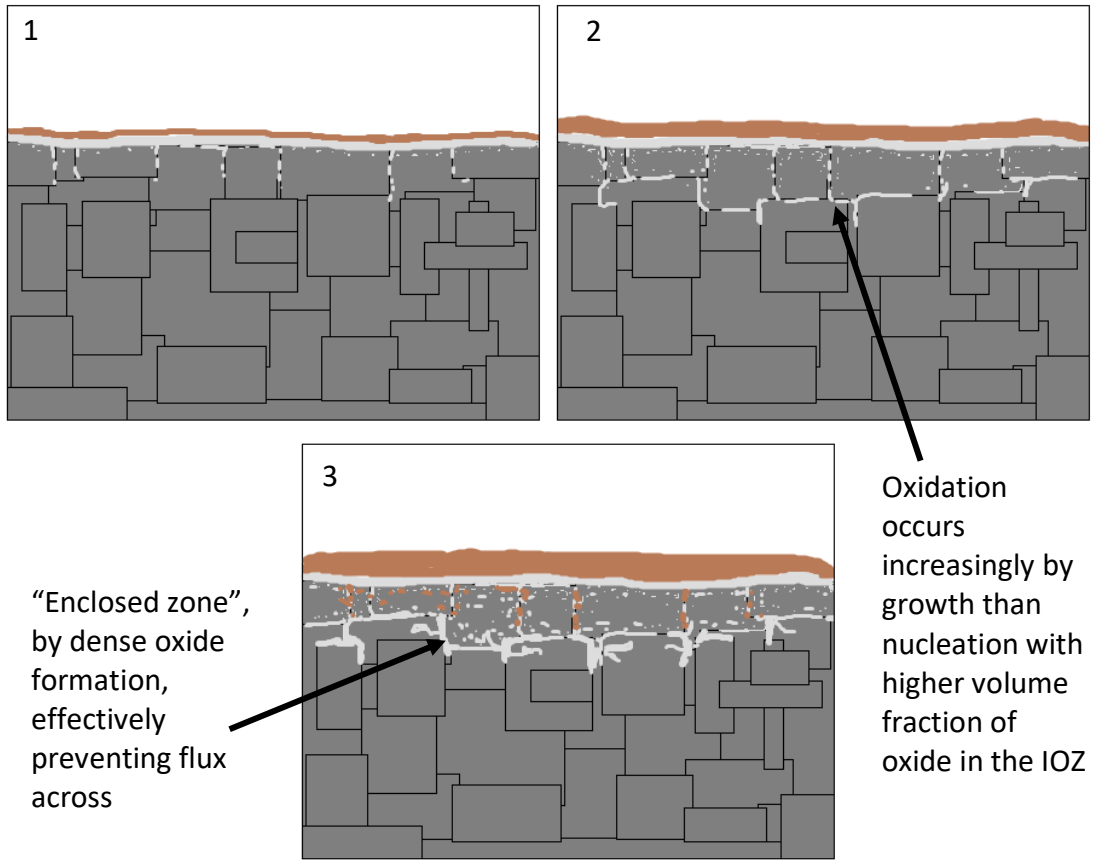

Figure 7.3 A microscopic schematic of the internal oxidation of a random Fe-Al-Mn-C microstructure. 1. Oxygen penetrates both grain boundaries and grains, oxidation of grain boundaries is faster and more prevalent with oxides nucleating at a greater depth, oxide growth is minor if oxygen flux is much higher than a proportional aluminium flux. External oxides consists of a thin alumina layer below a manganese-rich layer with some iron present. 2. External and internal oxidation continues, manganese-rich scale grows, the scale and internal oxides reduce oxygen flux, tending favour towards oxide growth, likely spherical particles in the grains become larger and grain boundary oxides are more connected with depth. 3. Flux equality has been reached in some areas, lateral growth of oxides occurs along applicable grain boundaries and invasion of adjacent grains occurs. Enclosed zones possible. Manganese aluminate formation conditions reached near the surface (high free oxygen, and depleted free aluminium)

The diffusive length ratio between aluminium grain boundary and grain diffusion is calculated to be 45 times [76], however this is using the methods of calculating grain boundary diffusion speeds detailed in Section 2.8 and incorporates a significant amount of uncertainty. Regardless, grain boundary diffusion is much higher than grain diffusion suggesting this could provide material for transport to the reaction zone from grains originating at a relatively large distance from the surface. For example, an aluminium atom over the course of 1 minute can travel in the grain boundary up to 23.1µm, whilst travelling 0.51µm in a grain. An aluminium atom at a

depth from the specimen surface of 20µm, with 0.2µm horizontally into an adjacent grain from the grain boundary could diffuse to the grain boundary then to the surface before an aluminium atom at a depth from the surface of 0.5µm diffuses vertically completely through the grain to the surface; mathematically this is due to the square root attached to the diffusive length formula. If this is possible then the internal oxidation of dual phase steels may not be greatly altered by the dual phase nature of the steel as the sum of metal solute contribution by the larger local area's phase composition dominates. Although the experimental results agree with this prediction, the diffusion data used in the model needs more research and clarification for Fe-Al-Mn-C steels.

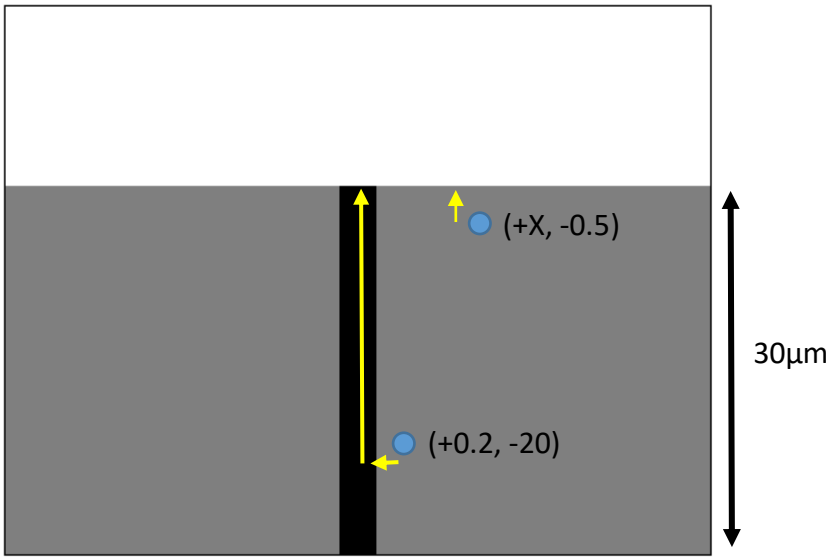

Figure 7.4 A schematic showing the distances two aluminium atoms could travel in one minute, where one atom is of coordinates: 0.5µm depth from the surface and Xµm within the grain, and the second atom is 0.2µm into the grain from the boundary and 20µm in depth

Continuing the scenario with a high partial pressure of oxygen, and high aluminium and manganese content, manganese will diffuse to a location which lacks significant aluminium - either a position internally with aluminium depletion and sufficient oxygen or the surface which aluminium is too preoccupied reacting at the RF to diffuse to. This produces the stark contrast of a majority external manganese/iron oxides and internal aluminium oxides produced with short annealing durations [107, 111, 119, 129].

The internal oxides continue to nucleate and grow increasing the IOZ, and the external scale is grown by the arrival of manganese and iron, further reducing the oxygen flux into the steel. Ultimately the reduction in oxygen flux into the steel will alter the balance of oxide formation to favour growth and will eventually reach equality with the aluminium flux which will create an oxide reaction zone that can spread on a general lateral trajectory, called an internal oxide barrier/layer. The grain boundary can be the site for creating a barrier and this barrier can sometimes occur vertically, however this is not a well-known phenomenon and a form of this called needle-shaped oxides might in fact exacerbate oxygen diffusion along the oxide-matrix interface. The creation of this internal oxide barrier is also modified by the dual phase nature of the steel where ferritic grains of high aluminium content and faster diffusivities can provide a higher flux than austenite. The tendency to form an internal oxide barrier will depend on the local phase and element compositions with a higher austenite and lower aluminium proportions resulting in an IOZ of greater depth. The internal barrier will have similar thermodynamic and kinetic consequences for the enclosed zone as mentioned above.

As the grain boundary provides a high diffusivity pathway, the oxygen penetration is massively increased, causing the oxidation of the initially dense steel substrate which transforms into an oxide product of lower density, this is volume expansion and leads to an increase in strain energy on the surrounding lattice that can be dispersed by several mechanisms the most important of which for oxidation purposes is the diffusion of metal to the surface forming pure metal or oxide nodules [105, 114]. This can occur inside the crystals, but the penetration of the grain boundaries is likely the most common initial locations and a sample with a higher ratio of grain boundaries to grains can significantly increase the rate of expansion. Atmospheres of oxygen partial pressure below the wüstite oxygen formation can form pure iron nodules at the surface through the reduction in lattice strain energy providing a driving force for iron diffusion. Discussed previously, this can be possible for manganese too, where a higher manganese flux could occur due to the additional lattice strain energy net driving force component alongside the chemical potential.

Oxidation and the related increase in volume fraction of oxide will continue to reduce the diffusion speed of oxygen, the IOZ will slowly grow inwards based on the miniscule flux across the internal oxide barrier whilst the enclosed zone will oxidise further, oxygen concentration permitting.

The existence and discussion of an internal oxide barrier is uncommon in oxidation research as it requires a metal solute that can form a dense oxygen-blocking oxide but of small enough concentration to not form a protective exclusive external scale, whilst incorporating a high temperature treatment with an oxygen exposure that lasts a short duration to interrogate the initial stages of oxidation. Most internal oxidation research focuses on external oxidation, and those that do look into internal oxidation focus on relatively long annealing durations.

The gap in knowledge that this thesis fills is apparent from the lack of comparisons to the published literature due to the vast array of conditions that significantly affect internal oxidation. The short annealing time, steel compositions, isothermal temperature, and modelling validation are the chief contributors of individuality of this industrially relevant project.

8. Final Conclusions

Experiments and modelling simulations have been conducted in order to investigate the effect that dual phase microstructure has on internal oxidation of Fe-Al-Mn-C dual phase steels with significant aluminium and manganese quantities and grain sizes up to 20µm in short annealing conditions with atmospheric water vapour. The specific variables that constitute this project's experiments are industrially focussed for the further investigation and subsequent implementation of low density Fe-Al-Mn-C steels which is hindered by the formation of internal and external oxides, reducing the wettability of protective zinc coatings and degradation of the finished product.

Experimental results suggest that the intergranular oxidation is not greatly affected on the Fe - (3 - 6 wt.%)Al - (5 – 15 wt.%) – C steels used in this project. The greater microstructure area is suggested to play a dominant role in the contribution of metal solute flux, this is counter to the hypothesis. Evidence of an apparent decrease in effective diffusivity of oxygen caused the lateral oxide growth into the adjacent grains from the grain boundaries. There also exists some measure of solute enrichment, seen by the significantly higher proportion of aluminium in the IOZ than either initial phase crystals comprise. The possibility of the aluminium flux contribution coming primarily from the immediate adjacent grains for the grain boundary oxidation and producing these oxidation profiles is unlikely, due to the much faster oxygen diffusion speed. Evidence suggests the individual oxides nucleated within grains all across the IOZ, without any apparent difference attributed to the different crystal phases. The most likely explanation is the grain oxides that nucleated separately are incorporated into the horizontally growing connected GB oxide, this could partially explain the seeming random direction of horizontal oxide growth.

The main conclusions that can be drawn from the results and work conducted in this project are as follows:

- The Fe-Al-Mn-C dual phase microstructure does affect the inter-granular oxidation behaviour. However, the grain boundary metal solute flux contributions are significant and dominate the internal oxidation behaviour due to the very fast diffusion speeds of both oxygen and aluminium. Affected by differences in grain sizes, and therefore total grain-boundary volume, the oxidation behaviour is more so altered by grain boundary - to - grain volume ratio than the differences in composition and diffusivity of ferrite and austenite in dual phase Fe-Al-Mn-C steels as the larger microstructure local area is suspected to provide a large cumulative role in metal solute flux than any two adjacent crystals.

- Effective diffusivity is a major component of the internal oxidation of the systems in question, this can be seen by the increasing connectivity of the oxide particles and the eventual “oxide barrier” forming and preventing further oxygen penetration, with an “enclosed zone” forming.

The knowledge generated by this project is specifically the affirmation of the roles of the effective diffusivity, oxygen and metal solute flux contributions, and the roles the grain boundary and grains play for the understanding of the internal oxidation behaviour of low density dual phase Fe-Al-Mn-C steels during short industrial annealing conditions with grain sizes up to 20μm.

9. Future Work

This project has been conducted with the aim of aiding industry in developing low density steels, mainly for automotive purposes related to carbon emissions. To continue along this avenue of research into low density dual phase Fe-Al-Mn-C steel internal oxidation, focus could be applied to those which relates to both the modelling and experimental aspects. The results from both the experiments and simulations of this project indicate some possible future projects:

- The investigation of the grain size on dual phase Fe-Al-Mn-C steel internal oxidation, to quantify a 'critical' grain size where the grain-boundary flux component is reduced to a point where the dual phase microstructure affects internal oxidation to a significantly visible degree. This would allow for the clarification of how large an effect the dual phase nature of the steel provides, which is not currently known for Fe-Al-Mn-C steels and it could help quantify diffusion coefficients needed for further research. This would also enable exploring the magnitude of the dual phase oxidation effects through manipulation of the phase fraction of ferrite-austenite.

- Research into the effect internal oxidation of Fe-Al-Mn-C steels has on the lattice strain energy and subsequent surface oxidation, by way of internal volume expansion. The diffusion of manganese and iron to the surface due to oxide volume expansion could lead to a greater depletion of metal from the IOZ, this could have microstructural consequences and therefore mechanical considerations for industry. Volume expansion due to internal oxidation is not a common area of research and the considerations for Fe-Al-Mn-C steels implementation could be significant.

- With current simulation software capabilities modelling the spatial occupation of a species in the microstructure for internal oxidation is not viable due to the massive resource requirements. However, the proper

implementation of effective diffusivity seems to rely upon the flux across the dense internal oxides in some fashion. Creating an internal oxidation model with spatial considerations could produce simulation results that accurately mimic the oxide growth when approaching flux equality. This new knowledge generated would further the entire field of internal oxidation knowledge by clarifying the magnitude of the effective diffusivity for different systems, relating to a precise model able to predict any system's IOZ depth.

10. References

1. World Steel Association. About Steel. https://www.worldsteel.org/about-steel.html.

2. Bel, T. The Modern Steel Manufacturing Process. https://www.thebalance.com/steel-production-2340173.

3. Chen, S., Rana, R., Haldar, A. & Ray, R. K. Current state of Fe-Mn-Al-C low density steels. *Prog. Mater. Sci.* **89**, 345–391 (2017).

4. Zambrano, O. A. "A General Perspective of Fe–Mn–Al–C Steels." Journal of Materials Science 53, no. 20 (2018): 14003–62. https://doi.org/10.1007/s10853-018-2551-6.

5. Young, D. J. *High Temperature Oxidation and Corrosion of Metals*. (2008).

6. Birks, N., Meier, G. F., *Introduction to the High Temperature Oxidation of Metals*. (Cambridge University Press, 2006).

7. Corris, R. A., Graham, M. J., Lindsay, R., Lyon, S. B., F. H. S. *Shreir's Corrosion - Volume 1: Basic Concepts, High Temperature Corrosion*. *Elsevier* vol. 1 (2013).

8. Callister, W. D. *Materials Science and Engineering An Introduction*. (John Wiley & Sons, Inc.).

9. MachineMFG. "Effects of Totally 48 Alloying Elements in Steel." Accessed December 12, 2020. https://www.machinemfg.com/alloying-elements-effects-on-steel/.

10. Satyendra Kumar, S., "Aluminum in Steels." Accessed December 12, 2020. https://www.ispatguru.com/aluminum-in-steels/.

11. Marshall, A. J., "Manganese Steel – 6 Things You Need to Know." Accessed January 11, 2021. https://ajmarshall.com/manganese-steel-6-things-you-need-to-know/#:~:text=%20%20%201%20What%20is%20manganese%20steel%3F%0AManganese,5%20How%20to%20weld%20manganese%20steel%20More%20

12. AZO Materials. "The Properties and Effects of Manganese as an Alloying Element." Accessed December 12, 2020. https://www.azom.com/article.aspx?ArticleID=13027

13. Free, M. “5 Facts About Manganese in Steel.” Accessed December 12, 2020. https://pmpaspeakingofprecision.com/2010/02/16/5-facts-about-manganese-in-steel/.

14. Frommeyer, G.; Brüx, U. Microstructures and mechanical properties of high-strength Fe-Mn-Al-C light-weight TRIPLEX steels. Steel Res. Int. 2006, 77, 627

15. Zhang, L.; Song, R.; Zhao, C.; Yang, F.; Xu, Y.; Peng, S. Evolution of the microstructure and mechanical properties of an austenite-ferrite Fe-Mn-Al-C steel. Mater. Sci. Eng. A 2015, 643, 183–193.

16. Wu, Z.Q.; Ding, H.; An, X.H.; Han, D.; Liao, X.Z. Influence of Al content on the strain-hardening behavior of aged low density Fe-Mn-Al-C steels with high Al content. Mater. Sci. Eng. A 2015, 639, 187–191

17. Kim, S.-H.; Kim, H.; Kim, N.J. Brittle intermetallic compound makes ultrastrong low-density steel with large ductility. Nature 2015, 518, 77–79.

18. Kim, H.; Suh, D.-W.; Kim, N.J. Fe-Al-Mn-C lightweight structural alloys: A review on the microstructures and mechanical properties. Sci. Technol. Adv. Mater. 2013, 14, 014205

19. Choi, K.; Seo, C.-H.; Lee, H.; Kim, S.K.; Kwak, J.H.; Chin, K.G.; Park, K.-T.; Kim, N.J. Effect of aging on the microstructure and deformation behavior of austenite base lightweight Fe-28Mn-9Al-0.8C steel. Scr. Mater. 2010, 63, 1028–1031.

20. Yoo, J. D., Hwang, S. W., Park, K. T., Origin of extended tensile ductility of a Fe-28Mn-10Al-1C steel. Metall Mater Trans A 2009;40:1520–3.

21. Cheng, W. C.; Lin, H. Y., The formation of austenite annealing twins from the ferrite phase during aging in an Fe-Mn-Al alloy. Mater. Sci. Eng. A 2003, 341, 106–111.

22. Chang, K. M., Chao, C. G., Liu, T. F., Excellent combination of strength and ductility in a Fe–9Al–28Mn–1.8C alloy. Scripta Mater 2010;63:162–5

23. Frommeyer, G., Brüx, U., Neumann, P., Supra-ductile and high-strength manganese-TRIP/TWIP steels for high energy absorption purposes. ISIJ Int 2003;43:438–46.

24. Schneider, A., Falat, L., Sauthoff, G., Frommeyer, G., Microstructures and mechanical properties of Fe3Al-based Fe–Al–C alloys. Intermetallics 2005;13:1322–31.

25. Ishii, H., Ohkubo, K., Miura, S., Mohri, T., Mechanical properties of a+c two-phase lamellar structure in Fe–Mn–Al–C alloy. Mater Trans 2003;44:1679–81

26. Chen, L., Zhao, Y. & Qin, X. Some aspects of high manganese twinning-induced plasticity (TWIP) steel, a review. ACTA METALL SIN 26, 1–15 (2013). https://doi.org/10.1007/s40195-012-0501-x

27. Rana, R., Liu, C., Ray, R. K., Low-density low-carbon Fe–Al ferritic steels. Scripta Mater 2013;68:354–9.

28. Brüx, U., Frommeyer, G., Jimenez, J., Light-weight steels based on iron-aluminium: Influence of micro alloying elements (B, Ti, Nb) on microstructures, textures and mechanical properties. Steel Res Int 2012;73:543–8.

29. Rana, R., Liu, C., Ray, R. K., Evolution of microstructure and mechanical properties during thermomechanical processing of a low-density multiphase steel for automotive application. Acta Mater 2014;75:227–45

30. Sohn, S. S., Lee, B. J., Lee, S., Kwak, J. H. Effect of Mn addition on microstructural modification and cracking behaviour of ferritic light-weight steels. Metall Mater Trans A 2014;45:5469–85

31. Sohn, S. S., Lee, B. J., Lee, S., Kim, N. J., Kwak, J. H., Effect of annealing temperature on microstructural modification and tensile properties in 0.35C–3.5Mn–5.8Al lightweight steel. Acta Mater 2013;61:5050–66.

32. Krivonogov, G. B., Alekseyenko, M. F., Solov'yeva, G. G., Phase transformation kinetics in steel 9G28Yu9MVB. Phys Met Metall 1975;4:86–92

33. Cheng, W. C., Phase transformations of an Fe-17.9Mn-7.1Al-0.85C austenitic steel after quenching and annealing. JOM 2014;66:1809–19

34. Sohn, S. S., Lee, B. J., Lee, S., Kwak, J. H., Effects of aluminium content on cracking phenomenon occurring during cold rolling of three ferrite-based lightweight steel. Acta Mater 2013;61:5626–35

35. Shin, S. Y., Lee, H., Han, S. Y., Seo, C. H., Choi, K., Lee, S., et al. Correlation of microstructure and cracking phenomenon occurring during hot rolling of lightweight steel plates. Metall Mater Trans A 2010;41:138–48

36. Seo, C. H., Kwon, K. H., Choi K., Kim, K. H., Kwak, J. H., Leed S., et al. Deformation behaviour of ferrite–austenite duplex lightweight Fe–Mn–Al–C steel. Scripta Mater 2012;66:519–22.

37. Krzanowski, J. E., The effects of heat-treatment and cold working on the room-temperature and cryogenic mechanical properties of Fe–30Mn–9Al–0.9C steel. Metall Trans 1988;19:1873–6

38. Oliver, D. A., Proposed new criteria of ductility from a new law connecting the percentage elongation with size of test-piece. Proc Inst Mech Eng 1928;2:827–64.

39. Krzanowski, J. E., The effects of heat-treatment and cold working on the room-temperature and cryogenic mechanical properties of Fe–30Mn–9Al–0.9C steel. Metall Trans 1988;19:1873–6.

40. Mohamadizadeh, A., Zarei-Hanzaki, A., Abedi, H. R., Mehtonen, S., Porter, D., Hot deformation characterization of duplex low-density steel through 3D processing map development. Mater Character 2015;107:293–301.

41. Lee, S., Jeong, J., Lee, Y. K., Precipitation and dissolution behaviour of j-carbide during continuous heating in Fe-9.3Mn-5.6Al-0.16C lightweight steel. J Alloys Compd 2015;648:149–53.

42. Jeong, J., Lee, C. Y., Park, I. J., Lee, Y. K., Isothermal precipitation behaviour of j-carbide in the Fe–9Mn–6Al–0.15C lightweight steel with a multiphase microstructure. J Alloys Compd 2013;574:299–304.

43. Chin, K. G., Lee, K. J., Kwak, J. H., Kang, J. Y., Lee, B. J., Thermodynamic calculation on the stability of (Fe, Mn)3AlC carbide in high aluminum steels. J Alloys Compd 2010;505:217–23.

44. Cheng, W. C., Song, Y. S., Lin, Y. S., Chen, K. F., Pistorius, P. C., On the eutectoid reaction in a quaternary Fe-C-Mn-Al alloy: austenite ? ferrite + kappa-carbide + M23C6 carbide. Metall Mater Trans A 2014;45A:1199–216.

45. Huang, H., Gan, D., Kao, P. W., Effect of alloying additions on the j phase precipitation in austenitic Fe-Mn-Al-C alloys. Scripta Metall Mater 1994;30:499–504

46. Jackson, P. R. S., Wallwork, G. R., High temperature oxidation of iron-manganese-aluminium based alloys. Oxidation Met 1984;21:135–70.

47. Kao, C. H., Wan, C. M., Effect of temperature on the oxidation of Fe-7.5Al-0.65C alloy. J Mater Sci 1988;23:1943–7.

48. Garcia, J. C., Rosas, N., Rioja, R. J., Development of oxidation resistant Fe-Mn-Al alloys. Met Prog 1982;122(3):47–50.

49. Gau, Y. J., Wu, J. K., The influence of alloying elements on the corrosion behaviour of Fe-Mn-Al alloys. Corr Prevent Cont 1997;44:55–60.

50. Tuan, Y. H., Wang, C. S., Tsai, C. Y., Chao, C. G., Liu, T. F., Corrosion behaviours of austenitic Fe–30Mn–7Al–xCr–1C alloys in 3.5% NaCl solution. Mater Chem Phys 2009;114:595–8.

51. Wang, C. S., Tsai, C. Y., Chao, C. G., Liu, T. F., Effect of chromium content on corrosion behaviours of Fe-9Al-30Mn-(3,5,6.5,8)Cr-1C alloys. Mater Trans 2007;48:2973–7.

52. Schmalzried, H. *Chemical Kinetics of Solids*. (VCH Verlagsgesellschaft).

53. Chieh, C. 'Chemical Equilibria - The Law of Mass Action' Chemical reactions, chemical equilibria, and electrochemistry. https://web.archive.org/web/20181003141012/http://www.science.uwaterloo.ca/~cchieh/cact/c123/massacti.html (2017).

54. Bale, C. W., Bélisle, E., Chartrand, P., Decterov, S. A., Eriksson, G., Gheribi, A. E., Hack, K., Jung, I. H., Kang, Y. B., Melançon, J.,Pelton, A. D., Petersen, S., Robelin, C., Sangster, J., P. S. and M.-A. V. E. FactSage Thermochemical Software and Databases - 2010 - 2016, Calphad, vol. 54, pp 35-53, 2016 <www.factsage.com>.

55. Andersson J.O., Helander T., Höglund L., Shi, P.F., and S. B. Thermo-Calc and DICTRA, Computational tools for materials science 2002. Calphad, 26, 273-312.

56. DerSilberspiegel. Ellingham Diagram. *Encyclopedia of Inorganic Chemistry* https://en.wikipedia.org/wiki/Ellingham_diagram#/media/File:Ellingham_Richardson-diagram_english.svg (2006) doi:10.1002/0470862106.id289.

57. Ellingham, H. J. T. Reducibility of oxides and sulphides in metallurgical processes. *J. Soc. Chem. Ind.* **63**, 125 (1944).

58. Sente Software Ltd. (2021) JMatPro® version 12.4 January 2021, http://www.sentesoftware.co.uk/

59. *Introduction to Aerospace Materials*. (Woodhead Publishing, 2012).

60. Caesar, A. G., Iron -Carbon Phase Diagram. https://en.wikipedia.org/wiki/File:Iron_carbon_phase_diagram.svg.

61. Diffusion of Metals: Factors and Atomic Models, Metallurgy. http://www.engineeringenotes.com/metallurgy/diffusion/diffusion-of-metals-factors-and-atomic-models-metallurgy/25600.

62. Heuer, A. H., Hovis, D. B., Smialek, J. L. & Gleeson, B., Alumina Scale Formation: A New Perspective. *J. Am. Ceram. Soc.* **94**, S146–S153 (2011).

63. Paul, A., Laurila, T., Vuorinen, V. & Divinski, S. V. *Thermodynamics, diffusion and the kirkendall effect in solids*. *Thermodynamics, Diffusion and the Kirkendall Effect in Solids* (2014).

64. Fisher, J. C., Calculation of diffusion penetration curves for surface and grain boundary diffusion. *J. Appl. Phys.* **22**, 74–77 (1951).

65. Le Claire, A. D., The analysis of grain boundary diffusion measurements. *Br. J. Appl. Phys.* **14**, 351 (1963).

66. Harrison, L. G., Influence of dislocations on diffusion kinetics in solids with particular reference to the alkali halides. *Trans. Faraday Soc.* **57**, 1191 (1961).

67. Hart, E. W., On the role of dislocations in bulk diffusion. *Acta Metall.* **5**, 597 (1957).

68. Zimbitas, G. & Sloof, W. G., Modeling internal oxidation of binary Ni alloys. *Mater. Sci. Forum* **696**, 82–87 (2011).

69. Trindade, V. B., Christ, H.-J. & Krupp, U., Computer-based simulation of kinetics of internal corrosion of engineering alloys at high-temperatures. *Metal. Mater.* (2009).

70. Auinger, M., Naraparaju, R., Christ, H. J. & Rohwerder, M., Modelling High Temperature Oxidation in Iron–Chromium Systems: Combined Kinetic and Thermodynamic Calculation of the Long-Term Behaviour and Experimental Verification. *Oxid Met* **76**, 247–258 (2011).

71. Mao, W., Ma, Y. & Sloof, W. G., Internal Oxidation of Fe–Mn–Cr Steels, Simulations and Experiments. *Oxid Met* **90**, 237–253 (2018).

72. Aghaei Lashgari, V., *Internal and External Oxidation of Manganese in Advanced High Strength Steels*. (2014).

73. De-Ping, L., Zhang, X.-F. & Yan, C., High temperature oxidation behavior of low density steel with high Al content. *J. Iron Steel Res.* **27**, 54–59 (2015).

74. Bedu-Amissah, K., Rickman, J. M., Chan, H. M. & Harmer, M., Impact of microstructure on grain-boundary diffusion in polycrystals. *J. Appl. Phys.* **98**, 063511 (2005).

75. Mehrer, H., *Numerical Data and Functional Relationships in Science and Technology, New Series, Group III: Crystal and Solid State Physics, Vol. 26, Diffusion in Metals and Alloys*. (Landolt-Bornstein, 1993).

76. Huin, D., Flauder, P. & Leblond, J. B., Numerical simulation of internal oxidation of steels during annealing treatments. *Oxid. Met.* **64**, 131–167 (2005).

77. Yin, H., Yuen, W. Y. D., & Young, D. J., Effects of water vapour and oxygen partial pressures on low carbon steel oxidation in N2-H2-H2O mixtures. *Mater. Corros.* **63**, 869–877 (2012).

78. Hooshyar, H. *et al.,* The Effect of H2 and H2O on the Oxidation of 304L-Stainless Steel at 600 °C: General Behaviour (Part I). *Oxid. Met.* **85**, 321–342 (2016).

79. Kavitha, R. & McDermid, J. R., On the in-situ aluminothermic reduction of manganese oxides in continuous galvanizing baths. *Surf. Coatings Technol.* **212**, 152–158 (2012).

80. Feulvarch, E., Finite element simulation of diffusion and precipitation with application to internal oxidation of Ni-Xwt%Cr alloys at 950°C. *Mater. Sci. Forum* **783**–**786**, 126–135 (2014).

81. Kirkaldy, J. S., Ternary diffusion and its relationship to oxidation and sulfidation. *Oxid. Met. Alloy. Douglass, ed., Am. Soc. Met. Met. Park* 101–114 (1971).

82. Bose, S. K. & Grabke, H. J., Diffusion coefficient of carbon in Fe-Ni austenite in the temperature range 950-1100 C. *Zeitschrift für Met.* **69**, 8–15 (1978).

83. Jao, C., Activity and diffusion of metals in binary aluminum alloys. (Illinois Institute of Technology, 1980).

84. Sieverts, A., The Absorption of Gases by Metals. *Zeitschrift für Met.* **21**, 37–46 (1929).

85. Burke, J., Solubility Parameters: Theory and Application. https://cool.culturalheritage.org/coolaic/sg/bpg/annual/v03/bp03-04.html (1984).

86. Wagner, C., *Zeitschrift für Elektrochemie* **63**, 772 (1959).

87. Task, M. N., Gleeson, B., Pettit, F. S. & Meier, G. H., Compositional factors affecting protective alumina formation under type ii hot corrosion conditions. *Oxid. Met.* **80**, 541–552 (2013).

88. Zhao, W., Kang, Y., Orozco, J. M. A. & Gleeson, B., Quantitative Approach for Determining the Critical Volume Fraction for the Transition from Internal to External Oxidation. *Oxid. Met.* **89**, 2157–2163 (2016).

89. Heuer, A. H., Oxygen and aluminum diffusion in α-Al2O3: How much do we really understand? *J. Eur. Ceram. Soc.* **28**, 1495–1507 (2008).

90. Van Orman, J. A. & Crispin, K. L., Diffusion in Oxides. *Rev. Mineral. Geochemistry* **72**, 757–825 (2010).

91. Hooshyar, H., High Temperature Corrosion of Stainless Steels in Low Oxygen Activity Environments. Chalmers University of Technology Department, 2016.

92. Tanaka, S., Watanabe, T., Terashima, K., and Yamazaki, T., Microstructural Change and Internal Oxidation of Fe-1.26 and 2.12mass %Al Alloys Oxidized in H 2 -H 2 O-Ar Gas Mixtures, Vo1.48, Na (1977).

93. Jin, X., Hu, G., Qian, H., and Wang, H., Effect of Dew Point on Galvanizability in 4 Mass% Al Added Low Density Steel. ISIJ International 58, no. 9 (2018): 1584–91. https://doi.org/10.2355/isijinternational.ISIJINT-2018-010.

94. Filipovic, L., "Simulating Oxide Growth Using Volume Expansion," Accessed 14. 04.2021, https://www.iue.tuwien.ac.at/phd/filipovic/node43.html.

95. Chen, Z., Wang, L., Yu, Z., Li, F., Sun, Z., Zhao, H., and Chou, K. C., Corrosion Process of Stainless Steel 441 with Heated Steam at 1,000 °C. High Temperature Materials and Processes 36, no. 7 (2017): 717–24. https://doi.org/10.1515/htmp-2015-0238.

96. Li, Z. F., Gao, Y., Cao, G. M., and Liu, Z. Y., High-Efficiency Reduction Behavior for the Oxide Scale Formed on Hot-Rolled Steel in a Mixed Atmosphere of Hydrogen and Argon. Journal of Materials Science 55, no. 4 (2020): 1826–39. https://doi.org/10.1007/s10853-019-04027-0.

97. Galerie, A., Toscan, F., Dupeux, M., Mougin, J., Lucazeau, G., Valot, C., Huntz, A.-M., and Antoni, L., Stress and Adhesion of Chromia-Rich Scales on Ferritic Stainless Steels in Relation with Spallation. Materials Research 7, no. 1 (2004): 81–88. https://doi.org/10.1590/s1516-14392004000100012.

98. Yamazaki, S., Takahashi, F., Kubota, T., and Yanagihara, K., Internal Oxidation of Fe-3%Si Alloys Annealed under H2O-H 2 Atmosphere. Materials and Corrosion 62, no. 6 (2011): 476–80. https://doi.org/10.1002/maco.201005862.

99. Yanagihara, K., and Yamazaki, S., Characterization of Oxidation Behavior at Fe-Si Alloy Surface. Nippon Steel Technical Report, no. 100 (2011): 27–32.

100. Jin, X. Y., Xie, Y. X., and Wang, H., Proc. 11th Int. Conf. on Zinc and Zinc Alloy Coated Steel Sheet (Galvatech 2017), The Iron and Steel Institute of Japan,Tokyo, (2017), 506.

101. Guruswamy, S., Park, S. M., Hirth, J. P., and Rapp, R. A., Internal Oxidation of Ag-in Alloys: Stress Relief and the Influence of Imposed Strain. Oxidation of Metals 26, no. 1–2 (1986): 77–100. https://doi.org/10.1007/BF00664274.

102. Wang, H., Jin, X., Hu, G., and He, Y., Changing Oxide Layer Structures with Respect to the Dew Point Prior to Hot-Dip Galvanizing of δ-TRIP Steel. Surface and Coatings Technology 337, no. September 2017 (2018): 260–69. https://doi.org/10.1016/j.surfcoat.2017.12.046.

103. Douglass, D. L. A Critique of Internal Oxidation in Alloys during the Post-Wagner Era. Oxidation of Metals 44, no. 1–2 (1995): 81–111. https://doi.org/10.1007/BF01046724.

104. Wang, C.-J., and Chang, Y.-C., Formation and Growth Morphology of Nodules in the High-Temperature Oxidation of Fe-Mn-Al-C Alloy. Materials Chemistry and Physics 77, no. 3 (2003): 738–43. https://doi.org/10.1016/S0254-0584(02)00134-7.

105. Bott, J. H., Subsurface Aluminum Nitride Formation in Iron-Aluminum Alloys. (Carnegie Mellon University, 2014).

106. Peng, W., Wang, J., Zhang, H., Hong, X., Wu, Z., Xu, Y., Li, J., and Xiao, X., Insights into the Role of Grain Refinement on High-Temperature Initial Oxidation Phase Transformation and Oxides Evolution in High Aluminium Fe-Mn-Al-C Duplex Lightweight Steel. Corrosion Science 126, no. March (2017): 197–207. https://doi.org/10.1016/j.corsci.2017.07.002.

107. Rapp, R. A., Kinetics, Microstructures and Mechanism of Internal Oxidation-Its Effect and Prevention in High Temperature Alloy Oxidation. Corrosion 21, no. 12 (1965): 382–401.

108. Cahn, R. W., Haasen, P., and Kramer, E. J., Materials Science and Technology, 2000.

109. I. Frenkel, Z. Physik. 35 (1926) 652; W. Schottky, C. Wagner, Z. Phys. Chem. B11 (1950) 163.; Wagner electrochem ref; High Temperature oxidation and corrosion of metals

110. Peng, W., Zhaoyu, W., Yulai, X., and Qingxuan, R., Internal Oxidation Behaviour of Fe-Mn-Al-C Duplex Light-Weight Steels with Good Combination of Strength and Ductility. Corrosion Science 120 (2017): 148–57.

111. Yang, F., Song, R., Li, R., Sun, T., and Wang, K., Tensile Deformation of Low Density Duplex Fe-Mn-Al-C Steel. Materials and Design 76 (2015): 32–39. https://doi.org/10.1016/j.matdes.2015.03.043.

112. Orman, J., Van, A., and Crispin, K. L., Diffusion in Oxides. Reviews in Mineralogy and Geochemistry 72 (2010): 757–825. https://doi.org/10.2138/rmg.2010.72.17.

113. Tomaszewicz, P., and Wallwork, G. R., Observations of Nodule Growth during the Oxidation of Pure Binary Iron-Aluminum Alloys. Oxidation of Metals 19, no. 5–6 (1983): 165–85. https://doi.org/10.1007/BF00666643.

114. Sauer, J. P., Rapp, R. A., and Hirth, J. P., Oxidation of Iron-Manganese-Aluminum Alloys at 850 and 1000°C. Oxidation of Metals 18, no. 5–6 (1982): 285–94. https://doi.org/10.1007/BF00656572.

115. Jackson, P. R. S., and Wallwork, G. R., High Temperature Oxidation of Iron-Manganese-Aluminum Based Alloys. Oxidation of Metals 21, no. 3–4 (1984): 135–70. https://doi.org/10.1007/BF00741468.

116. Bellhouse, E. M., and McDermid, J. R., Selective Oxidation and Reactive Wetting during Galvanizing of a CMnAl TRIP-Assisted Steel. Metallurgical and Materials Transactions A: Physical Metallurgy and

Materials Science 42, no. 9 (2011): 2753–68. https://doi.org/10.1007/s11661-011-0685-0.

117. Erhart, H., Wang, R., and Rapp, R. A., In Situ SEM Study of the High-Temperature Oxidation of an Fe-Mn-Al-Si Alloy. Oxidation of Metals 21, no. 1–2 (1984): 81–88. https://doi.org/10.1007/BF00659469.

118. Jeong, T. K., Jung, G., Lee, K., Kang, Y. B., Bhadeshia, H. K. D. H., and Suh, D.-W., Selective Oxidation of Al Rich Fe–Mn–Al–C Low Density Steels. Materials Science and Technology 30:14 (2014): 1805–14.

119. Peng, W., Yang, Z., Jia, G., Hu, G., Zhao, H., Wu, Z., Xu, W., Li, J., Xiao, X., and Dong, H., Distinct Oxidation Behaviour Attributed to Phase Constitution Transformation at Different Hot Processing Temperatures in Fe-10Mn-5.5Al-0.25C Steel. Corrosion Science 150, no. January (2019): 235–45. https://doi.org/10.1016/j.corsci.2019.01.045.

120. Auinger, M., Praig, V. G., Linder, B., and Danninger, H., (2015) Grain boundary oxidation in iron-based alloys, investigated by 18O enriched water vapour: the effect of mixed oxides in binary and ternary Fe-{Al, Cr, Mn, Si} systems. Corrosion Science, 96 . pp. 133-143. doi:10.1016/j.corsci.2015.04.009

121. Dogan, O. N, Michal, G. M., Kwon, H. W., Pinning of Austenite Grain 540 541 Boundaries by AlN Precipitates and Abnormal Grain Growth, Metall. 542 Mater. Trans. A 23 (1992) 2121-2129.

122. Liu, H., He, Y., Swaminathan, S., Rohwerder, M., and Li, L., Effect of Dew Point on the Surface Selective Oxidation and Subsurface Microstructure of TRIP-Aided Steel. Surface and Coatings Technology 206, no. 6 (2011): 1237–43. https://doi.org/10.1016/j.surfcoat.2011.08.038.

123. Hayashi, S., Competitive Effect of Water Vapor and Oxygen on the Oxidation of Fe-5wt.%Al Alloy at 1073 K., Oxidation of Metals 56, no. 3–4 (2001): 251–70. http://www.springerlink.com/index/V6784P37424511U6.pdf.

124. Tjong, S. C., and Swart, H. C., Auger Characterization of the Surface Oxidation of Austenitic Fe-26Mn-7Al-0.9C Alloy. Applied Surface Science 47, no. 4 (1991): 311–21. https://doi.org/10.1016/0169-4332(91)90084-W.

125. Swart, H. C., and Berning, G. L. P., Auger Electron Spectroscopy and X-Ray Photoelectron Spectroscopy Characterization of the Oxidation of Austenitic Fe-26Mn-7Al-0.9C Alloy in Atmosphere., Materials Chemistry &

Physics 41, no. 4 (1995): 251–56. https://doi.org/10.1016/0254-0584(95)01536-1.

126. Barella, S., Ciuffini, A. F., Gruttadauria, A., Mapelli, C., Mombelli, D., and Longaretti, E., Corrosion and Oxidation Behavior of a Fe-Al-Mn-C Duplex Alloy. Materials 12, no. 16 (2019). https://doi.org/10.3390/ma12162572.

127. Alaoui Mouayd, A., Koltsov, A., Sutter, E., and Tribollet, B., Effect of Silicon Content in Steel and Oxidation Temperature on Scale Growth and Morphology. Materials Chemistry and Physics 143, no. 3 (2014): 996–1004. https://doi.org/10.1016/j.matchemphys.2013.10.037.

128. Lindell, D., Ekman, T., and Pettersson, R., Fast and Efficient Annealing of Stainless Steel Strip Using Oxyfuel Burners. Steel Research International 86, no. 5 (2015): 557–66. https://doi.org/10.1002/srin.201400168.

129. Liu, S., Lee, C., Kao, C., and Perng, T., High-Temperature Oxidation Behavior of Two-Phase Iron-Manganese-Aluminum Alloys 56, no. 4 (2000): 339–49.

130. Gutierrez-Urrutia, I., and Raabe, D., Influence of Al Content and Precipitation State on the Mechanical Behavior of Austenitic High-Mn Low-Density Steels. Scripta Materialia 68, no. 6 (2013): 343–47. https://doi.org/10.1016/j.scriptamat.2012.08.038.

131. Vanden Eynde, X., Servais, J. P., and Lamberigts, M., Investigation into the Surface Selective Oxidation of Dual-Phase Steels by XPS, SAM and SIMS. Surface and Interface Analysis 35, no. 12 (2003): 1004–14. https://doi.org/10.1002/sia.1639.

132. Lins, V. D. F. C., Freitas, M. A., and e Silva, E. M. D. P., Oxidation Kinetics of an Fe-31.8Mn-6.09Al-1.60Si-0.40C Alloy at Temperatures from 600 to 900 °C." Corrosion Science 46, no. 8 (2004): 1895–1907. https://doi.org/10.1016/j.corsci.2003.10.015.

133. Huang, Z., Jiang, Y., Hou, A., Wang, P., Shi, Q., Hou, Q., and Liu, X., Rietveld Refinement, Microstructure and High-Temperature Oxidation Characteristics of Low-Density High Manganese Steels. Journal of Materials Science and Technology 33, no. 12 (2017): 1531–39. https://doi.org/10.1016/j.jmst.2017.09.012.

134. Tjong, S. C., SEM, EDX and XRD Studies of the Scales Formed on the Fe–Mn–Al–C System in Oxidizing–Sulphidizing Environments. X-Ray Spectrometry 20, no. 5 (1991): 225–38. https://doi.org/10.1002/xrs.1300200504.

135. Kavitha, R., and McDermid, J. R., On the In-Situ Aluminothermic Reduction of Manganese Oxides in Continuous Galvanizing Baths. Surface and Coatings Technology 212 (2012): 152–58. https://doi.org/10.1016/j.surfcoat.2012.09.038.

136. Liu, H., He, Y., and Li, L., Application of Thermodynamics and Wagner Model on Two Problems in Continuous Hot-Dip Galvanizing. Applied Surface Science 256, no. 5 (2009): 1399–1403. https://doi.org/10.1016/j.apsusc.2009.08.095.

137. Prabhudev, S., Swaminathan, S., and Rohwerder, M., Effect of Oxides on the Reaction Kinetics during Hot-Dip Galvanizing of High Strength Steels. Corrosion Science 53, no. 7 (2011): 2413–18. https://doi.org/10.1016/j.corsci.2011.03.027.

138. Neumaier, A., Mathematical Model Building, Chapter 3 in: Modeling Languages in Mathematical Optimization (J. Kallrath, ed.), Applied Optimization, Vol. 88, Kluwer, Boston 2004.

139. COMSOL Multiphysics® v. 5.5. www.comsol.com. COMSOL AB, Stockholm, Sweden.

140. Feulvarch, E., Finite Element Simulation of Diffusion and Precipitation with Application to Internal Oxidation of Ni-Xwt%cr Alloys at 950°C. Materials Science Forum 783–786 (2014): 126–35. https://doi.org/10.4028/www.scientific.net/msf.783-786.126.

141. Jaseliunaite, J., and Galdikas, A., Kinetic Modeling of Grain Boundary Diffusion: The Influence of Grain Size and Surface Processes. Materials 13, no. 5 (2020). https://doi.org/10.3390/ma13051051.

142. Naumann, R. J., Introduction to the Physics and Chemistry of Materials CRC Press, 2008, ISBN 978-1-4200-6134-5. Retrieved 15 April 2018.

143. Maxwell, J. C., 1904. A Treatise on Electricity and Magnetism. Oxford University Press. Cambridge, UK.

144. Lide, D. R., *CRC Handbook of Chemistry and Physics*. (CRC Press, 2004).

145. Zeiss Group, Fe-SEM Zeiss Sigma, Date accessed 14.04.21 https://www.zeiss.com/microscopy/int/products/scanning-electron-microscopes/sigma.html

146. Oxford Instruments, Aztec. Date accessed 14. 04. 21, https://nano.oxinst.com/campaigns/product/eds-for-sem-and-fib

147. Yoo, J. D., and Park, K. T., Microband-Induced Plasticity in a High Mn-Al-C Light Steel. Materials Science and Engineering A 496, no. 1–2 (2008): 417–24. https://doi.org/10.1016/j.msea.2008.05.042.

148. Wang, C. J., and Chang, Y. C., TEM Study of the Internal Oxidation of an Fe-Mn-Al-C Alloy after Hot Corrosion. Oxidation of Metals 57, no. 3–4 (2002): 363–78. https://doi.org/10.1023/A:1014834620707.

149. Su, C. W., Lee, J. W., Wang, C. S., Chao, C. G., and Liu, T. F., The Effect of Hot-Dipped Aluminum Coatings on Fe-8Al-30Mn-0.8C Alloy. Surface and Coatings Technology 202, no. 9 (2008): 1847–52. https://doi.org/10.1016/j.surfcoat.2007.08.011.

150. Ritchie, I. M., Metal Oxidation Kinetics and the Transition from Thin to Thick Films. A Journal of Theoretical Experimental and Applied Physics 19, no. 158 (1969): 421–22. https://doi.org/DOI: 10.1080/14786436908217798.

151. Samal, S., and Mitra, S. K., Influence of Grain Shape, Size, and Grain Boundary Diffusion on High-Temperature Oxidation of Pure Metal Fe, Cu, and Zn. Metallurgical and Materials Transactions A: Physical Metallurgy and Materials Science 46, no. 8 (2015): 3324–32. https://doi.org/10.1007/s11661-015-2987-0.

152. Trindade, V. B., Krupp, U., Hanjari, B. Z., Yang, S., and Christ, H. J., Effect of Alloy Grain Size on the High-Temperature Oxidation Behavior of the Austenitic Steel TP 347. Materials Research 8, no. 4 (2005): 371–75. https://doi.org/10.1590/S1516-14392005000400003.

153. Royal Society of Chemistry 2021. “Periodic Table.” Accessed April 14, 2021. https://www.rsc.org/periodic-table/.

154. Mark Winter, and WebElements. “Manganese: Radii of Atoms and Ions.” Accessed April 14, 2021. https://www.webelements.com/manganese/atom_sizes.html.

155. Mark Winter, and WebElements. “Iron: Radii of Atoms and Ions.” Accessed April 14, 2021. https://www.webelements.com/iron/atom_sizes.html.

156. Quadakkers, W. J., The Effect of Implanted Yttrium on the Growth and Adherence of Alumina Scales on Fe-20Cr-5Al 47 (1991): 261–72.

157. Quadakkers, W. J., Naumenko, D., Wessel, E., and Kochubey, V., Growth Rates of Alumina Scales on Fe – Cr – Al Alloys. Oxidation of Metals 61, no. February (2004): 17–37. https://doi.org/10.1007/s11085-005-8534-4.

158. Divinski, S. V., Lukianova, O. A., Wilde, G., Dash, A., Esakkiraja, N., Paul, A., High-Entropy Alloys: Diffusion, Reference Module in Materials Science and Materials Engineering, Elsevier, 2020, ISBN 9780128035818, https://doi.org/10.1016/B978-0-12-803581-8.11771-0.

159. French, D. N., Grain Boundaries, 1991. Accessed 14.04.21 https://www.nationalboard.org/Index.aspx?pageID=164&ID=194.

160. Heitjans, P., and Kärger, J., Diffusion in Condensed Matter: Methods, Materials, Models. Diffusion in Condensed Matter: Methods, Materials, Models, 2005. https://doi.org/10.1007/3-540-30970-5.

161. Geers, C., and Panas, I., Impact of Grain Boundary Density on Oxide Scaling Revisited. Oxidation of Metals 91, no. 1–2 (2019): 55–75. https://doi.org/10.1007/s11085-018-9867-0.

162. Samal, S., and Mitra, S. K., Influence of Grain Shape, Size, and Grain Boundary Diffusion on High-Temperature Oxidation of Pure Metal Fe, Cu, and Zn. Metallurgical and Materials Transactions A: Physical Metallurgy and Materials Science 46, no. 8 (2015): 3324–32. https://doi.org/10.1007/s11661-015-2987-0.

163. Study of Grain Boundary Character (Tomasz Arkadiusz Tański, Wojciech Borek), DOI: 10.5772/63043; ((Grain Boundary in Oxide Scale During High-Temperature Metal Processing By Xianglong Yu and Ji Zhou DOI: 10.5772/66211)) https://www.intechopen.com/books/study-of-grain-boundary-character/grain-boundary-in-oxide-scale-during-high-temperature-metal-processing

Appendix

Full parameters list

Name	***Expression***	***Value***	***Units***	***Description***
D0FefV	1.90*10^-4	1.90E-04	m^2/s	Fe in Ferrite Volume Diffusion D0
D0AlfV	1.80*10^-4	1.80E-04	m^2/s	Al "
D0MnfV	1.49*10^-4	1.49E-04	m^2/s	Mn "
D0OfV	1*10^-5	1.00E-05	m^2/s	O "
D0FeaV	1.80*10^-5	1.80E-05	m^2/s	Fe in Austenite Vol. Diffusion D0
D0AlaV	1.80*10^-4	1.80E-04	m^2/s	Al "
D0MnaV	1.60*10^-5	1.60E-05	m^2/s	Mn "
D0OaV	1.3*10^-4	1.30E-04	m^2/s	O "
D0FefGB	D0FefV*100	1.90E-02	m^2/s	Fe in Ferrite GB Diffusion Arrhenius D0
D0AlfGB	D0AlfV*100	1.80E-02	m^2/s	Al "
D0MnfGB	D0MnfV*100	1.49E-02	m^2/s	Mn "
D0OfGB	D0OfV*100	1.00E-03	m^2/s	O "
D0FeaGB	D0FeaV*100	1.80E-03	m^2/s	Fe in Ferrite GB Diffusion Arrhenius D0
D0AlaGB	D0AlaV*100	1.80E-02	m^2/s	Al "
D0MnaGB	D0MnaV*100	1.60E-03	m^2/s	Mn "
D0OaGB	D0OaV*100	1.30E-02	m^2/s	O "
QFefV	239500	239500	J/mol	Fe in Ferrite Vol. Activation Energy
QAlfV	228200	228200	J/mol	Al "
QMnfV	233600	233600	J/mol	Mn "
QOfV	111120	111120	J/mol	O "
QFeaV	270000	270000	J/mol	Fe in Austenite Vol. Activation Energy
QAlaV	228200	228200	J/mol	Al "
QMnaV	261700	261700	J/mol	Mn"
QOaV	166000	166000	J/mol	O "
QFefGB	QFefV/2	119750	J/mol	Fe in Ferrite GB Activation Energy
QAlfGB	QAlfV/2	114100	J/mol	Al "
QMnfGB	QMnfV/2	116800	J/mol	Mn "
QOfGB	QOfV/2	55560	J/mol	O "
QFeaGB	QFeaV/2	135000	J/mol	Fe in Austenite GB Activation Energy

QAlaGB	QAlaV/2	114100	J/mol	Al "
QMnaGB	QMnaV/2	130850	J/mol	Mn"
QOaGB	QOaV/2	83000	J/mol	O "
R	8.31445	8.31445	J/(mol*K)	Gas Constant
T	273.15+TC [K]	1123.15	K	Temperature (TC in K)
TC	850	850	°C	Temperature (C)
DFefV	(D0FefV)*exp(-(QFefV)/(R*T))	1.38E-15	m2/s	Fe in Ferrite Volume Diffusivity
DAlfV	(D0AlfV)*exp(-(QAlfV)/(R*T))	4.39E-15	m2/s	Al "
DMnfV	(D0MnfV)*exp(-(QMnfV)/(R*T))	2.04E-15	m2/s	Mn "
DOfV	(D0OfV)*exp(-(QOfV)/(R*T))	6.80E-11	m2/s	O "
DFeaV	(D0FeaV)*exp(-(QFeaV)/(R*T))	5.00E-18	m2/s	Fe in Austenite Volume Diffusivity
DAlaV	(D0AlaV)*exp(-(QAlaV)/(R*T))	4.39E-15	m2/s	Al "
DMnaV	(D0MnaV)*exp(-(QMnaV)/(R*T))	1.08E-17	m2/s	Mn "
DOaV	(D0OaV)*exp(-(QOaV)/(R*T))	2.48E-12	m2/s	O "
DFefGB	(D0FefGB)*exp(-(QFefGB)/(R*T))	5.12E-08	m2/s	Fe in Ferrite GB Diffusivity
DAlfGB	(D0AlfGB)*exp(-(QAlfGB)/(R*T))	8.89E-08	m2/s	Al "
DMnfGB	(D0MnfGB)*exp(-(QMnfGB)/(R*T))	5.51E-08	m2/s	Mn "
DOfGB	(D0OfGB)*exp(-(QOfGB)/(R*T))	2.61E-06	m2/s	O "
DFeaGB	(D0FeaGB)*exp(-(QFeaGB)/(R*T))	9.48E-10	m2/s	Fe in Austenite GB Diffusivity
DAlaGB	(D0AlaGB)*exp(-(QAlaGB)/(R*T))	8.89E-08	m2/s	Al "
DMnaGB	(D0MnaGB)*exp(-(QMnaGB)/(R*T))	1.31E-09	m2/s	Mn "
DOaGB	(D0OaGB)*exp(-(QOaGB)/(R*T))	1.79E-06	m2/s	O "
p	6800	6800	$kg*m^{-3}$	Avg density of LDS
pf	p*PratBF	6.25E+03	$kg*m^{-3}$	~ Density Ferritic Steel (Not LDS)
pa	p*PratFB	7.40E+03	$kg*m^{-3}$	" Austenite
PratBF	BCC/FCC	0.918919		BCC/FCC Packing Ratio
PratFB	FCC/BCC	1.088235		FCC/BCC "
FCC	0.74	0.74		FCC Packing Structure
BCC	0.68	0.68		BCC "
MmFe	55.845	0.055845	kg/mol	Molar Mass of Fe
MmAl	26.982	0.026982	kg/mol	Al "
MmMn	54.938	0.054938	kg/mol	Mn "
MmO	15.999	0.015999	kg/mol	O_2 "
MmC	12.011	0.012011	kg/mol	C "
MmAl2O3	(2*MmAl+3*MmO)	0.101961	kg/mol	Al_2O_4 "

MmMnAl2O4	(MmAl2O3+MmMnO)	0.172898	kg/mol	$MnAl_2O_4$ "
MmFeAl2O4	(MmAl2O3+MmFeO)	0.173805	kg/mol	$FeAl_2O_4$ "
MmMnO	(MmMn+MmO)	0.070937	kg/mol	MnO "
MmFeO	(MmFe+MmO)	0.071844	kg/mol	FeO "
GBrat	200	200		Grain/GB ratio factor
h_	10	10	µm	Model GB Height factor
GBw	((h_)/GBrat)	0.05	µm	Average GB Width
Lx	h_	10	µm	Base Length X (Horizontal)
Ly	h_*3	30	µm	Base Length Y (Vertical) (Input)
Lyt	Ly+(4*GBw)	30.2	µm	Base Length Y (Vertical) (True Ly)
Lz	h_	10	µm	Base Length Z (Depth (For 3D Model))
A_	Lx*Lyt	3.02E-10	m^2	Area of Model
V_	A_*Lz	3.02E-15	m^3	Volume of Model with Depth = Lz

AlWt	0.0475		Al Composition (Wt. % - From User)
MnWt	0.0485		Mn "
CWt	0.0016		C "
OthWt	0.0051		Other
FeWt	0.8873		Fe (Remainder)
CFef	110280	mol/m³	Fe Concentration in Ferrite Phase
CAlf	12578	mol/m³	Al "
CMnf	4878.8	mol/m³	Mn "
CCf	50.953	mol/m³	C "
CFea	106950	mol/m³	Fe Concentration in Ferrite Phase
CAla	10592	mol/m³	Al "
CMna	8562.8	mol/m³	Mn "
CCa	2842.1	mol/m³	C "
CFe	108610	mol/m³	Fe Conc. Ferrite – Austenite Average
CAl	11585	mol/m³	Al "
CMn	6719.8	mol/m³	Mn "
Nof	1.31E-06		Ferrite Oxygen Solubility [mole Fraction]
Noa	1.20E-06		Austenite "
COf	0.1665	mol/m³	Ferrite solubility [mol/m^3]
COa	0.1533	mol/m³	Austenite "
CsO	0.095331	mol/m³	Oxygen Surface Conc.
NOs	7.48E-07		Oxygen Surface Mole Fraction
pH2OpH2	0.1		Ratio of pH2O/pH2
cOox_Al2O3	4.19E-53	mol/m³	Al_2O_3 oxygen Dissociation Concentration
cOox_MnO	1.32E-18	mol/m³	MnO "
cOox_MnAl2O4	1.28E-23	mol/m³	$MnAl_2O_4$ "
cOox_FeOf	1.19E-14	mol/m³	FeOf "
cOox_FeOa	1.15E-14	mol/m³	FeOa "
cOox_FeAl2O4f	2.21E-15	mol/m³	$FeAl_2O_4$f "
cOox_FeAl2O4a	2.14E-15	mol/m³	$FeAl_2O_4$a "

MM	p*V_	2.05E-11	kg	Initial Mass of Model, with Volume V_
DL	2*((DOfGB*(37.328-37.244))^(1/2))	1.31E-06	µm	Diffusion Length
QLOf	-41.57	-41.57	kJ/mol	QL Ferrite
QLOa	-33.67	-33.67	kJ/mol	Austenite "
Na	6.02E+23	6.02E+23	1/mol	Avogadro's Constant
amu	1.66E-27	1.66E-27	kg	Atomic Mass Unit
VmAl2O3	1/(pAl2O3/MmAl2O3)	2.58E-05	m^3/mol	Al_2O_3 Molar Volume
VmMnAl2O4	1/(pMnAl2O4/MmMnAl2O4)	4.17E-05	m^3/mol	$MnAl_2O_4$ "
VmFeAl2O4	1/(pFeAl2O4/MmFeAl2O4)	3.96E-05	m^3/mol	$FeAl_2O_4$ "
VmMnO	1/(pMnO/MmMnO)	1.31E-05	m^3/mol	MnO "
Vmf	(1/(pf/MmFe))	8.94E-06	m^3/mol	Ferrite "
Vma	(1/(pa/MmFe))	7.55E-06	m^3/mol	Austenite "
pAl2O3	3950	3950	kg/mol	Al_2O_3 (Corundum) Density
pMnAl2O4	4150	4150	kg/mol	$MnAl_2O_4$ (Galaxite) Density
pFeAl2O4	4390	4390	kg/mol	$FeAl_2O_4$ (Hercynite) Density
pMnO	5430	5430	kg/mol	MnO (Manganosite) Density
CAl2O3max	pAl2O3/MmAl2O3	38740.3	mol/m^3	Max Al2O3 Conc.
CMnAl2O4max	pMnAl2O4/(MmMnO+MmAl2O3)	24002.59	mol/m^3	$MnAl_2O_4$ "
CFeAl2O4max	pFeAl2O4/(MmFeO+MmAl2O3)	25258.19	mol/m^3	$FeAl_2O_4$ "
CMnOmax	pMnO/MmMnO	76546.8	mol/m^3	MnO "
pO2FeOf	exp(2*rFeOf/(R*T))	1.67E-18	atm	FeO Ferrite Dissoc. pressure of Oxide
pO2FeOa	exp(2*rFeOa/(R*T))	1.57E-18	atm	Austenite "
pO2Al2O3	exp(2*rAl2O3/(R*T))	2.31E-62	atm	Al_2O_3 "

deltaHf	-155600	-155600	J/mol	Fe-O Ferrite Equilibrium Gibbs Enthalpy
deltaHa	-175100	-175100	J/mol	Austenite "
deltaSf	-81	-81	J/(mol*K)	Fe-O Ferrite Equilibrium Gibbs Entropy
deltaSa	-98.8	-98.8	J/(mol*K)	Austenite "
Nof	exp((-(deltaHf)+(T*deltaSf)+((1/2)*R*T*log(pO2FeOf)))/(R*T))	1.31E-06		Ferrite Solubility Limit mol Fraction
Noa	exp((-(deltaHa)+(T*deltaSa)+((1/2)*R*T*log(pO2FeOa)))/(R*T))	1.20E-06		Austenite "
COf	Nof*(CFe+CAl+CMn)	0.1665	mol/m³	Ferrite solubility [mol/m^3]
COa	Noa*(CFe+CAl+CMn)	0.1533	mol/m³	Austenite "
rAl2O3	(0.5*GAl2O3)-(GAl)-((3/2)*(GOg))	-662670	J	Al_2O_3 Delta Gibbs Energy of Formation
rMnO	GMnO-GMn-GOg	-302950	J	MnO "
rMnAl2O4	GMnAl2O4-GMn-GOg-GAl2O3	-329180	J	$MnAl_2O_4$ #1
rFeOf	GFeO-GFef-GOg	-191140	J	FeOf "
rFeOa	GFeO-GFea-GOg	-191420	J	FeOa "
rFeAl2O4f	GFeAl2O4-GFef-GOg-GAl2O3	-206850	J	$FeAl_2O_4$f "
rFeAl2O4a	GFeAl2O4-GFea-GOg-GAl2O3	-207130	J	$FeAl_2O_4$a "
KeqAl2O3	(exp((-rAl2O3)/(R*T)))	6.58E+30	J	Al_2O_3 reaction Equilibrium Constant
KeqMnO	(exp((-rMnO)/(R*T)))	1.23E+14	J	MnO "
KeqFeOf	exp((-rFeOf)/(R*T))	7.75E+08	J	FeOf "
KeqFeOa	exp((-rFeOa)/(R*T))	7.98E+08	J	FeOa "
KeqMnAl2O4	(exp((-rMnAl2O4)/(R*T)))	2.04E+15	J	$MnAl_2O_4$ "
KeqFeAl2O4f	(exp((-rFeAl2O4f)/(R*T)))	4.17E+09	J	$FeAl_2O_4$f "
KeqFeAl2O4a	(exp((-rFeAl2O4a)/(R*T)))	4.30E+09	J	$FeAl_2O_4$a "
cOox_Al2O3	((1/(KeqAl2O3*((CAl))))^(1.5))	4.19E-53	mol/m³	Al_2O_3 Oxygen dissoc. concentration
cOox_MnO	((1)/(KeqMnO*(CMn)))	1.32E-18	mol/m³	MnO "
cOox_MnAl2O4	((1)/(KeqMnAl2O4*((CMn)^2)))	1.28E-23	mol/m³	$MnAl_2O_4$ "
cOox_FeOf	((1)/(KeqFeOf*(CFe)))	1.19E-14	mol/m³	FeOf "
cOox_FeOa	((1)/(KeqFeOa*(CFe)))	1.15E-14	mol/m³	FeOa "
cOox_FeAl2O4f	((1)/(KeqFeAl2O4f*(CFe)))	2.21E-15	mol/m³	$FeAl_2O_4$f "
cOox_FeAl2O4a	((1)/(KeqFeAl2O4a*(CFe)))	2.14E-15	mol/m³	$FeAl_2O_4$a "
CsO	(10^((log10(pH2OpH2))-(4050/T)-1.52))*	0.095331	mol/m³	Oxygen Surface Conc.

	(CFe+CAl+CMn)			
NOs	(10^((log10(pH2OpH2))-(4050/T)-1.52))	7.48E-07		Oxygen Surface Mole Fracton
pH2OpH2	0.1	0.1		Ratio of pH2O/pH2
DOOx	(D0OOx/GBw)*exp(-QOOx/(R*T))	1.16E-27	m^2/s	Oxygen Diffusivity in Oxides
D0OOx	8.40E-06	8.40E-06	m^2/s	D0 "
QOOx	627000	627000	J/mol	Activation energy "

vAl2O3		1.5		Al_2O_3 ratio oxygen to metal
vMnAl2O4		1.3333		$MnAl_2O_4$ "
vFeAl2O4		1.3333		$FeAl_2O_4$ "
vMnO		1		MnO "
CAlf	CAl*(1+Ck)	13861	mol/m^3	Al Ferrite Equilibrium Additions
CMnf	CMn-(CAl*Ck)	4928.7	mol/m^3	Mn Ferrite Equilibrium Subtractions
CAla	CAl*(1-Ck)	11341	mol/m^3	Al Austenite Equilibrium Subtractions
CMna	CMn+(CAl*Ck)	7448.9	mol/m^3	Mn Ferrite Equilibrium Additions
Ck	0.1	0.1	mol/m^3	Equilibrium Solute Difference Fraction